Technische Universität München
TUM School of Engineering and Design

Model-based Control for the Improvement of the Operating Strategy of Fuel Cell Systems

Maximilian Karl Eisner

Vollständiger Abdruck der von der TUM School of Engineering and Design der Technischen Universität München zur Erlangung eines

Doktors der Ingenieurwissenschaften (Dr.-Ing.)

genehmigten Dissertation.

Vorsitz: Prof. Dr. Malte Jaensch

Prüfende der Dissertation:

1. Prof. Dr.-Ing. Dr. h.c. Ralph Kennel
2. Prof. Dr.-Ing. Kai-Olaf Hinrichsen

Die Dissertation wurde am 15.05.2024 bei der Technischen Universität München eingereicht und durch die TUM School of Engineering and Design am 08.10.2024 angenommen.

Acknowledgment

The findings in the present work were compiled during my three-year doctorate at the BMW Group in collaboration with the Technical University of Munich. During this challenging time, I received a lot of support from various people, whom I would like to thank from the bottom of my heart.

In particular, I thank my doctoral supervisor Prof. Kennel. Initially, he gave me the opportunity to pursue this work, even though he did not know me beforehand and despite my lack of prior experience in control engineering. He further supported me during my doctorate with constant feedback on my work and always reassured me that it would be a success.

In the same way, I wish to express my gratitude to Prof. Hinrichsen for taking over as second examiner in my doctoral examination. Thank you also for accompanying me during my studies in chemical engineering not only as a professor but also as a mentor within the Max Weber Program. My sincere thanks also go to Prof. Jaensch, the chair of my doctoral examination.

In a work like this, small nudges in the right direction are often all it takes to find the solution to a seemingly impossible challenge. In this context, I would like to thank Prof. Tor A. Johansen for sharing his insights in the field of explicit nonlinear model predictive control, which helped me find a solution to my optimization problem. Similarly, I thank Valentin Krespach for his brief introduction to the world of neural networks and for introducing me to Keras.

As in many areas of life, thorough preparation is the key to success with a doctorate. A big thank you therefore goes out to my two Master's thesis supervisors Robert Kender and Felix Rößler, who prepared me thoroughly for all the upcoming aspects of my doctorate by constantly challenging and encouraging me.

During my three years in the fuel cell department at the BMW Group, I had many helpful and supportive colleagues. First and foremost, however, I thank my supervisors Zheng Zhou and Volker Formanski. Zheng, without your constant support in all aspects of control engineering in general and air control in the fuel cell system in particular, I would probably not have been able to complete any part of my work. And Volker, your constant challenges helped me to stay focused on the main objectives of the work, and sharing your immense knowledge on all topics related to fuel cells was one of the key factors that made this work a success.

And although I definitely spent a lot of time on my dissertation, I wouldn't have made it over the finish line without the balance that my friends and family gave me. Thank you so much for that! In particular, I would like to thank my long-term flatmate Daniel

Siebe, with whom I not only spent a lot of my free-time, but who also tolerated me during my most stressful times. Last but certainly not least, I would like to thank my parents and my sisters, who have supported me through all the ups and downs in the three years I have been working on this thesis and have always been there for me.

Abstract

The present experimental study demonstrates the benefits of applying linear and nonlinear model predictive control to an automotive fuel cell system. The examined fuel cell system is part of the powertrain of the BMW iX5 Hydrogen, a recently developed fuel cell electric vehicle. The overall dynamic behavior of this fuel cell system is limited by the cathode subsystem, which is why air supply and hydrogen dilution control are mainly considered in this study. The controlled variables are two air mass flows, which are manipulated with the quadrature current of the air compressor motor and the position of the bypass valve. The application of a model predictive controller requires the repeated optimization of a cost function, which is not real-time capable on the electronic control unit of the fuel cell system. Instead, the explicit solution to the optimization problem is implemented. The exact explicit solution is available for linear model predictive control, whereas the explicit solution to the nonlinear model predictive control problem is approximated with a neural network.

The parameters of each cost function are adjusted through closed-loop simulations before the explicit solution is determined. Thus, a semi-empirical simulation model is developed in this work, which includes the fundamental dynamic and stationary correlations between the controlled air mass flows and the control variables. The accuracy of the proposed model is validated with measurements from a fuel cell system test stand and the fuel cell electric vehicle. The established model correctly predicts the dynamics of the cathode subsystem, and the low computational cost of the zero-dimensional approach outweighs the stationary deviations.

In the first step, the explicit linear and the explicit nonlinear model predictive controller are validated individually on the fuel cell system test stand and in the BMW iX5 Hydrogen. Then, the two proposed controllers are compared to the reference control setup with two PI controllers. On the one side, the high accuracy of the nonlinear prediction model decreased the impact of perturbations on the closed-loop behavior, which is why the nonlinear outperforms the linear model predictive controller. On the other side, the accurate representation of the dynamic correlations in the nonlinear prediction model improved the transient behavior of the fuel cell system in comparison to the two PI controllers.

Eventually, the nonlinear model predictive controller is extended to include the fuel cell system net power as a controlled variable. This approach further optimizes the dynamics of the fuel cell system within the boundaries of the operating range, which is demonstrated with closed-loop simulations.

Contents

Symbols

Latin Symbols

A	opening area	m^2
$\boldsymbol{A}$	state matrix	-
a	water vapor activity	-
$\boldsymbol{B}$	input matrix	-
$\boldsymbol{C}$	output matrix	-
C_{AirBear}	air bearing flow factor	m^2
C_{d}	discharge coefficient	$\frac{\mathrm{m}^2}{\mathrm{s}}$
C_{Trq}	torque model parameter	-
c_p	specific heat capacity at constant pressure	$\frac{\mathrm{J}}{\mathrm{kg\,K}}$
c_v	specific heat capacity at constant volume	$\frac{\mathrm{J}}{\mathrm{kg\,K}}$
$\boldsymbol{D}$	feedthrough matrix	-
d	diameter	m
$\hat{d}$	perturbation	-
F	Faraday constant	$\frac{\mathrm{s\,A}}{\mathrm{mol}}$
$\bar{g}$	equality constraint	
$\tilde{g}$	inequality constraint	
I	electric current	A
i_q	quadrature current	A
J	MPC cost function	-
J_{Cmpr}	compressor intertia	$\mathrm{kg\,m}^2$
$\mathcal{L}$	Lagrangian function	-
$\boldsymbol{L}_{\mathrm{d}}$	observer gain matrix	-
$\bar{M}$	molar mass	$\frac{\mathrm{g}}{\mathrm{mol}}$
Ma	mach number	-
$\dot{m}$	mass flow	$\frac{\mathrm{kg}}{\mathrm{s}}$
$\dot{\tilde{m}}$	scaled mass flow	$\frac{\mathrm{kg}}{\mathrm{s}}$
N_u	control horizon	-

N_y	prediction horizon	-
n	quantity	-
n_{Cmpr}	compressor rotational speed	$\frac{1}{\mathrm{min}}$
$\tilde{n}$	scaled rotational speed	$\frac{1}{\mathrm{min}}$
P	power	W
$\boldsymbol{P}$	terminal weight matrix	-
p	pressure	Pa
p_{rat}	pressure ratio	-
pos	position	-
$\boldsymbol{Q}$	control deviation weight matrix	-
R	specific gas constant	$\frac{\mathrm{J}}{\mathrm{kg\,K}}$
$\boldsymbol{R}$	control effort weight matrix	-
T	temperature	K
t	time	s
t_{d}	time delay	s
U	voltage	V
$\boldsymbol{U}$	MPC optimization variable	-
$\boldsymbol{U}^*$	optimized $\boldsymbol{U}$	-
U_{c}	compressor blade tip speed	$\frac{\mathrm{m}}{\mathrm{s}}$
$\left(\frac{U}{C}\right)_{\mathrm{Trb}}$	blade speed ratio	-
u_q	quadrature voltage	V
u	input variable	-
V	volume	m^3
x	state variable	-
y	output variable	-
y_i	molar fraction of component i in gas phase	-

Greek Symbols

γ	ratio of heat capacities	-
Δ	difference	-
δ	corrected pressure	-
ϵ	relative tolerance	-
η	efficiency	-
Θ	set of feasible parameter $\boldsymbol{\theta}$	-
θ	corrected temperature	-

$\boldsymbol{\theta}$	parameter vector explicit MPC	-
λ_{H_2}	hydrogen excess ratio	-
λ_{O_2}	oxygen excess ratio	-
ρ	density	$\frac{\mathrm{kg}}{\mathrm{m}^3}$
σ	weighted sum	-
τ	torque	$\mathrm{N\,m}$
Φ	normalized mass flow	-
φ	opening angle	$^\circ$
Ψ	dimensionless head parameter	-
ψ_{Mem}	fuel cell membrane humidity	-
ω	rotational speed	$\frac{\mathrm{rad}}{\mathrm{s}}$

Subscript Indices

Air	air
AirBear	air bearing
AirFil	air filter
Amb	ambient condition
An	anode
BPV	back pressure valve
Byp	cathode bypass
BypVlv	cathode bypass valve
Ca	cathode
Cell	fuel cell
Cmpr	air compressor
CmprMo	air compressor motor
Con	constraints
Cool	coolant
Data	data points
Dil	dilution
Exh	exhaust gas
FCS	fuel cell system
H_2	hydrogen
$H_2O\,(v)$	water vapor
HByp	humidifier bypass valve
Hmdf	humidifier

Is	isentropic
Max	maximum
Min	minimum
Noz	nozzle
O_2	oxygen
Op	operating
PT	polytopes
Sm	supply manifold
Srg	air compressor surge
Stck	fuel cell stack
Trb	turbine
Vlv	valve
VMf	Venturi mass flow sensor
VTG	variable turbine geometry

Superscript Indices

corr	correction
crit	critical
dry	dry
eff	effective
el	electric
expl	explicit solution of MPC optimization problem
ff	feedforward
impl	implicit solution of MPC optimization problem
in	inlet
meas	measured
mech	mechanic
norm	normalized
out	outlet
reac	reacted
ref	reference
sp	setpoint
wet	wet

Abbreviations

ANN	artificial neural network

BEV	battery electric vehicle
BPV	back pressure valve
CAN	controller area network
CPC	constrained predictive control
CWS	cathode water separator
DMC	dynamic matrix control
ECU	electronic control unit
FCEV	fuel cell electric vehicle
FCS	fuel cell system
GPC	generalized predictive control
HV	high voltage
LP	linear programming
LTI	linear time-invariant
MFC	mass flow controller
MIMO	multiple-input-multiple-output
mp	multi-parametric
MPC	model predictive control
NLP	nonlinear programming
NMPC	nonlinear model predictive control
NN	neural network
OCV	open circuit voltage
ODE	ordinary differential equation
PDE	partial differential equation
PEM	polymer electrolyte membrane
PMSM	permanent magnet synchronous motor
PWA	piecewise affine
pQP	parametric quadratic programming
QP	quadratic programming
RBF	radial basis function
ReLU	rectified linear unit
RMSE	root-mean-square error
SMC	sliding mode control
SOC	state-of-charge

TWS	turbine water separator
VTG	variable turbine geometry

1 Introduction

In the scientific community, human-made climate change is a clear consensus [75]. Nevertheless, global CO_2 emissions continue to rise, despite the significant impact of greenhouse gases on global warming. In 2022, CO_2 emissions grew by 0.9 % in comparison to 2021 [51], with the transportation sector accounting for as much as 50 % of this increase. At 77 %, road transport remained the leading contributor to the total CO_2 emissions of the transport sector [50]. Hence, electrified powertrains have substantially increased in market share over the recent years to reduce these emissions. The highest potential is attributed to battery electric vehicles (BEVs), especially in the passenger car segment. In 2022, 70 % of the 26 million electric vehicles worldwide were BEVs [52]. Nevertheless, fuel cell electric vehicles (FCEVs) can complement BEVs in decarbonizing the road transport sector [100]. Possible use cases include regions with limited access to renewable energy sources, which will heavily rely on energy imports. These imports will most likely come in the form of hydrogen. Additionally, applying hydrogen as a power source reduces the strain on electric grids. As a result, the transition towards an emission-free road transport sector can be accelerated.

In this work, the BMW iX5 Hydrogen was considered an example of a state-of-the-art FCEV. This vehicle was initially presented on the IAA Mobility 2021 in Munich, and in 2023, the BMW Group announced the launch of a pilot fleet.

1.1 Motivation

The viability of FCEVs as a supplement to BEVs depends significantly on the purchase price and the offered performance, i.e., the associated driving pleasure and the vehicle range and refueling time. A possible cost reduction factor is the secondary power source in the vehicle powertrain, which is often a high-voltage battery with a high power output at the cost of a low capacity. This battery buffers the transients that the fuel cell system (FCS) does not achieve. As a result, optimized FCS dynamics enable batteries with a reduced capacity and peak power. This capacity reduction additionally enlarges the accessible storage space for hydrogen, extending the available vehicle range. Furthermore, the vehicle range depends considerably on the efficiency of the FCS as the primary energy source of the FCEV powertrain. This efficiency is partly enhanced by optimizing the hardware components. Nevertheless, optimal FCS control is the decisive factor for high system efficiencies. Moreover, proper controlling of the fuel cell stack and the necessary auxiliary components is crucial to achieve rapid FCS dynamics.

Model predictive control (MPC) is a promising approach for optimally controlling the

FCS. This advanced control method relies on system models predicting future trajectories of the controlled variables in dependence on the considered control variables. During operation, these predicted trajectories are optimized by minimizing a cost criterion while taking into account the system constraints. Furthermore, MPC allows the integration of multiple control and controlled variables into one controller. As a result, cross-coupling between the various control tasks is considered, which occurs throughout the FCS with its multiple subsystems and the high number of actuators. Another benefit of MPC is the easy transferability to modified systems, which is necessary for the automotive sector due to its short development cycles and the scalability requirements of the components. In general, only the modified system parts must be updated in the model, while the overall control setup and the controller parameter values are retained.

1.2 Contributions and Thesis Overview

The main goal of this work is to improve the closed-loop behavior of the FCS in the BMW iX5 Hydrogen. More precisely, the dynamics of the FCS net power are considered, which are decisive for the performance of the FCEV powertrain. The cathode subsystem is the limiting subsystem in the dynamic response of the FCS, which is why air mass flow control is considered the primary control task in this work.

In most past studies on FCS air mass flow control, the only considered control target has been the air mass flow supplied to the fuel cell stack. By contrast, the cathode subsystem in an FCEV is also responsible for diluting hydrogen in the exhaust gas. In the closed anode subsystem, nitrogen and water accumulate over time and reduce the concentration of hydrogen. Therefore, gas is frequently released from the anode subsystem, removing the excess nitrogen and water. The remaining hydrogen in these gas flows must be diluted, ensuring compliance with safety regulations. Thus, one contribution of this work is the additional consideration of hydrogen dilution control in the FCS air mass flow controller.

The development of a model-based hydrogen dilution controller also requires a simulation model with a detailed air exhaust path, which is not considered in many established control-oriented FCS models. In this work, the air exhaust path includes the wet side of the membrane humidifier as well as a humidifier bypass valve, a turbine with variable turbine geometry (VTG) and an exhaust with a significant pressure loss.

The aforementioned simulation model is also a prerequisite for developing an explicit MPC, which facilitates real-time capability on the limited computational resources of an electronic control unit (ECU). At first, an explicit linear MPC was implemented, a well-established control method. In FCS control, explicit linear MPC has been applied in simulations and on test stands, whereas this work extends the scope to FCEVs, using the BMW iX5 Hydrogen as an example. By contrast, the second approach of approximating an explicit nonlinear MPC (NMPC) with a neural network is not as common, and this approach has yet to be applied to FCS control. Furthermore, the development of a linear and a nonlinear MPC for the same FCS allows an in-depth

comparison of both approaches.

The present work also implemented an extension of the NMPC to include FCS net power control. Accordingly, the principle difference to previous studies on FCS net power control is the additional consideration of hydrogen dilution control. Hence, another contribution of this study is the discussion on the implications on the control of the FCS net power.

This work is structured as follows. At first, the fundamentals of explicit linear and nonlinear MPC are introduced in Chapter 2 alongside the applied nomenclature. Subsequently, the literature on FCS control is reviewed, and the FCS of the BMW iX5 Hydrogen, together with the FCS net power control architecture, is presented in Chapter 3. The closed-loop simulations in this work were conducted with a lumped parameter model, which is established in Chapter 4. The simulation model was also validated with measurements from an FCS test stand and the BMW iX5 Hydrogen. Then, complementary results to the previous study [27] on the explicit linear MPC for air mass flow control are given in Chapter 5. The shortcomings of this control approach prompted the development of an explicit NMPC for air mass flow control. This controller is introduced and validated in Chapter 6. Eventually, the two proposed MPCs were compared to each other and to the reference control setup for air mass flow control, which consists of two adaptive PI controllers. The associated results are displayed in Chapter 7. Furthermore, the extension of the proposed NMPC to include FCS net power control is established in Chapter 8, which also contains the validation of the NMPC with closed-loop simulations. In the end, the present work is summarized in Chapter 9, and ideas on potential future works are shared.

2 Explicit Model Predictive Control

Explicit linear and nonlinear MPC are the control methods that were applied and compared in this work. Thus, the fundamentals of MPC and the corresponding nomenclature are presented first in Section 2.1. Subsequently, the concept of explicit MPC is introduced for both the linear and the nonlinear case. Additionally, previously published approaches regarding explicit MPC were reviewed. These revisions are shown in Sections 2.2 and 2.3.

2.1 Fundamentals of Model Predictive Control

MPC is a control technique that optimizes the closed-loop behavior of a system by repeatedly minimizing a cost function J. J is an assessment criterion for the system trajectory on a finite prediction horizon. After each minimization, the first step of the optimized control strategy for the entire prediction horizon is applied to the plant, and the response is evaluated. Then, the prediction horizon is moved one time step forward, and the optimization is repeated. Accordingly, MPC is often also referred to as receding horizon control. The prediction in J is based on a dynamic model of the system that is often given in its discrete state-space representation.

$$\boldsymbol{x}\left(k+1\right) = \boldsymbol{f}\left(\boldsymbol{x}\left(k\right), \boldsymbol{u}\left(k\right)\right) \tag{2.1}$$

$$\boldsymbol{y}\left(k\right) = \boldsymbol{h}\left(\boldsymbol{x}\left(k\right), \boldsymbol{u}\left(k\right)\right) \tag{2.2}$$

In the state equation (Eq. (2.1)), $\boldsymbol{x}\left(k\right)$ is the vector of state variables at time step k. What is more, $\boldsymbol{u}\left(k\right)$ is the vector of input variables, which are often the control variables under consideration. In the output equation (Eq. (2.2)), $\boldsymbol{y}\left(k\right)$ is the vector of output variables that often coincide with the controlled variables of the system. While MPC is often used to stabilize a given steady state, it can also be used for reference tracking. The state-space representation for reference tracking is often modified to include control effort $\Delta\boldsymbol{u}\left(k\right) = \boldsymbol{u}\left(k\right) - \boldsymbol{u}\left(k-1\right)$ instead of $\boldsymbol{u}\left(k\right)$.

$$\boldsymbol{x}\left(k+1\right) = \boldsymbol{f}\left(\boldsymbol{x}\left(k\right), \boldsymbol{u}\left(k-1\right), \Delta\boldsymbol{u}\left(k\right)\right) \tag{2.3}$$

$$\boldsymbol{y}\left(k\right) = \boldsymbol{h}\left(\boldsymbol{x}\left(k\right), \boldsymbol{u}\left(k-1\right), \Delta\boldsymbol{u}\left(k\right)\right) \tag{2.4}$$

The penalization of $\Delta\boldsymbol{u}$ in J influences the transients of the closed control loop, whereas stationary operation is unaffected. As a result, zero control deviation for the desired setpoints is ensured after reaching stationary operation. In J, the assessment of the system trajectory along a prediction horizon N_y is therefore based on an initial

state $\boldsymbol{x}(k)$, the control variables applied in the previous step $\boldsymbol{u}(k-1)$, and a set of future $\Delta\boldsymbol{u}(k+j)$ along a control horizon N_u. The values of all $\Delta\boldsymbol{u}(k+j)$ are often summarized in one vector $\boldsymbol{U}$. Additionally, setpoints for the system outputs $\boldsymbol{y}^{\mathrm{sp}}$ need to be considered in J for reference tracking. In this work and for most applications, it is sufficient to consider a constant $\boldsymbol{y}^{\mathrm{sp}}(k)$ along the prediction horizon. Nonetheless, it is also possible to consider a setpoint trajectory along the prediction horizon that allows for achieving desired closed-loop behavior. Moreover, future values of $\boldsymbol{y}^{\mathrm{sp}}$ may be predictable if additional information is available on the operating strategy.

$$\begin{aligned} J(\boldsymbol{x}(k), \boldsymbol{y}^{\mathrm{sp}}(k), \boldsymbol{u}(k-1), \boldsymbol{U}) = \\ & [\boldsymbol{y}^{\mathrm{sp}}(k) - \boldsymbol{y}(k+N_y)]^T \boldsymbol{P} [\boldsymbol{y}^{\mathrm{sp}}(k) - \boldsymbol{y}(k+N_y)] \\ & + \sum_{i=1}^{N_y-1} [\boldsymbol{y}^{\mathrm{sp}}(k) - \boldsymbol{y}(k+i)]^T \boldsymbol{Q} [\boldsymbol{y}^{\mathrm{sp}}(k) - \boldsymbol{y}(k+i)] \\ & + \sum_{j=0}^{N_u-1} \Delta\boldsymbol{u}^T(k+j) \boldsymbol{R} \Delta\boldsymbol{u}(k+j) \end{aligned} \tag{2.5}$$

The most common choice for J is the quadratic form that is shown in Equation (2.5).

One advantage of MPC is its ability to deal with multiple-input-multiple-output (MIMO) control problems. In J, the various controlled variables can be prioritized by choosing different weights in the terminal weight matrix $\boldsymbol{P}$ and the control deviation weight matrix $\boldsymbol{Q}$. What is more, the trajectories of the input variables can be smoothed by specifying the control effort weight matrix $\boldsymbol{R}$. Eventually, the vector of optimal control actions $\boldsymbol{U}^*$ is determined by minimizing J under constraints.

$$\boldsymbol{U}^* = \arg\min_{\boldsymbol{U}} J(\boldsymbol{x}(k), \boldsymbol{y}^{\mathrm{sp}}(k), \boldsymbol{u}(k-1), \boldsymbol{U}) \tag{2.6}$$

$$\text{s.t. } \boldsymbol{x}(k+1) = \boldsymbol{f}(\boldsymbol{x}(k), \boldsymbol{u}(k-1), \Delta\boldsymbol{u}(k)) \tag{2.7}$$

$$\boldsymbol{y}(k) = \boldsymbol{h}(\boldsymbol{x}(k), \boldsymbol{u}(k-1), \Delta\boldsymbol{u}(k)) \tag{2.8}$$

$$\bar{\boldsymbol{g}}(\boldsymbol{x}(k), \boldsymbol{u}(k-1), \boldsymbol{U}) = \boldsymbol{0} \tag{2.9}$$

$$\tilde{\boldsymbol{g}}(\boldsymbol{x}(k), \boldsymbol{u}(k-1), \boldsymbol{U}) \leq \boldsymbol{0} \tag{2.10}$$

$$\boldsymbol{u}_{\mathrm{Min}} \leq \boldsymbol{u}(k+j) \leq \boldsymbol{u}_{\mathrm{Max}} \tag{2.11}$$

$$\boldsymbol{x}_{\mathrm{Min}} \leq \boldsymbol{x}(k+j) \leq \boldsymbol{x}_{\mathrm{Max}} \tag{2.12}$$

$$\boldsymbol{y}_{\mathrm{Min}} \leq \boldsymbol{y}(k+j) \leq \boldsymbol{y}_{\mathrm{Max}} \tag{2.13}$$

The solution $\boldsymbol{U}^*$ is often characterized by a set of active inequality constraints $\tilde{g}_i = 0$. This characterization also includes the inequality constraints regarding the minimum (Min) or maximum (Max) values of $\boldsymbol{x}$, $\boldsymbol{y}$, and $\boldsymbol{u}$.

2.2 Explicit Linear Model Predictive Control

One of the most common variants of MPC is linear MPC based on a linear time-invariant (LTI) state-space representation.

$$\boldsymbol{x}\left(k+1\right) = \boldsymbol{A}\boldsymbol{x}\left(k\right) + \boldsymbol{B}\boldsymbol{u}\left(k\right) \tag{2.14}$$

$$\boldsymbol{y}\left(k\right) = \boldsymbol{C}\boldsymbol{x}\left(k\right) + \boldsymbol{D}\boldsymbol{u}\left(k\right) \tag{2.15}$$

For many applications, it is sufficient to only consider linear constraints in addition to the upper and lower bounds from Equations (2.11) - (2.13).

$$\bar{\boldsymbol{g}}\left(\boldsymbol{x}\left(k\right), \boldsymbol{u}\left(k-1\right), \boldsymbol{U}\right) = \bar{\boldsymbol{A}}_{\mathrm{Con}} \begin{bmatrix} \boldsymbol{x}\left(k\right) \\ \boldsymbol{u}\left(k-1\right) \end{bmatrix} + \bar{\boldsymbol{B}}_{\mathrm{Con}}\boldsymbol{U} = 0 \tag{2.16}$$

$$\tilde{\boldsymbol{g}}\left(\boldsymbol{x}\left(k\right), \boldsymbol{u}\left(k-1\right), \boldsymbol{U}\right) = \tilde{\boldsymbol{A}}_{\mathrm{Con}} \begin{bmatrix} \boldsymbol{x}\left(k\right) \\ \boldsymbol{u}\left(k-1\right) \end{bmatrix} + \tilde{\boldsymbol{B}}_{\mathrm{Con}}\boldsymbol{U} \leq 0 \tag{2.17}$$

The MPC optimization problem based on an LTI plant model and linear constraints is equivalent to a problem of quadratic programming (QP). Thus, QP solvers are usually applied to determine $\boldsymbol{U}^*$ during operation. An alternative approach based on multi-parametric QPs (mp-QPs) was proposed by Bemporad *et al.* [11]. An mp-QP is derived by summarizing the variable inputs $\boldsymbol{x}\left(k\right)$, $\boldsymbol{y}^{\mathrm{sp}}\left(k\right)$, and $\boldsymbol{u}\left(k-1\right)$ into the QP problem in one parameter vector $\boldsymbol{\theta}$. Then, a function $\boldsymbol{u}\left(\boldsymbol{\theta}\right)$ is determined offline that calculates or approximates $\boldsymbol{U}^*$ for all feasible $\boldsymbol{\theta}$. The set of all feasible $\boldsymbol{\theta}$ is denoted Θ in the remainder of this work. The additional effort beforehand is accepted if the evaluation of $\boldsymbol{u}\left(\boldsymbol{\theta}\right)$ is faster compared to the online execution of any available QP solver. In their work, Bemporad *et al.* [11] further showed that for a mp-QP problem, $\boldsymbol{U}^*$ is a piecewise affine (PWA) function.

$$\boldsymbol{u}\left(\boldsymbol{\theta}\right) = \boldsymbol{F}_{i,\mathrm{PT}}\boldsymbol{\theta} + \boldsymbol{g}_{i,\mathrm{PT}}, \qquad i = 1, ..., n_{\mathrm{PT}} \tag{2.18}$$

Each linear function $\boldsymbol{F}_{i,\mathrm{PT}}\boldsymbol{\theta} + \boldsymbol{g}_{i,\mathrm{PT}}$ corresponds to a polytope within Θ. The number of polytopes n_{PT}, and hence the complexity of the polytopic partition of Θ, depends on the number of constraints n_{Con}. In the context of mp-QP, a polytope is uniquely defined by a set of active inequality constraints $\tilde{g}_i = 0$. Hence, $n_{\mathrm{PT}} = 2^{n_{\mathrm{Con}}}$ if only inequality constraints are used [16]. Firstly, this correlation can prevent the application of mp-QP algorithms based on the geometric exploration of Θ for large-scale MPC problems [28]. Secondly, the polytopic partition for determining the control law on the ECU can potentially violate the requirement of real-time capability.

Therefore, many approaches have been reported in the literature that reduce the computations required to evaluate the explicit control law. Kvasnica *et al.* [64] aimed to reduce n_{PT} with classification. The authors separated polytopic regions with saturated from those with unsaturated control variables. Subsequently, all regions where the control variables are saturated at the maximum were merged. The same was done

for saturation at the minimum. Hence, only two function evaluations determining the boundaries to the unsaturated regions were necessary initially, while the polytopes related to unsaturated control variables remained in their original state.

Another reported approach used an approximation of the exact control law. Bemporad *et al.* [12] argued that approximations are often sufficient since the parameterization of cost functions is generally carried out empirically. The authors utilized canonical PWA functions on a simplicial partition of Θ because these functions can be directly implemented on electronic circuits. The weights of the functions were adapted to the exact control law while ensuring a perfect agreement at the vertices of the simplices. Canale *et al.* [14] and Domahidi *et al.* [23] also based their approximation approaches on the exact control law at fixed points $\boldsymbol{\theta}$. On the one side, in [14], set membership methodologies were used to display a systematic procedure for approximating the explicit MPC control law. On the other side, kernel regression was applied in [23]. Similarly, [108] used second-order interpolating wavelets to approximate $\boldsymbol{U}^*$ in Θ.

Another concept to realize real-time capable linear MPC is the combination of implicit and explicit MPC. Pannocchia *et al.* [88] proposed explicit storing of solutions that refer to the most frequently active constraints. The resulting table was used during operation as a first instance to determine the control law. If the table did not contain a solution, a suboptimal control action was taken. Simultaneously, a QP solver determined the optimal solution, which was added to the table afterward. The advantage of this approach is that the QP solver did not need to meet the real-time requirement. Likewise, Zeilinger [126] used an approximate explicit MPC to determine an optimal initial point for the optimization on the ECU. Thus, a limited number of optimization steps were sufficient to reach the optimum or an adjacent value.

2.3 Explicit Nonlinear Model Predictive Control

Linear MPC is feasible for many applications. However, it is sometimes desirable to utilize a more general nonlinear model (Eqs. (2.1) and (2.2)) that better represents the plant dynamics [56]. Implementing an NMPC requires solving a nonlinear programming (NLP) problem, which has a higher computational burden than QP solvers. Hence, explicit NMPC is often the only possibility to achieve real-time capability for fast processes. Unfortunately, there is no exact solution to the general NLP problem comparable to the results of [11]. Nonetheless, various suboptimal polytopic or function approximation methods have been proposed.

Among the first studies were the ones by Parisini *et al.* [89], [90]. The authors used a multilayer feedforward neural network (NN) to approximate the solution to the NLP problem. A few years later, Johansen [54], [55] published two approaches based on suboptimal polytopic partitions of Θ. In the first study [54], the NLP problem was transformed into local QP problems by using the Taylor expansion around fixed solutions of the original NLP problem. Hypercubes were then used to determine the area around each fixed solution for which the corresponding local QP problem was assumed to be

feasible and accurate. Afterward, each local mp-QP problem was solved exactly inside the respective hypercube. If the approximation error of the obtained solution exceeded a threshold, the hypercube was split, and the procedure was repeated for each of the resulting sub-regions. The solution to each mp-QP and the overall solution to the mp-NLP were thus PWA functions. The second method of Johansen [55] also evolved around the splitting of Θ into hypercubes and obtaining a PWA approximation of the exact NMPC control law. The linear functions were obtained by solving the NLP at the vertices of each hypercube and then interpolating the results with a linear function. This approach was further developed in the works of Grancharova *et al.* [33], [34]. Ulbig *et al.* [117] also utilized the exact PWA solution to the general mp-QP problem in their approach for an mp-NLP solver. However, their linearization already started with the system model. Jacobi linearizations were used to obtain a PWA representation of the nonlinear model. The mp-NLP was thus transformed into multiple mp-QP problems that were each solved by PWA functions. The final explicit representation of the NMPC was obtained by approximating the overall PWA function with one polynomial over Θ to decrease the computational burden of the online function evaluation. A PWA control law was also obtained with the approach of Domínguez *et al.* [24]. The authors used linearizations of the Lagrangian function $\mathcal{L}(\boldsymbol{\theta}, \boldsymbol{U})$ of the NLP to obtain the polytopic regions inside Θ and to calculate the resulting explicit control law.

$$\mathcal{L}(\boldsymbol{\theta}, \boldsymbol{U}, \boldsymbol{\lambda}, \boldsymbol{\mu}) = J(\boldsymbol{\theta}, \boldsymbol{U}) + \sum_i \lambda_i \cdot \tilde{g}_i(\boldsymbol{\theta}, \boldsymbol{U}) + \sum_j \mu_j \cdot \bar{g}_j(\boldsymbol{\theta}, \boldsymbol{U}) \tag{2.19}$$

Another approach similar to [117] was presented by Kvasnica *et al.* [63]. The authors used a PWA representation of the original nonlinear model to create a set of mp-QP problems that are solved exactly by PWA functions. A polynomial then approximated the combined PWA function for Θ. The polynomial coefficients were obtained by solving a new linear programming (LP) problem.

Nonetheless, the NN approach of Parisini *et al.* [90] was applied in this work for explicit NMPC due to its simple implementation and scalability. The scalability was necessary to ensure the real-time capability of the approach. Generally, NNs comprise multiple neurons within one or more layers. A NN with one layer is called shallow, while NNs with multiple layers are called deep NNs. Each neuron is characterized by its connection to the previous and the following layer and by its activation function. The activation function $act(\sigma_i)$ calculates the output value y_i of the i-th neuron based on the weighted sum σ_i of the input values x_j from all the connected neurons of the previous layer.

$$\sigma_i = \sum_{j=1}^{n_{\text{in}}} w_{i,j} \cdot x_j + b_i \tag{2.20}$$

A summary of the most common activation functions is given in Figure 1. While saturated activation functions best represent the physical limitations of control variables in real systems, they suffer from vanishing gradients close to the saturated value [48]. Thus, the learning performance is usually worse than with linear and Rectified Linear

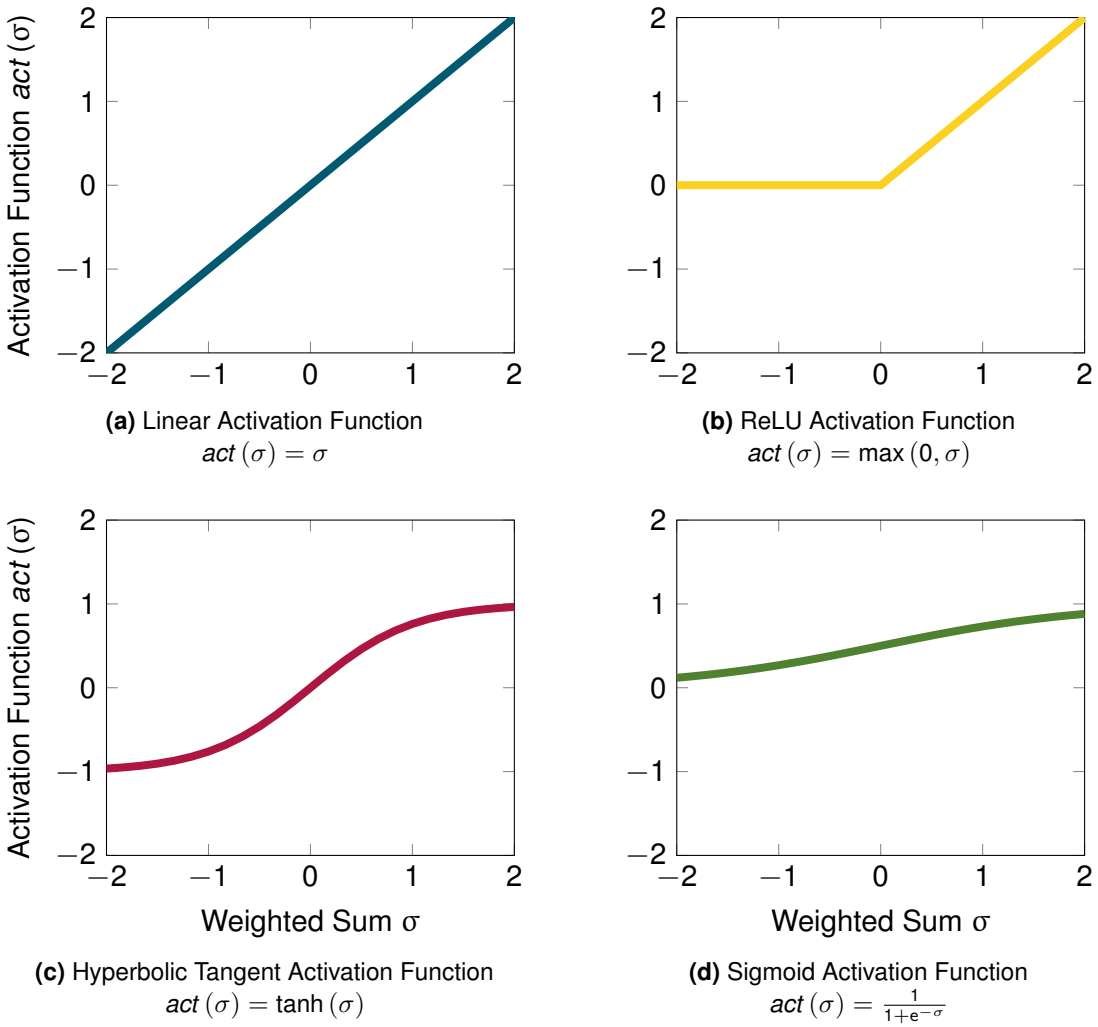

(a) Linear Activation Function
$act(\sigma) = \sigma$

(b) ReLU Activation Function
$act(\sigma) = \max(0, \sigma)$

(c) Hyperbolic Tangent Activation Function
$act(\sigma) = \tanh(\sigma)$

(d) Sigmoid Activation Function
$act(\sigma) = \frac{1}{1+e^{-\sigma}}$

Figure 1: Overview of the most common activation functions in feedforward NNs.

Unit (ReLU) activation functions. Nonetheless, successful applications of all these activation functions in NNs for explicit MPC have been reported in the literature.

Chen *et al.* [16] utilized a deep neural network to approximate an explicit linear MPC. The NN consisted of two hidden layers with the ReLU activation function. Additionally, the linear output layer was fed into Dykstra's projection algorithm to avoid constraint violations due to approximation errors. A similar approach was chosen by Karg *et al.* [58]. Their study was further motivated by the immense memory requirement of an exact explicit linear MPC. The six hidden layers with ReLU activation functions comprised six or ten neurons. Maddalena *et al.* [78] also used a deep NN to approximate the solution to the MPC optimization problem for LTI systems. The authors stated time limitations and safety regulations as motivation for explicit MPC. Additionally, high memory requirements and a high computational burden of the exact solution required an approximation approach for real-time capability. But unlike [16] and [58], each layer in [78] had a different activation function. A parametric QP (pQP) layer was used between two linear layers, while the output layer was implemented as a saturated

projection layer to account for the control variable boundaries.

$$\boldsymbol{y}_{\mathrm{pQP}} = \arg\min_{\boldsymbol{z}\geq 0} \|\boldsymbol{L}\boldsymbol{z} + \boldsymbol{x}\|^2 + \epsilon\|\boldsymbol{z}\|^2 \tag{2.21}$$

Zhang *et al.* [128] applied a NN to approximate the explicit solution of the MPC problem for a linear, parameter-varying system. A helpful assumption in this work was that the parameter variations in the system are known and can be perfectly predicted. The study aimed to approximate the complex exact solution with very few parameters and to allow a simple evaluation during operation. Hence, a deep neural network was used based on three hidden layers with ReLU activation functions.

Additionally, NNs have been used to approximate the explicit solution of mixed-integer QPs. Mixed-integer QPs can arise in MPC if a PWA system model is used [17] or some control variables are integers [57]. Cseko *et al.* [17] used a NN to avoid the exponential growth in the number of polytopes for exact explicit MPC. Furthermore, the authors took advantage of the fact that a NN controller does not generally require a complete state measurement. The applied NN was shallow and utilized the radial basis function (RBF) in the hidden layer with up to 250 neurons.

$$y_{i,\mathrm{RBF}} = e^{-\frac{\|\boldsymbol{x}-\boldsymbol{c}_i\|^2}{2\cdot b_i^2}} \tag{2.22}$$

The training data for the NN was taken from the exact explicit MPC, with one sample from each region. Karg *et al.* [57] also stated computational burden and memory requirements as the primary motivation for applying a NN. The authors used a deep neural network with five hidden layers with ReLU activation functions. Furthermore, the output layer was chosen to be linear.

Nonetheless, the goal of this study was to apply a NN as an approximation for the solution to an mp-NLP. This approach has been reported by Hertneck *et al.* [45] and Lucia *et al.* [72]. In [45], the lack of a straightforward extension of the exact solution of mp-QPs [11] to mp-NLPs was quoted as the primary motivation for approximate solutions like NNs. The authors applied a deep neural network that consisted of hyperbolic tangent activation functions in the hidden layers and a linear output layer. Similarly, Lucia *et al.* [72] utilized a NN to avoid the complexity of solving an NMPC optimization problem under uncertainty. They trained a deep neural network with nine hidden and one output layer, with each layer using the hyperbolic tangent activation function.

3 Control of an Automotive Fuel Cell System

In this work, explicit linear and nonlinear MPC was applied to control the FCS of the BMW iX5 Hydrogen. This vehicle is BMW's first FCEV produced in a pilot series. In this chapter, the FCS setup and the power control architecture are presented in Section 3.2. Beforehand, an overview of publications concerning the control of fuel cell systems is given in Section 3.1, focusing on control tasks and applications.

3.1 Literature Review

The optimal control of the FCS is crucial for successfully integrating fuel cell technology in FCEVs. Among the essential control tasks are voltage control, air or oxygen and hydrogen supply control, and temperature and humidity control [19], [29]. Additional control tasks include maximizing the FCS efficiency and lifetime during the operation, and particular scenarios like cold start [29]. The comprehensive review of Gao *et al.* [29] on FCS control also emphasized that air supply control is the limiting factor in the dynamic response of an FCS. Therefore, much research has been conducted regarding this control task. The most commonly controlled variable under consideration has been the oxygen excess ratio λ_{O_2} [49], the ratio of supplied (in) to reacted (reac) oxygen in the fuel cell stack.

$$\lambda_{\mathrm{O}_2} = \frac{\dot{m}_{\mathrm{O}_2}^{\mathrm{in}}}{\dot{m}_{\mathrm{O}_2}^{\mathrm{reac}}} \tag{3.1}$$

Air supply control aims to prevent oxygen starvation in the fuel cells by keeping $\lambda_{\mathrm{O}_2} > 1$. In automotive applications, ambient air supplies oxygen to the fuel cell stack. The utilized air compressor is, therefore, the main actuator in air supply control. For a small laboratory FCS, a DC motor is adequate to power the air compressor. As a result, the air compressor motor voltage U_{Cmpr} has been the most commonly used control variable in the literature. One approach is directly controlling λ_{O_2} with U_{Cmpr}, without considering any other variables. Pilloni *et al.* [91] used second-order sliding mode control (SMC) to steer λ_{O_2} to a fixed setpoint $\lambda_{\mathrm{O}_2}^{\mathrm{sp}} = 2.06$. Similarly, Baroud *et al.* [10] applied a combination of fuzzy and PID control to reach $\lambda_{\mathrm{O}_2}^{\mathrm{sp}} = 2.05$. A comparable hybrid fuzzy-PID controller was also reported by AbouOmar *et al.* [1]. The difference between the two studies was the utilization of a load-dependent setpoint $\lambda_{\mathrm{O}_2}^{\mathrm{sp}} = f\left(I_{\mathrm{Stck}}\right)$ in [1]. This map was determined by maximizing the FCS efficiency through variations in λ_{O_2} for different electric currents I_{Stck} drawn from the fuel cell stack.

Apart from the load dependency, λ_{O_2} also depends directly on I_{Stck}. The amount of oxygen $\dot{m}_{O_2}^{reac}$ consumed in the electrochemical reaction of the fuel cells is directly proportional to I_{Stck}.

$$\dot{m}_{O_2}^{reac} = \frac{n_{Cell} \cdot I_{Stck}}{4 \cdot F} \cdot \bar{M}_{O_2} \tag{3.2}$$

Accordingly, many proposed controllers for λ_{O_2} also considered I_{Stck} as a measurable disturbance. For fixed values, the successful application of an implicit ([93], $\lambda_{O_2}^{sp} = 2.3$) and an explicit ([92], $\lambda_{O_2}^{sp} = 2.0$) linear MPC was reported. Similarly, Yang *et al.* [124] utilized a control Lyapunov function to maintain $\lambda_{O_2}^{sp} = 2.0$. An alternative has been the utilization of a map $\lambda_{O_2}^{sp} = f(I_{Stck})$ alongside I_{Stck} as a measurable disturbance. Regarding this control setup, Grujicic *et al.* [38] compared a static with a dynamic feedforward controller, while Yang *et al.* [123] applied generalized predictive control (GPC). An additional PID controller was used in [123] to compensate for model errors. Likewise, Zhang *et al.* [127] applied robust linearizing control, complemented with an interval type-2 fuzzy logic system to estimate unmodeled dynamics. While the three mentioned studies used a predetermined offline map $\lambda_{O_2}^{sp} = f(I_{Stck})$, Chang *et al.* [15] implemented an extremum-seeking controller that detects the optimal value of $\lambda_{O_2}^{sp}$ during operation. At the optimum, the maximum FCS net power P_{FCS} was provided for a given I_{Stck}. There have also been several studies with controller validations for oxygen starvation prevention with a fixed setpoint $\lambda_{O_2}^{sp} > 1$ and efficiency maximization with $\lambda_{O_2}^{sp} = f(I_{Stck})$. Among these studies were Bordons *et al.* [13] with constrained predictive control (CPC), Arce *et al.* [6] with explicit linear MPC, and Gruber *et al.* with dynamic matrix control (DMC) [36] and NMPC [35]. While these four studies considered I_{Stck} directly in their controller formulations, Garcia-Gabin *et al.* [30] and Wang *et al.* [121] compensated the disturbance of I_{Stck} with an additional feedforward map $U_{Cmpr}^{ff} = f(I_{Stck})$. This map was added to their respective controllers: a sliding mode controller [30] and a time delay compensation controller [121].

An alternative to the direct control of λ_{O_2} with U_{Cmpr} is utilizing an intermediate control target in a controller cascade. Gruber *et al.* [37] and Matraji *et al.* [82] used the mass flow $\dot{m}_{Cmpr}$ supplied by the compressor as the intermediate control variable. On the one side, in [37], the superordinate controller used nonlinear predictive control, while the subordinate controller was implemented as a PI controller. On the other side, in [82], both controllers were realized with second-order SMC. Both studies steered the FCS to a fixed setpoint $\lambda_{O_2}^{sp} = 2.0$. Damour *et al.* [18] also utilized a mass flow setpoint as the control variable of their superordinate PID controller. An artificial neural network (ANN) determined the corresponding controller parameters during operation. Nonetheless, unlike the other two studies, this control target was handled by a built-in mass flow controller (MFC) after a pressurized oxygen tank. Another possibility is to use the compressor rotational speed n_{Cmpr} in a controller cascade [21], [22]. Both studies applied a fixed setpoint $\lambda_{O_2}^{sp} = 2.05$ and a feedforward map $U_{Cmpr}^{ff} = f(I_{Stck})$ alongside a feedback controller based on cascaded adaptive SMC.

In large-scale fuel cell systems with high power densities, permanent magnet synchronous

motors (PMSM) are employed to drive the air compressor. The utilization of a PMSM often renders the direct utilization of U_{Cmpr} infeasible. Instead, the torque of the PMSM is controlled with the quadrature current $i_{q,\mathrm{Cmpr}}$ through field-oriented control. This current is usually set by the subordinate controller using the space vector modulation technique. Thus, the setpoint $i_{q,\mathrm{Cmpr}}^{\mathrm{sp}}$ can be considered an alternative control variable of the air supply controller. This control variable was used by Matraji *et al.* [81] and Liu *et al.* [69] in their sliding mode controller cascades. In [69], the superordinate controller steered the FCS to an operating point with a load-dependent $\lambda_{\mathrm{O_2}}^{\mathrm{sp}} = f\left(I_{\mathrm{Stck}}\right)$, while the subordinate controller regulated $\dot{m}_{\mathrm{Cmpr}}$ using $i_{q,\mathrm{Cmpr}}$. In [81], n_{Cmpr} was utilized as the intermediate control variable for the air supply controller with $\lambda_{\mathrm{O_2}}^{\mathrm{sp}} = f\left(I_{\mathrm{Stck}}\right)$. Talj *et al.* [111], [113] also used $i_{q,\mathrm{Cmpr}}$ as the control variable of their sliding mode controller and a constant setpoint $\lambda_{\mathrm{O_2}}^{\mathrm{sp}} = 2$. However, only the most low-level controllers for $\dot{m}_{\mathrm{Cmpr}}$ [111] and the compressor rotational speed ω_{Cmpr} [113] were specified. The upper-level control tasks starting from $\lambda_{\mathrm{O_2}}^{\mathrm{sp}}$ were neglected.

Apart from cascaded control, $\lambda_{\mathrm{O_2}}^{\mathrm{sp}}$ can also be used to directly calculate a mass flow setpoint $\dot{m}_{\mathrm{Ca}}^{\mathrm{in,sp}}$ for the air at the inlet of the fuel cell stack. The calculation is based on two assumptions, the availability of the measured value $I_{\mathrm{Stck}}^{\mathrm{meas}}$ and air with a constant composition ($y_{\mathrm{O_2,Air}} \approx 0.21$). These two assumptions can be used with Equations (3.1) and (3.2) to obtain $\dot{m}_{\mathrm{Ca}}^{\mathrm{in,sp}}$.

$$\dot{m}_{\mathrm{Ca}}^{\mathrm{in,sp}} = \frac{n_{\mathrm{Cell}} \cdot I_{\mathrm{Stck}}}{4 \cdot F} \cdot \frac{\bar{M}_{\mathrm{Air}}}{y_{\mathrm{O_2,Air}}} \cdot \lambda_{\mathrm{O_2}}^{\mathrm{sp}} \tag{3.3}$$

Consequently, $\dot{m}_{\mathrm{Ca}}^{\mathrm{in}}$ can be directly controlled with U_{Cmpr}. This approach was realized by Kunusch *et al.* [60], Niknezhadi *et al.* [86], Li *et al.* [65], and Han *et al.* [41]. In [60], second-order SMC was combined with $\lambda_{\mathrm{O_2}}^{\mathrm{sp}} = 2.05$. Niknezhadi *et al.* [86] implemented a linear quadratic Gaussian controller and validated their approach for a fixed setpoint $\lambda_{\mathrm{O_2}}^{\mathrm{sp}} = 2$ and a varying one. The underlying operating strategy to vary the setpoint was not further specified. In [65], a load-dependent setpoint $\lambda_{\mathrm{O_2}}^{\mathrm{sp}} = f\left(I_{\mathrm{Stck}}\right)$ was selected for the presented PI controller. The novelty of this work was the specification of the controller gains by a NN during operation. Finally, Han *et al.* [41] used model reference adaptive control with $\lambda_{\mathrm{O_2}}^{\mathrm{sp}} = 2.2$. Nevertheless, unlike the other three studies, the opening angle of the air inlet valve throttle was used as a second control variable.

Besides air mass flow control, valves can also be used to regulate various pressures within the cathode subsystem of an FCS. The most common choice has been to use the back pressure valve (BPV) to regulate the pressure p_{Ca} on the cathode side of the fuel cells. What is more, pressures and mass flows are directly coupled. Many studies have taken advantage of the coupling by combining the air supply controller with a cathode pressure controller. Li *et al.* [66] and Sun *et al.* [110] used the position of the BPV pos_{BPV} alongside U_{Cmpr} to control $\dot{m}_{\mathrm{Ca}}^{\mathrm{in}}$ and p_{Ca}. In [66], observer-based feedback linearization control was applied. The setpoints of the two controlled variables were load-dependent, and I_{Stck} was additionally considered a measurable disturbance. In [110], a decoupling internal model controller was demonstrated that did not consider

I_{Stck} a measurable disturbance. Nonetheless, a load-dependency was found for $\dot{m}_{\mathrm{Ca}}^{\mathrm{in,sp}}$ and $p_{\mathrm{Ca}}^{\mathrm{sp}}$. Rodatz *et al.* [101] chose a similar control setup using linear quadratic Gaussian control. However, the valve was directly controlled with the voltage of the valve motor U_{BPV}. This modification omitted the necessity of an intermediate position controller for pos_{BPV}. Bao *et al.* [8], [9] extended this approach by further controlling the pressure difference between the cathode and anode with the hydrogen supply valve as an additional actuator. For both valves, the voltage of the motor was controlled. This MIMO controller was realized with MPC based on a NN model.

A modified version of the control setup from [110] is also found in the studies of Zhao *et al.* [130], Liu *et al.* [71], and Yuan *et al.* [125]. All of them used n_{Cmpr} as the second control variable instead of U_{Cmpr}. In [130], disturbance decoupling control was used. In [71], fuzzy PID control was applied, and the mass flow controller was validated independently from $\lambda_{\mathrm{O_2}}$. In [125], SMC was used in a superordinate controller to generate a mass flow reference $\dot{m}_{\mathrm{Ca}}^{\mathrm{in,sp}}$. This reference steered $\lambda_{\mathrm{O_2}}$ to its desired constant setpoint $\lambda_{\mathrm{O_2}}^{\mathrm{sp}}$ during load changes. The subordinate mass flow and pressure controller was implemented with inverted decoupling and active disturbance rejection control. This control approach is similar to [130]. A different approach is based on the proportional correlation between the cathode inlet pressure loss $\Delta p_{\mathrm{Ca}}^{\mathrm{in}} = p_{\mathrm{Sm}} - p_{\mathrm{Ca}}$ and $\dot{m}_{\mathrm{Ca}}^{\mathrm{in}}$. Ma *et al.* [77] used this correlation to calculate a virtual setpoint $\Delta p_{\mathrm{Ca}}^{\mathrm{in,sp}}$ instead of $\dot{m}_{\mathrm{Ca}}^{\mathrm{sp,in}}$ from $\lambda_{\mathrm{O_2}}^{\mathrm{sp}}$. Their nonlinear triple-step controller then used U_{Cmpr} to steer the system to this setpoint. Similarly, Hernandez-Torres *et al.* [43] used the correlation between $\dot{m}_{\mathrm{Cmpr}}$ and ω_{Cmpr} and p_{Sm} to define an air supply controller for $\omega_{\mathrm{Cmpr}}^{\mathrm{sp}}$ and $p_{\mathrm{Sm}}^{\mathrm{sp}}$. The resulting H_∞ polytopic controller also used U_{Cmpr} as the sole control variable. For both studies, the pressure in the air supply manifold p_{Sm} was also the pressure at the air compressor outlet.

Apart from $\dot{m}_{\mathrm{Ca}}^{\mathrm{in}}$, $p_{\mathrm{Ca}}^{\mathrm{in}}$ also relates directly to the gas humidity since it impacts the water vapor activity a_{Ca}.

$$a_{\mathrm{Ca}} = \frac{p_{\mathrm{Ca,H_2O\,(v)}}}{p_{\mathrm{Ca}}} \tag{3.4}$$

Thus, air supply and pressure control can be coupled with humidity control. This approach was demonstrated in the work of Xu *et al.* [122]. The authors applied adaptive second-order SMC to reach a load-dependent $\lambda_{\mathrm{O_2}}^{\mathrm{sp}} = f\left(I_{\mathrm{Stck}}\right)$ and a fixed $a_{\mathrm{Ca}}^{\mathrm{sp}} = 0.9$. The corresponding control variables included the heated water temperature of the membrane humidifier alongside ω_{Cmpr} and pos_{BPV}.

Nonetheless, air supply control has not only been combined with pressure and humidity control. The air compressor also accounts for the majority of the auxiliary power losses in the FCS [95]. Hence, power control has often been connected with air supply control. In [94], [95], the authors used the setpoint $P_{\mathrm{FCS}}^{\mathrm{sp}}$ to determine I_{Stck} from a static map. This static map was determined beforehand from simulations but can also be obtained from measurements. In the next step, I_{Stck} was used as the input of a static feedforward controller to determine $\dot{m}_{\mathrm{Cmpr}}^{\mathrm{sp}}$. Eventually, $\dot{m}_{\mathrm{Cmpr}}^{\mathrm{sp}}$ was controlled by a state feedback controller that acted on U_{Cmpr}.

Air supply control does not only impact the power consumption of the compressor P_{Cmpr}. Moreover, an increased p_{Ca} increases the stack voltage U_{Stck} due to a higher open circuit voltage (OCV). This correlation enables combined control approaches for air supply and cell voltage control, which was realized by Hernández-Torres *et al.* [44], Kim *et al.* [59], and Tekin *et al.* [114]. In [44], $\dot{m}_{\mathrm{Cmpr}}$ and U_{Stck} were directly controlled with $\omega_{\mathrm{Cmpr}}^{\mathrm{sp}}$. In this work, H_∞ control was applied. On the contrary, Kim *et al.* [59] and Tekin *et al.* [114] manipulated a term added to $\dot{m}_{\mathrm{Ca}}^{\mathrm{in,sp}}$ to reach $U_{\mathrm{Stck}}^{\mathrm{sp}}$. While PI control was applied in [59], [114] utilized Takagi-Sugeno fuzzy-logic control.

While most of the studies assume I_{Stck} to be identical to its setpoint $I_{\mathrm{Stck}}^{\mathrm{sp}}$, Sun *et al.* [109] correctly pointed out that this assumption generally requires conservative choices for $\lambda_{\mathrm{O_2}}$ or slow dynamics. Instead, they proposed a load governor to limit I_{Stck} during transients. This load governor enforced $\lambda_{\mathrm{O_2}} > 1$ while allowing significant changes in $I_{\mathrm{Stck}}^{\mathrm{sp}}$. A limitation of I_{Stck} during transients was also realized in [99]. In this work, the definition of a slew rate for P_{FCS} restricted the electric current that the DC/DC boost converter could draw. What is more, a dynamic map for U_{Cmpr} was utilized as an air supply controller. The inputs to this map were I_{Stck} and $\lambda_{\mathrm{O_2}}^{\mathrm{sp}} - \lambda_{\mathrm{O_2}}$, with a load-dependent setpoint $\lambda_{\mathrm{O_2}}^{\mathrm{sp}} = f\left(I_{\mathrm{Stck}}\right)$. The overall system under consideration in [99] was a hybrid setup with an additional capacitor covering the power transients of the load. A similar hybrid setup was also regarded in the works of Vahidi *et al.* [118], [119]. The authors used linear MPC to control the state-of-charge (SOC) of the capacitor alongside $\lambda_{\mathrm{O_2}}^{\mathrm{sp}} = 2$. As control variables, U_{Cmpr} and I_{Stck} were chosen.

While air supply and power control are decisive for the transient response of an FCS, the regulation of the hydrogen excess ratio $\lambda_{\mathrm{H_2}}$ and the fuel cell stack temperature T_{Stck} are also necessary to properly operate the FCS. In their study, Sankar *et al.* [102] added $T_{\mathrm{Stck}}^{\mathrm{sp}}$ to the more common control targets $U_{\mathrm{Stck}}^{\mathrm{sp}}$ and $\dot{m}_{\mathrm{Cmpr}}^{\mathrm{sp}}$. The authors applied SMC to determine values for the hydrogen supply pressure $p_{\mathrm{H_2}}^{\mathrm{in}}$, U_{Cmpr}, and the cooling water mass flow $\dot{m}_{\mathrm{Cool}}$. Another comprehensive controller was introduced by Ziogou *et al.* [132]. The authors applied NMPC to track $P_{\mathrm{FCS}}^{\mathrm{sp}}$, $\lambda_{\mathrm{O_2}}^{\mathrm{sp}}$, and $\lambda_{\mathrm{H_2}}^{\mathrm{sp}}$ simultaneously. The controller manipulated I_{Stck}, the setpoint for the supplied air $\dot{m}_{\mathrm{Air}}^{\mathrm{in,sp}}$, and the setpoint for the supplied hydrogen $\dot{m}_{\mathrm{H_2}}^{\mathrm{in,sp}}$. In contrast to most of the studies presented so far, the FCS in [132] was directly supplied from high-pressure air and hydrogen tanks. The respective mass flows were thus directly controlled by MFCs, and an air compressor was not required. Nonetheless, using an air tank also means this approach is not directly transferable to automotive applications. An extension of this work is found in [133]. In this study, the authors added an explicit linear MPC to control T_{Stck}. As additional actuators, a heating resistance and a cooling fan were included.

All the studies above have in common that they directly specified a setpoint for $\lambda_{\mathrm{O_2}}$ or a derived variable to avoid oxygen starvation. Alternatively, model-based approaches like MPC allow the usage of constraints on $\lambda_{\mathrm{O_2}}$. Goshtasbi *et al.* [32] implemented a controller for P_{FCS} and the efficiency of the FCS, η_{FCS}, that only considered a lower bound on $\lambda_{\mathrm{O_2}}$. This implementation was based on linear time-variant MPC that uses model linearizations around the current operating point. Similarly, Neisen *et al.* [85] utilized NMPC to control P_{FCS} and η_{FCS} with a lower bound on $\lambda_{\mathrm{O_2}}$.

Another possibility is the consideration of boundaries on the oxygen concentrations within the fuel cells. This approach requires a more detailed model of a fuel cell. Nonetheless, it was considered by Luna *et al.* [73], [74] in their works on NMPC. In [73], η_{FCS} was controlled while enforcing upper and lower boundaries on the oxygen concentration in the fuel cell gas channels. By contrast, in [74], the electrochemically active surface area was controlled with boundaries on the oxygen concentration in the catalyst layer. This layer is the part of a fuel cell where oxygen starvation occurs.

Alternatively, the air supply controller can be considered a part of the FCS. This approach is similar to the utilization of MFCs in [18], [132], [133]. Accordingly, $\dot{m}_{\mathrm{Ca}}^{\mathrm{in,sp}}$ or $\lambda_{\mathrm{O_2}}^{\mathrm{sp}}$ are the controller outputs. In [31], the authors developed a controller for η_{FCS} with $\dot{m}_{\mathrm{Ca}}^{\mathrm{in,sp}}$ as one of the control variables. This controller was based on NMPC and thus enabled the implementation of a lower bound on $\lambda_{\mathrm{O_2}}$. Similarly, Vrlić *et al.* [120] considered $\dot{m}_{\mathrm{Ca}}^{\mathrm{in}}$ as a control variable of their linear MPC based on successive linearization of a nonlinear model. The authors assumed that the air supply controller is significantly faster than the superordinate MPC. As a result, $\dot{m}_{\mathrm{Ca}}^{\mathrm{in}}$ could be used instead of its setpoint. The controlled variables in [120] included η_{FCS}, P_{FCS}, the pressure difference across the membrane, and the distance from the optimal line in the compressor map. A comparable study on MPC based on successive model linearization was published by Hahn *et al.* [39]. In their work, $\lambda_{\mathrm{O_2}}$ was used as a control variable. The goal of this controller was to steer P_{FCS} to its setpoint while minimizing hydrogen consumption. Additionally, a lower and an upper bound on $\lambda_{\mathrm{O_2}}$ were considered as control variable constraints (see Eq. (2.11)).

Lastly, approaches for the control of P_{FCS} have been published that consider neither $\lambda_{\mathrm{O_2}}$ nor $\dot{m}_{\mathrm{Ca}}^{\mathrm{in}}$ explicitly in the controller formulation. One example is the study of O'Rourke *et al.* [87]. The authors proposed an extremum-seeking controller that varies U_{Cmpr} and pos_{BPV} to maximize P_{FCS} for a given I_{Stck}. This maximization was based on the dependency of U_{Stck} on p_{Ca}, which could also be translated into a dependency of U_{Stck} on $\dot{m}_{\mathrm{Ca}}^{\mathrm{in}}$. Nonetheless, neither $\dot{m}_{\mathrm{Ca}}^{\mathrm{in}}$ nor p_{Ca} were considered directly. Instead, only changes in P_{FCS} were regarded by the controller. A similar dependency was considered in a lookup table in [70]. This lookup table determined $\omega_{\mathrm{Cmpr}}^{\mathrm{sp}}$ and $I_{\mathrm{Stck}}^{\mathrm{sp}}$ from a given $P_{\mathrm{FCS}}^{\mathrm{sp}}$. The selection of the operating points was based on the maximization of P_{FCS} due to a changing $\dot{m}_{\mathrm{Ca}}^{\mathrm{in}}$. However, similar to [87], no air mass flows appeared explicitly in the controller formulation. While [87] and [70] considered a compressor to supply air to the FCS, the required oxygen in [40] was supplied by an air tank. Hence, oxygen starvation could be prevented by regulating p_{Ca} instead of a mass flow. The controller was based on NMPC and regulated P_{Stck} by specifying $p_{\mathrm{Ca}}^{\mathrm{sp}}$, $p_{\mathrm{An}}^{\mathrm{sp}}$, and $I_{\mathrm{Stck}}^{\mathrm{sp}}$. Additionally, no constraints for $\lambda_{\mathrm{O_2}}$ were considered in [40]. Instead, only a gradient limit for I_{Stck} was utilized to prevent reactant starvation during transients. Two other FCS power controllers that entirely neglect the cathode subsystem were reported. Instead, these controllers prioritized hydrogen supply. In [105], an additional methanol reformer delivered $\dot{m}_{\mathrm{H_2}}^{\mathrm{in}}$. Thus, only the PI controller cascade from $P_{\mathrm{FCS}}^{\mathrm{sp}}$ down to the reformer was considered. This control cascade contained an intermediate control target for hydrogen supply instead of oxygen supply. In another study, Methekar *et*

al. [83] utilized a sensitivity analysis to determine $\dot{m}_{\mathrm{H_2}}^{\mathrm{in}}$ and the coolant temperature setpoint $T_{\mathrm{Cool}}^{\mathrm{sp}}$ as the most significant control variables. These control variables were the outputs of two PI controllers for the FCS power density and T_{Stck}. Therefore, the influence of air supply was also neglected in [83].

3.2 Application Case: BMW iX5 Hydrogen

In this study, the proposed controllers were experimentally validated with the FCS of the BMW iX5 Hydrogen. Therefore, the FCS hardware and control setup is introduced next, which defines the boundaries between the controlled plant and the applied controller.

3.2.1 Fuel Cell System Setup

This work focused on the air supply and net power control of the FCS. Therefore, the schematic overview of the FCS in Figure 2 mainly displays the cathode subsystem and the electric connection of the leading power producers and consumers, namely the fuel cell stack, the electric motor of the air compressor, and the FCEV powertrain. Minor power consumers, such as the cooling pump and the ECU, were neglected in the control problem formulation. In the cathode subsystem, the atmospheric air was filtered before entering the air compressor. This filtering was motivated by the fact that the iX5 Hydrogen is driven alongside vehicles with conventional combustion or diesel engines. The exhaust fumes of these engines contain $\mathrm{CH_x}$, $\mathrm{NO_x}$, or $\mathrm{SO_x}$ fractions that can lead to irreversible degradation of the polymer electrolyte membrane (PEM) fuel cells. The feed air mass flow $\dot{m}_{\mathrm{AirFil}}$ was measured directly after the air filter. The sensor position led to $\dot{m}_{\mathrm{Ca}}^{\mathrm{in}} = \dot{m}_{\mathrm{AirFil}}$ during stationary operation. The compressor additionally supplied the air bearing mass flow $\dot{m}_{\mathrm{AirBear}}$, which is indicated by the dashed arrows into and out of the compressor motor. Nonetheless, since this mass flow was recycled before the cathode inlet of the fuel cell stack, it did not provide oxygen to the electrochemical reaction. Hence, $\dot{m}_{\mathrm{Ca}}^{\mathrm{in}} \neq \dot{m}_{\mathrm{Cmpr}}$ stood during stationary operation. The original sensor signal $\dot{m}_{\mathrm{AirFil}}^{\mathrm{meas}}$ contained significant signal noise. Thus, it had been improved beforehand by employing a mass flow model, as described in [26].

Operating points with $\dot{m}_{\mathrm{Ca}}^{\mathrm{in}} \neq \dot{m}_{\mathrm{AirFil}}$ only occurred when the utilization of the cathode bypass path was required. This bypass path increased the amount of air in the exhaust without raising $\dot{m}_{\mathrm{Ca}}^{\mathrm{in}}$. Especially during low loads, the oxygen-depleted air at the fuel cell stack outlet was insufficient to dilute the hydrogen in the exhaust gas of the anode subsystem. Therefore, additional air was required to meet the safety requirements. What is more, the bypass path allowed to reduce the pressure at the compressor outlet quickly. As a result, compressor surge events could be prevented [115].

Another two measures to ensure the safe operation of the FCS were the cathode water separator (CWS) and the turbine water separator (TWS). The CWS prevented water droplets from entering the fuel cells, where they could block the gas flow channels. Otherwise, local oxygen starvation occurred. The TWS prevented water droplets from

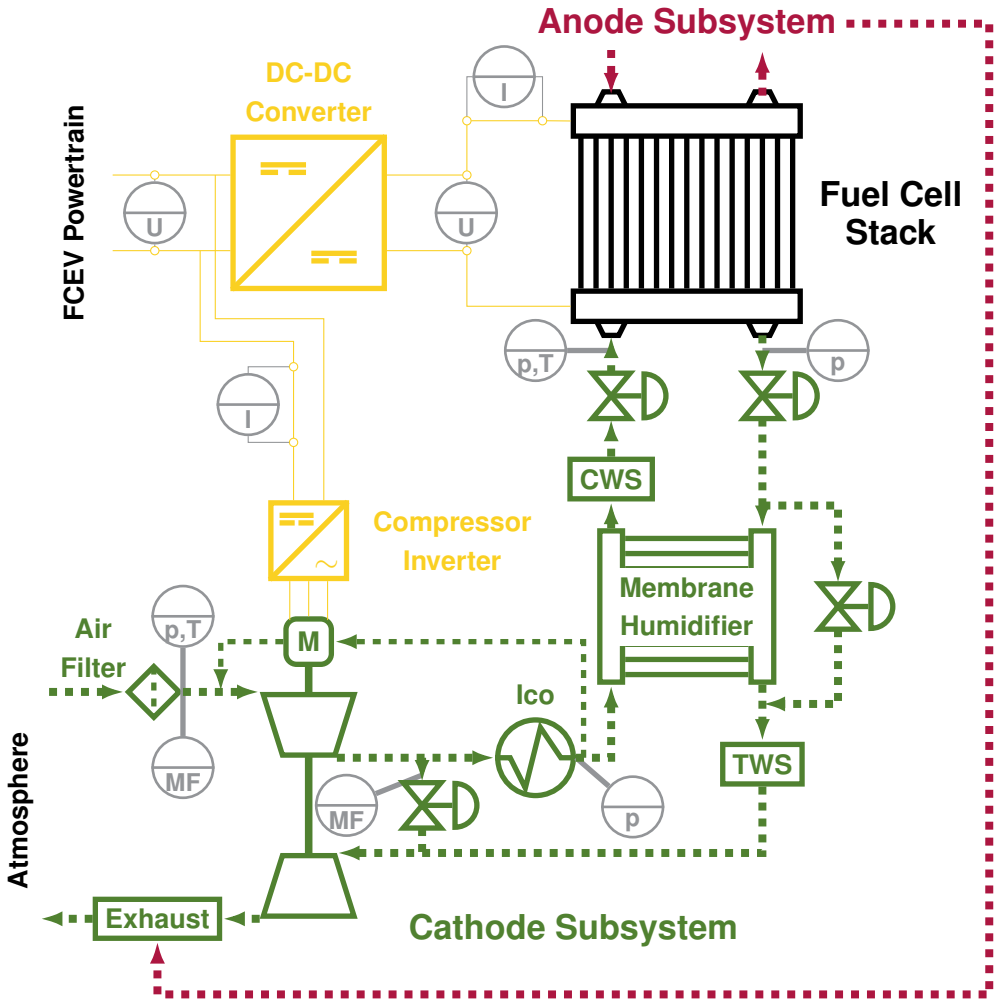

Figure 2: Cathode and electric subsystem of the FCS in the powertrain of the BMW iX5 Hydrogen with the available sensors for electric current (I), electric voltage (U), gas pressure (p), and temperature (T) as well as mass flows (MF).

causing erosion on the turbine blades [131]. While liquid water was not desirable during the operation of the FCS, some of the product water of the electrochemical reaction was recycled as water vapor through the membrane humidifier. This recycling led to a better distribution of water vapor in the fuel cells. Consequently, the polymer electrolyte membrane was well-humidified. Low humidity caused a high membrane resistance leading to unnecessary power losses in the fuel cell stack. The degree of water vapor recycling was manipulated with the membrane humidifier bypass valve.

The electric power from the fuel cell stack was the product of the DC load current I_{Stck} and the resulting U_{Stck} under load. The level of U_{Stck} was lower than that of the high voltage (HV) bus, which was determined by the voltage of the HV battery in the FCEV powertrain. Thus, energy transport over this voltage jump was only achievable through a DC-DC boost converter, depicted in Figure 2. The fuel cell stack was connected to the primary side of this DC-DC boost converter. By contrast, the DC interface of the compressor inverter was connected to the secondary side of the DC-DC boost converter. Therefore, the power consumption of the compressor P_{Cmpr} was determined by the DC

current drawn from the compressor inverter and the voltage level of the HV bus.

3.2.2 Fuel Cell Net Power and Hydrogen Dilution Control Architecture

P_{Cmpr} had a major influence on the control of P_{FCS}. It significantly reduced P_{FCS} in comparison to P_{Stck}. The impact of P_{Cmpr} could be divided into stationary and dynamic parts. On the one side, the stationary part depended on the stationary operating point of the air compressor, with higher n_{Cmpr} resulting in a higher P_{Cmpr}. On the other side, the acceleration and braking of the compressor motor determined the dynamic part. Higher levels of $i_{q,\mathrm{Cmpr}}$ resulted in faster acceleration of the compressor motor at the cost of higher levels of P_{Cmpr} during transients. Hence, the subordinate air supply controller that determined $i_{q,\mathrm{Cmpr}}^{\mathrm{sp}}$ significantly influenced the central FCS power controller. This influence is also indicated in the control cascade of Figure 3. In this work, the control

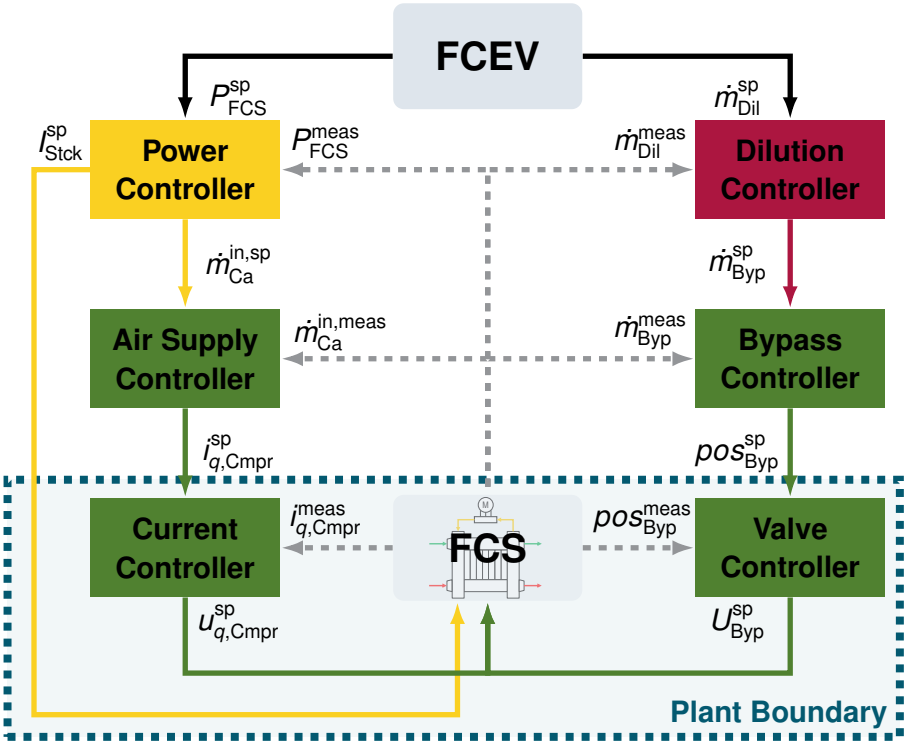

Figure 3: FCS net power and hydrogen dilution control cascades for the FCS in the BMW iX5 Hydrogen with the boundary of the controlled plant (dark blue dashed line) for the proposed controllers in this work.

variables of the power controller were the two setpoints $\dot{m}_{\mathrm{Ca}}^{\mathrm{in,sp}}$ and $I_{\mathrm{Stck}}^{\mathrm{sp}}$. Hydrogen supply, as well as fuel cell humidity and temperature control, were omitted due to the different time constants of the corresponding control tasks. While the pressure in the anode subsystem was adjusted rapidly, the temperature and humidity of the fuel cells only changed relatively slowly.

The utilization of $\dot{m}_{\mathrm{Ca}}^{\mathrm{in,sp}}$ as the setpoint for the air supply controller transferred the control of $\lambda_{\mathrm{O_2}}$ to the power controller. Therefore, $I_{\mathrm{Stck}}^{\mathrm{sp}}$ could be adapted by the power

controller to avoid large undershoots in λ_{O_2} while maintaining maximum dynamics. This control setup is similar to the approach proposed by Sun *et al.* [109]. Additionally, utilizing mass flow setpoints enabled the air supply and bypass controller to be developed independently from the power and dilution controller. The reference state of the control cascade for this work included two PI controllers for the air supply and the bypass controller. The control target $\dot{m}_{\mathrm{Ca}}^{\mathrm{in,meas}}$ for the air supply controller was calculated from the two sensor values $\dot{m}_{\mathrm{AirFil}}^{\mathrm{meas}}$ and $\dot{m}_{\mathrm{Byp}}^{\mathrm{meas}}$. The two air mass flow controllers acted on the subordinate current and valve controllers. On the one side, using a separate controller for $i_{q,\mathrm{Cmpr}}$ was necessary due to the considerably higher sampling frequency of the compressor inverter compared to the FCS ECU with 100 Hz. Thus, this work considered the current controller part of the controlled plant. On the other side, the valve controller was retained because the position of a throttle valve was better interpretable in a physical model than the voltage of its motor. Therefore, the valve controller was also considered part of the controlled plant.

The primary objective of this work was to improve the control setup of Figure 3. In previous works, the closed-loop behavior of the air supply subsystem had been optimized with MPC (e.g., [36]). Additionally, MPC could control MIMO systems comparable to the cathode subsystem in this work. The cross-coupling between $\dot{m}_{\mathrm{Ca}}^{\mathrm{in}}$ and $\dot{m}_{\mathrm{Byp}}$ could be directly considered in the controller formulation of the MPC. By contrast, each of the two PI controllers could only react to the perturbation caused by the other PI controller. Furthermore, utilizing a state and perturbation observer with the MPC introduced integral behavior without the risk of an integrator wind-up.

Compared to other studies on FCS air supply control, the control of p_{Ca} was neglected in this work. Pressure control was considered a separate control task that did not require similarly rapid dynamics. Additionally, the cathode inlet and outlet throttle valves were not used for dynamic control. Instead, these valves only sealed the fuel cell stack after shutting down the FCS. The VTG was also not used for air mass flow control since the impact of the VTG on the air mass flows was small. By contrast, the bypass valve was intended to be actively used for air supply control, which is why a MIMO linear and a MIMO nonlinear MPC for $\dot{m}_{\mathrm{Ca}}^{\mathrm{in}}$ and $\dot{m}_{\mathrm{Byp}}$ were implemented in this work. The real-time capability of both approaches was achieved with the explicit solution to the linear and nonlinear MPC optimization problem.

After the initial proof-of-concept for both approaches, the developed controllers were experimentally validated on an FCS test stand and in the FCEV. Moreover, the resulting closed-loop behavior was compared to the reference control setup. This validation step was conducted on an FCS test stand and in the FCEV. Additionally, the extension of the nonlinear approach to include the power and dilution controller was investigated in a small simulation study. The goal of this additional study was to determine the feasibility of the controller extension.

4 Control-Oriented Model of an Automotive Fuel Cell System

The primary goal of this study was to develop an improved air supply and bypass controller for an FCS. This goal was achieved with linear and nonlinear MPC. The real-time capability of both approaches was attained by using an explicit solution to the corresponding QP and NLP problem. Thus, a precise simulation model was required to efficiently adjust the parameter values in the cost function of the MPC. The availability of closed-loop simulations prevented comprehensive parameter studies on the FCS test stand. For each set of parameters, the explicit control law would have to be calculated first and then implemented on the ECU to be evaluated on the FCS test stand.

The employed simulation model was derived from available literature on control-oriented modeling of an FCS. This literature was revised, and the results are summarized in the first section of this chapter. Subsequently, the simulation model equations for the cathode subsystem and P_{FCS} were selected and parameterized. Since this study focused on air supply and power control, hydrogen supply, temperature, and humidity were assumed to be perfectly controlled. Thus, the anode subsystem, and temperature and humidity dynamics, were neglected. The accuracy of each component model of the cathode subsystem is displayed in Section 4.2. Similarly, the individual terms required to determine P_{FCS} are introduced in Section 4.3. In the final step, the complete simulation model was validated with measurement data from an FCS test stand and an FCEV. The validation results are presented in Section 4.4.

4.1 Literature Review

One of the first studies on fuel cell modeling was conducted by Springer *et al.* [106]. The authors presented a one-dimensional model of a single fuel cell with semi-empirical correlations for the membrane water content, its diffusion coefficient, and the membrane conductivity. These correlations helped characterize the influence of water on the fuel cell performance. Three years later, Amphlett *et al.* [4] developed a lumped-parameter model for the polarization curve of a fuel cell. The model parameters linked the fuel cell voltage to the cell temperature, the electric current, and the oxygen partial pressure. Initially, the values of these parameters had been determined empirically from experimental data. In a follow-up work [3], the lumped parameters were replaced with physical constants to derive an entirely mechanistic model. The authors further complemented this stationary model with temperature dynamics through the addition of energy balances in [5]. Additionally, Mann *et al.* [79] applied the model to a broader

operating range and added geometrical parameters to the correlation for the membrane resistance.

A more detailed three-dimensional fuel cell model with a focus on mass transfer was presented by Dutta *et al.* [25]. In this model, the data from [106] was used to develop empirical correlations for the water content in the membrane, the electro-osmotic drag coefficient, and the water diffusion coefficient. These correlations have been used in recently published control-oriented fuel cell system models (e.g., Sankar *et al.* [102]).

One of the first control-oriented fuel cell system models was developed by Pukrushpan [96], [97]. This lumped-parameter model incorporated findings from all the aforementioned studies. It targeted automotive applications and has been widely accepted for controller development. The focus of the model and the corresponding works [94], [95] was on the fuel cell stack and the cathode subsystem. In the cathode subsystem, the compressor is the main component that needs to be considered for control. Therefore, the compressor model was also the most detailed of all the auxiliary components. Over the years, the model [96], [97] has been used in many studies focused on the development of air supply and power controllers for FCS (e.g., [13], [85], [92]). The original ninth-order model was reduced to a fourth-order model in a follow-up work by Suh [107]. This reduction was based on three assumptions. Firstly, the dynamics of the anode subsystem were wholly neglected. Secondly, the constant atmospheric pressure was used as the cathode outlet pressure. Lastly, air in the fuel cell stack was assumed to be saturated with water vapor. The study of Suh [107] focused on air supply control, but the system model was further extended by a DC/DC converter and a battery model in a hybrid system setup. The model of Suh [107] has also been widely used in later studies on air supply and power control (e.g., [1], [37]). While the assumption of perfectly humidified air is feasible in some scenarios, it is not generally valid in real applications. Thus, Liu *et al.* [69] added the dynamics of water vapor on the cathode side of the fuel cell stack to the fourth-order model of Suh [107]. This extension enabled the consideration of a variable water transport through the membrane and water production due to the electrochemical reaction. Whilst Pukrushpan [96] and Liu *et al.* [69] only considered the humidifier as a means of changing the air humidity, Kunusch *et al.* [61] also contemplated the associated pressure loss. This model was used to develop an air supply controller in the study of Niknezhadi *et al.* [86].

Nonetheless, not only extended versions of the model of Suh [107] have been used. A further reduction of this model was reported by Talj *et al.* [112]. In this study, the partial pressures of oxygen, nitrogen, and water were merged into a novel state variable of the cathode subsystem. The goal was to increase the applicability of the resulting model in nonlinear control approaches (e.g., [77], [82]). This third-order model was extended by Li *et al.* [66] to include the dynamics of the BPV opening angle. The dynamic correlation between the setpoint and the actual value of the valve opening angle represented the closed-loop behavior of the BPV opening angle controller. Similarly, Sun *et al.* [109] included a controller for λ_{O_2} in their model. In both models, the setpoint of the respective control variable was considered as an input, while the actual value was viewed as a state.

A constant cathode outlet pressure has been a common assumption for models used to develop air supply controllers. Nonetheless, this assumption is only valid if the oxygen-depleted air is directly released into the environment (e.g., [107]) or if the cathode outlet pressure is well regulated (e.g., [61]). Otherwise, a dynamic cathode outlet pressure needs to be considered, as shown in the model of Kunusch *et al.* [60]. This model was also based on [96], [97] and only neglected the dynamics of the anode subsystem and the water vapor in the cathode subsystem. The model was used for controller development by Pilloni *et al.* [91], Deng *et al.* [21], [22], and Zhang *et al.* [127]. Similar models were reported by Rakhtala *et al.* [98] and Li *et al.* [65].

In all the FCS models above, the oxygen concentration in the fuel cell stack was lumped into one state variable. Thus, oxygen starvation only occurred in the simulation if the amount of oxygen supplied to the fuel cell stack was smaller than the amount of oxygen consumed by the electrochemical reaction. In actual fuel cells, oxygen starvation occurs in the catalyst layer. Thus, oxygen starvation also depends on mass transport through the gas diffusion layer. This diffusive transport was considered in the models of del Real *et al.* [20] and Ziogou *et al.* [134]. The former additionally implemented simple correlations for the auxiliary components, and their model was used to develop an air supply and power controller by Arce *et al.* [6] and Ramos-Paja *et al.* [99]. By contrast, the model of Ziogou *et al.* [134] considered the anode and cathode inlet mass flows as model inputs. As a result, this model is unsuitable for controller development concerning automotive fuel cell systems. The dynamic of automotive systems strongly depends on the dynamics of their auxiliary components.

In addition to the one-dimensional resolution of mass transport in the fuel cell stack, del Real *et al.* [20] and Ziogou *et al.* [134] took temperature dynamics into account. The temperature dynamics were the result of the implemented heat balances. Likewise, Sankar *et al.* [102] reported a lumped-parameter model of an FCS that included heat balances for the anode and cathode gases and the fuel cell body. Thus, efficient temperature control was enabled alongside the air supply and fuel cell voltage control.

While lumped-parameter models are generally based on semi-empirical correlations, purely empirical modeling approaches have also been reported with regard to control applications. The proposed approaches include ANNs [18], [130], an impulse response model [36], a Volterra series model [35], and linear transfer functions [59], [71], [110].

4.2 Model of the Cathode Subsystem

In this work, the controlled variables in the cathode subsystem were $\dot{m}_{\mathrm{Ca}}^{\mathrm{in}}$ and $\dot{m}_{\mathrm{Byp}}$. Thus, the main requirement for the simulation model of the cathode subsystem was accurately predicting the dynamic behavior and the stationary operating points of $\dot{m}_{\mathrm{Ca}}^{\mathrm{in}}$ and $\dot{m}_{\mathrm{Byp}}$ as a result of the control variables $i_{q,\mathrm{Cmpr}}^{\mathrm{sp}}$ and $pos_{\mathrm{Byp}}^{\mathrm{sp}}$. Pukrushpan *et al.* [97] showed that it is sufficient to implement a lumped-parameter model for FCS control applications, which is why this approach was also implemented in this study. Moreover, the utilization of a zero-dimensional model facilitated efficient closed-loop simulations.

The resulting system of ordinary differential equations (ODEs) was easier to solve than a system of partial differential equations (PDE) that would have resulted from utilizing spatial derivatives of state variables in one-dimensional models.

The total gas volume was divided into discrete manifolds for the lumped-parameter approach. The state of each manifold was determined by its pressure and temperature under the assumption of an ideal gas. This assumption of an ideal gas was feasible in the cathode subsystem of this work because the gas under consideration was air at approximately 70 °C. This temperature was the operating temperature $T_{\mathrm{Op,FCS}}$ of the FCS. Additionally, the associated assumption of constant gas temperature in the cathode subsystem enabled the derivation of a pressure state equation from the mass balance of a manifold.

$$\frac{\mathrm{d}p}{\mathrm{d}t} = \frac{R \cdot T}{V} \cdot \left(\sum \dot{m}^{\mathrm{in}} - \sum \dot{m}^{\mathrm{out}} \right) \tag{4.1}$$

Equation (4.1) shows that the rate of change of a manifold pressure p depended on the gas composition via the specific gas constant R and the manifold volume V. The incoming and outgoing mass flows $\dot{m}^{\mathrm{in}}$ and $\dot{m}^{\mathrm{out}}$ generally depended on the pressure difference between two manifolds. Therefore, the mass flows connected the manifolds. For the cathode subsystem in this work, this connection is shown in Figure 4. Hence, the state variables of the cathode subsystem model included the compressor outlet pressure $p^{\mathrm{out}}_{\mathrm{Cmpr}}$, the cathode inlet pressure $p^{\mathrm{in}}_{\mathrm{Ca}}$, the cathode outlet pressure $p^{\mathrm{out}}_{\mathrm{Ca}}$, the turbine inlet pressure $p^{\mathrm{in}}_{\mathrm{Trb}}$, and the turbine outlet pressure $p^{\mathrm{out}}_{\mathrm{Trb}}$. The corresponding manifold volumes were determined from the gas volume of the adjacent components and piping. Their values are summarized in Table 1. Further states of the model

Table 1: Values of the manifold volumes in the cathode subsystem model.

Parameter	Value
$V^{\mathrm{out}}_{\mathrm{Cmpr}}$	$2 \cdot 10^{-3}\,\mathrm{m}^3$
$V^{\mathrm{in}}_{\mathrm{Ca}}$	$9.6 \cdot 10^{-4}\,\mathrm{m}^3$
$V^{\mathrm{out}}_{\mathrm{Ca}}$	$9.6 \cdot 10^{-4}\,\mathrm{m}^3$
$V^{\mathrm{in}}_{\mathrm{Trb}}$	$1.1 \cdot 10^{-3}\,\mathrm{m}^3$
$V^{\mathrm{out}}_{\mathrm{Trb}}$	$1.1 \cdot 10^{-3}\,\mathrm{m}^3$

were related to the two primary actuators, the air compressor, and the bypass valve. Since the current and the valve controller were also part of the plant and had to be modeled, the quadrature current $i_{q,\mathrm{Cmpr}}$ of the air compressor motor, and the position of the bypass valve pos_{Byp} were the two controller states. The corresponding state equations are introduced in Section 4.2.1. Lastly, the rotational speed n_{Cmpr} of the air compressor was considered a state variable. The associated state equation is displayed in Section 4.2.2.

In addition to the manifold pressures, Figure 4 displays the mass flows calculated with stationary correlations in the cathode subsystem model. Another reason for the

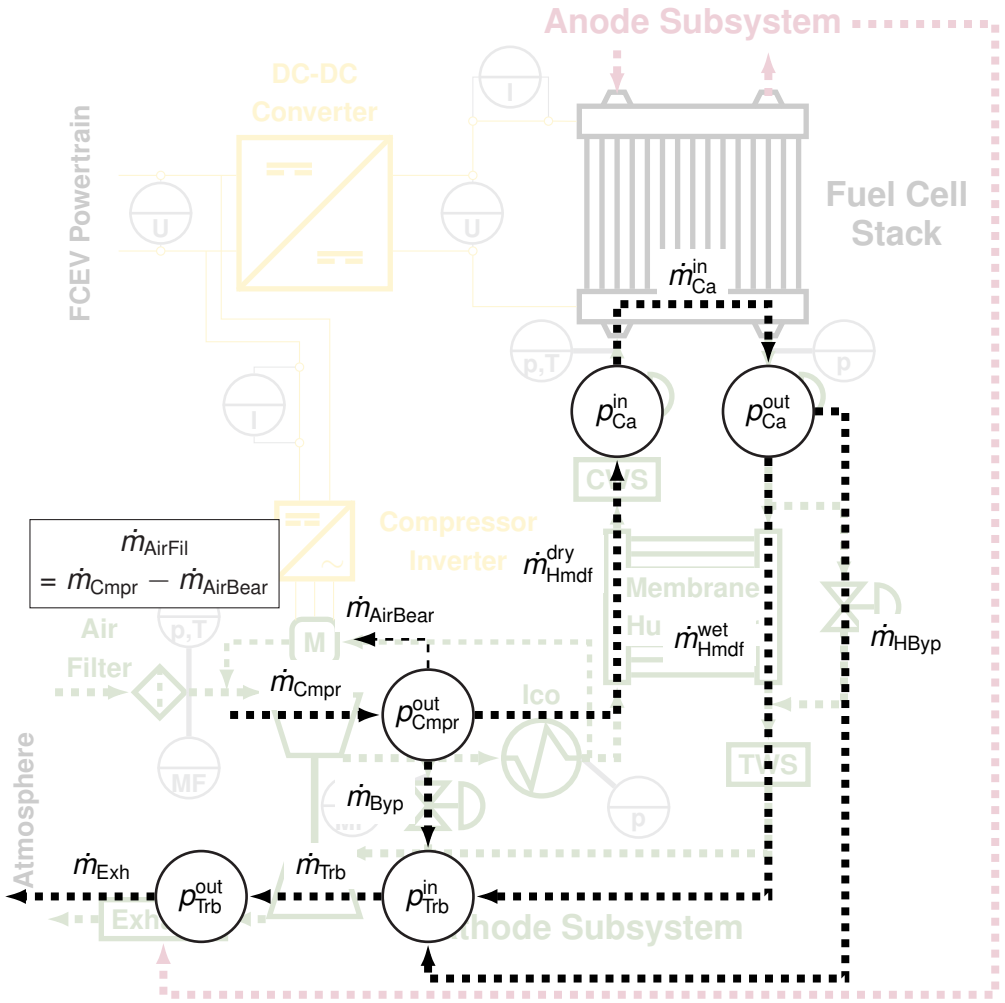

Figure 4: Schematic overview of the cathode subsystem model with pressure manifolds and connecting mass flows with their labeling.

lumped-parameter modeling approach was the ability to separately develop stationary correlations between mass flows and the pressure losses for each component in the considered system. These correlations were only combined in the last step to form a dynamic model. Thus, the model parameters were easily adapted to modified components. The development process in the automotive industry is highly dynamic, thus leading to frequent and independent component updates that need to be considered in a simulation model for controller development. The model equations for the compressor mass flow $\dot{m}_{\text{Cmpr}}$, the turbine mass flow $\dot{m}_{\text{Trb}}$, and the air bearing mass flow $\dot{m}_{\text{AirBear}}$ are all established in Section 4.2.2. In the subsequent Section 4.2.3, the correlation for the air mass flow into the stack $\dot{m}^{\text{in}}_{\text{Ca}}$ is presented. For the humidifier, the mass flows through the dry side $\dot{m}^{\text{dry}}_{\text{Hmdf}}$ and the wet side $\dot{m}^{\text{wet}}_{\text{Hmdf}}$ were determined as shown in Section 4.2.4. Next, $\dot{m}_{\text{Byp}}$ and the mass flow through the humidifier bypass valve $\dot{m}_{\text{HByp}}$ are introduced in Section 4.2.5. Lastly, the correlation for the mass flow through the cathode exhaust $\dot{m}_{\text{Exh}}$ is set up in Section 4.2.6.

What is more, Figure 4 also indirectly establishes further simplifications that were made to reduce the computational time of the closed-loop simulations. The pressure loss through the air filter was neglected because it was below 4 kPa throughout the entire operating range of the FCS. Similarly, the slight pressure losses through the intercooler and the cathode and turbine water separators enabled the neglection of these components in the simulation model. Additionally, the accessible pressure measurements of the FCS indicated that these two components did not significantly contribute to the overall pressure loss in the cathode subsystem. On the contrary, the cathode inlet and outlet valve significantly increased the pressure loss in the cathode subsystem, but only if partially closed. Moreover, since these two valves were fully open during regular operation, the respective pressure losses of both throttle valves were neglected throughout this work. Furthermore, the water content of the air in the cathode subsystem and the change in the air composition due to the electrochemical reaction were neglected throughout this work. R was the only variable in the cathode subsystem model dependent on the water content of the air. For fully humidified, oxygen-depleted air at $p = 1.5\,\mathrm{bar}$ with $\lambda_{\mathrm{O_2}} = 1.8$, R changes from $288.2\,\frac{\mathrm{J}}{\mathrm{kg\,K}}$ to $315.5\,\frac{\mathrm{J}}{\mathrm{kg\,K}}$. This difference in R is equivalent to an increase of 9.5 %. The consideration of a changing air composition would have required an additional ten state equations, two in each pressure manifold. This additional computational effort was regarded as more severe than the deviation in R. As a result, the water transport through the membrane humidifier was likewise neglected.

The main difference between this model and the previously reported models (e.g., [97], [102]) was the cathode bypass path and the more complex air exhaust path that included the wet side of the membrane humidifier together with its bypass valve, the turbine and an exhaust pipe that all contributed to the pressure loss in the cathode subsystem. Additionally, most studies have neglected subordinate controllers in their models. One of the few exceptions is the model implemented by Li *et al.* [66]. This model included the dynamics of the BPV valve position controller. Moreover, a compressor rotational speed controller was modeled by Zhao *et al.* [130].

4.2.1 Quadrature Current and Valve Position Controller Models

In this work, the outputs of the proposed air mass flow controller were $i_{q,\mathrm{Cmpr}}^{\mathrm{sp}}$ and $pos_{\mathrm{Byp}}^{\mathrm{sp}}$. Therefore, the controlled plant further included the current and valve controllers of Figure 3. Since the dynamics of these controllers were observable within a step size of $\Delta t = 10\,\mathrm{ms}$, separate models had to be developed that describe the correlations between the states $i_{q,\mathrm{Cmpr}}$ and pos_{Byp} and their respective setpoints (sp).

$$i_{q,\mathrm{Cmpr}}(k+1) = 0.6065 \cdot i_{q,\mathrm{Cmpr}}(k) + 0.3935 \cdot i_{q,\mathrm{Cmpr}}^{\mathrm{sp}}(k-5) \tag{4.2}$$

$$\begin{aligned} pos_{\mathrm{Byp}}(k+1) = {} & 0.3650 \cdot pos_{\mathrm{Byp}}(k) - 0.5488 \cdot pos_{\mathrm{Byp}}(k-1) \\ & + 0.1013 \cdot pos_{\mathrm{Byp}}^{\mathrm{sp}}(k-1) + 0.0825 \cdot pos_{\mathrm{Byp}}^{\mathrm{sp}}(k-2) \end{aligned} \tag{4.3}$$

The current controller (Eq. (4.2)) was approximated with a first-order low-pass filter. The corresponding time constant was set to $t_{i_q} = 20\,\text{ms}$, and an additional delay of $t_{d,I_q} = 50\,\text{ms}$ had to be considered. This time delay was caused by the controller area network (CAN) communication between the FCS ECU and the compressor inverter ECU. The validation of the current controller model for two positive and two negative step changes with different heights is shown in Figure 5. The stationary values of $i^{\text{sp}}_{q,\text{Cmpr}}$

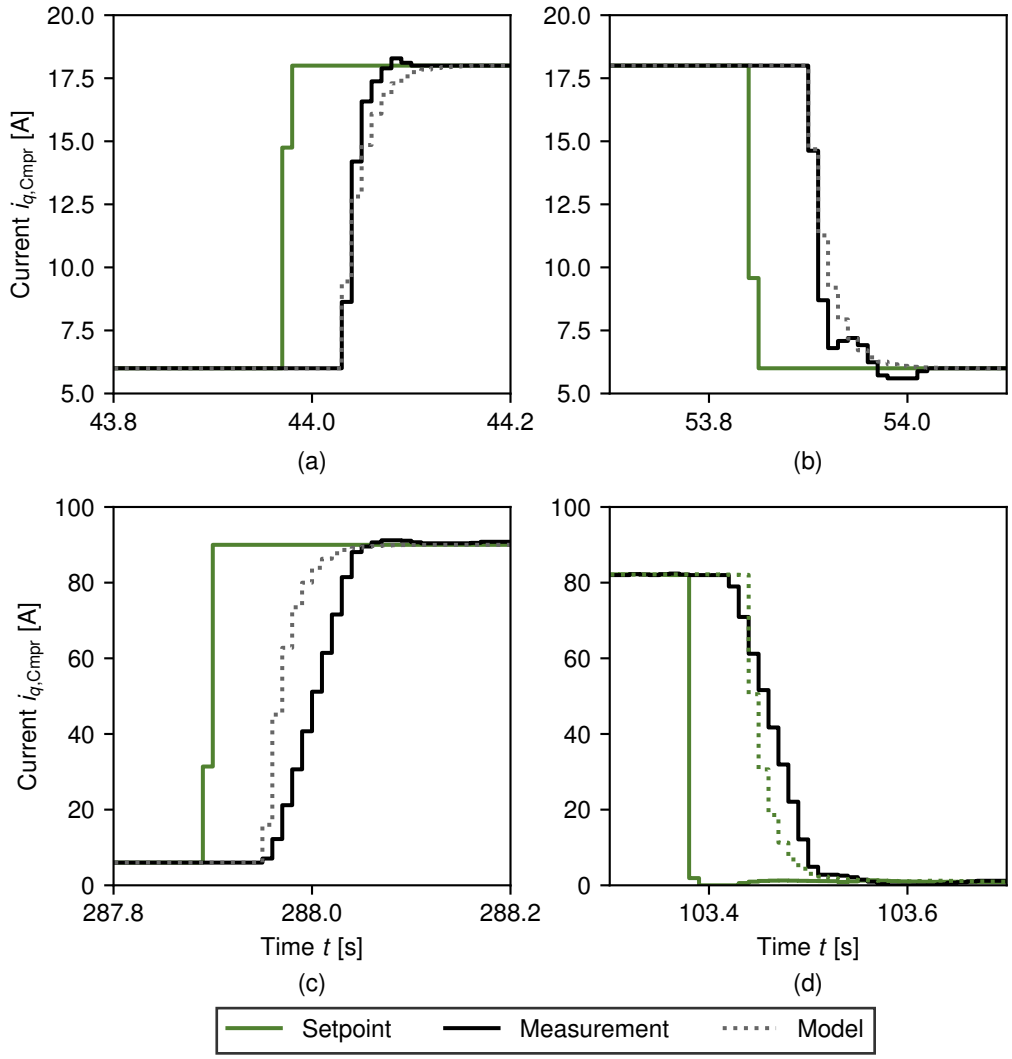

Figure 5: Experimental validation of the quadrature current controller model for step changes in $i^{\text{sp}}_{q,\text{Cmpr}}$.

in Figure 5c) and d) differed slightly because high negative step changes in $i^{\text{sp}}_{q,\text{Cmpr}}$ were only possible with an active air mass flow controller to avoid compressor surge. All the other step changes were executed manually to achieve higher reproducibility. The comparison of a) and b) to c) and d) from Fig 5 shows an overestimation of the controller time constant for low step changes and an underestimation for high step changes. Therefore, it is likely that the fundamental dynamic correlation between $i^{\text{sp}}_{q,\text{Cmpr}}$ and $i_{q,\text{Cmpr}}$ was nonlinear. Nonetheless, the deviation between the model and the measurement was acceptable for validating control approaches in a simulation.

The closed-loop behavior of the valve controller (Eq. (4.3)) was estimated with a second-order low-pass filter with a time constant $t_{pos} = 20\,\text{ms}$ and a damping factor of 0.6. The possibility of over- and undershoots with this transfer function required an additional limitation of pos_{Byp} to the physically feasible range [0 %, 100 %]. Furthermore, the time delay for the valve controller was smaller with $t_{d,pos} = 10\,\text{ms}$. The order of two was chosen to replicate the overshoots of the valve controller during positive step changes in $pos^{\text{sp}}_{\text{Byp}}$, as shown in the validation of the valve controller model in Fig. 6. The

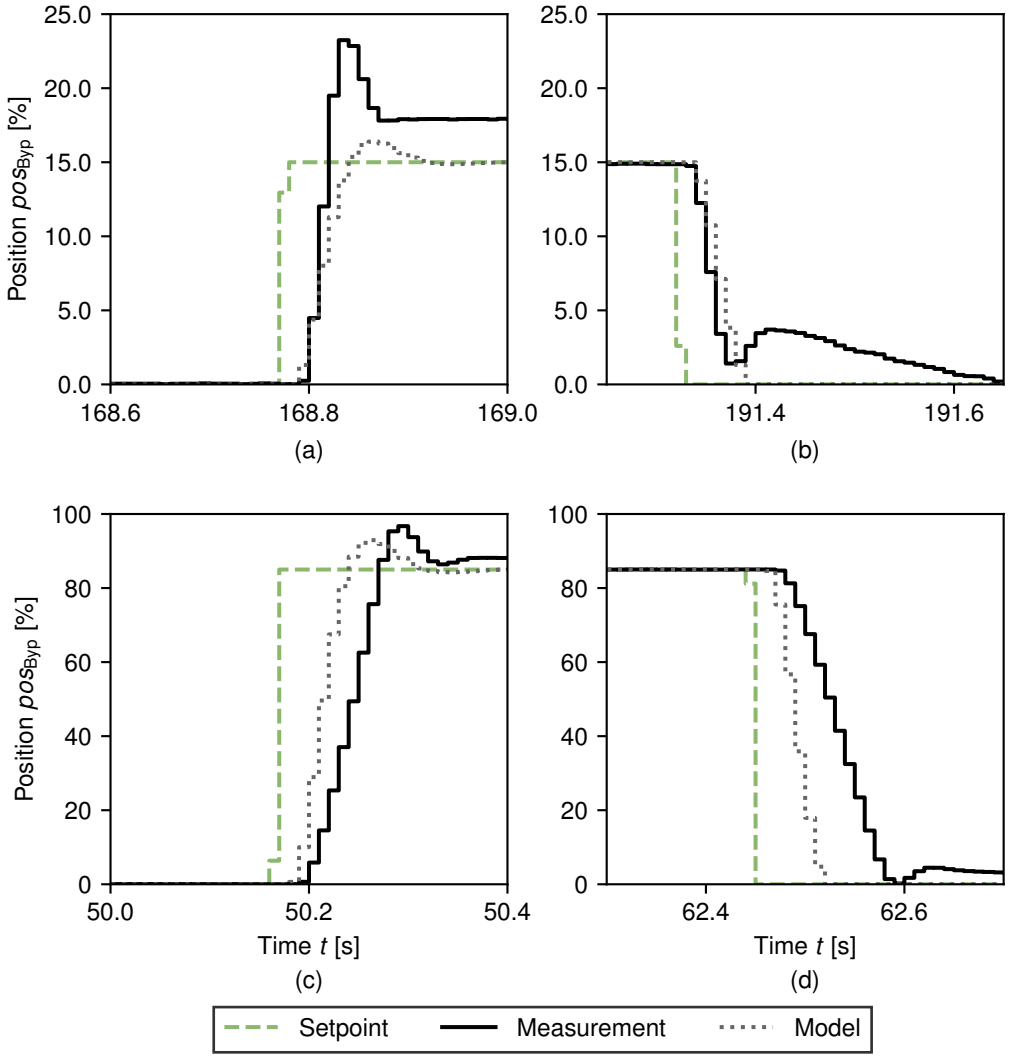

Figure 6: Experimental validation of the model of the bypass valve position controller for step changes in $pos^{\text{sp}}_{\text{Byp}}$.

comparison of Fig 6 to Figure 5 displays a significantly higher deviation for the position controller model. One reason was the suboptimal behavior of the actual position controller for negative step changes to 0 %. After the controller initially reduced the position close to the setpoint, it was increased again. This behavior differed from the behavior during positive step changes, during which the controller initially overshot the setpoint. Nonetheless, only one model was used throughout the entire operating range to retain a low controller model complexity. The second reason for the high deviation

between the model and measurement was the significant difference in the controller time constant between small and high step changes. This difference was assumed to be another nonlinearity similar to the one of the current controller. However, the deviation was found to be acceptable concerning the low complexity of the second-order low-pass filter and therefore used for the cathode subsystem simulation model.

4.2.2 Air Compressor and Turbine Model

In the cathode subsystem of an FCS, the air compressor was the component with the most significant impact on air mass flow and power control. It supplied the necessary oxygen from ambient air to the FCS, and its motor was the most substantial auxiliary power consumer. Therefore, the precise modeling of the air compressor was crucial for correctly predicting the dynamic behavior of an FCS. The corresponding model is shown first in this section. In this work, the air compressor was also mechanically connected to a turbine with a VTG. Thus, the air compressor model had to be extended with a turbine model presented subsequently. Eventually, the state equation for n_{Cmpr} is established at the end of this section.

Air Compressor Model In an air compressor, $\dot{m}_{\mathrm{Cmpr}}$ depends on the compressor inlet pressure $p^{\mathrm{in}}_{\mathrm{Cmpr}}$ and temperature $T^{\mathrm{in}}_{\mathrm{Cmpr}}$ as well as $p^{\mathrm{out}}_{\mathrm{Cmpr}}$ and n_{Cmpr}. This correlation is often visually illustrated in the compressor map. In this work, the stationary compressor map model from Moraal *et al.* [84] was used, based on the work of Jensen *et al.* [53]. The only modifications from the original model [84] were the factors eliminating the mass flow dependency on the compressor inlet conditions. The temperature and pressure correction terms $\theta^{\mathrm{in}}_{\mathrm{Cmpr}}$ and $\delta^{\mathrm{in}}_{\mathrm{Cmpr}}$ were taken from [96] because they are dimensionless.

$$\theta^{\mathrm{in}}_{\mathrm{Cmpr}} = \frac{T^{\mathrm{in}}_{\mathrm{Cmpr}}}{T^{\mathrm{ref}}_{\mathrm{Cmpr}}}, \qquad T^{\mathrm{ref}}_{\mathrm{Cmpr}} = 298.15\,\mathrm{K} \tag{4.4}$$

$$\delta^{\mathrm{in}}_{\mathrm{Cmpr}} = \frac{p^{\mathrm{in}}_{\mathrm{Cmpr}}}{p^{\mathrm{ref}}_{\mathrm{Cmpr}}}, \qquad p^{\mathrm{ref}}_{\mathrm{Cmpr}} = 1\,\mathrm{bar} \tag{4.5}$$

The correction terms from Equations (4.4) and (4.5) were used to calculate a scaled compressor mass flow $\dot{\tilde{m}}_{\mathrm{Cmpr}}$ and a scaled compressor rotational speed $\dot{\tilde{n}}_{\mathrm{Cmpr}}$.

$$\dot{\tilde{m}}_{\mathrm{Cmpr}} = \dot{m}_{\mathrm{Cmpr}} \cdot \frac{\sqrt{\theta^{\mathrm{in}}_{\mathrm{Cmpr}}}}{\delta^{\mathrm{in}}_{\mathrm{Cmpr}}} \tag{4.6}$$

$$\tilde{n}_{\mathrm{Cmpr}} = n_{\mathrm{Cmpr}} \cdot \frac{1}{\sqrt{\theta^{\mathrm{in}}_{\mathrm{Cmpr}}}} \tag{4.7}$$

The normalized compressor flow rate Φ_{Cmpr} was another necessary dimensionless quantity of the compressor map model derived from $\dot{\tilde{m}}_{\mathrm{Cmpr}}$.

$$\Phi_{\mathrm{Cmpr}} = \frac{\dot{\tilde{m}}_{\mathrm{Cmpr}}}{\rho_{\mathrm{Air}}^{\mathrm{ref}} \cdot \frac{\pi}{4} \cdot d_{\mathrm{Cmpr}}^2 \cdot U_{\mathrm{c}}} \tag{4.8}$$

In addition, Φ_{Cmpr} was also dependent on the air density at reference conditions $\rho_{\mathrm{Air}}^{\mathrm{ref}}$, the compressor blade diameter d_{Cmpr}, and the air speed at the compressor blade tip U_{c}.

$$U_{\mathrm{c}} = \frac{\pi}{60} \cdot d_{\mathrm{Cmpr}} \cdot \tilde{n}_{\mathrm{Cmpr}} \tag{4.9}$$

The crucial part of this compressor map model was the correlation between Φ_{Cmpr} and the dimensionless head parameter Ψ_{Cmpr}.

$$\Phi_{\mathrm{Cmpr}} = \frac{k_3 \cdot \Psi_{\mathrm{Cmpr}} - k_1}{k_2 + \Psi_{\mathrm{Cmpr}}} \tag{4.10}$$

Equation (4.10) was taken from [84]. It differs from the correlation used in the FCS model of Pukrushpan [96], which has been widely used within the FCS control community. The correlation from Moraal *et al.* [84] was chosen because it contains fewer fitting parameters while showing a similar fitting capability. There were six fitting parameters $k_{i,j}$ that make up the three model parameters k_i of Equation (4.10).

$$k_i = k_{i,1} + k_{i,2} \cdot Ma_{\mathrm{Cmpr}} \tag{4.11}$$

The compressor inlet Mach number Ma_{Cmpr} was another dimensionless quantity that related U_{c} to the speed of sound of air at reference conditions, which was calculated from the specific gas constant R_{Air} and the ratio of heat capacities $\gamma_{\mathrm{Air}} = \frac{c_{p,\mathrm{Air}}}{c_{v,\mathrm{Air}}}$ for dry air.

$$Ma_{\mathrm{Cmpr}} = \frac{U_{\mathrm{c}}}{\sqrt{\gamma_{\mathrm{Air}} \cdot R_{\mathrm{Air}} \cdot T^{\mathrm{ref}}}} \tag{4.12}$$

Finally, Ψ_{Cmpr} was the ratio of the isentropic enthalpy change over the air compressor to the kinetic energy of air at the compressor blade tip.

$$\Psi_{\mathrm{Cmpr}} = \frac{2 \cdot c_{p,\mathrm{Air}} \cdot T^{\mathrm{ref}} \cdot \left[\left(\frac{p_{\mathrm{Cmpr}}^{\mathrm{out}}}{p_{\mathrm{Cmpr}}^{\mathrm{in}}} \right)^{\frac{\gamma_{\mathrm{Air}}-1}{\gamma_{\mathrm{Air}}}} - 1 \right]}{U_{\mathrm{c}}^2} \tag{4.13}$$

The isentropic enthalpy change was also connected to the isentropic efficiency of the compressor $\eta_{Is,\mathrm{Cmpr}}$.

$$\eta_{Is,\mathrm{Cmpr}} = \frac{T_{Is,\mathrm{Cmpr}}^{\mathrm{out}} - T_{\mathrm{Cmpr}}^{\mathrm{in}}}{T_{\mathrm{Cmpr}}^{\mathrm{out}} - T_{\mathrm{Cmpr}}^{\mathrm{in}}} \tag{4.14}$$

$T^{\text{out}}_{Is,\text{Cmpr}}$ was the air temperature at the outlet of the air compressor for an ideal isentropic process.

$$T^{\text{out}}_{Is,\text{Cmpr}} = T^{\text{in}}_{\text{Cmpr}} \cdot \left(\frac{p^{\text{out}}_{\text{Cmpr}}}{p^{\text{in}}_{\text{Cmpr}}} \right)^{\frac{\gamma_{\text{Air}}-1}{\gamma_{\text{Air}}}} \tag{4.15}$$

The value of $\eta_{Is,\text{Cmpr}}$ has been assumed to be constant (e.g., 0.8 in [102]) or determined by a lookup table [96]. In this work, the continuous model of Moraal *et al.* [84] was applied.

$$\eta_{Is,\text{Cmpr}} = 100 \cdot a_1 \cdot \Phi^2_{\text{Cmpr}} + 10 \cdot a_2 \cdot \Phi_{\text{Cmpr}} + a_3 \tag{4.16}$$

The factors 100 and 10 in front of a_1 and a_2 were chosen to have all values of $a_{i,j}$ of a similar magnitude to improve the parameter fitting. The model of Equation (4.16) required the determination of nine fitting parameters $a_{i,j}$ from measurement data.

$$a_i = \frac{a_{i,1} + a_{i,2} \cdot Ma_{\text{Cmpr}}}{a_{i,3} - Ma_{\text{Cmpr}}} \tag{4.17}$$

With the model for $\eta_{Is,\text{Cmpr}}$, the real enthalpy change of the air in the air compressor was calculated in the simulation model. This enthalpy change was directly proportional to the load moment τ_{Cmpr} of the air compressor.

$$\tau_{\text{Cmpr}} = \frac{\dot{m}_{\text{Cmpr}} \cdot c_{p,\text{Air}} \cdot T^{\text{in}}_{\text{Cmpr}}}{\omega_{\text{Cmpr}} \cdot \eta_{Is,\text{Cmpr}}} \cdot \left[\left(\frac{p^{\text{out}}_{\text{Cmpr}}}{p^{\text{in}}_{\text{Cmpr}}} \right)^{\frac{\gamma_{\text{Air}}-1}{\gamma_{\text{Air}}}} - 1 \right] \tag{4.18}$$

The fitting of $k_{i,j}$ achieved a coefficient of determination $R^2 = 0.9976$ for $\dot{\tilde{m}}_{\text{Cmpr}}$, while $R^2 = 0.9269$ with regard to $\eta_{Is,\text{Cmpr}}$ was accomplished during the fitting of $a_{i,j}$. The fitted values of k_{ij} and a_{ij} are listed in Table 2. While $\dot{m}_{\text{Cmpr}}$ and $\eta_{Is,\text{Cmpr}}$ described

Table 2: Values of the fitting parameter for the air compressor model.

Parameter	Value	Parameter	Value	Parameter	Value
$k_{1,1}$	0.1446	$k_{3,2}$	0.0107	$a_{2,2}$	–8.8598
$k_{1,2}$	0.0093	$a_{1,1}$	–0.5737	$a_{2,3}$	–1.2758
$k_{2,1}$	–1.4833	$a_{1,2}$	3.3724	$a_{3,1}$	–9.2242
$k_{2,2}$	0.1410	$a_{1,3}$	–0.5676	$a_{3,2}$	9.7296
$k_{3,1}$	0.1156	$a_{2,1}$	2.9500	$a_{3,3}$	–5.1665

the air compressor in its operating range, it was also essential to know the limits of this operating range. Only the surge line had to be considered for the combination of an air compressor with a turbine in this work. The approximation of the surge line was based

on data from the air compressor manufacturer.

$$\left(\frac{p^{\text{out}}_{\text{Cmpr}}}{p^{\text{in}}_{\text{Cmpr}}}\right)_{\text{Srg}} = 1.31 \cdot 10^{-4} \cdot \dot{m}^2_{\text{Cmpr}} + 2.1425 \cdot 10^{-2} \cdot \dot{m}_{\text{Cmpr}} + 0.859209 \quad (4.19)$$

The choke line was negligible due to the additional operation requirement to keep a minimum inlet pressure at the turbine inlet. As a result, the choke line was never reached. Furthermore, the turbine inlet pressure condition was enforced through the cathode pressure operating points and, thus, not considered in the scope of this work.

The fitted compressor map and efficiency model is depicted in Figure 7, together with the surge line. In Figure 7, normalized values for $\left(\frac{p^{\text{out}}_{\text{Cmpr}}}{p^{\text{in}}_{\text{Cmpr}}}\right)$ and $\eta_{Is,\text{Cmpr}}$ are used.

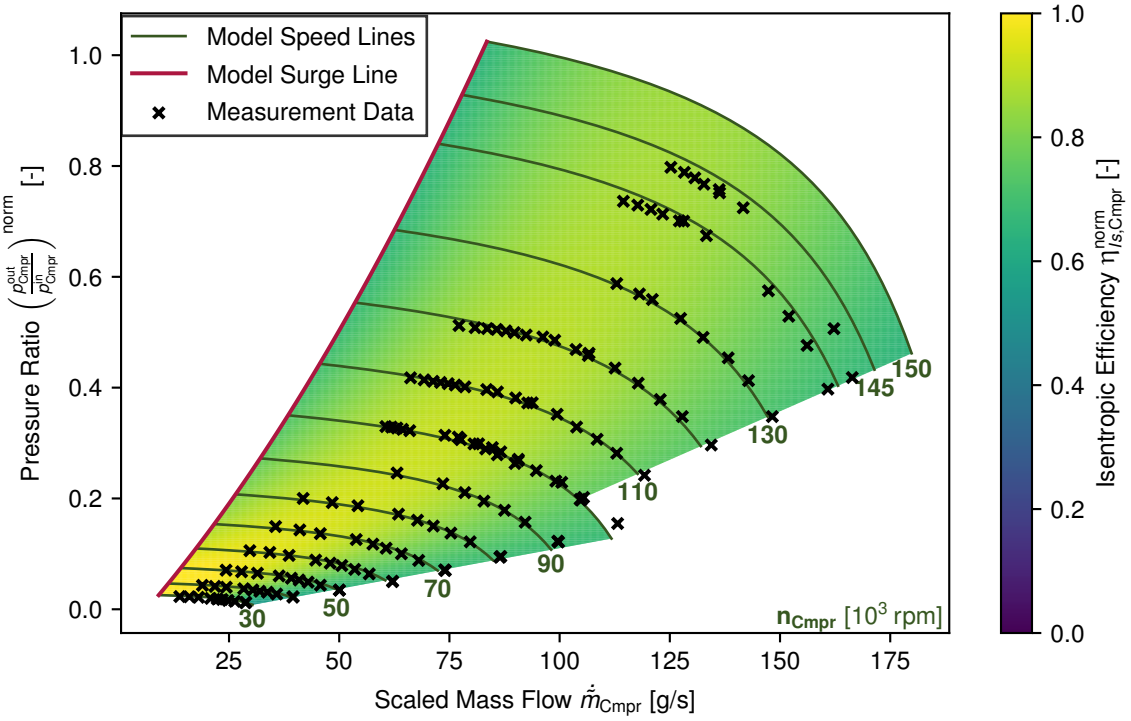

Figure 7: Compressor map model including the speed lines and the surge line as well as $\eta^{\text{norm}}_{Is,\text{Cmpr}}$ for $T^{\text{in}}_{\text{Cmpr}} = 15$ °C with the stationary measurement points from the parameter fitting for comparison.

$$\left(\frac{p^{\text{out}}_{\text{Cmpr}}}{p^{\text{in}}_{\text{Cmpr}}}\right)^{\text{norm}} = \frac{\left(\frac{p^{\text{out}}_{\text{Cmpr}}}{p^{\text{in}}_{\text{Cmpr}}}\right) - \left(\frac{p^{\text{out}}_{\text{Cmpr}}}{p^{\text{in}}_{\text{Cmpr}}}\right)_{\text{Min}}}{\left(\frac{p^{\text{out}}_{\text{Cmpr}}}{p^{\text{in}}_{\text{Cmpr}}}\right)_{\text{Max}} - \left(\frac{p^{\text{out}}_{\text{Cmpr}}}{p^{\text{in}}_{\text{Cmpr}}}\right)_{\text{Min}}} \quad (4.20)$$

$$\eta^{\text{norm}}_{Is,\text{Cmpr}} = \frac{\eta_{Is,\text{Cmpr}}}{\eta_{Is,\text{Cmpr,Max}}} \quad (4.21)$$

The comparison of the stationary measurement points with the speed lines of the compressor map model in Figure 7 shows a good agreement throughout the operating range.

Similarly, Figure 8 demonstrates that the model for $\eta_{Is,\mathrm{Cmpr}}$ matched well the measurement points. The only significant deviations occurred for low efficiencies around

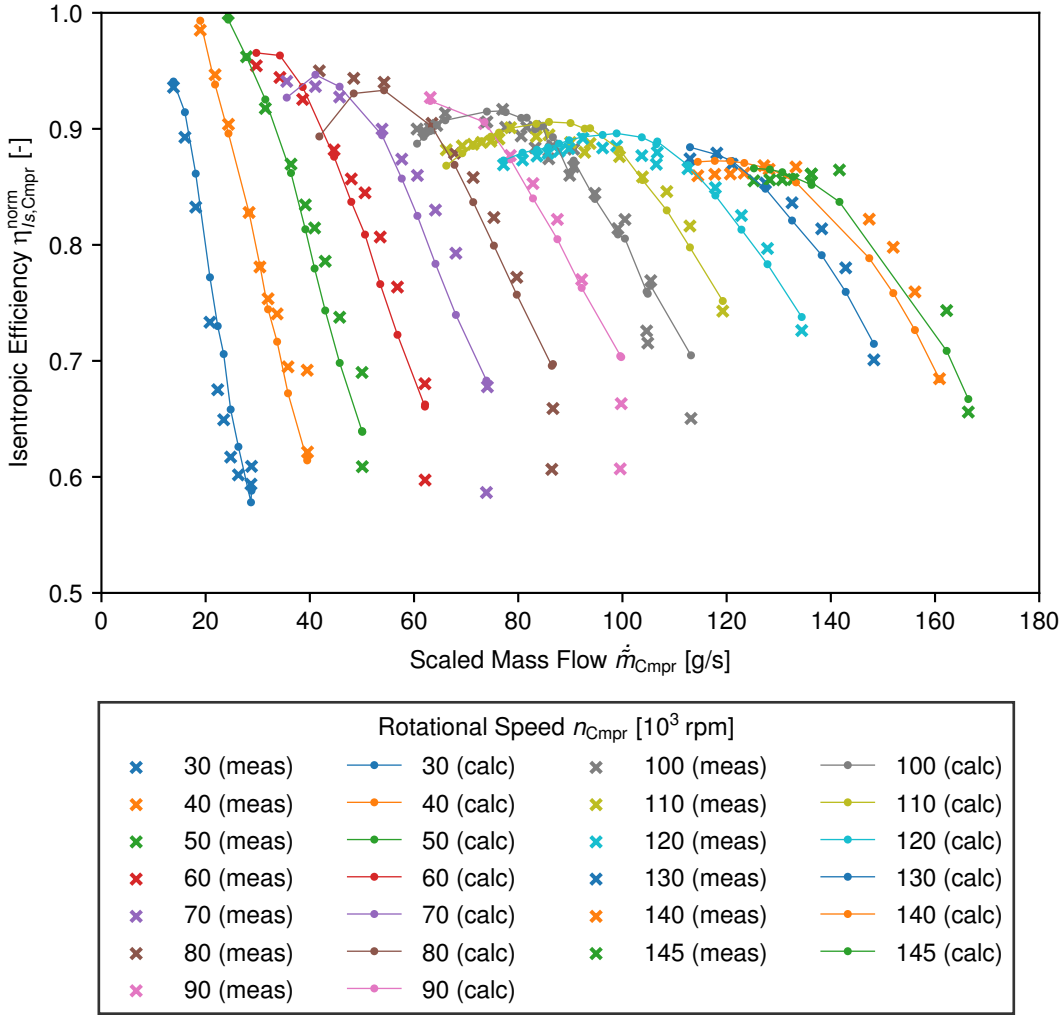

Figure 8: Comparison of measurement data (meas) and model calculations (calc) for $\eta^{\mathrm{norm}}_{Is,\mathrm{Cmpr}}$.

$\eta^{\mathrm{norm}}_{Is,\mathrm{Cmpr}} = 0.65$. Since these deviations were at the edge of the air compressor operating range, their impact on the simulation model accuracy was acceptable nonetheless.

Air Bearing Model The air compressor supplied oxygen to the fuel cell stack from the ambient air. While $\dot{m}_{\mathrm{Cmpr}}$ was a good approximation for the available mass flow, a small share of $\dot{m}_{\mathrm{Cmpr}}$ was deducted for the air bearing. Thus, $\dot{m}_{\mathrm{AirBear}}$ had to be considered in the cathode subsystem simulation model.

$$\dot{m}_{\mathrm{AirBear}} = C_{\mathrm{AirBear}} \cdot \sqrt{\rho^{\mathrm{in}}_{\mathrm{AirBear}} \cdot (p^{\mathrm{in}}_{\mathrm{AirBear}} - p^{\mathrm{out}}_{\mathrm{AirBear}})}, \qquad \rho^{\mathrm{in}}_{\mathrm{AirBear}} = \frac{p^{\mathrm{in}}_{\mathrm{AirBear}}}{R_{\mathrm{Air}} \cdot T^{\mathrm{in}}_{\mathrm{AirBear}}} \quad (4.22)$$

Equation (4.22) was based on the assumption of tube flow in the air bearing with a constant tube friction coefficient [26]. This tube friction coefficient was part of the

model parameter $C_{\mathrm{AirBear}} = 9.26 \cdot 10^{-6}\,\mathrm{m}^2$, which was determined from measurement. This fitting achieved $R^2 = 0.9978$ for $\dot{m}_{\mathrm{AirBear}}$. The comparison of measurement data to the corresponding model calculations in Figure 9 shows an excellent agreement.

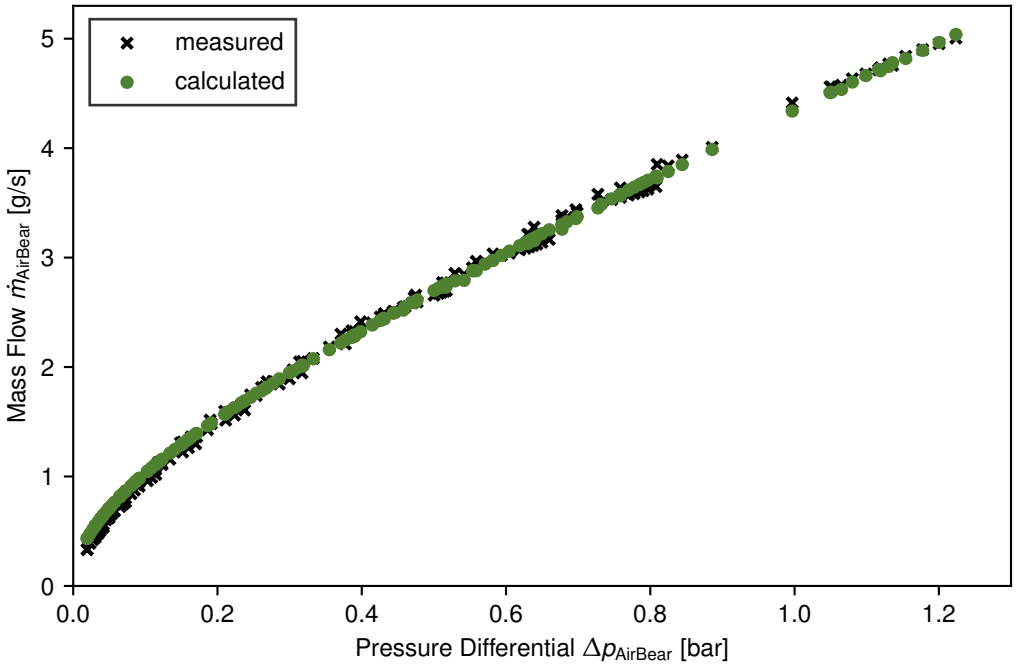

Figure 9: Comparison of measurement data (measured) and model calculations (calculated) for $\dot{m}_{\mathrm{AirBear}}$.

Turbine Model Turbines have been considered as part of an FCS [80], [103], [129]. Nonetheless, the turbine model of Moraal *et al.* [84] was best suited to calculate $\dot{m}_{\mathrm{Trb}}$ and the isentropic efficiency of the turbine $\eta_{Is,\mathrm{Trb}}$, which were required in the cathode simulation model of this work. This turbine model was also based on the results of Jensen *et al.* [53]. Similar to the air compressor model, correction terms θ_{Trb} and δ_{Trb} for the turbine inlet temperature $T^{\mathrm{in}}_{\mathrm{Trb}}$ and pressure $p^{\mathrm{in}}_{\mathrm{Trb}}$ were included.

$$\theta^{\mathrm{in}}_{\mathrm{Trb}} = \frac{T^{\mathrm{in}}_{\mathrm{Trb}}}{T^{\mathrm{ref}}_{\mathrm{Cmpr}}} \tag{4.23}$$

$$\delta^{\mathrm{in}}_{\mathrm{Trb}} = \frac{p^{\mathrm{in}}_{\mathrm{Trb}}}{p^{\mathrm{ref}}_{\mathrm{Cmpr}}} \tag{4.24}$$

The turbine was mechanically connected to the compressor. Thus, the turbine had the same rotational speed n_{Trb} as the compressor. Therefore, the scaled rotational speed $\tilde{n}_{\mathrm{Trb}}$ was calculated from n_{Cmpr}. Furthermore, θ_{Trb} and δ_{Trb} were utilized to determine a scaled mass flow $\dot{\tilde{m}}_{\mathrm{Trb}}$.

$$\dot{\tilde{m}}_{\mathrm{Trb}} = \dot{m}_{\mathrm{Trb}} \cdot \frac{\sqrt{\theta^{\mathrm{in}}_{\mathrm{Trb}}}}{\delta^{\mathrm{in}}_{\mathrm{Trb}}} \tag{4.25}$$

$$\tilde{n}_{\mathrm{Trb}} = n_{\mathrm{Cmpr}} \cdot \frac{1}{\sqrt{\theta^{\mathrm{in}}_{\mathrm{Trb}}}} \tag{4.26}$$

The correlation between $\dot{\tilde{m}}_{\mathrm{Trb}}$ and the pressure ratio over the turbine in [84] was derived from a nozzle flow equation as presented in [46].

$$\dot{\tilde{m}}_{\mathrm{Trb}} = A^{\mathrm{eff}}_{\mathrm{Trb}} \cdot \sqrt{\frac{2 \cdot \gamma_{\mathrm{Air}}}{\gamma_{\mathrm{Air}} - 1} \cdot \left[\left(\frac{p^{\mathrm{out}}_{\mathrm{Trb}}}{p^{\mathrm{in}}_{\mathrm{Trb}}} - p^{\mathrm{corr}}_{\mathrm{rat,VTG}} \right)^{\frac{2}{\gamma_{\mathrm{Air}}}} - \left(\frac{p^{\mathrm{out}}_{\mathrm{Trb}}}{p^{\mathrm{in}}_{\mathrm{Trb}}} - p^{\mathrm{corr}}_{\mathrm{rat,VTG}} \right)^{\frac{\gamma_{\mathrm{Air}}+1}{\gamma_{\mathrm{Air}}}} \right]} \tag{4.27}$$

Like nozzles, choked flow is observed in a turbine for $\frac{p^{\mathrm{out}}_{\mathrm{Trb}}}{p^{\mathrm{in}}_{\mathrm{Trb}}} \leq p^{\mathrm{crit}}_{\mathrm{rat}}$. For choked flow, the nozzle factor under the square root in Equation (4.27) no longer depends on the pressure ratio over the turbine. This effect was represented in the correlation for $\dot{\tilde{m}}_{\mathrm{Trb}}$ by replacing $\frac{p^{\mathrm{out}}_{\mathrm{Trb}}}{p^{\mathrm{in}}_{\mathrm{Trb}}}$ with the constant $p^{\mathrm{crit}}_{\mathrm{rat}}$.

$$\dot{\tilde{m}}_{\mathrm{Trb}} = A^{\mathrm{eff}}_{\mathrm{Trb}} \cdot \sqrt{\frac{2 \cdot \gamma_{\mathrm{Air}}}{\gamma_{\mathrm{Air}} - 1} \cdot \left[\left(p^{\mathrm{crit}}_{\mathrm{rat}} - p^{\mathrm{corr}}_{\mathrm{rat,VTG}} \right)^{\frac{2}{\gamma_{\mathrm{Air}}}} - \left(p^{\mathrm{crit}}_{\mathrm{rat}} - p^{\mathrm{corr}}_{\mathrm{rat,VTG}} \right)^{\frac{\gamma_{\mathrm{Air}}+1}{\gamma_{\mathrm{Air}}}} \right]} \tag{4.28}$$

The value of $p^{\mathrm{crit}}_{\mathrm{rat}}$ was dependent on the composition of the gas that flowed through the turbine. Since the turbine was positioned at the outlet of the cathode subsystem, the gas was oxygen-depleted air with varying compositions. Still, the air composition was approximated with dry air for each component in the cathode subsystem model. Thus, R_{Air} and γ_{Air} were used to compute $p^{\mathrm{crit}}_{\mathrm{rat}}$.

$$p^{\mathrm{crit}}_{\mathrm{rat}} = \left(\frac{2}{\gamma_{\mathrm{Air}} + 1} \right)^{\frac{\gamma_{\mathrm{Air}}}{\gamma_{\mathrm{Air}}-1}} \tag{4.29}$$

The second term influencing $\dot{\tilde{m}}_{\mathrm{Trb}}$ was the effective opening area of the turbine $A^{\mathrm{eff}}_{\mathrm{Trb}}$. This variable contained the fitting parameters $k_{i,j}$ for the turbine map model.

$$A^{\mathrm{eff}}_{\mathrm{Trb}} = \left(c^{\mathrm{corr}}_{1,\mathrm{VTG}} \cdot pos_{\mathrm{VTG}} + c^{\mathrm{corr}}_{2,\mathrm{VTG}} \right) \cdot \left[\frac{k_1}{\left(\frac{p^{\mathrm{out}}_{\mathrm{Trb}}}{p^{\mathrm{in}}_{\mathrm{Trb}}} \right)} + k_2 \right] \tag{4.30}$$

$$k_i = k_{i,1} \cdot \tilde{n}_{\mathrm{Trb}} + k_{i,2} \tag{4.31}$$

The VTG position pos_{VTG} impacted both $A^{\mathrm{eff}}_{\mathrm{Trb}}$ and the pressure ratio correction term $p^{\mathrm{corr}}_{\mathrm{rat,VTG}}$ in Equations (4.27) and (4.28).

$$p^{\mathrm{corr}}_{\mathrm{rat,VTG}} = k^{\mathrm{corr}}_{1,\mathrm{VTG}} \cdot pos^2_{\mathrm{VTG}} + k^{\mathrm{corr}}_{2,\mathrm{VTG}} \cdot pos_{\mathrm{VTG}} + k^{\mathrm{corr}}_{3,\mathrm{VTG}} \tag{4.32}$$

The three model parameters $k_{i,\mathrm{VTG}}$ from Equation (4.32) were fitted to measurement data together with $k_{i,j}$ and $c_{i,\mathrm{VTG}}$. This fitting achieved $R^2 = 0.9964$ with regard to $\dot{\tilde{m}}_{\mathrm{Trb}}$. A comparison of the adapted model and the corresponding measurement data is displayed in Figure 10, with a normalized pressure ratio equivalent to Equation (4.20).

The calculated model values for $\dot{m}_{\mathrm{Trb}}$ matched the stationary measurement points

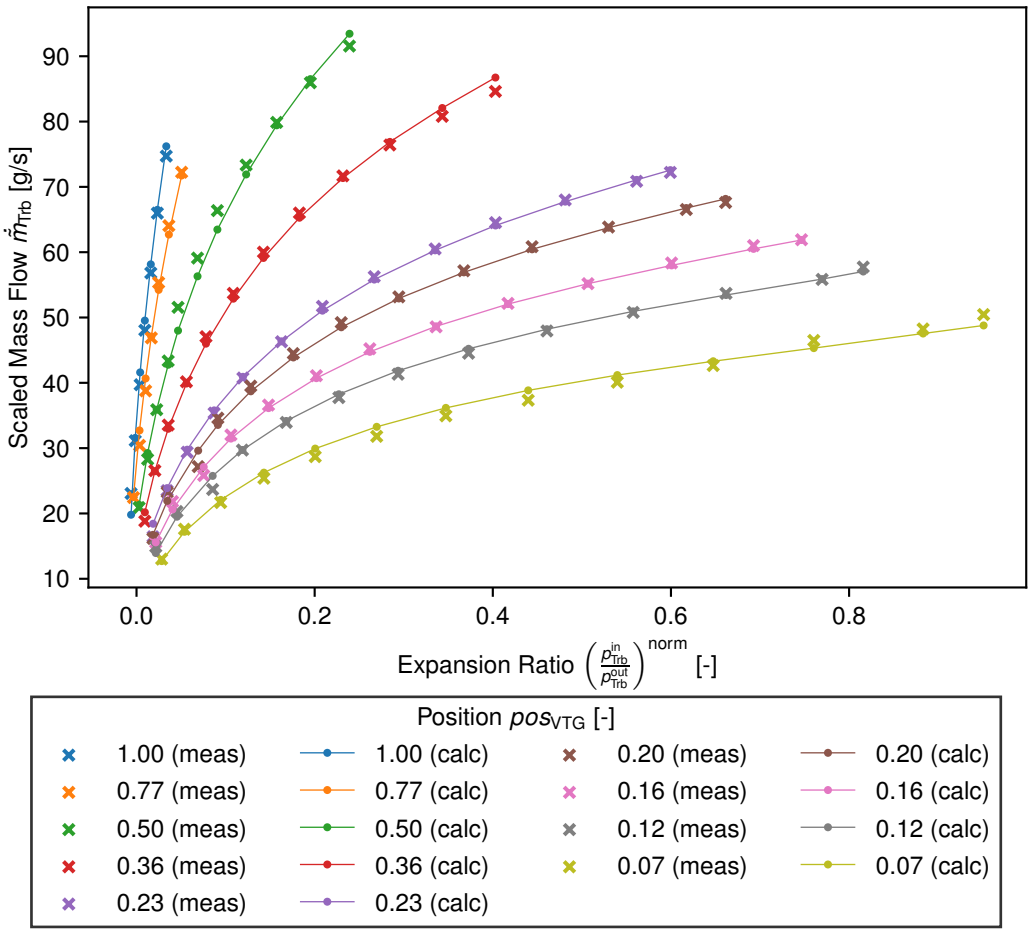

Figure 10: Turbine map model for the operating range of pos_{VTG} with the stationary measurement points from the parameter fitting for comparison.

remarkably well throughout the operating range.

The turbine was included in the cathode subsystem to regain a share of the power supplied by the air compressor motor. The recovered energy depended on the turbine load moment τ_{Trb}.

$$\tau_{\mathrm{Trb}} = \frac{\eta_{Is,\mathrm{Trb}} \cdot \dot{m}_{\mathrm{Trb}} \cdot c_{p,\mathrm{Air}} \cdot T^{\mathrm{in}}_{\mathrm{Cmpr}}}{\omega_{\mathrm{Cmpr}}} \cdot \left[1 - \left(\frac{p^{\mathrm{out}}_{\mathrm{Trb}}}{p^{\mathrm{in}}_{\mathrm{Trb}}}\right)^{\frac{\gamma_{\mathrm{Air}}-1}{\gamma_{\mathrm{Air}}}}\right] \tag{4.33}$$

Similar to the compressor, τ_{Trb} correlated with the isentropic efficiency $\eta_{Is,\mathrm{Trb}}$ of the turbine.

$$\eta_{Is,\mathrm{Trb}} = \frac{T^{\mathrm{in}}_{\mathrm{Trb}} - T^{\mathrm{out}}_{\mathrm{Trb}}}{T^{\mathrm{in}}_{\mathrm{Trb}} - T^{\mathrm{out}}_{Is,\mathrm{Trb}}}, \qquad T^{\mathrm{out}}_{Is,\mathrm{Trb}} = T^{\mathrm{in}}_{\mathrm{Trb}} \cdot \left(\frac{p^{\mathrm{out}}_{\mathrm{Trb}}}{p^{\mathrm{in}}_{\mathrm{Trb}}}\right)^{\frac{\gamma_{\mathrm{Air}}-1}{\gamma_{\mathrm{Air}}}} \tag{4.34}$$

In this work, the continuous model of Moraal *et al.* [84] was used to calculate $\eta_{Is,\mathrm{Trb}}$.

$$\eta_{Is,\mathrm{Trb}} = b_0 + b_1 \cdot \tilde{n}_{\mathrm{Trb}} + (b_2 + b_3 \cdot \tilde{n}_{\mathrm{Trb}}) \cdot \left(\frac{U}{C}\right)_{\mathrm{Trb}} + (b_4 + b_5 \cdot \tilde{n}_{\mathrm{Trb}}) \cdot \left(\frac{U}{C}\right)^2_{\mathrm{Trb}} \quad (4.35)$$

The definition of the blade speed ratio $\left(\frac{U}{C}\right)_{\mathrm{Trb}}$ was comparable to the definition of Ψ_{Cmpr} in Equation (4.13).

$$\left(\frac{U}{C}\right)_{\mathrm{Trb}} = \frac{\pi \cdot d_{\mathrm{Trb}} \cdot \tilde{n}_{\mathrm{Trb}}}{60 \sqrt{2 \cdot c_{p,\mathrm{Air}} \cdot T^{\mathrm{ref}} \cdot \left[1 - \left(\frac{p^{\mathrm{out}}_{\mathrm{Trb}}}{p^{\mathrm{in}}_{\mathrm{Trb}}}\right)^{\frac{\gamma_{\mathrm{Air}}-1}{\gamma_{\mathrm{Air}}}}\right]}} \quad (4.36)$$

The model parameters b_i from Equation (4.35) were again fitted to measurement data, and $R^2 = 0.8961$ was achieved for $\eta_{Is,\mathrm{Trb}}$. Figure 11 compares the utilized stationary measurement points with the associated model values, with a normalized isentropic efficiency equivalent to Equation (4.21). In comparison to $\eta_{Is,\mathrm{Cmpr}}$, the model for $\eta_{Is,\mathrm{Trb}}$

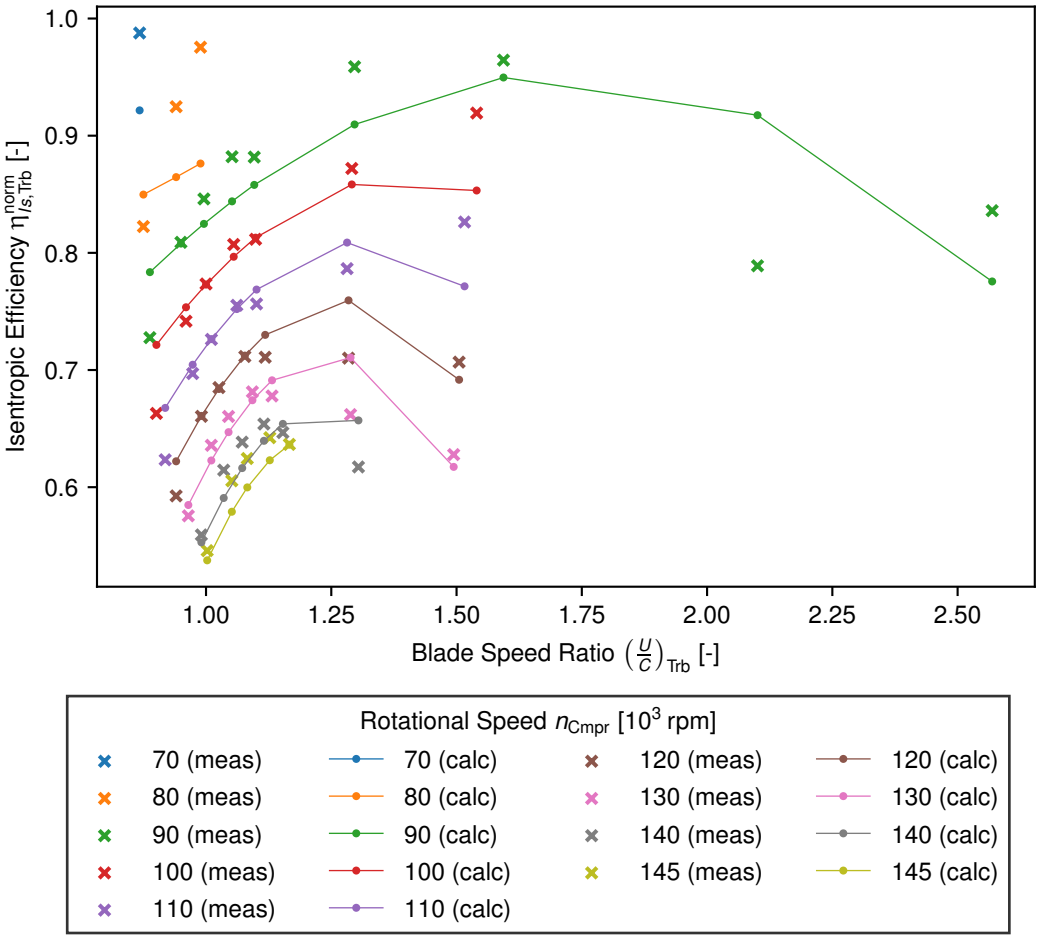

Figure 11: Comparison of measurement data (meas) and model calculations (calc) for $\eta^{\mathrm{norm}}_{Is,\mathrm{Trb}}$.

showed a far worse agreement with the measurement points. It was reasonable to assume

that the poor measurement quality of $T_{\mathrm{Trb}}^{\mathrm{in}}$ and $T_{\mathrm{Trb}}^{\mathrm{out}}$ partly caused these deviations. Especially at low loads with $n_{\mathrm{Cmpr}} \geq 70\,000\,\mathrm{rpm}$, the temperature measurements were not plausible. They returned either $\eta_{Is,\mathrm{Trb}} < 0$ or $\eta_{Is,\mathrm{Trb}} > 1$. Therefore, only data points for $n_{\mathrm{Cmpr}} \geq 70\,000\,\mathrm{rpm}$ with $0 < \eta_{Is,\mathrm{Trb}} < 1$ were used for fitting. Nonetheless, there was also a high chance that some of these acceptable data points were inaccurate, which might have caused poor parameter fitting. The fitted turbine model was used regardless due to the lack of further measurement data. The values of all the fitting parameters are summarized in Table 3.

Table 3: Values of the fitting parameter for the turbine model.

Parameter	Value	Parameter	Value	Parameter	Value
$k_{1,1}$	0.2157	$c_{2,\mathrm{VTG}}^{\mathrm{corr}}$	0.0107	b_1	–8.0234
$k_{1,2}$	0.0638	$k_{1,\mathrm{VTG}}^{\mathrm{corr}}$	–0.5737	b_2	–6.1855
$k_{2,1}$	0.0243	$k_{2,\mathrm{VTG}}^{\mathrm{corr}}$	3.3724	b_3	12.578
$k_{2,2}$	0.8929	$k_{3,\mathrm{VTG}}^{\mathrm{corr}}$	–0.5676	b_4	2.7773
$c_{1,\mathrm{VTG}}^{\mathrm{corr}}$	1.8276	b_0	4.7115	b_5	–5.4079

Air Compressor Dynamics Model The air compressor and turbine models as mentioned above only covered the stationary operating points in dependence on n_{Cmpr}. The dynamics were predicted with a moment balance equation that included the torque τ_{CmprMo} supplied by the electric motor and the moment of inertia J_{Cmpr} of the combined air compressor and turbine.

$$\frac{\mathrm{d}\omega_{\mathrm{Cmpr}}}{\mathrm{d}t} = \frac{1}{J_{\mathrm{Cmpr}}} \cdot (\tau_{\mathrm{CmprMo}} - \tau_{\mathrm{Cmpr}} + \tau_{\mathrm{Trb}}) \tag{4.37}$$

The values of J_{Cmpr} and all the other physical parameters of the air compressor and turbine model are summarized in Table 4.

Table 4: Values of the physical parameters in the air compressor and turbine model.

Parameter	Value	Parameter	Value
J_{Cmpr}	$3.98 \cdot 10^{-5}\,\mathrm{kg\,m^2}$	$\rho_{\mathrm{Air}}^{\mathrm{ref}}$	$1.1638\,\frac{\mathrm{kg}}{\mathrm{m^3}}$
p^{ref}	1.00 bar	R_{Air}	$288.19\,\frac{\mathrm{J}}{\mathrm{kg\,K}}$
T^{ref}	298.15 K	d_{Cmpr}	0.06 m
$c_{p,\mathrm{Air}}$	$1.015 \cdot 10^3\,\frac{\mathrm{J}}{\mathrm{kg\,K}}$	d_{Trb}	0.05 m
γ_{Air}	1.4		

In most works on air supply control of an FCS (e.g., [95]), a correlation for τ_{CmprMo} for a DC motor based on U_{Cmpr} has been used. For the PMSM in this work, this correlation

was modified to include $i_{q,\mathrm{Cmpr}}$ instead.

$$\tau_{\mathrm{CmprMo}} = C_{\mathrm{Trq}}^{\mathrm{el}} \cdot i_{q,\mathrm{Cmpr}} - C_{\mathrm{Trq}}^{\mathrm{mech}} \cdot \omega_{\mathrm{Cmpr}} \tag{4.38}$$

The model parameters $C_{\mathrm{Trq}}^{\mathrm{el}} = 1.15 \cdot 10^{-2}\,\frac{\mathrm{N\,m}}{\mathrm{A}}$ and $C_{\mathrm{Trq}}^{\mathrm{mech}} = 1.93 \cdot 10^{-5}\,\mathrm{N\,m\,s}$ were adjusted with measurement data. The value of $C_{\mathrm{Trq}}^{\mathrm{el}}$ approximately complied with the nominal value from the compressor motor spec sheet, which is why the value of $C_{\mathrm{Trq}}^{\mathrm{mech}}$ was also accepted.

4.2.3 Stack Air Mass Flow Model

In most studies on air supply control, $\dot{m}_{\mathrm{Ca}}^{\mathrm{in}}$ has been the mass flow between the cathode inlet manifold and an intermediate cathode manifold (see, e.g., [97], [102]). This intermediate manifold has mainly been used to predict the composition change in the air mass flow and the respective partial pressures. Moreover, the correlation between the mass flow and the pressure loss has primarily been approximated with a linear term. In this work, measurements with a pressure value between the inlet and outlet manifold were unavailable, and the composition change was neglected. Thus, $\dot{m}_{\mathrm{Ca}}^{\mathrm{in}}$ was the mass flow from the inlet manifold directly to the outlet manifold of the fuel cell stack. Mass flow measurements showed that the simple tube flow approach used for the air bearing (see Eq. (4.22)) did not fit accurately. Therefore, a slightly modified version was introduced for the calculation of $\dot{m}_{\mathrm{Ca}}^{\mathrm{in}}$.

$$\dot{m}_{\mathrm{Ca}}^{\mathrm{in}} = C_{1,\mathrm{Ca}}^{\mathrm{in}} \cdot \left[\rho_{\mathrm{Ca}}^{\mathrm{in}} \cdot \left(p_{\mathrm{Ca}}^{\mathrm{in}} - p_{\mathrm{Ca}}^{\mathrm{out}}\right)\right]^{C_{2,\mathrm{Ca}}^{\mathrm{in}}}, \qquad \rho_{\mathrm{Ca}}^{\mathrm{in}} = \frac{p_{\mathrm{Ca}}^{\mathrm{in}}}{R_{\mathrm{Air}} \cdot T_{\mathrm{Ca}}^{\mathrm{in}}} \tag{4.39}$$

The parameter fitting returned the model parameters $C_{1,\mathrm{Ca}}^{\mathrm{in}} = 2.78 \cdot 10^{-2}$ and $C_{2,\mathrm{Ca}}^{\mathrm{in}} = 0.715$, which achieved $R^2 = 0.9984$ with regard to $\dot{m}_{\mathrm{Ca}}^{\mathrm{in}}$. A comparison of the utilized measurement values and the corresponding model values is displayed in Figure 12. Throughout the operating range of the FCS, the measurements and the stack air mass flow model showed a good agreement.

4.2.4 Humidifier Model

Similar to the work of Kunusch *et al.* [61], the pressure losses over both sides of the membrane humidifier were considered in this work. The part of the humidifier before the fuel cell stack inlet was considered the dry side, while the wet side contained the oxygen-depleted air from the fuel cell stack outlet. On both sides, the gas flowed through multiple channels comparable to the fuel cell stack. Thus, the same modeling approach was applied to $\dot{m}_{\mathrm{Hmdf}}^{\mathrm{dry}}$ and $\dot{m}_{\mathrm{Hmdf}}^{\mathrm{wet}}$.

$$\dot{m}_{\mathrm{Hmdf}}^{\mathrm{dry}} = C_{1,\mathrm{Hmdf}}^{\mathrm{dry}} \cdot \left[\rho_{\mathrm{Hmdf}}^{\mathrm{dry,in}} \cdot \left(p_{\mathrm{Hmdf}}^{\mathrm{dry,in}} - p_{\mathrm{Hmdf}}^{\mathrm{dry,out}}\right)\right]^{C_{2,\mathrm{Hmdf}}^{\mathrm{dry}}}, \qquad \rho_{\mathrm{Hmdf}}^{\mathrm{dry,in}} = \frac{p_{\mathrm{Hmdf}}^{\mathrm{dry,in}}}{R_{\mathrm{Air}} \cdot T_{\mathrm{Hmdf}}^{\mathrm{dry,in}}} \tag{4.40}$$

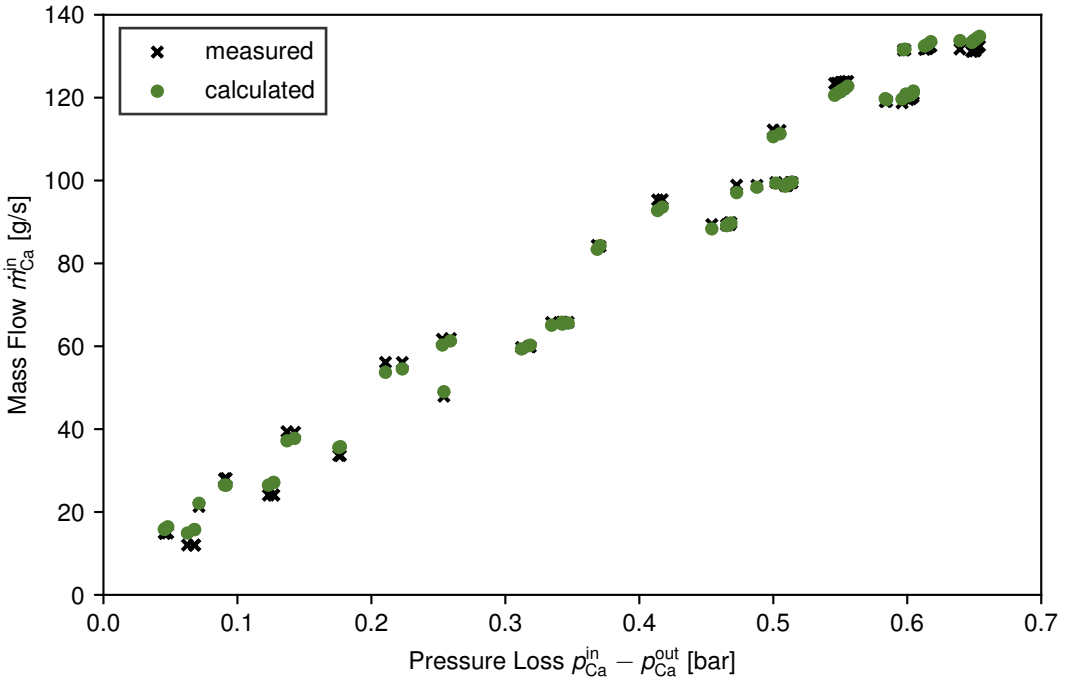

Figure 12: Comparison of measurement data and model calculations for $\dot{m}_{Ca}^{in}$.

$$\dot{m}_{Hmdf}^{wet} = C_{1,Hmdf}^{wet} \cdot \left[\rho_{Hmdf}^{wet,in} \cdot \left(p_{Hmdf}^{wet,in} - p_{Hmdf}^{wet,out}\right)\right]^{C_{2,Hmdf}^{wet}}, \qquad \rho_{Hmdf}^{wet,in} = \frac{p_{Hmdf}^{wet,in}}{R_{Air} \cdot T_{Hmdf}^{wet,in}} \quad (4.41)$$

In the cathode subsystem simulation model, the humidifier dry side inlet pressure $p_{Hmdf}^{dry,in}$ was p_{Cmpr}^{out}, while the humidifier dry side outlet pressure $p_{Hmdf}^{dry,out}$ was equivalent to p_{Ca}^{in}. On the wet side of the humidifier, the inlet pressure $p_{Hmdf}^{wet,in}$ was equated with p_{Ca}^{out}, whilst the outlet pressure $p_{Hmdf}^{wet,out}$ was replaced with p_{Trb}^{in}.

For $\dot{m}_{Hmdf}^{dry}$, the model parameters $C_{1,Hmdf}^{dry} = 0.1595$ and $C_{2,Hmdf}^{dry} = 0.7094$ were fitted to measurement data with $R^2 = 0.9756$. A graphical comparison of the measurement values and the calculated model values is presented in Figure 13. The model predictions for $\dot{m}_{Hmdf}^{dry}$ were not as precise as for $\dot{m}_{Ca}^{in}$. One possible explanation was based on the significantly lower pressure loss in the humidifier compared to the fuel cell stack. The applied pressure sensors had a measurement tolerance. For the small pressure losses in the humidifier, this tolerance had a higher impact on the overall measurement accuracy than for components with high pressure losses. As a result, the fitting of the model parameters was less accurate.

The model parameter fitting for $\dot{m}_{Hmdf}^{wet}$ resulted in a comparable prediction accuracy of $R^2 = 0.9690$ with $C_{1,Hmdf}^{wet} = 0.0643$ and $C_{1,Hmdf}^{wet} = 0.7693$. The utilized measurement values and the respective model values are presented in Figure 14.

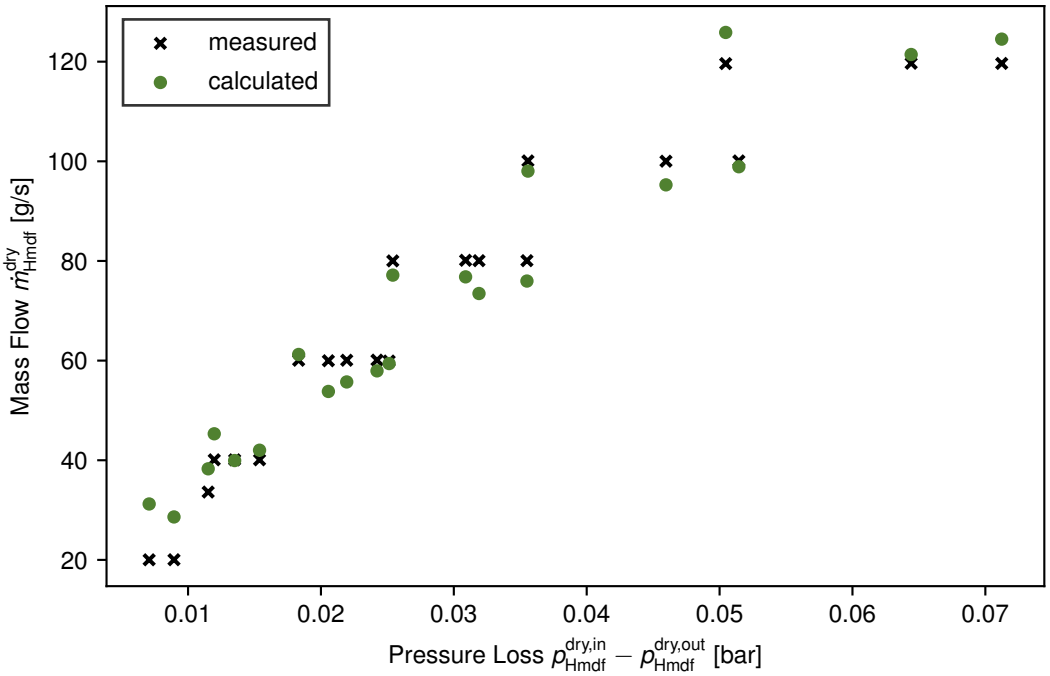

Figure 13: Comparison of measurement data and model calculations for $\dot{m}^{dry}_{Hmdf}$.

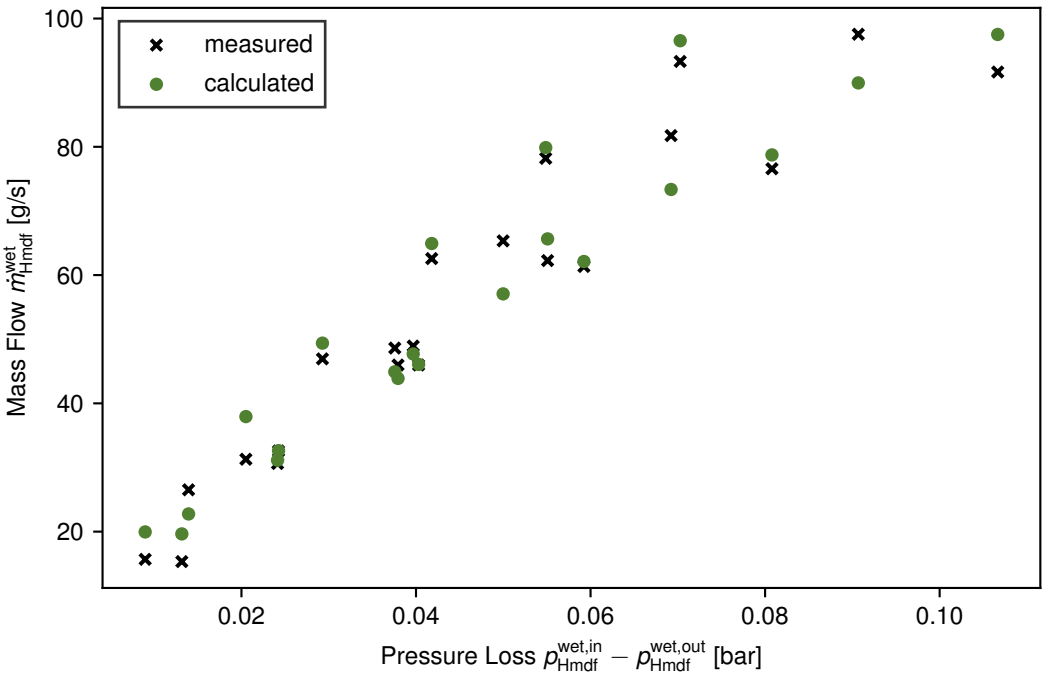

Figure 14: Comparison of measurement data and model calculations for $\dot{m}^{wet}_{Hmdf}$.

4.2.5 Throttle Valve Models

The cathode bypass and humidifier bypass were the two throttle valves considered in the cathode subsystem simulation model. Analogous to Pukrushpan *et al.* [97], the correlation between the throttle valve mass flow $\dot{m}_{Vlv}$ and the corresponding pressure

ratio $\frac{p^{\text{out}}}{p^{\text{in}}}$ from [46] was applied in this work.

$$\dot{m}_{\text{Vlv}} = C_{\text{d}} \cdot \frac{A_{\text{Vlv}}^{\text{eff}} \cdot p^{\text{in}}}{\sqrt{R \cdot T^{\text{in}}}} \cdot f_{\text{Noz}} \left(\frac{p^{\text{out}}}{p^{\text{in}}} \right) \tag{4.42}$$

The nozzle factor f_{Noz} represented the dependency of $\dot{m}_{\text{Vlv}}$ on $\frac{p^{\text{out}}}{p^{\text{in}}}$. For $\frac{p^{\text{out}}}{p^{\text{in}}}$ below a critical threshold $p_{\text{rat}}^{\text{crit}}$, f_{Noz} was limited by the occurrence of choked flow.

$$f_{\text{Noz}} \left(\frac{p^{\text{out}}}{p^{\text{in}}} \right) = \sqrt{\frac{2\gamma}{\gamma - 1}} \cdot \begin{cases} \sqrt{\left(\frac{p^{\text{out}}}{p^{\text{in}}} \right)^{\frac{2}{\gamma}} - \left(\frac{p^{\text{out}}}{p^{\text{in}}} \right)^{\frac{\gamma+1}{\gamma}}}, & \text{for } \frac{p^{\text{out}}}{p^{\text{in}}} > p_{\text{rat}}^{\text{crit}} \\ \sqrt{\left(p_{\text{rat}}^{\text{crit}} \right)^{\frac{2}{\gamma}} - \left(p_{\text{rat}}^{\text{crit}} \right)^{\frac{\gamma+1}{\gamma}}}, & \text{for } \frac{p^{\text{out}}}{p^{\text{in}}} \leq p_{\text{rat}}^{\text{crit}} \end{cases} \tag{4.43}$$

The discharge coefficient C_{d} in Equation (4.42) was fitted to each throttle valve individually. On the other hand, the effective opening area $A_{\text{eff,Vlv}}$ of each valve was calculated from the valve diameter d_{Vlv} and the opening angle of the valve φ_{Vlv}, which were known values.

$$A_{\text{Vlv}}^{\text{eff}} = \frac{\pi}{4} \cdot d_{\text{Vlv}}^2 \cdot \left[1 - \cos \left(\varphi_{\text{Vlv}} \right) \right] \tag{4.44}$$

Equation (4.44) was a simplified version of the correlation used in [46] to reduce the computational cost of the cathode subsystem simulation model. In this work, the additional assumption was an infinitesimally thin throttle plate that only reduced the opening area for $\varphi_{\text{Vlv}} < 90°$.

Humidifier Bypass Path In the humidifier bypass path, the only significant pressure loss was caused by the humidifier bypass valve. Unfortunately, the only available measurement data was for throttle valves with $d_{\text{Vlv}} = 35\,\text{mm}$ and $d_{\text{Vlv}} = 48\,\text{mm}$, while the humidifier bypass valve had a diameter of $d_{\text{HByp}} = 55\,\text{mm}$. Thus, $C_{\text{d,HByp}} = 1.0213$ was fitted to the measurement data of the most alike throttle valve with $d_{\text{Vlv}} = 48\,\text{mm}$. This fitting achieved $R^2 = 0.9931$ for $\dot{m}_{\text{Vlv}}$ and is shown in Figure 15. The most significant deviations between measured and calculated values of $\dot{m}_{\text{Vlv}}$ in Figure 15 occurred for $\frac{p^{\text{out}}}{p^{\text{in}}}$ close to one. These data points were linked to values of φ_{Vlv} at approximately 90°. At these angles, $A_{\text{Vlv}}^{\text{eff}}$ changed rapidly with φ_{Vlv} due to the cosine function in Equation (4.44). Thus, a small measurement error in pos_{Byp} led to a significant deviation in the calculated value of $A_{\text{Vlv}}^{\text{eff}}$. This deviation then resulted in a significant deviation in $\dot{m}_{\text{Vlv}}$. Additionally, the calculation of $A_{\text{Vlv}}^{\text{eff}}$ with Equation (4.44) was based on the assumption of an infinitesimally thin throttle plate. In reality, the measured throttle valve had a plate with a width of a few millimeters. Therefore, $A_{\text{Vlv}}^{\text{eff}}$ for the fully opened valve was slightly smaller in reality compared to the valve model. In spite of these deviations, $R^2 = 0.9931$ was considered sufficient for a control-oriented simulation model.

On the ECU, the position of the humidifier bypass throttle valve pos_{HByp} was given instead of φ_{HByp}. The correlation between pos_{HByp} and φ_{HByp} was taken from the

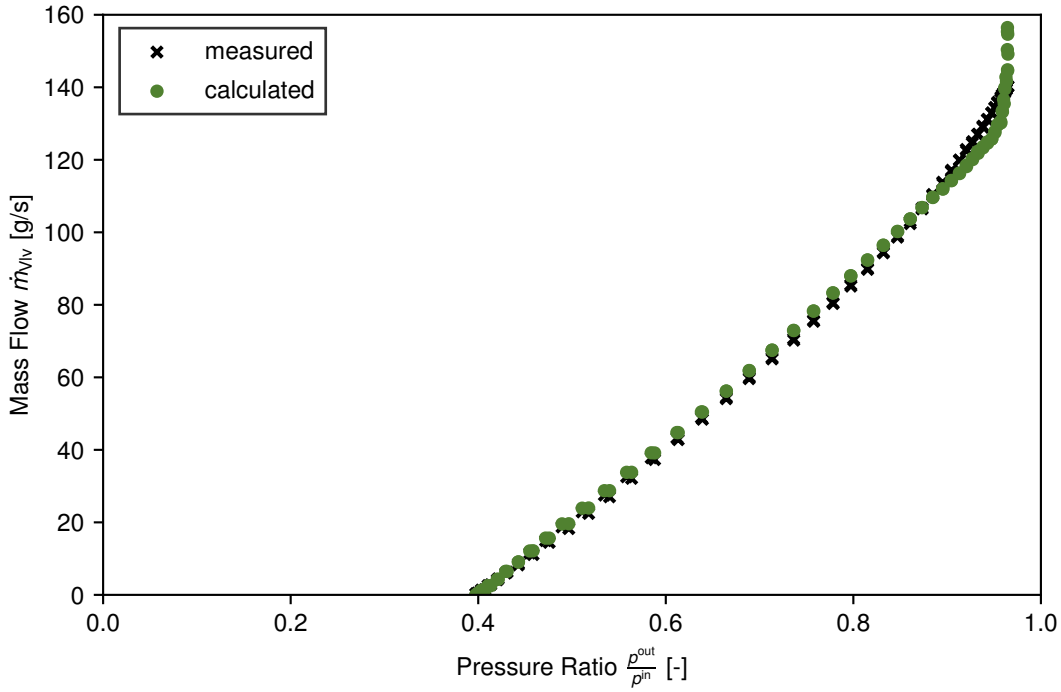

Figure 15: Comparison of measurement data and model calculations for $\dot{m}_{Vlv}$ with $d_{Vlv} = 48\,\text{mm}$ as the replacement measurement for $\dot{m}_{HByp}$.

throttle valve data sheet that existed for $d_{\text{HByp}} = 55\,\text{mm}$.

$$\varphi_{\text{HByp}} = pos_{\text{HByp}} \cdot 80° \tag{4.45}$$

According to the data sheet, the humidifier bypass valve was considered to be wide open with $pos_{\text{HByp}} = 100\,\%$ for $\varphi_{\text{HByp}} = 80°$.

Cathode Bypass Path In the cathode bypass path, the pressure loss resulted from a Venturi mass flow sensor and the subsequent bypass throttle valve. This sensor had a significant pressure loss that reduced the inlet pressure of the bypass valve $p^{\text{in}}_{\text{BypVlv}}$ compared to the inlet pressure of the cathode bypass path $p^{\text{in}}_{\text{Byp}}$. Thus, a correction term $\Delta p^{\text{corr}}_{\text{Byp}} = p^{\text{in}}_{\text{Byp}} - p^{\text{in}}_{\text{BypVlv}}$ was included in the valve model that calculated the mass flow $\dot{m}_{\text{Byp}}$ through the cathode bypass path.

$$\begin{aligned}\Delta p^{\text{corr}}_{\text{Byp}} = &\left(c^{\text{corr}}_{1,\text{Byp}} \cdot \Delta p^2_{\text{Byp}} + c^{\text{corr}}_{2,\text{Byp}} \cdot \Delta p_{\text{Byp}} + c^{\text{corr}}_{3,\text{Byp}}\right) \\ &\cdot \left[c^{\text{corr}}_{4,\text{Byp}} \cdot \left(\frac{A^{\text{eff}}_{\text{Byp}}}{A_{\text{Byp}}}\right)^4 + c^{\text{corr}}_{5,\text{Byp}} \cdot \left(\frac{A^{\text{eff}}_{\text{Byp}}}{A_{\text{Byp}}}\right)^3 + c^{\text{corr}}_{6,\text{Byp}} \cdot \left(\frac{A^{\text{eff}}_{\text{Byp}}}{A_{\text{Byp}}}\right)^2\right. \\ &\left. + c^{\text{corr}}_{7,\text{Byp}} \cdot \left(\frac{A^{\text{eff}}_{\text{Byp}}}{A_{\text{Byp}}}\right) + c^{\text{corr}}_{8,\text{Byp}}\right]\end{aligned} \tag{4.46}$$

$$\dot{m}_{\text{Byp}} = C_{\text{d,Byp}} \cdot \frac{A^{\text{eff}}_{\text{Byp}} \cdot p^{\text{in}}_{\text{BypVlv}}}{\sqrt{R_{\text{Air}} \cdot T^{\text{in}}_{\text{Byp}}}} \cdot f_{\text{Noz}}\left(\frac{p^{\text{out}}_{\text{Byp}}}{p^{\text{in}}_{\text{BypVlv}}}\right) \tag{4.47}$$

Equation (4.46) was designed to depend solely on state variables and constants of the cathode subsystem simulation model given during simulations. Therefore, the total pressure loss $\Delta p_{\mathrm{Byp}} = p_{\mathrm{Byp}}^{\mathrm{in}} - p_{\mathrm{Byp}}^{\mathrm{out}}$ over the cathode bypass path was chosen as one of the variables. This pressure loss was calculated during simulations from the difference between $p_{\mathrm{Cmpr}}^{\mathrm{out}}$ and $p_{\mathrm{Trb}}^{\mathrm{in}}$. Additionally, the ratio $\frac{A_{\mathrm{Byp}}^{\mathrm{eff}}}{A_{\mathrm{Byp}}}$ of the effective and total opening area of the bypass valve was simplified to the term $1 - \cos(\varphi_{\mathrm{Byp}})$. For the cathode bypass valve, the angle φ_{Byp} of the throttle plate was again the result of pos_{Byp}.

$$\varphi_{\mathrm{Byp}} = pos_{\mathrm{Byp}} \cdot 90^{\circ} \tag{4.48}$$

According to the data sheet, the cathode bypass valve was considered wide open for $\varphi_{\mathrm{Byp}} = 90^{\circ}$.

The first model parameter to be fitted was the discharge coefficient $C_{\mathrm{d,Byp}}$ of the cathode bypass valve. For this throttle valve with $d_{\mathrm{Byp}} = 35\,\mathrm{mm}$, measurement data was available. The parameter fitting returned $C_{\mathrm{d,Byp}} = 0.9646$ and achieved $R^2 = 0.9800$ with regard to $\dot{m}_{\mathrm{Byp}}$. This fitting is depicted in Figure 16, which contains the utilized measurement data and the corresponding model values. Similar to $\dot{m}_{\mathrm{Vlv}}$ in Figure 15,

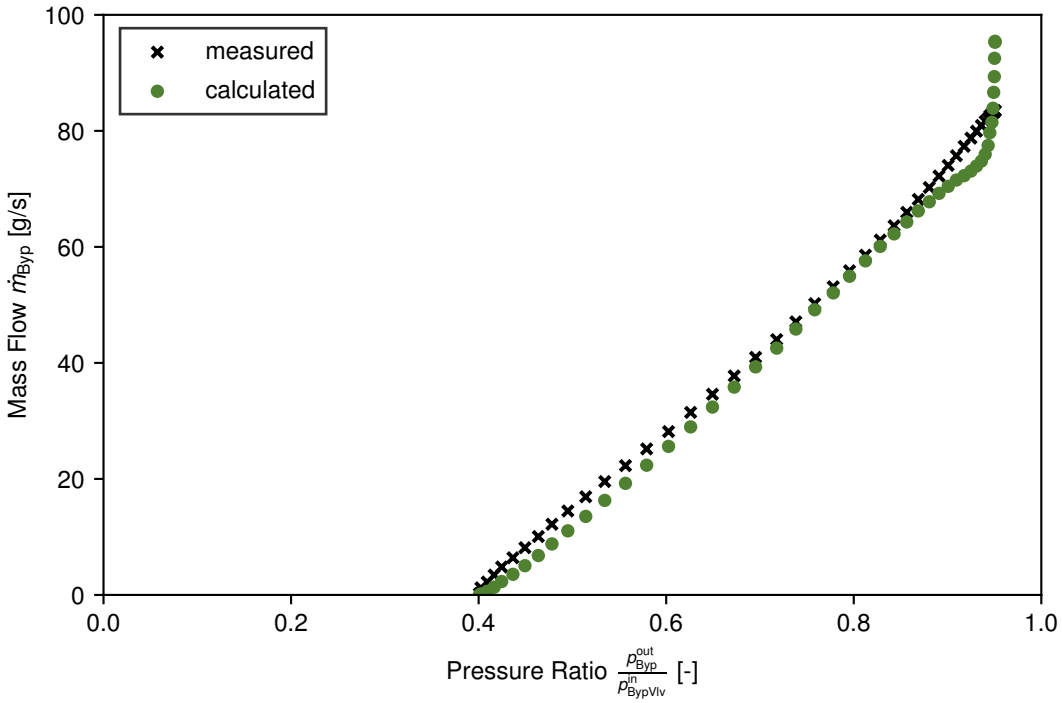

Figure 16: Comparison of measurement data and model calculations for $\dot{m}_{\mathrm{Byp}}$.

the most significant deviation for $\dot{m}_{\mathrm{Byp}}$ in Figure 16 arose for pressure ratios close to one. Therefore, these deviations most likely resulted from measurement errors of pos_{Byp} and the assumption of an infinitesimally thin throttle plate.

The next step towards fitting the parameters $c_{i,\mathrm{Byp}}^{\mathrm{corr}}$ for $\Delta p_{\mathrm{Byp}}^{\mathrm{corr}}$ was to model the Venturi mass flow sensor. The correlation between the mass flow $\dot{m}_{\mathrm{VMf}}$ and the pressure loss Δp_{VMf} was described by tube flow with a constant friction coefficient. This correlation

has already been introduced in Equation (4.22).

$$\dot{m}_{\mathrm{VMf}} = C_{\mathrm{VMf}} \cdot \sqrt{\rho^{\mathrm{in}}_{\mathrm{VMf}} \cdot \Delta p_{\mathrm{VMf}}}, \qquad \rho^{\mathrm{in}}_{\mathrm{VMf}} = \frac{p^{\mathrm{in}}_{\mathrm{VMf}}}{R_{\mathrm{Air}} \cdot T^{\mathrm{in}}_{\mathrm{VMf}}} \tag{4.49}$$

The fitting of $C_{\mathrm{VMf}} = 3.09 \cdot 10^{-4}\,\mathrm{m}^2$ achieved $R^2 = 0.9850$ with regard to $\dot{m}_{\mathrm{VMf}}$. The utilized measurement data and the resulting model values are displayed in Figure 17. For high pressure losses, the model slightly overestimated $\dot{m}_{\mathrm{VMf}}$. A possible explanation

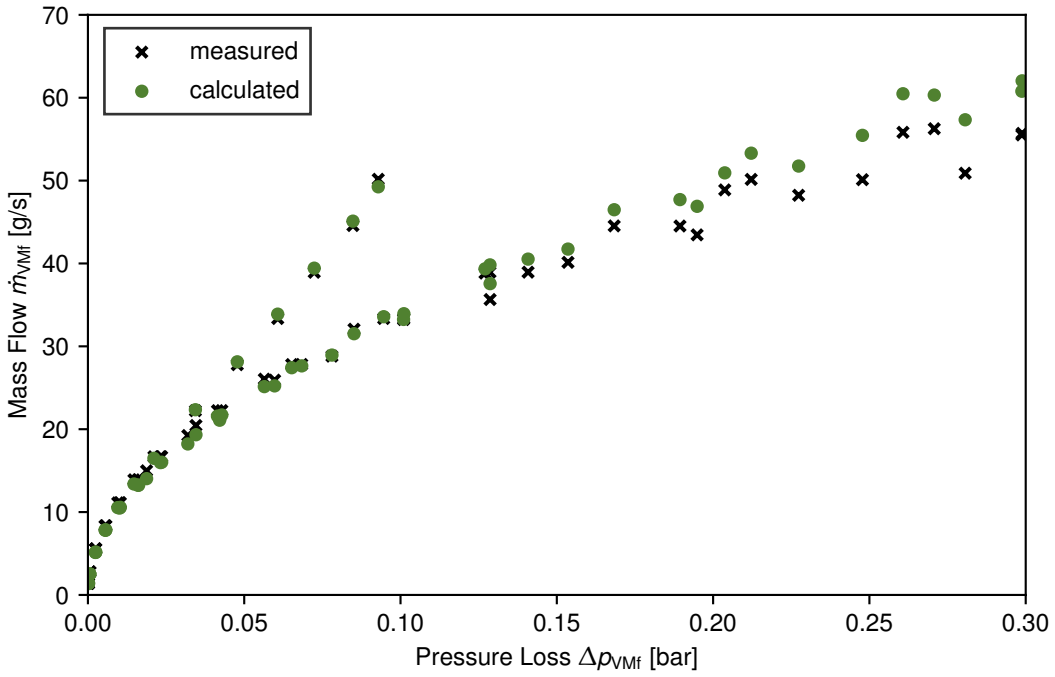

Figure 17: Comparison of measurement data and model calculations for $\dot{m}_{\mathrm{VMf}}$.

was based on the shape of the Venturi mass flow sensor, which was comparable to a nozzle. Hence, it was reasonable to assume that the deviations were caused by a saturation effect similar to the throttle valves.

Eventually, the model for $\Delta p^{\mathrm{corr}}_{\mathrm{Byp}}$ was parameterized based on the bypass valve model and the Venturi mass flow sensor model. For a constant set of $p^{\mathrm{in}}_{\mathrm{Byp}}$, $T^{\mathrm{in}}_{\mathrm{Byp}}$, pos_{Byp}, and $p^{\mathrm{out}}_{\mathrm{Byp}}$, the matching values for $p^{\mathrm{in}}_{\mathrm{BypVlv}}$ and $\dot{m}_{\mathrm{Byp}}$ were determined by enforcing $\dot{m}_{\mathrm{Byp}} = \dot{m}_{\mathrm{VMf}}$. This procedure was repeated for variations in $p^{\mathrm{in}}_{\mathrm{Byp}}$, $T^{\mathrm{in}}_{\mathrm{Byp}}$ and pos_{Byp} while retaining $p^{\mathrm{out}}_{\mathrm{Byp}} = 1\,\mathrm{bar}$. The resulting data points was then used for the parameter fitting of $c^{\mathrm{corr}}_{i,\mathrm{Byp}}$. This fitting returned the values that are summarized in Table 5. The parameter fitting of $c^{\mathrm{corr}}_{i,\mathrm{Byp}}$ further achieved $R^2 = 0.9966$ with regard to $\dot{m}_{\mathrm{Byp}}$. The utilized data set from $\dot{m}_{\mathrm{Byp}} = \dot{m}_{\mathrm{VMf}}$ and the corresponding model values are shown in Figure 18. Overall, Figure 18 confirms that the model for $\Delta p^{\mathrm{corr}}_{\mathrm{Byp}}$ was feasible as a substitution for $\dot{m}_{\mathrm{Byp}} = \dot{m}_{\mathrm{VMf}}$ in the cathode subsystem model.

Table 5: Values of the fitting parameter for the bypass pressure correction model.

Parameter	Value	Parameter	Value	Parameter	Value
$c^{\text{corr}}_{1,\text{Byp}}$	–50.00	$c^{\text{corr}}_{4,\text{Byp}}$	191.3	$c^{\text{corr}}_{7,\text{Byp}}$	261.7
$c^{\text{corr}}_{2,\text{Byp}}$	716.1	$c^{\text{corr}}_{5,\text{Byp}}$	–360.9	$c^{\text{corr}}_{8,\text{Byp}}$	–4.546
$c^{\text{corr}}_{3,\text{Byp}}$	0.0405	$c^{\text{corr}}_{6,\text{Byp}}$	45.71		

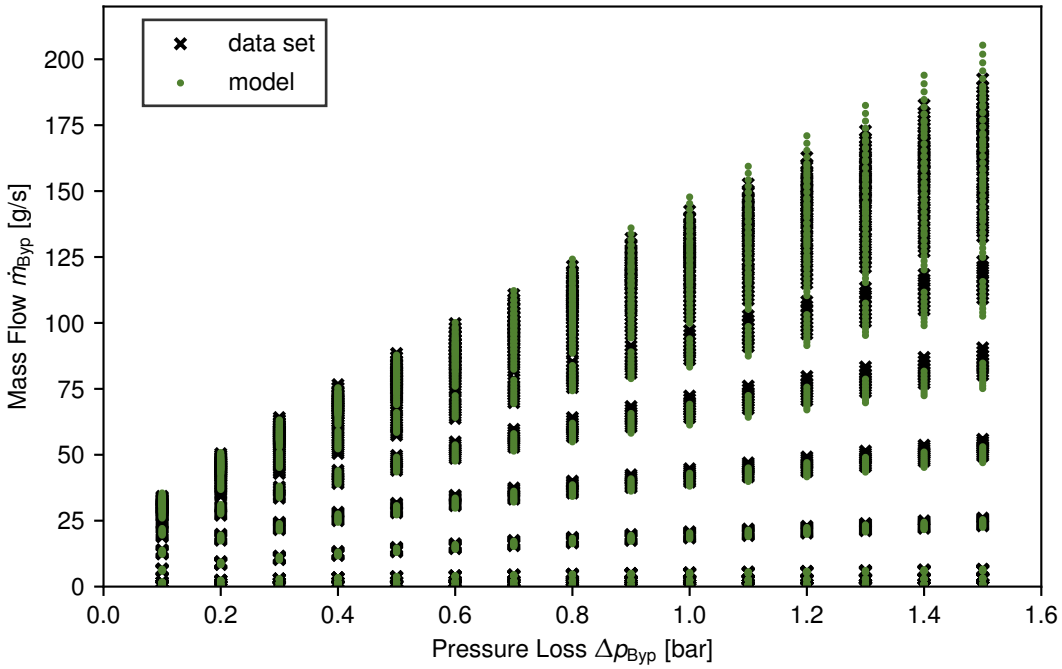

Figure 18: Comparison of $\dot{m}_{\text{Byp}}$ from the data set with $\dot{m}_{\text{Byp}} = \dot{m}_{\text{VMf}}$ and from the model with $\Delta p^{\text{corr}}_{\text{Byp}}$ calculated with Equation (4.46).

4.2.6 Exhaust Model

In the cathode subsystem simulation model, the final correlation between mass flow and pressure loss was for the air exhaust. Once again, tube flow with a constant friction coefficient was assumed to calculate the mass flow $\dot{m}_{\text{Exh}}$ through the exhaust.

$$\dot{m}_{\text{Exh}} = C_{\text{Exh}} \cdot \sqrt{\rho^{\text{in}}_{\text{Exh}} \cdot (p^{\text{in}}_{\text{Exh}} - p^{\text{out}}_{\text{Exh}})}, \qquad \rho^{\text{in}}_{\text{Exh}} = \frac{p^{\text{in}}_{\text{Exh}}}{R_{\text{Air}} \cdot T^{\text{in}}_{\text{Exh}}} \tag{4.50}$$

The parameter fitting returned the model parameter $C_{\text{Exh}} = 1.5376 \cdot 10^{-3}\,\text{m}^2$ and achieved $R^2 = 0.9986$ for $\dot{m}_{\text{Exh}}$. A summary of the utilized data points and the corresponding model values is displayed in Figure 19. As shown in Figure 19, the model almost perfectly matched the real correlation between $\dot{m}_{\text{Exh}}$ and $p^{\text{in}}_{\text{Exh}} - p^{\text{out}}_{\text{Exh}}$ throughout the full operating range.

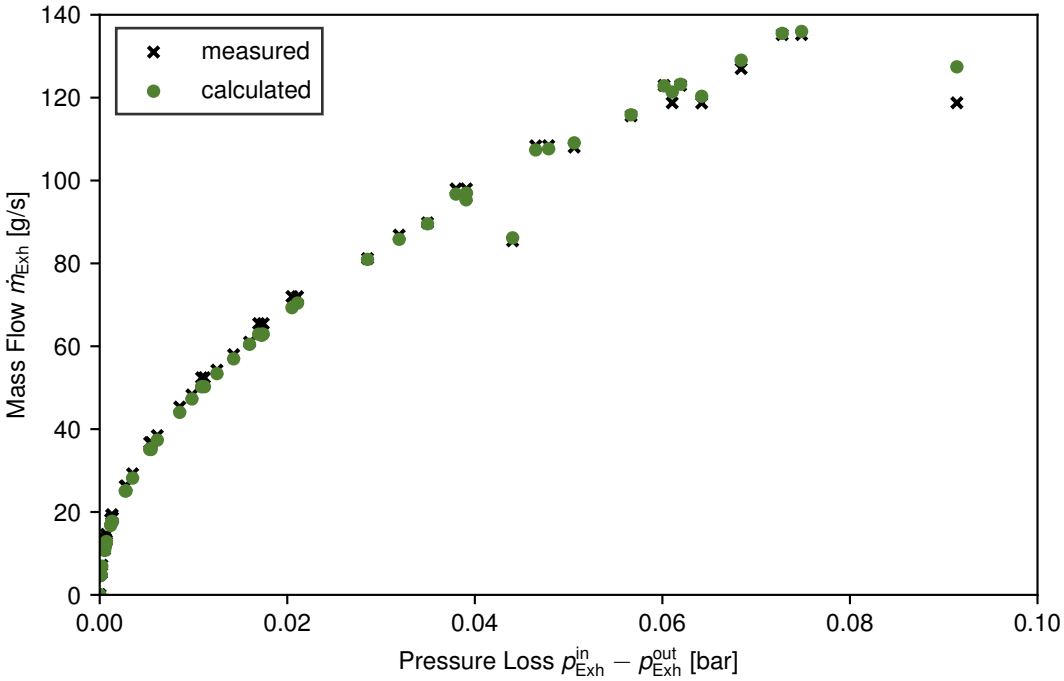

Figure 19: Comparison of measurement data and model calculations for $\dot{m}_{Exh}$.

4.3 Model of the Fuel Cell System Net Power

This work was mainly dedicated to the air supply control and the cathode subsystem of an FCS. Nonetheless, a small simulation study was additionally conducted on the control of P_{FCS}, which was the difference between P_{Stck} and P_{Cmpr}. All the other auxiliary electric power consumers, like the high-voltage cooling pump, required significantly less than 0.5 kW, which is why these components were neglected throughout this work. Thus, two models for P_{Stck} and P_{Cmpr} had to be implemented with the cathode subsystem simulation model to enable closed-loop simulations with a power controller.

4.3.1 Fuel Cell Stack Power Model

The model for P_{FCS} was based on a polarization curve, the correlation between the fuel cell current I_{Cell} and the fuel cell voltage U_{Cell}.

$$U_{Cell} = f\left(I_{Cell}, p_{O_2}, p_{H_2}, T_{Cell}, \psi_{Mem}\right) \tag{4.51}$$

The fitted polarization curve model had been developed at the fuel cell department of the BMW Group based on stack test stand measurements before this study. The other relevant variables in Equation (4.51) were the partial pressure of oxygen on the cathode side of the fuel cell p_{O_2}, the partial pressure of hydrogen on the anode side of the fuel cell p_{H_2}, the fuel cell temperature T_{Cell} and the humidity of the fuel cell membrane ψ_{Mem}. In this work, the power controller only regulated the oxygen supply and the electric current. The time constant of the anode subsystem was significantly smaller than the

time constant of the cathode subsystem, which is why p_{H_2} was assumed to be perfectly controlled. Moreover, the dynamics of T_{Cell} and ψ_{Mem} were considerably slower than the air supply dynamics. Thus, these two variables were controlled separately. As a result, average values were assumed for the remaining variables p_{H_2}, T_{Cell}, and ψ_{Mem}. The impact of this simplification on the polarization curve model accuracy is shown in Figure 20. The absolute values of I_{Cell} and U_{Cell} were confidential. Thus, normalized

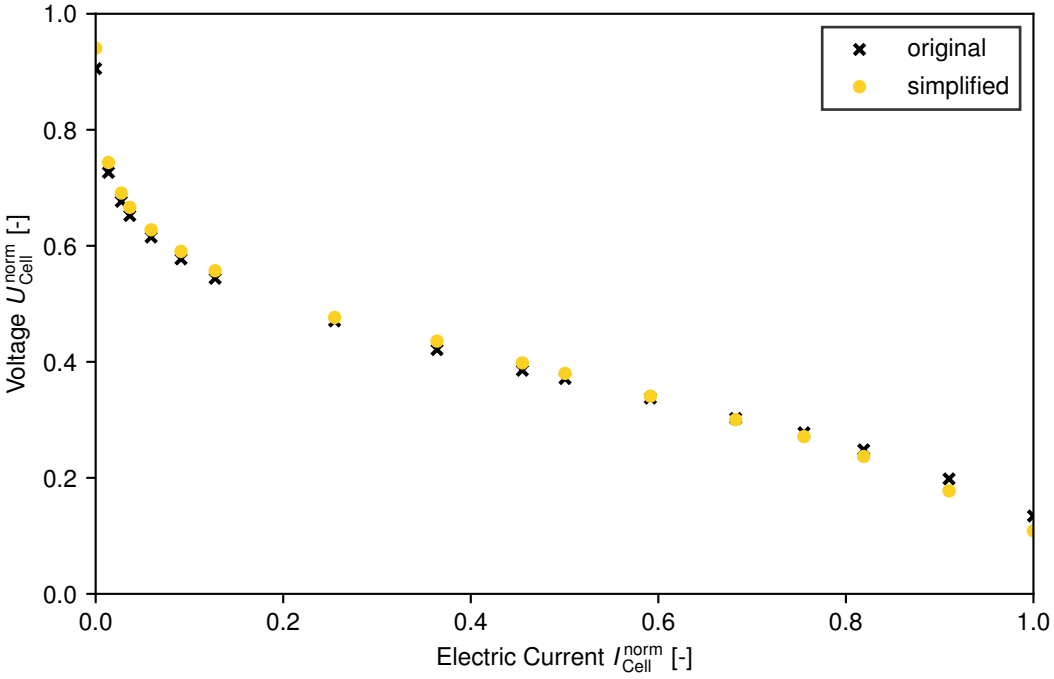

Figure 20: Comparison of the original model for the polarization curve and the simplified model with constant p_{H_2}, T_{Cell}, and ψ_{Mem}.

values I_{Cell}^{norm} and U_{Cell}^{norm} were used.

$$I_{Cell}^{norm} = \frac{I_{Cell}}{I_{Cell,Max}} \tag{4.52}$$

$$U_{Cell}^{norm} = \frac{U_{Cell} - U_{Cell,Min}}{U_{Cell,Max} - U_{Cell,Min}} \tag{4.53}$$

In Figure 20, the deviations between the original and simplified models resulted from the assumed average p_{H_2}. For small I_{Cell}, p_{H_2} was lower than the average value, which led to the overestimation of U_{Cell}. On the contrary, for high I_{Cell}, p_{H_2} was higher than the average value, leading to the underestimation of U_{Cell}. Nonetheless, the dependency on I_{Cell} was correctly displayed, so the simplifications were accepted.

In the fuel cell stack of the FCS, the fuel cells were arranged in a series connection. As a result, I_{Cell} was equivalent to I_{Stck}, while the fuel cell stack voltage U_{Stck} was the sum of the individual cell voltages.

$$U_{Stck} = n_{Cell} \cdot U_{Cell} \tag{4.54}$$

The lumped-parameter modeling approach prohibited spatially distributed variables. Thus, the calculated U_{Cell} was considered the average value within the fuel cell stack and consequently multiplied by the number of fuel cells in the fuel cell stack n_{Cell} to obtain U_{Stck}.

4.3.2 Air Compressor Motor Power Consumption Model

The calculation of P_{FCS} was based on the DC power consumption P_{Cmpr} of the compressor inverter. This inverter further provided the necessary AC power P_{CmprMo} to drive the PMSM of the air compressor. In this work, the power losses in the inverter were negligible, thus leading to $P_{\mathrm{Cmpr}} = P_{\mathrm{CmprMo}}$. The PMSM provided the electric torque $\tau^{\mathrm{el}}_{\mathrm{CmprMo}}$ required to compress the inlet air and maintain ω_{Cmpr}.

$$P_{\mathrm{CmprMo}} = \tau^{\mathrm{el}}_{\mathrm{CmprMo}} \cdot \omega_{\mathrm{Cmpr}} \tag{4.55}$$

$$\tau^{\mathrm{el}}_{\mathrm{CmprMo}} = C^{\mathrm{el}}_{\mathrm{Trq}} \cdot i_{q,\mathrm{Cmpr}} \tag{4.56}$$

As mentioned in Section 4.2.2, the model parameter $C^{\mathrm{el}}_{\mathrm{Trq}}$ was approximated from measurement data. This approximation included the efficiency between $\tau^{\mathrm{el}}_{\mathrm{CmprMo}}$ and the provided mechanical torque on the compressor rotor. Thus, this efficiency was not explicitly used in the description of the available compressor motor torque τ_{CmprMo} in Equation (4.38).

4.4 Validation of the Fuel Cell System Model

The first step of the simulation model development was to determine the individual model equations and the values of the fitting parameters. In the next step, the individual models were merged with the mass balances of Equation (4.1) to form the dynamic FCS simulation model. Afterward, the simulation model was validated at stationary operating points by comparing the model outputs to measurements from the FCS test stand. This comparison is summarized in Section 4.4.1. Lastly, measurements from the FCEV were utilized to ascertain the correctness of the predicted transient behavior of the FCS using the nonlinear simulation model. This final validation step is displayed in Section 4.4.2.

The simulation model was implemented in MATLAB Simulink (Release R2018b). The system of ODEs was solved using the variable-step solver ode15s with a relative tolerance $\epsilon = 1 \cdot 10^{-4}$. The boundary conditions were the constant ambient pressure $p_{\mathrm{Amb}} = 1\,\mathrm{bar}$ and the constant ambient temperature $T_{\mathrm{Amb}} = 25\,^{\circ}\mathrm{C}$.

4.4.1 Stationary Model Validation with an FCS Test Stand Measurement

The simulation accuracy for stationary operating points of the cathode subsystem was validated with the parameter fitting measurement from [27]. In this measurement, the

entire operating ranges of $i^{\mathrm{sp}}_{q,\mathrm{Cmpr}}$ and $pos^{\mathrm{sp}}_{\mathrm{Byp}}$ were evaluated. The model inputs for this measurement are displayed in Figure 21. All step changes were executed with manual

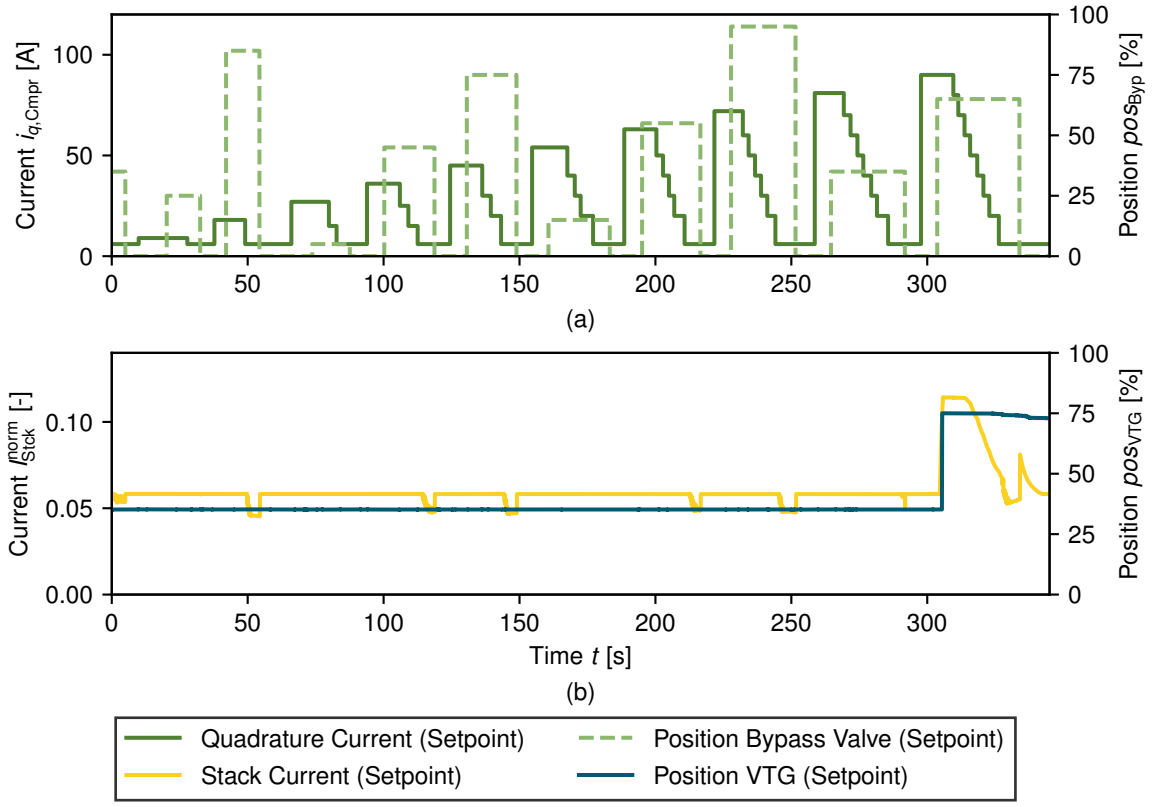

Figure 21: Inputs into the FCS simulation model for the FCS test stand measurement to validate the stationary operating points of the cathode subsystem.

overrides for $i^{\mathrm{sp}}_{q,\mathrm{Cmpr}}$ and $pos^{\mathrm{sp}}_{\mathrm{Byp}}$ at a stationary $P_{\mathrm{FCS}} = 10\,\mathrm{kW}$. This constant net power setpoint was used to neglect the influence of the power controller on the FCS response. What is more, $pos^{\mathrm{sp}}_{\mathrm{HByp}} = 100\,\%$ was kept constant throughout the validation scenario. The changes in $I^{\mathrm{sp}}_{\mathrm{Stck}}$ and $pos^{\mathrm{sp}}_{\mathrm{VTG}}$ in Figure 21b) were the result of the FCS net power and the cathode pressure controllers, which were still active during the measurement. $I^{\mathrm{sp}}_{\mathrm{Stck}}$ was also normed according to Equation (4.52) to fit the polarization curve in Figure 20.

The pressures and mass flows in the cathode subsystem significantly depended on n_{Cmpr}. Therefore, an accurate prediction of the stationary values of n_{Cmpr} was mandatory for a precise cathode subsystem simulation model. The calculated model values and the corresponding measurement data points for n_{Cmpr} are compared in Figure 22. The main increases and decreases in n_{Cmpr} were caused by $i_{q,\mathrm{Cmpr}}$. Nonetheless, opening the bypass valve also led to an increase in n_{Cmpr} due to a reduction of $p^{\mathrm{out}}_{\mathrm{Cmpr}}$. This reduction resulted in a decrease of τ_{Cmpr}, which increased the stationary value of n_{Cmpr} as a consequence of the compressor moment balance (Eq. (4.37)). Qualitatively, these effects were displayed correctly by the simulation model. Quantitatively, the model calculated slightly lower values of n_{Cmpr} throughout the operating range. These lower values included the stationary value of n_{Cmpr} for $i_{q,\mathrm{Cmpr}} = 6\,\mathrm{A}$. In the simulation model, this difference

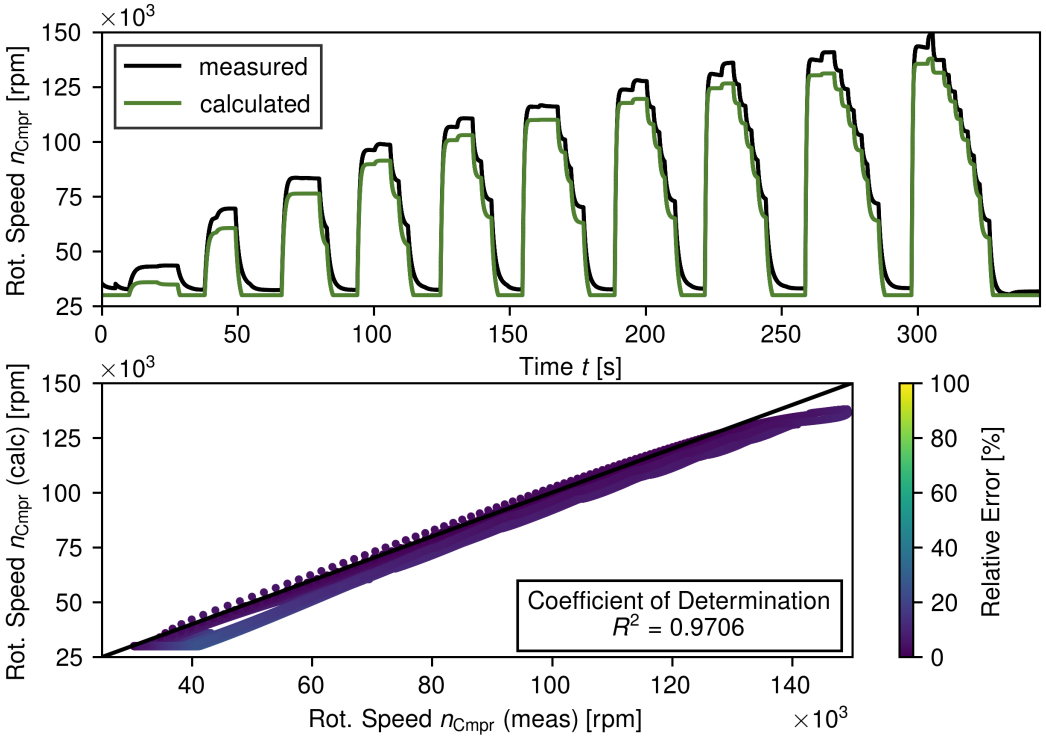

Figure 22: Comparison of n_{Cmpr} for the FCS test stand measurement and the corresponding simulation model calculations.

caused rather sharp transitions to the lower operating limit $n_{\mathrm{Cmpr}} = 30\,000\,\mathrm{rpm}$ of the air compressor. The stationary model value of n_{Cmpr}, according to Equation (4.37), was lower without the operating range limitations, which implies inaccurate model parameters $C_{\mathrm{Trq}}^{\mathrm{el}}$ and $C_{\mathrm{Trq}}^{\mathrm{mech}}$. Nonetheless, measurements to improve the corresponding parameter fitting were unavailable throughout this study.

The lower values of n_{Cmpr} further resulted in the calculation of smaller values for P_{Cmpr} with the simulation model. The comparison of the model calculations to the FCS measurement is shown in Figure 23. Furthermore, P_{Cmpr} depended on $C_{\mathrm{Trq}}^{\mathrm{el}}$ and $i_{q,\mathrm{Cmpr}}$. While $i_{q,\mathrm{Cmpr}}$ was known during stationary operation from the model input $i_{q,\mathrm{Cmpr}}^{\mathrm{sp}}$, $C_{\mathrm{Trq}}^{\mathrm{el}}$ was only approximated. Thus, this model parameter also brought about some deviations regarding P_{Cmpr}. Additionally, the efficiency of the inverter was assumed to be 100 %. The increasing deviation between the measurement and the model values for higher P_{Cmpr} suggests smaller inverter efficiencies. Unfortunately, the necessary measurements to prove these statements were unavailable for this work.

Despite the significantly smaller values of n_{Cmpr} in the simulation model, $\dot{m}_{\mathrm{AirFil}}$ was well approximated. The associated comparison between the simulation model and the FCS test stand measurement in Figure 24 only shows slightly higher values. These deviations were partly caused by the higher values of $p_{\mathrm{Cmpr}}^{\mathrm{in}}$ in the simulation model due to the neglected pressure loss through the air filter. What is more, calculating the overall pressure loss in the cathode subsystem neglected components like the intercooler or the CWS. This neglection led to smaller values of $p_{\mathrm{Cmpr}}^{\mathrm{out}}$ in the simulation model.

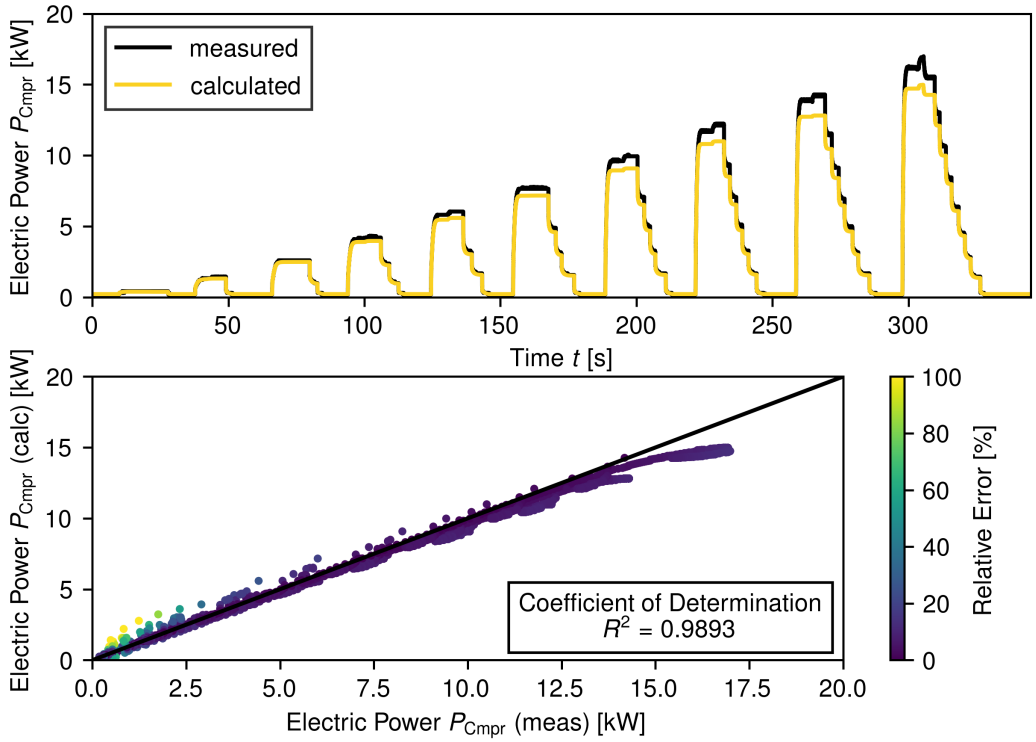

Figure 23: Comparison of P_{Cmpr} for the FCS test stand measurement and the corresponding simulation model calculations.

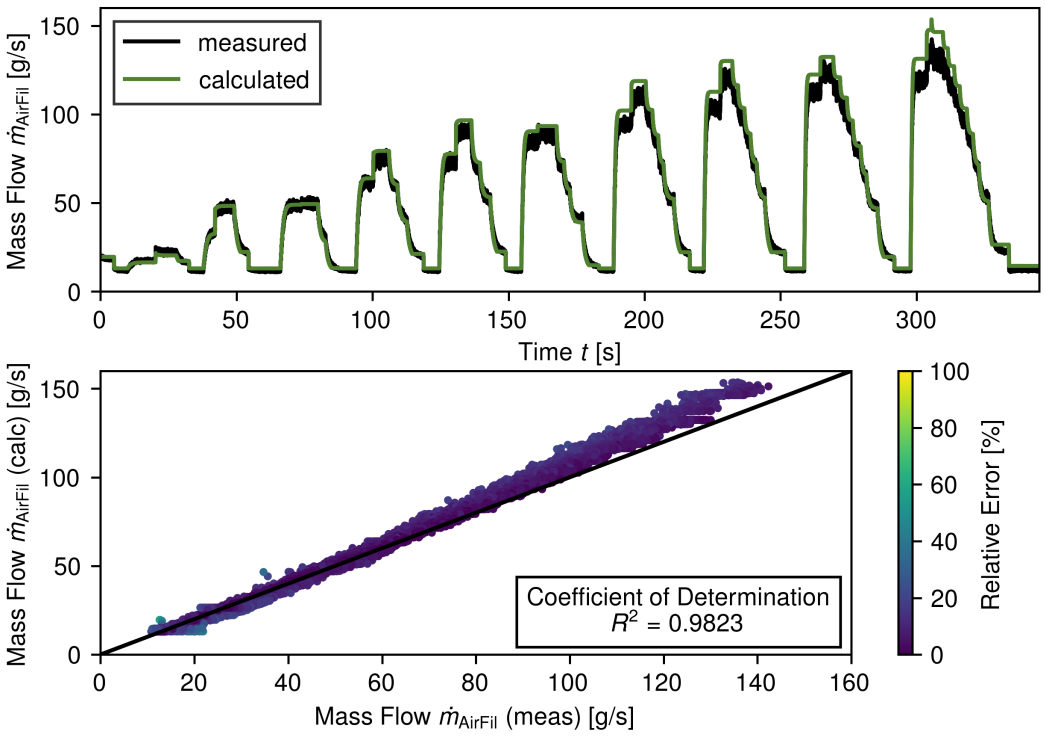

Figure 24: Comparison of $\dot{m}_{AirFil}$ for the FCS test stand measurement and the corresponding simulation model calculations.

Altogether, the resulting smaller values of $\frac{p^{\mathrm{out}}_{\mathrm{Cmpr}}}{p^{\mathrm{in}}_{\mathrm{Cmpr}}}$ led to an increase in $\dot{m}_{\mathrm{Cmpr}}$ despite smaller values of n_{Cmpr}. Nonetheless, the prediction was generally very accurate, with the relative error below 10 % for most of the operating range. Figure 24 also shows high levels of sensor noise for $\dot{m}_{\mathrm{AirFil}}$. Artificial white noise was added to the model output to replicate this characteristic of the FCS.

For most of the operating range, $\dot{m}_{\mathrm{Byp}}$ was also predicted accurately by the simulation model, as shown in Figure 25. Apart from the deviations in the stationary operating

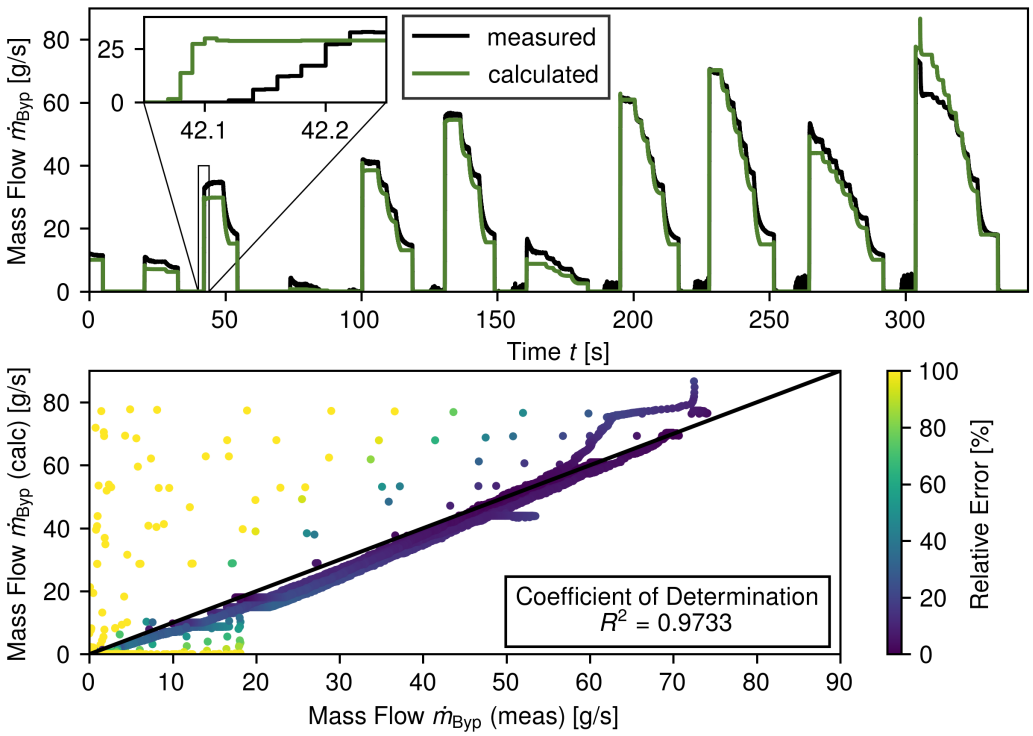

Figure 25: Comparison of $\dot{m}_{\mathrm{Byp}}$ for the FCS test stand measurement and the corresponding simulation model calculations.

points, the enlarged section in Figure 25 reveals a sensor delay for $\dot{m}_{\mathrm{Byp}}$ after the opening of the bypass valve. It took, on average, 40 ms to see a significant increase in $\dot{m}_{\mathrm{Byp}}$ after the actual opening of the throttle valve. Furthermore, slight sensor noise was also visible in Figure 25. Considering the time delay and the sensor noise in the simulation model led to an improved model accuracy with $R^2 = 0.9789$. Figure 25 also uncovers a bypass leakage for high compressor loads. The bypass leakage for $pos^{\mathrm{sp}}_{\mathrm{Byp}} = 0\,\%$ was caused by the valve controller. The force on the throttle plate was increased for higher $p^{\mathrm{out}}_{\mathrm{Cmpr}}$. This increase caused a higher deviation of pos_{Byp} from its setpoint that the valve controller did not counteract due to a valve motor current limitation. However, this effect was neglected in the simulation model of this work because the controller development in the simulation focused on the optimal dynamic behavior and the rejection of sensor noise. The effect of the bypass leakage was only considered during experiments on the FCS test stand and in the FCEV.

The accuracy of the simulation model concerning $p^{\mathrm{out}}_{\mathrm{Cmpr}}$ was likewise evaluated. The

comparison of the model calculations and the FCS test stand measurement is presented in Figure 26. Firstly, the higher values of $p_{\mathrm{Cmpr}}^{\mathrm{out}}$ in the model for small compressor loads

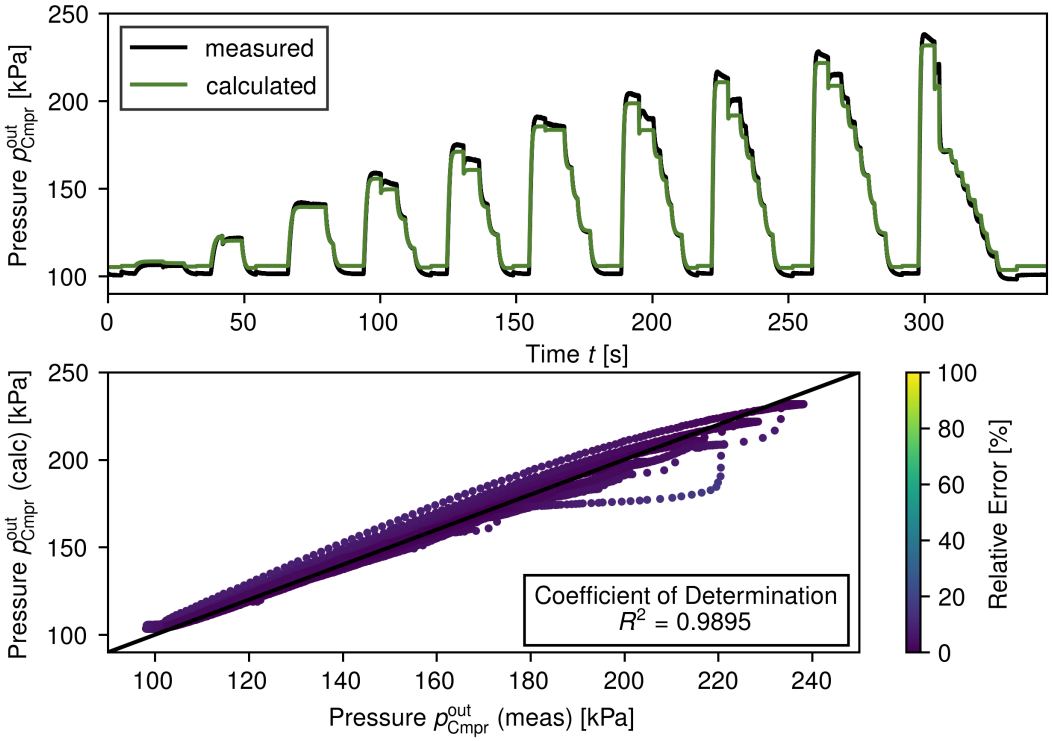

Figure 26: Comparison of $p_{\mathrm{Cmpr}}^{\mathrm{out}}$ for the FCS test stand measurement and the corresponding simulation model calculations.

was due to the assumption of a constant ambient pressure of $p_{\mathrm{Amb}} = 1\,\mathrm{bar}$. During the measurement, an additional sensor returned smaller values of around $p_{\mathrm{Amb}} = 0.955\,\mathrm{bar}$. Secondly, the pressure loss through the air filter was neglected in the model, which is why $p_{\mathrm{Cmpr}}^{\mathrm{in}}$ was smaller in the measurement than the simulation model. Consequently, a similar pressure ratio over the compressor led to smaller values of $p_{\mathrm{Cmpr}}^{\mathrm{out}}$ in the measurement. For higher compressor loads, this effect was negated by the smaller values of n_{Cmpr} in the simulation model. The result was a similar or smaller value for $p_{\mathrm{Cmpr}}^{\mathrm{out}}$ in the simulation model.

The values of $p_{\mathrm{Cmpr}}^{\mathrm{out}}$ further impacted $p_{\mathrm{Ca}}^{\mathrm{in}}$. The associated comparison between the FCS test stand measurement and the simulation is shown in Figure 27. Unexpectedly, the model values of $p_{\mathrm{Ca}}^{\mathrm{in}}$ were considerably smaller than the measurement values. This observation was in contrast to the accurate determination of the air mass flows in the simulation model while neglecting the pressure losses through the intercooler, the CWS, and the cathode inlet valve. Therefore, the differences between $p_{\mathrm{Cmpr}}^{\mathrm{out}}$ and $p_{\mathrm{Ca}}^{\mathrm{in}}$ should have been smaller in the simulation model, which should have led to higher values of $p_{\mathrm{Ca}}^{\mathrm{in}}$ in comparison to the measurement. The most likely explanation for these unexpected findings was an error in the sensor for $p_{\mathrm{Ca}}^{\mathrm{in}}$. This explanation was further supported by the observation that the pressure increased from $p_{\mathrm{Cmpr}}^{\mathrm{out}}$ to $p_{\mathrm{Ca}}^{\mathrm{in}}$ in the FCS test stand measurement for most of the stationary operating points. Consequently, the actual

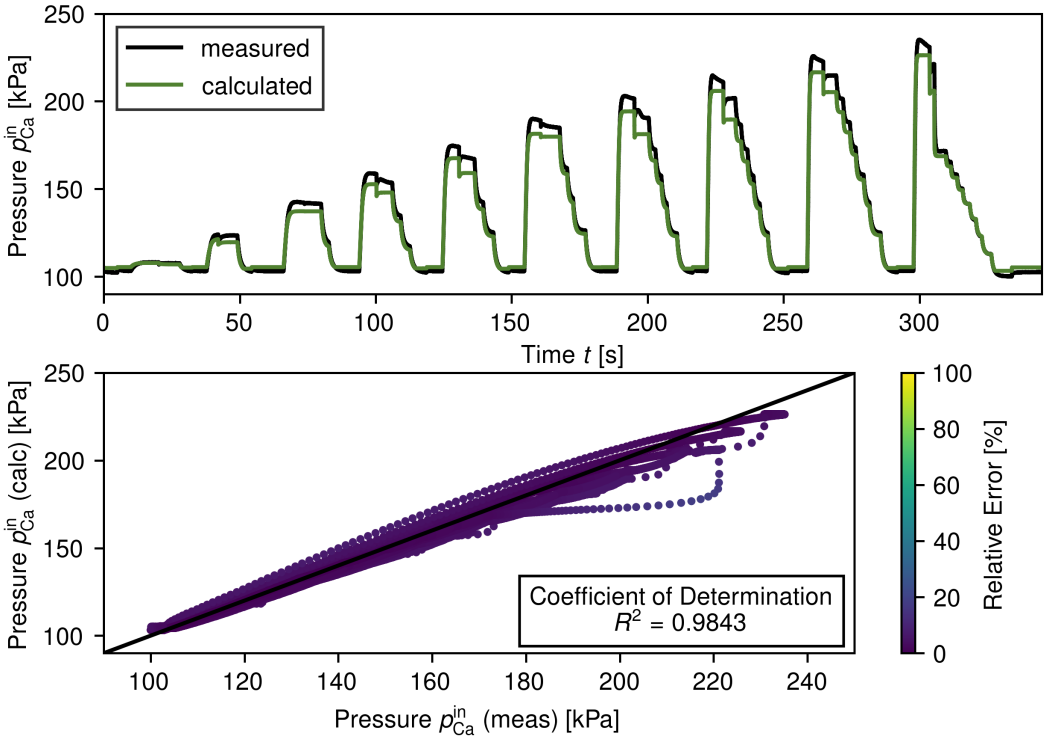

Figure 27: Comparison of p_{Ca}^{in} for the FCS test stand measurement and the corresponding simulation model calculations.

differences between the measurement values and the simulation model results for p_{Ca}^{in} were most likely smaller than displayed in Figure 27.

The findings for p_{Ca}^{in} additionally impacted the evaluation of p_{Ca}^{out}. Figure 28 demonstrates that the calculated values of the simulation model were even lower compared to the measurement. The higher differences between measurement and model values for p_{Ca}^{out} resulted from a higher pressure loss in the fuel cell stack for the simulation model. This higher pressure loss was in contrast to the accurate fitting of the stack air mass flow model with $R^2 = 0.9984$ in Section 4.2.3. The main differences between the measurement used for the parameter fitting and the measurement of Figure 28 were the higher values of I_{Stck} in the fitting measurement. Therefore, an increased pressure loss in the fuel cell stack with increasing electrochemical reactions was assumed. It is reasonable to assume that this correlation was the result of little droplets of liquid water forming in the cathode gas channels for high water production that increased the flow resistance of these gas channels. Thus, the pressure loss in the measurement of Figure 28 was smaller due to the absence of excess water. For the regular operation of the fuel cell system with an active power controller throughout the entire operating range, the simulation model was closer to the actual system concerning the pressure loss through the fuel cell stack. The suspected impact of liquid water was therefore included in the fitted model parameters $C_{1,Ca}^{in}$ and $C_{2,Ca}^{in}$.

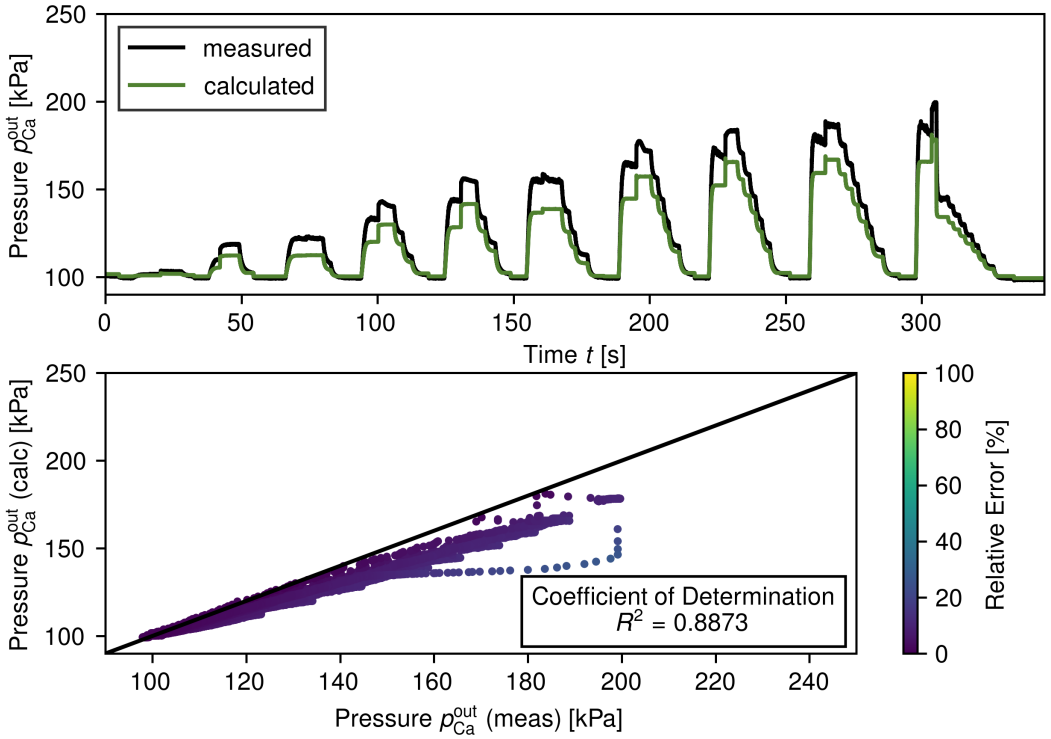

Figure 28: Comparison of p_{Ca}^{out} for the FCS test stand measurement and the corresponding simulation model calculations.

4.4.2 Dynamic Model Validation with an FCEV Measurement

After validating the stationary operating points of the cathode subsystem simulation model, the next step was to compare the dynamic transitions of the state variables, electric powers, and mass flows of the simulation model to the behavior of the actual FCS. A measurement from the FCEV was best suited for this task due to the variety of dynamic transitions. Additionally, this measurement was used to evaluate the transferability of findings from the test stand to the target system in the FCEV. The corresponding model inputs are summarized in Figure 29. The maximum value $i_{q,\mathrm{Cmpr}}^{\mathrm{sp}} = 140\,\mathrm{A}$ in Figure 29 was the nominal upper limit of the compressor inverter. However, the actual upper limit of the operating range of the compressor inverter was lower, which is why only $i_{q,\mathrm{Cmpr}}^{\mathrm{meas}} = 127\,\mathrm{A}$ was reached in the measurement. By contrast, the model went as high as $i_{q,\mathrm{Cmpr}} = 140\,\mathrm{A}$, because no limits were implemented in the current controller model of Section 4.2.1.

Despite this significant difference, the impact on n_{Cmpr} was negligible for both the FCEV measurement and the simulation model. Similar to the test stand measurement results, the comparison of n_{Cmpr} in Figure 30 reveals slightly smaller values for the simulation model. The dynamics of n_{Cmpr} were well predicted by the simulation model. The only significant deviation occurred during the negative load step of $i_{q,\mathrm{Cmpr}}^{\mathrm{sp}}$ at $t = 24\,\mathrm{s}$. This deviation was mainly caused by a lower stationary point of the model compared to the actual FCS for the same input values.

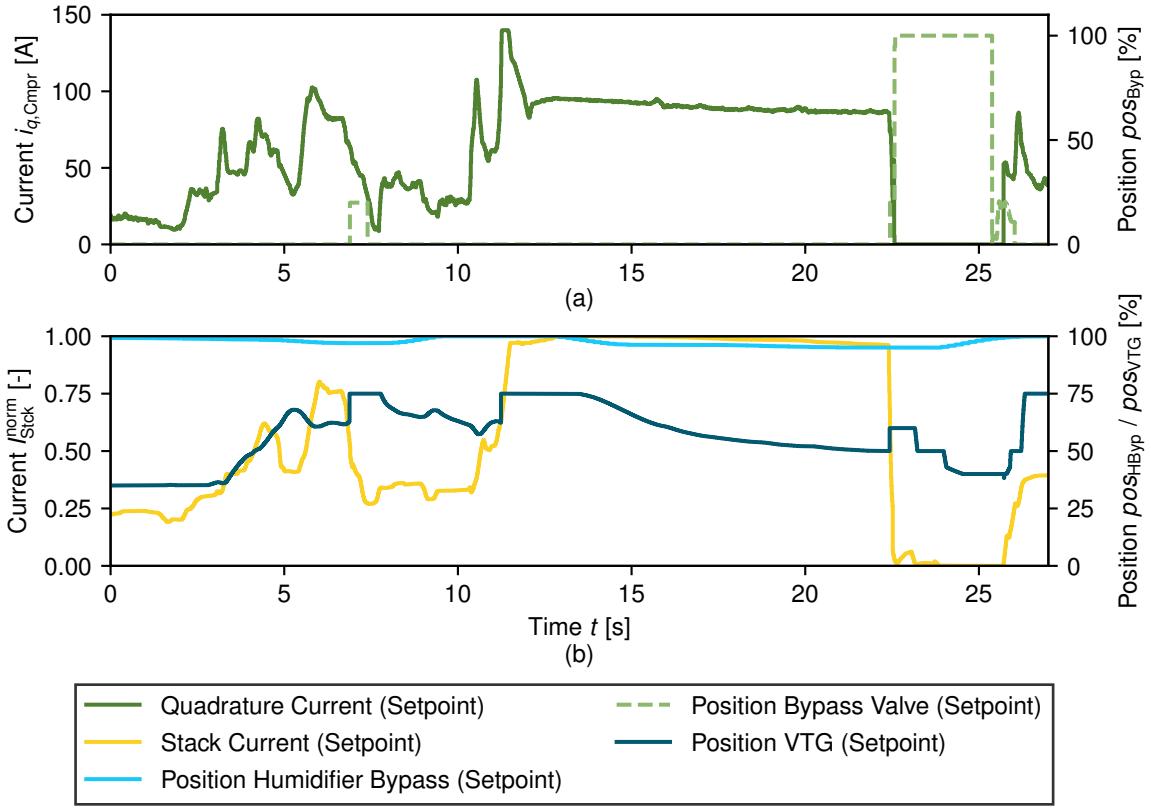

Figure 29: Inputs into the FCS simulation model for the FCEV measurement to validate the dynamic transitions of the electric powers and the cathode subsystem.

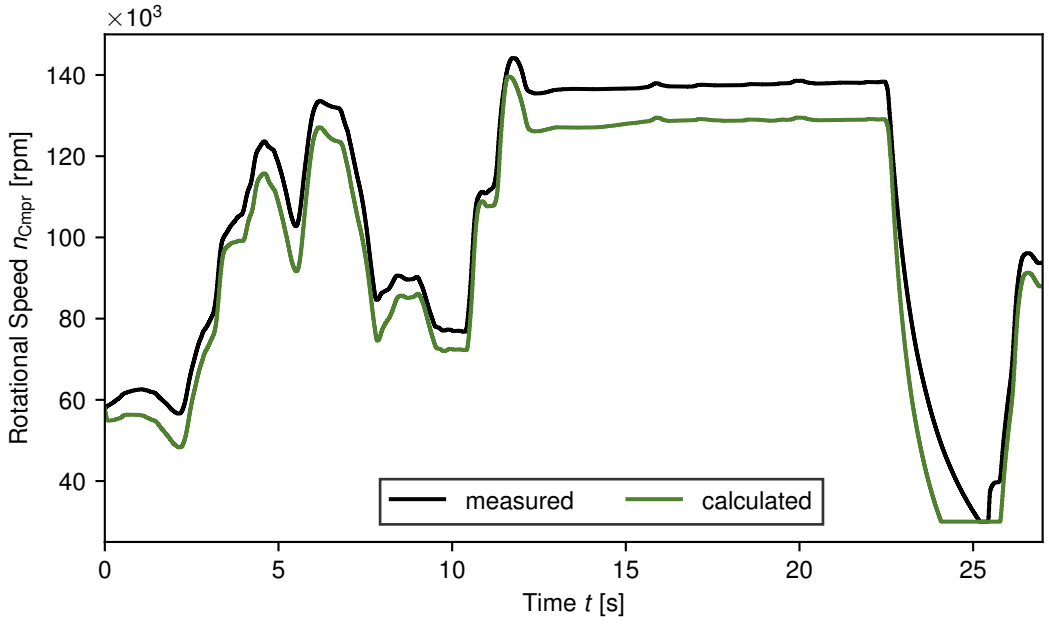

Figure 30: Comparison of n_{Cmpr} for the FCEV measurement and the corresponding simulation model calculations.

However, the impact of this deviation on P_{Cmpr} was negligible. The corresponding

comparison between measurement and model calculations is displayed in Figure 31. Unlike for n_{Cmpr}, the overshoot $i_{q,\mathrm{Cmpr}} = 140\,\mathrm{A}$ was visible in the peak of P_{Cmpr} for the

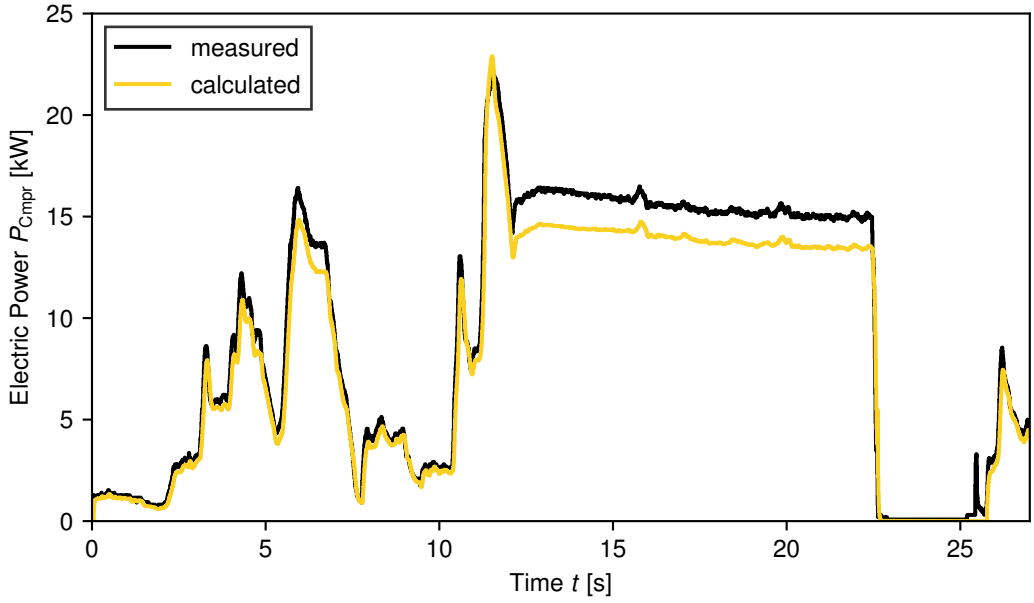

Figure 31: Comparison of P_{Cmpr} for the FCEV measurement and the corresponding simulation model calculations.

simulation model at $t = 11.5\,\mathrm{s}$ in Figure 31. In general, the dynamics of P_{Cmpr} resulted from the faster dynamics of $i_{,\mathrm{Cmpr}}$ and the slower dynamics of n_{Cmpr}. This combination of time constants was correctly predicted by the simulation model, which was a key prerequisite for the model-based development of an FCS net power controller.

For the development of the air mass flow controller, the correct determination of the dynamics of $\dot{m}_{\mathrm{AirFil}}$ with the simulation model was of great significance. This goal was achieved with the model presented in Section 4.2, as shown by the comparison of simulation and measurement in Figure 32. The deviations in the dynamic transitions aligned with those of n_{Cmpr}. Furthermore, the model value of $\dot{m}_{\mathrm{AirFil}}$ in Figure 32 included artificial white noise representing the sensor noise in the actual FCS. The comparison to the measurement values shows a good agreement for the noise levels throughout the operating range. Therefore, the noise rejection capabilities of the controllers were assessable during simulations. A difference between Figure 24 for the test stand measurement and Figure 32 for the FCEV measurement was the deviation for stationary operating points. While the model predicted higher values of $\dot{m}_{\mathrm{AirFil}}$ for the FCS test stand measurement, the model values in Figure 32 were lower compared to the measurement. This discrepancy was caused by the significantly lower ambient temperature $T_{\mathrm{Amb}} = 5\,^{\circ}\mathrm{C}$ in the FCEV measurement in contrast to $T_{\mathrm{Amb}} = 23\,^{\circ}\mathrm{C}$ for the FCS test stand. As a result, the air density at the compressor inlet was significantly lower for the model, which assumed $T_{\mathrm{Amb}} = 25\,^{\circ}\mathrm{C}$.

The difference in T_{Amb} further affected the model accuracy for $p_{\mathrm{Cmpr}}^{\mathrm{out}}$. The comparison of measurement and model prediction for $p_{\mathrm{Cmpr}}^{\mathrm{out}}$ is shown in Figure 33. At first, it

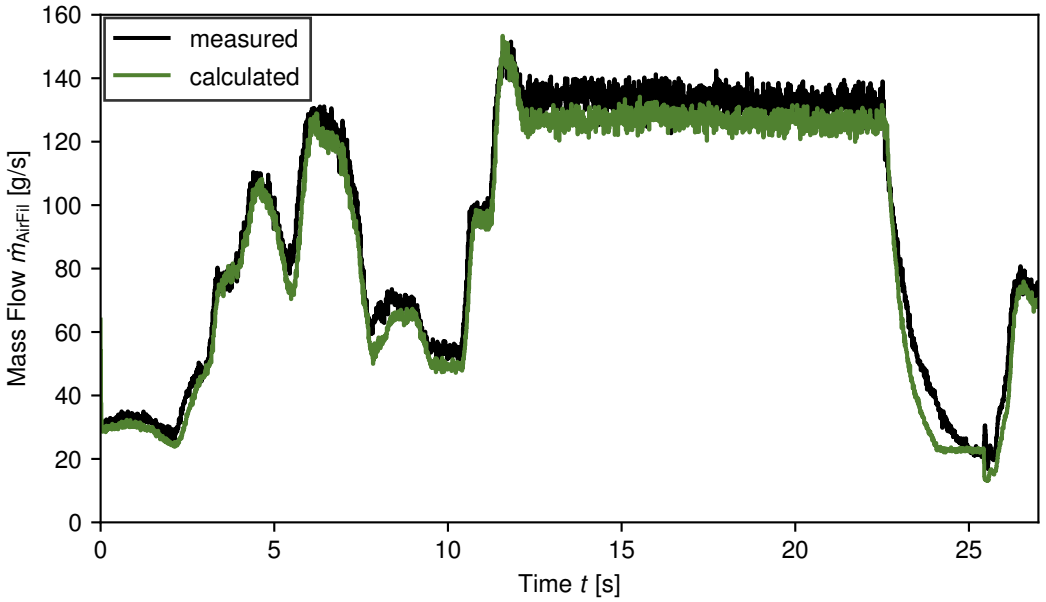

Figure 32: Comparison of $\dot{m}_{\mathrm{AirFil}}$ for the FCEV measurement and the corresponding simulation model calculations.

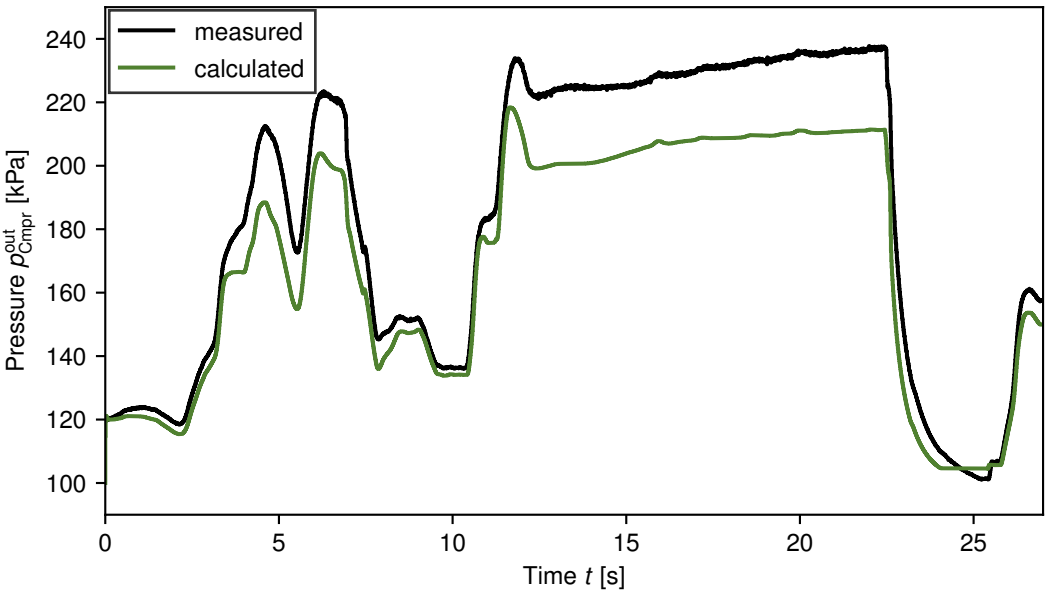

Figure 33: Comparison of $p^{\mathrm{out}}_{\mathrm{Cmpr}}$ for the FCEV measurement and the corresponding simulation model calculations.

is noteworthy that the dynamics of $p^{\mathrm{out}}_{\mathrm{Cmpr}}$ were well represented qualitatively by the simulation model. Nevertheless, the differences between measurement and model values were more significant compared to the FCS test stand measurement in Figure 26. The higher level of $p^{\mathrm{out}}_{\mathrm{Cmpr}}$ in the FCEV measurement was caused by a low $T_{\mathrm{Amb}} = 5\,^{\circ}\mathrm{C}$. Firstly, the resulting higher air density decreased the pressure loss through the air filter. Consequently, $p^{\mathrm{in}}_{\mathrm{Cmpr}}$ was higher for the same values of $\dot{m}_{\mathrm{AirFil}}$. Secondly, colder air temperatures at the compressor inlet moved the operating trajectory further to

the left in the compressor map. Low inlet temperatures increased $\dot{m}_{\mathrm{Cmpr}}$ for the same $\dot{\dot{m}}_{\mathrm{Cmpr}}$. As a result, the pressure loss through the systems increased due to the higher mass flow. This higher pressure loss increased $p_{\mathrm{Cmpr}}^{\mathrm{out}}$, which in turn decreased $\dot{m}_{\mathrm{Cmpr}}$. The new stationary operating point nonetheless evened out further on the left in the compressor map. Hence, higher pressure ratios occurred over the compressor. This effect was replicated with the model, as shown in Figure 34.

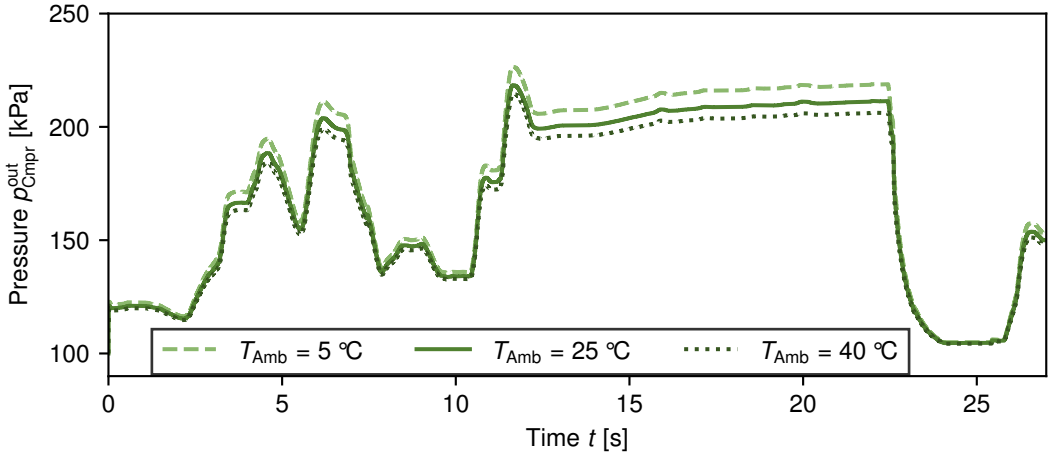

Figure 34: Compressor inlet temperature dependency of $p_{\mathrm{Cmpr}}^{\mathrm{out}}$ in the simulation model.

The simultaneous occurrence of differences in $p_{\mathrm{Cmpr}}^{\mathrm{out}}$ and $\dot{m}_{\mathrm{Byp}}$ between the simulation model and the FCEV measurement indicated a correlation between the two variables. The corresponding comparison for $\dot{m}_{\mathrm{Byp}}$ is depicted in Figure 35. The simulation results

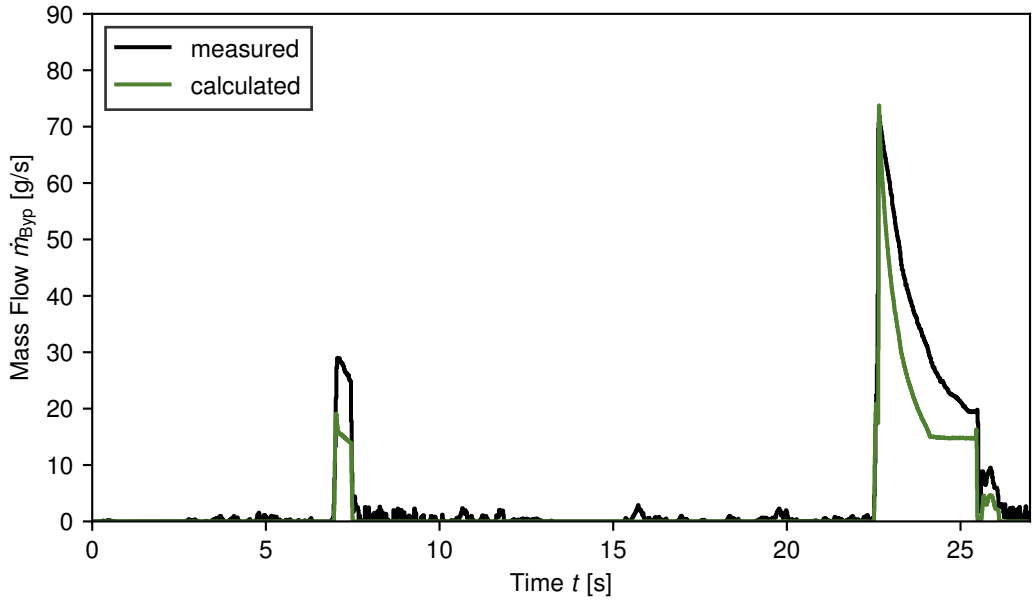

Figure 35: Comparison of $\dot{m}_{\mathrm{Byp}}$ for the FCEV measurement and the corresponding simulation model calculations.

in Figure 35 also included the modeled sensor noise of $\dot{m}_{\mathrm{Byp}}$ that was significantly lower

compared to $\dot{m}_{\mathrm{AirFil}}$. What is more, the dynamics of $\dot{m}_{\mathrm{Byp}}$ were accurately predicted by the simulation model.

Additionally, the dynamics of $p_{\mathrm{Ca}}^{\mathrm{in}}$ were very well predicted by the simulation model. The associated comparison of the measurement and the model values is shown in Figure 36. The measurement and simulation differences were similar to $p_{\mathrm{Cmpr}}^{\mathrm{out}}$ in Figure 33. Thus,

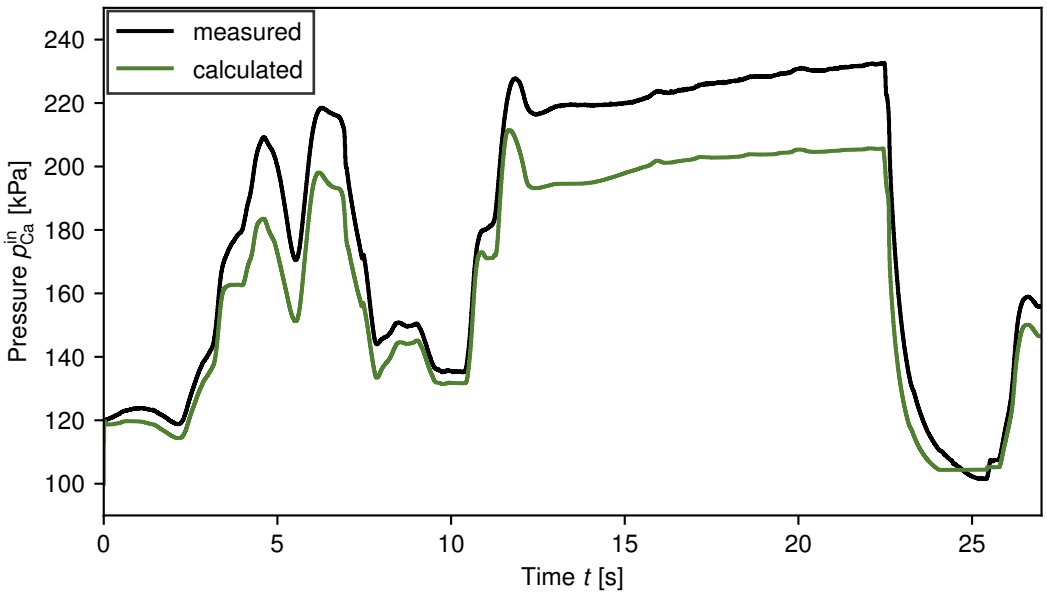

Figure 36: Comparison of $p_{\mathrm{Ca}}^{\mathrm{in}}$ for the FCEV measurement and the corresponding simulation model calculations.

the simulation model properly predicted the pressure loss between $p_{\mathrm{Cmpr}}^{\mathrm{out}}$ and $p_{\mathrm{Ca}}^{\mathrm{in}}$. Moreover, the measured values of $p_{\mathrm{Cmpr}}^{\mathrm{out}}$ were generally higher than $p_{\mathrm{Ca}}^{\mathrm{in}}$. These higher values imply that the FCEV measurement did not have the same error as the FCS test stand measurement.

For the development of an FCS power controller, one of the critical variables is U_{Stck}. The comparison between the measurement values for the FCEV measurement and the model values is displayed in Figure 37. The simulation model invariably calculated higher values, even though the simplified polarization curve was best fitted to an intermediate operating range. This observation strongly suggests that some of the deviations were caused by insufficiently humidified fuel cells, as the polarization curve model assumed perfect operating conditions with regard to humidity, temperature, and hydrogen partial pressure. However, the dynamics of U_{Stck} were accurately calculated since they mainly depended on the model input $I_{\mathrm{Stck}}^{\mathrm{sp}}$. The value of $I_{\mathrm{Stck}}^{\mathrm{sp}}$ was directly assigned to I_{Stck} with a time delay of $t_{d,I_{\mathrm{Stck}}} = 50\,\mathrm{ms}$.

The dynamics of $I_{\mathrm{Stck}}^{\mathrm{sp}}$ also substantially impacted the dynamics of P_{Stck}. Consequently, the dynamics of P_{Stck} were adequately predicted by the simulation model, as shown in Figure 38. The absolute value of P_{Stck} likewise depended on I_{Stck}, which is why the differences between the measurement and the model values were only significant for high values of I_{Stck}.

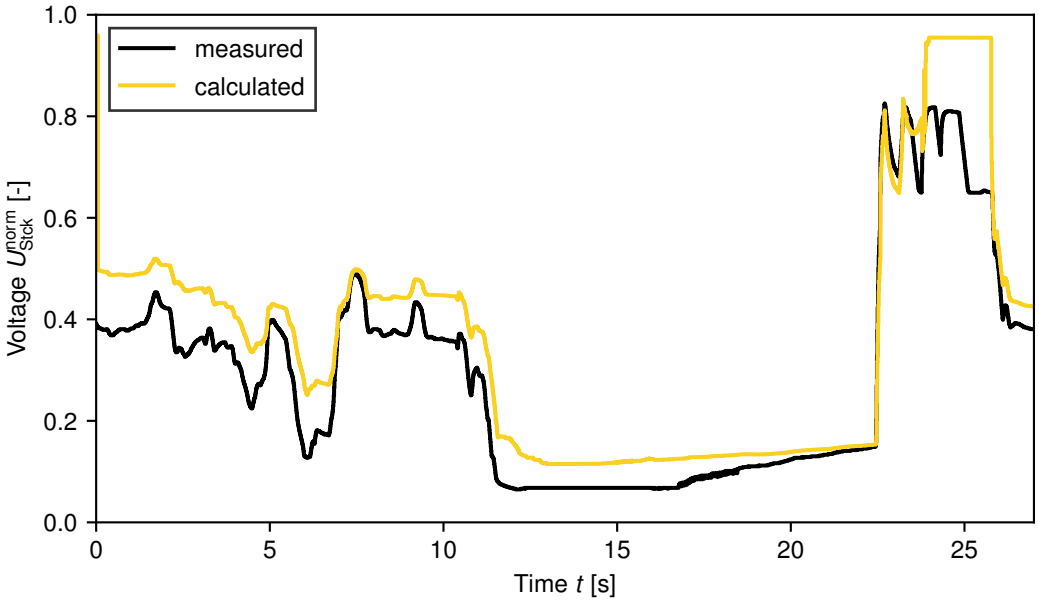

Figure 37: Comparison of U_{Stck}^{norm} for the FCEV measurement and the corresponding simulation model calculations.

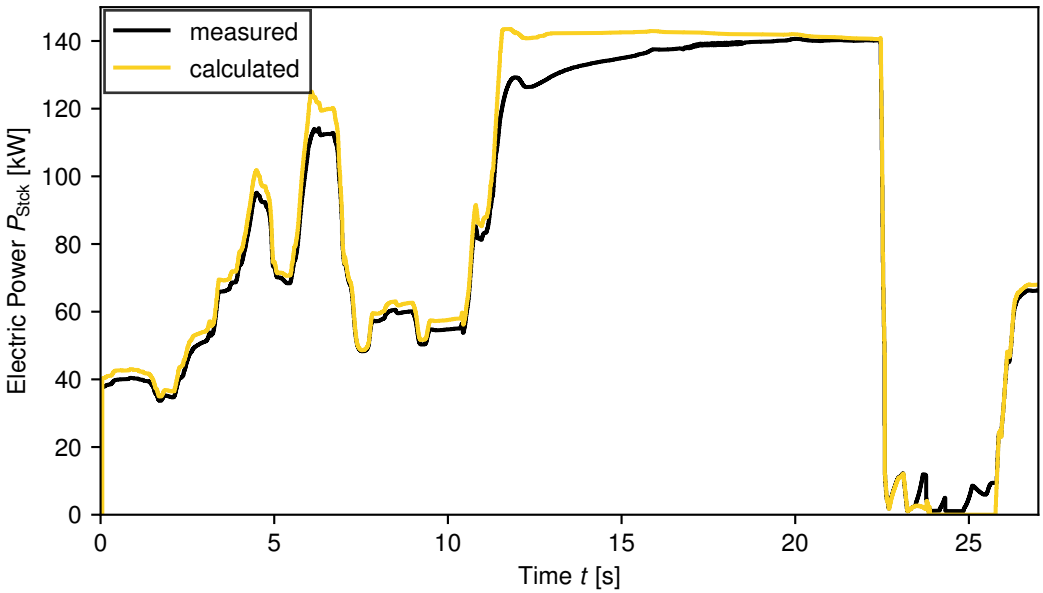

Figure 38: Comparison of P_{Stck} for the FCEV measurement and the corresponding simulation model calculations.

These differences further influenced the model accuracy with regard to P_{FCS}, whereas the simulation model precisely represented the dynamics of P_{FCS}. The comprehensive comparison between the FCEV measurement and the simulation model values of P_{FCS} is depicted in Figure 39. Overall, the FCS simulation model in this work was capable of accurately predicting the dynamics behavior of the air mass flows and the primary power sources and sinks, while the stationary values were partly deviating from the measurement. Therefore, the closed-loop dynamic behavior of all the proposed

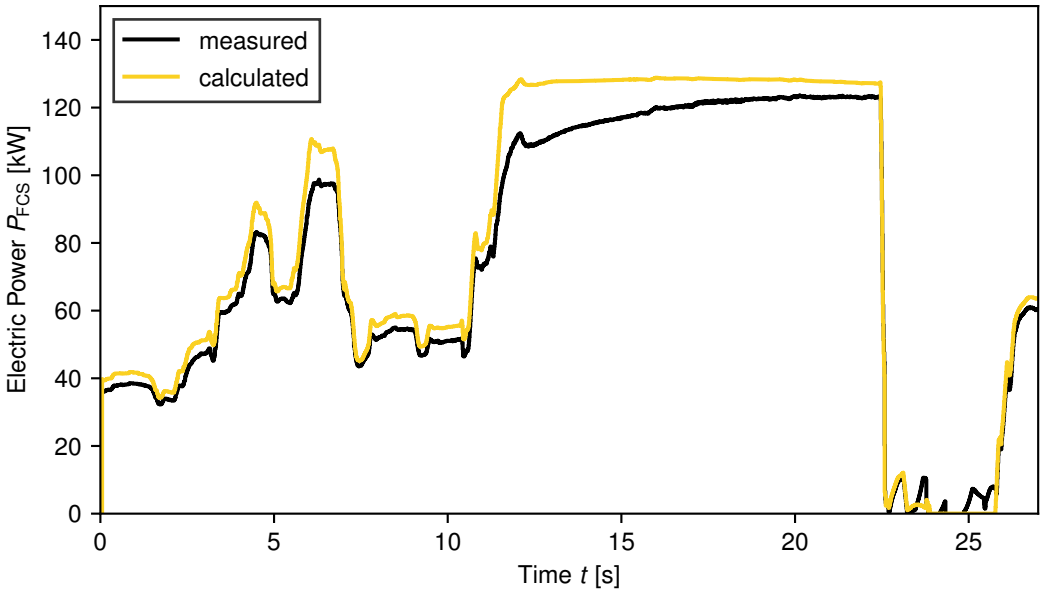

Figure 39: Comparison of P_{FCS} for the FCEV measurement and the corresponding simulation model calculations.

controllers in this work could be evaluated in the simulation. The capability to achieve zero control deviation, however, had to be evaluated separately on the FCS test stand and in the FCEV.

5 Air Mass Flow Control with Explicit Linear Model Predictive Control

The model equations in Chapter 4 highlighted the non-linearity of the cathode subsystem. However, the solution of an NLP problem with NMPC is significantly more complex than the solution of a QP problem with linear MPC. Thus, the initial air mass flow controller in this work was based on explicit linear MPC. This control method already improved the closed-loop behavior of the cathode subsystem compared to the PI controllers. Additionally, the shortcomings of this method were used as a motivation for the subsequent development of an explicit NMPC in Chapter 6.

The control variables of the explicit linear MPC were $\boldsymbol{u} = \left[i_{q,\mathrm{Cmpr}}^{\mathrm{sp}},\, pos_{\mathrm{Byp}}^{\mathrm{sp}}\right]^T$, while the controlled variables were $\boldsymbol{y} = [\dot{m}_{\mathrm{Ca}}^{\mathrm{in}},\, \dot{m}_{\mathrm{Byp}}]^T$. A recently published work [27] presented initial results regarding this controller. Supplementary findings are displayed in this chapter. In Section 5.1, the linear prediction model is briefly introduced. Subsequently, the main equations regarding the state and perturbation observer and the cost function are presented in Sections 5.2 and 5.3, respectively. These equations are followed by simulation results in Section 5.4, a step in the controller development process that was not presented in [27]. Lastly, additional experimental results are displayed in Section 5.5 for the FCS test stand.

In [27], the first application of an explicit linear MPC to the air supply control of an FCEV was reported. However, the utilization of explicit linear MPC for FCS control has been reported before. One of the first studies employing explicit linear MPC in an FCS was conducted by Puig *et al.* [92]. The authors used model linearization at a fixed operating point to control $\lambda_{\mathrm{O_2}}$. This approach was validated with simulations. The operating range was small with $I_{\mathrm{Stck}} \in [190\,\mathrm{A},\, 270\,\mathrm{A}]$ and included the linearization point with $I_{\mathrm{Stck},0} = 191\,\mathrm{A}$. Similarly, Arce *et al.* [6] applied a CARIMA model to regulate $\lambda_{\mathrm{O_2}}$ in a simulation. The model parameters were also obtained by linearizing a nonlinear model around a fixed operating point with $I_{\mathrm{Stck},0} = 15\,\mathrm{A}$. Additionally, the validation scenario only comprised a small operating range with $I_{\mathrm{Stck}} \in [13\,\mathrm{A},\, 35\,\mathrm{A}]$. In a later work, Arce *et al.* [7] further experimentally validated an explicit controller for T_{Stck}. The explicit linear MPC was based on a linear state-space model and operated at a sample time of $\Delta t = 400\,\mathrm{ms}$. The validated operating range was rather small with $I_{\mathrm{Stck}} \in [13\,\mathrm{A},\, 35\,\mathrm{A}]$. More recently, Liu *et al.* [70] utilized explicit linear MPC to control a hybrid system that consisted of a fuel cell and a battery. The control targets were the total power output of the hybrid system and the SOC of the battery. The validation was performed in a simulation, in which a driving cycle was used to test the full available operating range. Nonetheless, these reported applications of explicit

MPCs for FCS control have rarely been experimentally validated, especially concerning the large operating range of a modern automotive FCS. This research gap is partly addressed in the last section of this chapter, supplementing the results from [27].

5.1 Linear Prediction Model

A linear prediction model only coarsely approximates the dynamic behavior of a nonlinear system like the cathode subsystem of this work. Additionally, the nonlinear model of Chapter 4 was only an approximation of the actual system. Therefore, the linear prediction model was directly parameterized with measurements [27] instead of linearizing the available nonlinear model. Hence, an additional approximation error was avoided.

5.1.1 Model Equations

The dynamics of $\boldsymbol{y}$ were predicted with four first-order low-pass filters.

$$\dot{\boldsymbol{x}}(t) = \begin{bmatrix} -\frac{1}{T_{11}} & 0 & 0 & 0 \\ 0 & -\frac{1}{T_{12}} & 0 & 0 \\ 0 & 0 & -\frac{1}{T_{21}} & 0 \\ 0 & 0 & 0 & -\frac{1}{T_{22}} \end{bmatrix} \boldsymbol{x}(t) + \begin{bmatrix} \frac{k_{11}}{T_{11}} & 0 \\ 0 & \frac{k_{12}}{T_{12}} \\ \frac{k_{21}}{T_{21}} & 0 \\ 0 & \frac{k_{22}}{T_{22}} \end{bmatrix} \begin{bmatrix} u_1(t - 50\,\mathrm{ms}) \\ u_2(t - 20\,\mathrm{ms}) \end{bmatrix} \tag{5.1}$$

$$\boldsymbol{y}(t) = \begin{bmatrix} 1 & 1 & -1 & -1 \\ 0 & 0 & 1 & 1 \end{bmatrix} \boldsymbol{x}(t) \tag{5.2}$$

Each of the low-pass filters in Equation (5.1) represented the impact of one control variable on one controlled variable. A similar model was applied in [110].

5.1.2 Determination of Model Parameters

The initial parameterization of the linear prediction model was determined from a set of measured step changes detailed in [27]. Afterward, the average values of T_{11} and T_{21} were replaced with the smallest values from the highest step change of u_1. This parameter modification removed initial oscillations in the closed-loop behavior of $\boldsymbol{y}$ during step changes of y_1^{sp}. Furthermore, the cross-coupling between u_1 and y_2 was neglected in the prediction model to avoid oscillations after simultaneous step changes of y_1^{sp} and y_2^{sp}. Undershoots of y_2 were eliminated by replacing the average value of k_{22} with its maximum value from the measurements. Eventually, the continuous model was

discretized with a fixed step size $\Delta t = 10\,\mathrm{ms}$.

$$\begin{aligned}\boldsymbol{x}(k+1) = &\underbrace{\begin{bmatrix} 0.9780 & 0 & 0 & 0 \\ 0 & 0.9311 & 0 & 0 \\ 0 & 0 & 0.9759 & 0 \\ 0 & 0 & 0 & 0.8187 \end{bmatrix}}_{\boldsymbol{A}_\mathrm{d}} \boldsymbol{x}(k) \\ &+ \underbrace{\begin{bmatrix} 0.0389 & 0 \\ 0 & 0.0165 \\ 0.0181 & 0 \\ 0 & 0.2338 \end{bmatrix}}_{\boldsymbol{B}_\mathrm{d}} \begin{bmatrix} u_1(k-5) \\ u_2(k-2) \end{bmatrix}\end{aligned} \tag{5.3}$$

$$\boldsymbol{y}(k) = \begin{bmatrix} 1 & 1 & 0 & -1 \\ 0 & 0 & 0 & 1 \end{bmatrix} \boldsymbol{x}(k) \tag{5.4}$$

5.1.3 Validation of Linear Prediction Model

The closed-loop behavior of an MPC depends notably on the accuracy of its prediction model. Thus, the prediction accuracy was evaluated by comparing the predicted values of $\boldsymbol{y}$ with those from an FCS test stand measurement. The results for $\dot{m}_\mathrm{Ca}^\mathrm{in}$ are shown in Figure 40. The prediction accuracy of $\dot{m}_\mathrm{Ca}^\mathrm{in}$ was acceptable for operating points with $pos_\mathrm{Byp}^\mathrm{sp} = 0\,\%$. These findings indicate that the individual correlation between $\dot{m}_\mathrm{Ca}^\mathrm{in}$ and $i_{q,\mathrm{Cmpr}}^\mathrm{sp}$ was approximately linear. However, the opening of the bypass valve led to an error between measurement and predicted value upwards of 100 %. This substantial error resulted from a very inaccurate prediction of $\dot{m}_\mathrm{Byp}$, which is shown in Figure 41. The considerable deviation between the linear prediction model and the FCS test stand measurement arose from two model parameter modifications in [27]. The cross-coupling between $i_{q,\mathrm{Cmpr}}^\mathrm{sp}$ and $\dot{m}_\mathrm{Byp}$ was neglected, and the maximum value of k_{22} was chosen. The only advantage of the neglected cross-coupling was that it ensured the prediction of $\dot{m}_\mathrm{Byp} = 0\,\frac{\mathrm{g}}{\mathrm{s}}$ for $pos_\mathrm{Byp}^\mathrm{sp} = 0\,\%$. The parameterization of Equations (5.3) and (5.4) was kept, nevertheless, because it resulted in the best closed-loop behavior in [27].

5.2 State and Perturbation Observer

The significant deviations between the linear prediction model and the FCS test stand emphasized the need for perturbation compensation in the closed control loop. This compensation was achieved with the state and perturbation observer from [27]

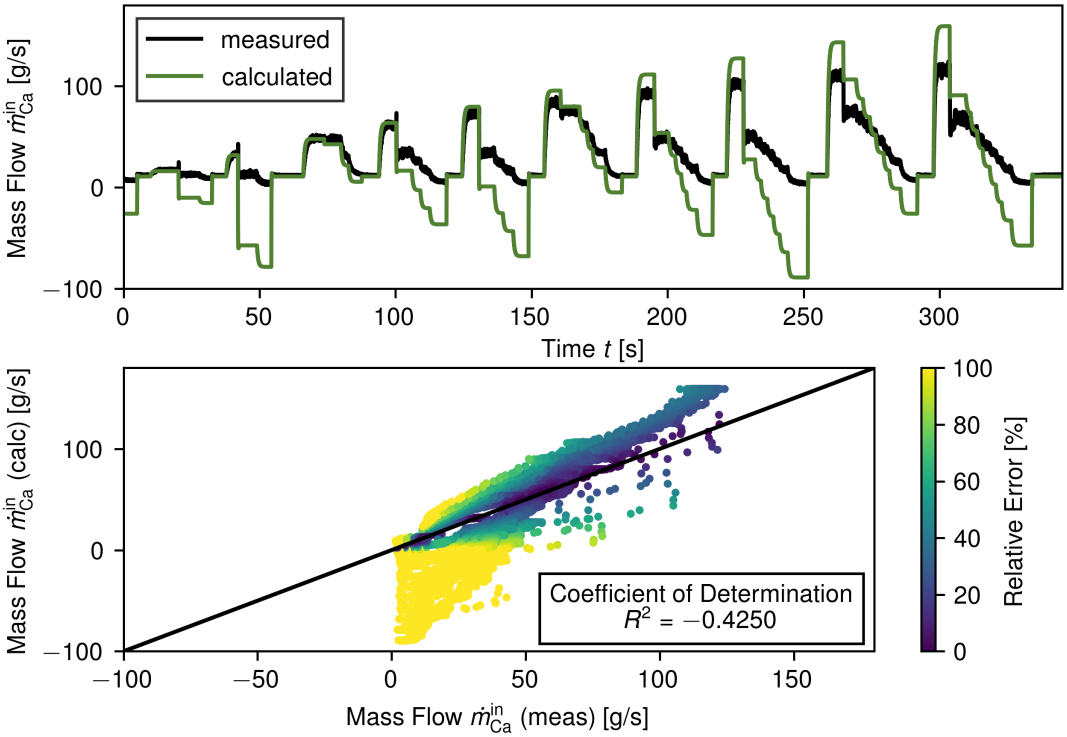

Figure 40: Comparison of $\dot{m}_{Ca}^{in}$ for the FCS test stand measurement and the corresponding linear prediction model calculations.

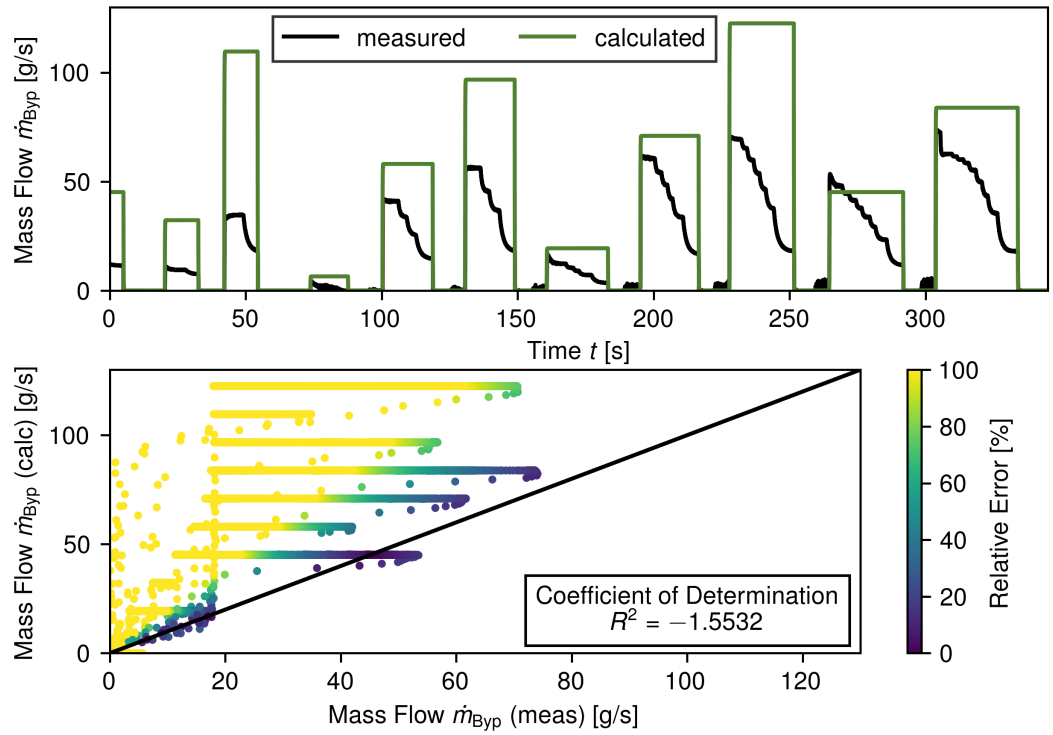

Figure 41: Comparison of $\dot{m}_{Byp}$ for the FCS test stand measurement and the corresponding linear prediction model calculations.

implemented as a Luenberger observer.

$$\begin{aligned}\begin{bmatrix}\hat{\boldsymbol{x}}(k+1)\\ \hat{\boldsymbol{d}}(k+1)\end{bmatrix} &= \begin{bmatrix}\boldsymbol{A}_\mathrm{d} & \boldsymbol{0}\\ \boldsymbol{0} & \boldsymbol{I}\end{bmatrix}\begin{bmatrix}\hat{\boldsymbol{x}}(k)\\ \hat{\boldsymbol{d}}(k)\end{bmatrix} + \begin{bmatrix}\boldsymbol{B}_\mathrm{d}\\ \boldsymbol{0}\end{bmatrix}\begin{bmatrix}u_1(k-5)\\ u_2(k-2)\end{bmatrix}\\ &\quad + \boldsymbol{L}_\mathrm{d}\left\{\boldsymbol{y}_\mathrm{FCS}^\mathrm{meas}(k) - \begin{bmatrix}\hat{y}_{1,\mathrm{FCS}}(k)\\ \hat{y}_{2,\mathrm{FCS}}(k-4)\end{bmatrix}\right\}\end{aligned} \tag{5.5}$$

$$\hat{\boldsymbol{y}}_\mathrm{FCS}(k) = \begin{bmatrix}1 & 1 & 0 & 0 & 1 & 0\\ 0 & 0 & 0 & 1 & 0 & 1\end{bmatrix}\begin{bmatrix}\hat{\boldsymbol{x}}(k)\\ \hat{\boldsymbol{d}}(k)\end{bmatrix} \tag{5.6}$$

In this work and in [27], $\dot{m}_\mathrm{Ca}^\mathrm{in}$ was not measured directly by a sensor. As a result, the measured outputs $\boldsymbol{y}_\mathrm{FCS} = [\dot{m}_\mathrm{AirFil},\, \dot{m}_\mathrm{Byp}]^T$ differed from the controlled variables $\boldsymbol{y}$ of the linear prediction model. The perturbation compensation was tuned with the observer gain matrix $\boldsymbol{L}_\mathrm{d}$ in Equation (5.5). In the closed control loop, the observed perturbations $\hat{\boldsymbol{d}}$ were used to determine modified setpoints $\tilde{\boldsymbol{y}}^\mathrm{sp}$ for the linear MPC.

$$\tilde{\boldsymbol{y}}^\mathrm{sp}(k) = \boldsymbol{y}^\mathrm{sp}(k) - \begin{bmatrix}\hat{d}_1(k) - \hat{d}_2(k)\\ \hat{d}_2(k)\end{bmatrix} \tag{5.7}$$

As shown in [27], these setpoints were the means to achieve zero control deviation during stationary operation.

5.3 Cost Function for Linear Model Predictive Controller

The values of $\tilde{\boldsymbol{y}}^\mathrm{sp}(k)$ were used in the quadratic cost function J of the linear MPC as part of the parameter vector $\boldsymbol{\theta}$.

$$\begin{aligned}J(\boldsymbol{\theta}(k), \boldsymbol{U}) &= \sum_{i=1}^{N_y}\left[\tilde{\boldsymbol{y}}^\mathrm{sp}(k) - \boldsymbol{y}(k+i)\right]^T \boldsymbol{Q}\left[\tilde{\boldsymbol{y}}^\mathrm{sp}(k) - \boldsymbol{y}(k+i)\right]\\ &\quad + \sum_{j=0}^{N_u-1}\Delta\boldsymbol{u}(k+j)^T\boldsymbol{R}\Delta\boldsymbol{u}(k+j)\end{aligned} \tag{5.8}$$

This optimization problem included the linear prediction model and the input constraints $\boldsymbol{u}_\mathrm{Min} = [0\,\mathrm{A},\, 0\,\%]^T$ and $\boldsymbol{u}_\mathrm{Max} = [120\,\mathrm{A},\, 100\,\%]^T$.

$$\min_{\boldsymbol{U}} \quad J(\boldsymbol{\theta}(k), \boldsymbol{U}) \tag{5.9}$$

$$\text{s.t.} \quad \boldsymbol{u}_\mathrm{Min} \le \boldsymbol{u}(k+j) \le \boldsymbol{u}_\mathrm{Max}, \qquad j = 0, 1, ..., N_u - 1 \tag{5.10}$$

$$\boldsymbol{x}(k+i) = \boldsymbol{A}_\mathrm{d}\boldsymbol{x}(k+i-1) + \boldsymbol{B}_\mathrm{d}\begin{bmatrix}u_1(k+i-6)\\ u_2(k+i-3)\end{bmatrix}, \quad i = 1, 2, ..., N_y \tag{5.11}$$

$$\boldsymbol{y}(k+i) = \begin{bmatrix}1 & 1 & 0 & -1\\ 0 & 0 & 0 & 1\end{bmatrix}\boldsymbol{x}(k+i), \qquad i = 1, 2, ..., N_y \tag{5.12}$$

The optimization problem of Equations (5.9)-(5.12) constituted a QP problem with only linear constraints.

5.4 Simulation Study with Implicit Linear Model Predictive Controller

The real-time capability of the proposed linear MPC was achieved by applying the explicit solution $\boldsymbol{u}(\boldsymbol{\theta})$ presented in [11]. For this approach, the CPU core load of the PWA solution mainly depended on n_{PT}. The exclusive presence of control variable constraints in the QP problem led to a correlation between n_{PT} and N_u introduced in [27].

$$n_{\mathrm{PT}} = 9^{N_u} \tag{5.13}$$

Nine combinations of active and inactive constraints were possible for every step along N_u. Thus, $N_u = 2$ was chosen in this work because it was the most extended real-time capable control horizon with a CPU core load of around 5 %. The 50 ms time delay for u_1 then led to a minimum length of the prediction horizon of $N_y = 7$. Furthermore, the considerable stationary differences between the linear prediction model and the FCS led to a significant dependence of the closed-loop behavior on the perturbation compensation with the state observer. Hence, the lack of a prediction model for $\hat{\boldsymbol{d}}$ rendered long prediction horizons impractical, which is why $N_y = 7$ was chosen in this work.

The small prediction and control horizons aligned with the findings from other authors that used linear MPC for air supply control in an FCS. Puig *et al.* [92], [93] used horizons as small as $N_y = N_u = 2$ in their application, while Arce *et al.* [6] and Bordons *et al.* [13] applied MPC with $N_y = N_u = 3$ and $N_y = N_u = 4$, respectively. Similarly, Yang *et al.* [123] implemented an air supply controller with linear MPC that worked with $N_y = 6$ and $N_u = 3$. The only works on linear MPC for air supply control with a significantly higher prediction and control horizon were by Vahidi *et al.* [118], [119]. In their application, the SOC control of the additional capacitor required a long prediction horizon. Otherwise, unstable closed-loop behavior was observed.

Successfully applying an explicit linear MPC required prior tuning of the cost function parameters. This development step was carried out with closed-loop simulation before the test stand validation shown in [27]. However, the simulation results were not presented in [27] to retain an acceptable length of the article. In these simulations, the QP problem of Equations (5.9)-(5.12) was solved with Hildreth's method [47], as described in [62]. The comparability of the tested parameter sets was accomplished by repeatedly using the same mass flow setpoint sequence presented in [27]. The corresponding values of $\dot{m}_{\mathrm{Ca}}^{\mathrm{in,sp}}$ and $\dot{m}_{\mathrm{Byp}}^{\mathrm{sp}}$ are displayed in Figure 42. Every step change in Figure 42 lasts 5 s, allowing the simultaneous evaluation of the dynamic system response and the steady-state closed-loop behavior. Additionally, the first step changes

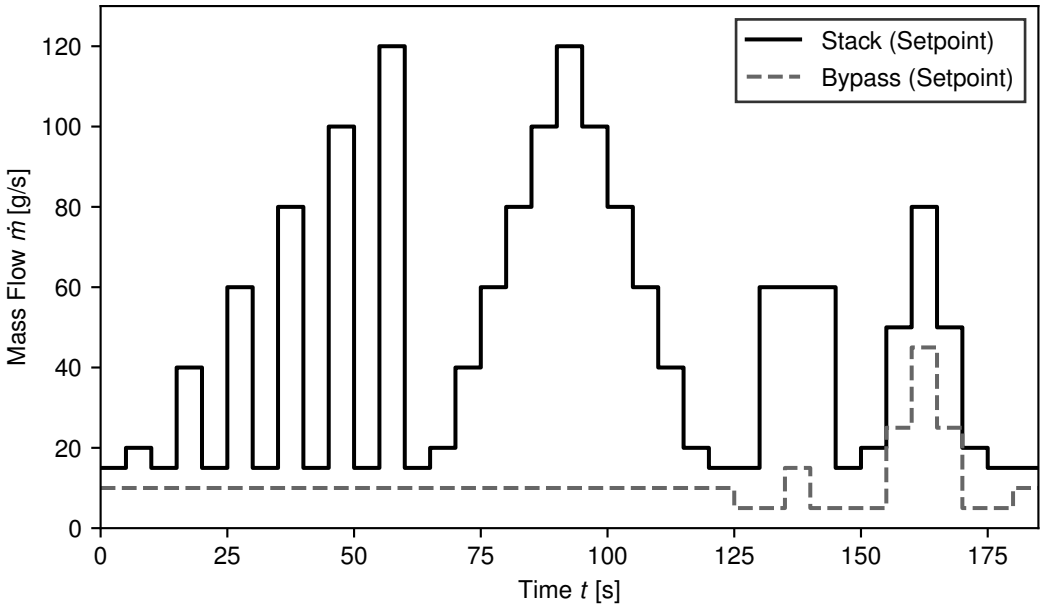

Figure 42: Setpoint sequence from [27] for comparing different parameterizations of the cost function *J*.

up to $t = 125\,\mathrm{s}$ were used to evaluate the air supply control part of the MPC. Then, the disturbance rejection capability was tested with the step changes between $t = 125\,\mathrm{s}$ and $t = 150\,\mathrm{s}$. In the last section of Figure 42, simultaneous step changes in $\dot{m}_{\mathrm{Ca}}^{\mathrm{in,sp}}$ and $\dot{m}_{\mathrm{Byp}}^{\mathrm{sp}}$ were applied to evaluate the MIMO characteristics of the proposed controller.

In the simulation study, different weights in $\boldsymbol{Q}$ and $\boldsymbol{R}$ were compared. The values were varied by a factor of ten, as shown in [9], [119], to have a slightly more systematic approach instead of the commonly mentioned trial-and-error [92], [93]. The comparison was conducted with a constant $N_y = 7$, $N_u = 2$, and $\boldsymbol{L}_{\mathrm{d}}$ from [27].

$$\boldsymbol{L}_{\mathrm{d}} = \begin{bmatrix} 0.05 & 0.05 & 0 & 0 & 0.1 & 0 \\ 0 & 0 & 0 & 0.05 & 0 & 0.15 \end{bmatrix}^T \tag{5.14}$$

The ratio of the weights in $\boldsymbol{Q}$ determined the prioritization of the two control tasks in the MPC. Three different weight matrices $\boldsymbol{Q}$ were compared with a constant $\boldsymbol{R} = \left[\begin{smallmatrix} 0.1 & 0 \\ 0 & 10 \end{smallmatrix}\right]$. Representative closed-loop simulation results for $\dot{m}_{\mathrm{Ca}}^{\mathrm{in}}$ and $\dot{m}_{\mathrm{Byp}}$ are shown in Figure 43. The variation of the weights in $\boldsymbol{Q}$ significantly impacted the closed-loop behavior. The prioritization of the air supply control task with higher weights in $\boldsymbol{Q}$ resulted in a faster response time of the air supply controller. Firstly, the control of $\dot{m}_{\mathrm{Byp}}$ was delayed after step changes. Secondly, the bypass valve was used to reduce $\dot{m}_{\mathrm{Ca}}^{\mathrm{in}}$ faster, even though this reduction increased the control deviation from $\dot{m}_{\mathrm{Byp}}^{\mathrm{sp}}$. The best dynamics were achieved with $\boldsymbol{Q} = \left[\begin{smallmatrix} 10 & 0 \\ 0 & 1 \end{smallmatrix}\right]$. These findings showed that the response time could not be reduced arbitrarily. Instead, it was most likely limited by the perturbation compensation with the observer. The dependence on the perturbation compensation was also indicated by the absence of significant over- and undershoots in $\dot{m}_{\mathrm{Ca}}^{\mathrm{in}}$ for $\boldsymbol{Q} = \left[\begin{smallmatrix} 10 & 0 \\ 0 & 1 \end{smallmatrix}\right]$. These over- and

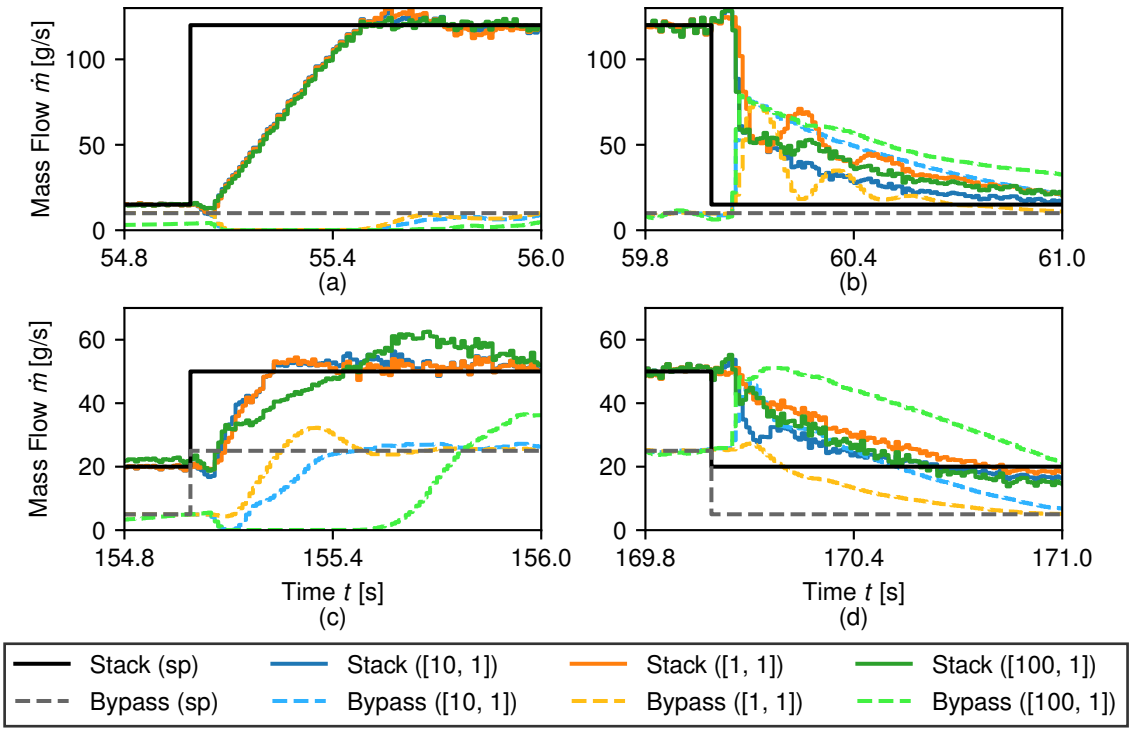

Figure 43: Air mass flows for closed-loop simulations of the implicit linear MPC with $N_y = 7$, $N_u = 2$, $\boldsymbol{R} = \left[\begin{smallmatrix} 0.1 & 0 \\ 0 & 10 \end{smallmatrix}\right]$, and $\boldsymbol{Q} = \left[\begin{smallmatrix} 10 & 0 \\ 0 & 1 \end{smallmatrix}\right]$, $\boldsymbol{Q} = \left[\begin{smallmatrix} 1 & 0 \\ 0 & 1 \end{smallmatrix}\right]$, or $\boldsymbol{Q} = \left[\begin{smallmatrix} 100 & 0 \\ 0 & 1 \end{smallmatrix}\right]$.

undershoots could only be avoided if the differences between the linear prediction model and the FCS were mostly compensated. As a result, the trajectories of the control variables were also smooth, as depicted in Figure 44. Moreover, smooth trajectories of $i_{q,\mathrm{Cmpr}}^{\mathrm{sp}}$ were beneficial to the superordinate power controller. P_{Cmpr} was the main perturbation in P_{FCS}, and its dynamics significantly depended on $i_{q,\mathrm{Cmpr}}$. Thus, fewer oscillations or over- and undershoots in $i_{q,\mathrm{Cmpr}}^{\mathrm{sp}}$ induced fewer perturbations on P_{FCS}. This reduction resulted in less power consumption of the fuel cell stack to compensate for the perturbations and, therefore, improved the FCS efficiency.

The dynamics of $i_{q,\mathrm{Cmpr}}^{\mathrm{sp}}$ were also affected by the first weight in $\boldsymbol{R}$. The next step was therefore to evaluate the effect of this weight. Three different factors of ten were used. Representative closed-loop simulation results for $\dot{m}_{\mathrm{Ca}}^{\mathrm{in}}$ and $\dot{m}_{\mathrm{Byp}}$ are shown in Figure 45. The results for $\boldsymbol{R} = \left[\begin{smallmatrix} 1 & 0 \\ 0 & 10 \end{smallmatrix}\right]$ indicated that high values for the first weight in $\boldsymbol{R}$ had to be avoided due to their impairment of the closed-loop dynamics. Nonetheless, the effect of smaller weights on the mass flows in the closed control loop was negligible. Instead, the variations were mainly visible for $i_{q,\mathrm{Cmpr}}$. The corresponding closed-loop simulation results for the control variables are displayed in Figure 46. These results confirmed that a small first weight in $\boldsymbol{R}$ was beneficial because it removed high-frequency oscillations in $i_{q,\mathrm{Cmpr}}^{\mathrm{sp}}$. Consequently, oscillations in P_{Cmpr} were avoided, which was advantageous for the superordinate FCS net power controller.

The final tuning parameter was the second weight in $\boldsymbol{R}$, which was varied again three times with different factors of ten. The resulting closed-loop values of $\dot{m}_{\mathrm{Ca}}^{\mathrm{in}}$ and $\dot{m}_{\mathrm{Byp}}$ for

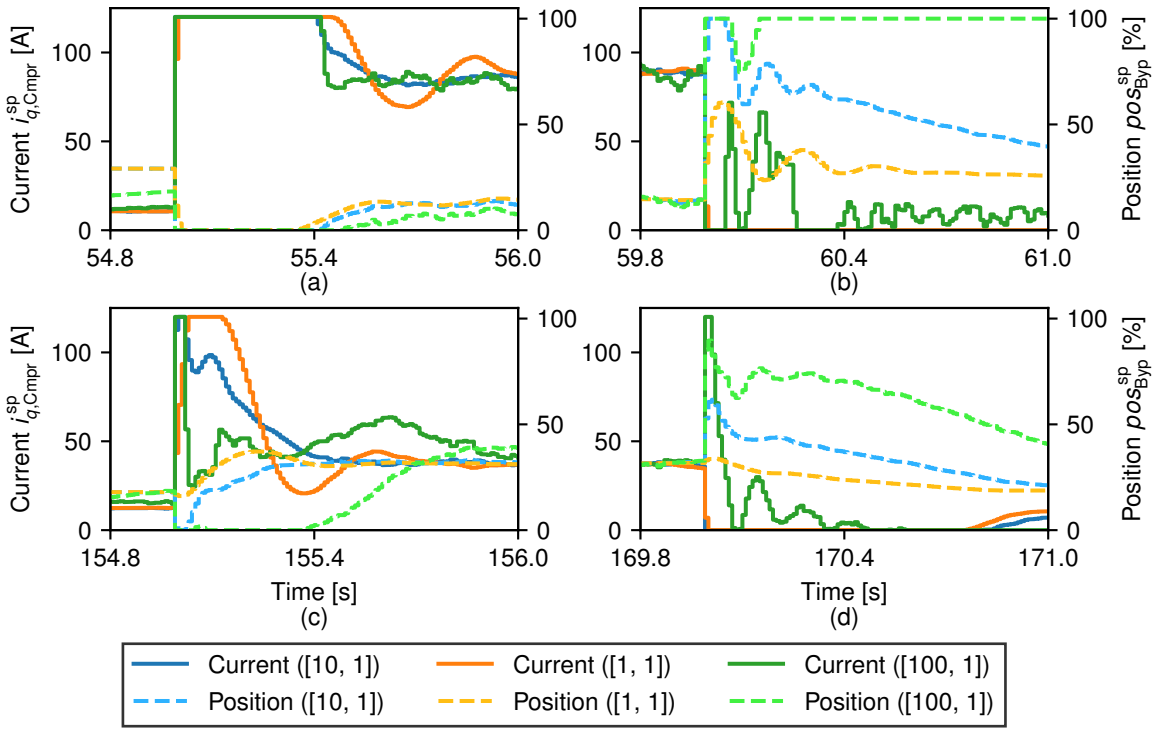

Figure 44: Control variables for closed-loop simulation results of the implicit linear MPC with $N_y = 7$, $N_u = 2$, $\boldsymbol{R} = \left[\begin{smallmatrix} 0.1 & 0 \\ 0 & 10 \end{smallmatrix}\right]$, and $\boldsymbol{Q} = \left[\begin{smallmatrix} 10 & 0 \\ 0 & 1 \end{smallmatrix}\right]$, $\boldsymbol{Q} = \left[\begin{smallmatrix} 1 & 0 \\ 0 & 1 \end{smallmatrix}\right]$, or $\boldsymbol{Q} = \left[\begin{smallmatrix} 100 & 0 \\ 0 & 1 \end{smallmatrix}\right]$.

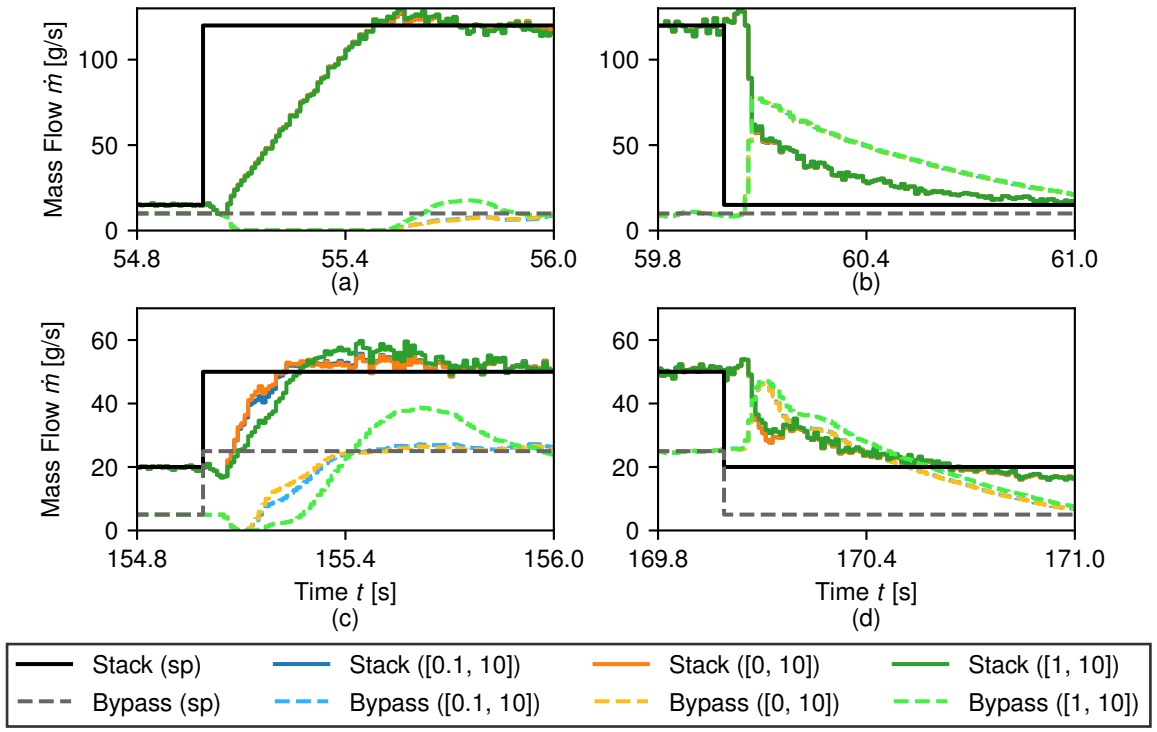

Figure 45: Air mass flows for closed-loop simulation results of the implicit linear MPC with $N_y = 7$, $N_u = 2$, $\boldsymbol{Q} = \left[\begin{smallmatrix} 10 & 0 \\ 0 & 1 \end{smallmatrix}\right]$, and $\boldsymbol{R} = \left[\begin{smallmatrix} 0.1 & 0 \\ 0 & 10 \end{smallmatrix}\right]$, $\boldsymbol{R} = \left[\begin{smallmatrix} 0 & 0 \\ 0 & 10 \end{smallmatrix}\right]$, or $\boldsymbol{R} = \left[\begin{smallmatrix} 1 & 0 \\ 0 & 10 \end{smallmatrix}\right]$.

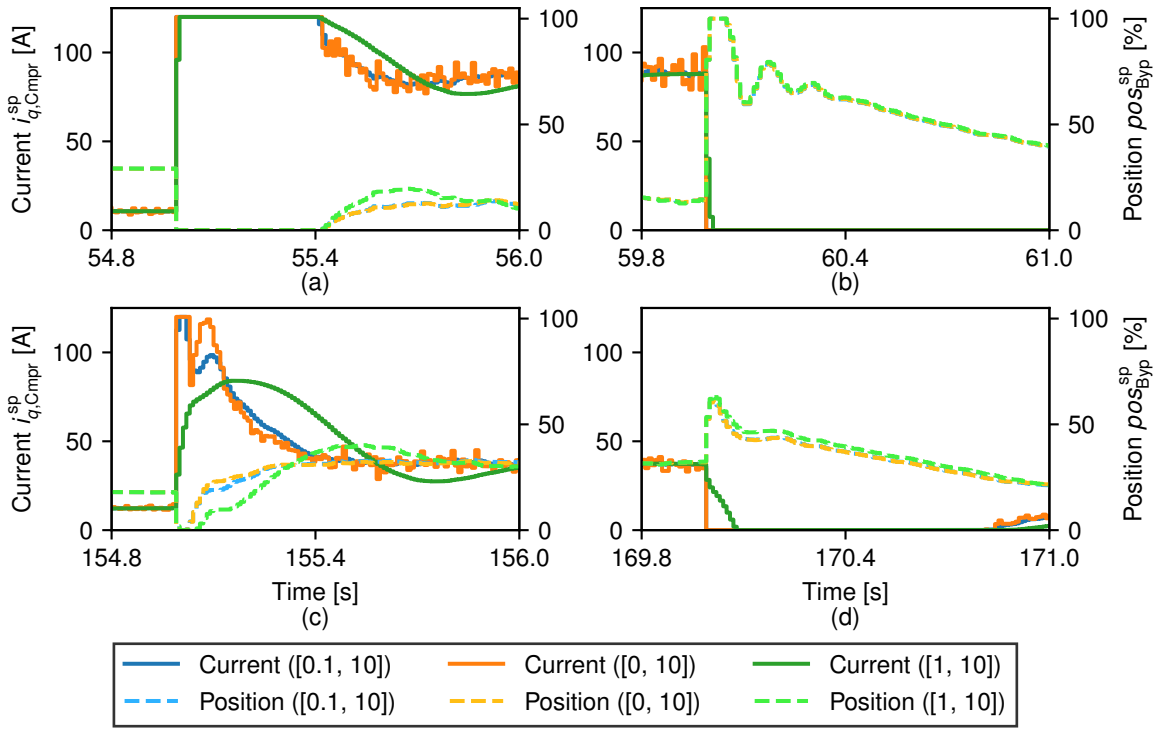

Figure 46: Control variables for closed-loop simulation results of the implicit linear MPC with $N_y = 7$, $N_u = 2$, $\boldsymbol{Q} = \left[\begin{smallmatrix} 10 & 0 \\ 0 & 1 \end{smallmatrix}\right]$, and $\boldsymbol{R} = \left[\begin{smallmatrix} 0.1 & 0 \\ 0 & 10 \end{smallmatrix}\right]$, $\boldsymbol{R} = \left[\begin{smallmatrix} 0 & 0 \\ 0 & 10 \end{smallmatrix}\right]$, or $\boldsymbol{R} = \left[\begin{smallmatrix} 1 & 0 \\ 0 & 10 \end{smallmatrix}\right]$.

four representative step changes are depicted in Figure 47. The differences in the closed-loop air mass flows for the three parameterizations of $\boldsymbol{R}$ were negligible. The decision for $\boldsymbol{R} = \left[\begin{smallmatrix} 0.1 & 0 \\ 0 & 10 \end{smallmatrix}\right]$ was based on the corresponding trajectories of the control variables. These trajectories are shown in Figure 48. The linear MPC with $\boldsymbol{R} = \left[\begin{smallmatrix} 0.1 & 0 \\ 0 & 10 \end{smallmatrix}\right]$ was the only one not inducing oscillations of $i^{\mathrm{sp}}_{q,\mathrm{Cmpr}}$. This parameterization, therefore, led to the best dynamic response of P_{Cmpr} for the superordinate FCS net power controller. Accordingly, the cost function with $N_y = 7$, $N_u = 2$, $\boldsymbol{Q} = \left[\begin{smallmatrix} 10 & 0 \\ 0 & 1 \end{smallmatrix}\right]$, and $\boldsymbol{R} = \left[\begin{smallmatrix} 0.1 & 0 \\ 0 & 10 \end{smallmatrix}\right]$ was used in this work and in [27].

5.5 Validation of Explicit Linear Model Predictive Controller on Fuel Cell System Test Stand

In this work, the explicit PWA solution $\boldsymbol{u}(\boldsymbol{\theta})$ for the linear MPC was determined with the MPT toolbox by M. Herceg *et al.* [76]. According to [11], this solution perfectly replicates the implicit linear MPC of Section 5.4, which is why an additional validation of $\boldsymbol{u}(\boldsymbol{\theta})$ was not necessary for this work. Instead, the first closed-loop measurements were used to validate that the findings from the simulation study of Section 5.4 were transferable to the FCS test stand. The corresponding comparison is summarized in Section 5.5.1. Afterward, variations in $\boldsymbol{L}_{\mathrm{d}}$ were compared to confirm the choices for the observer gains in [27]. The associated measurements are outlined in Section 5.5.2.

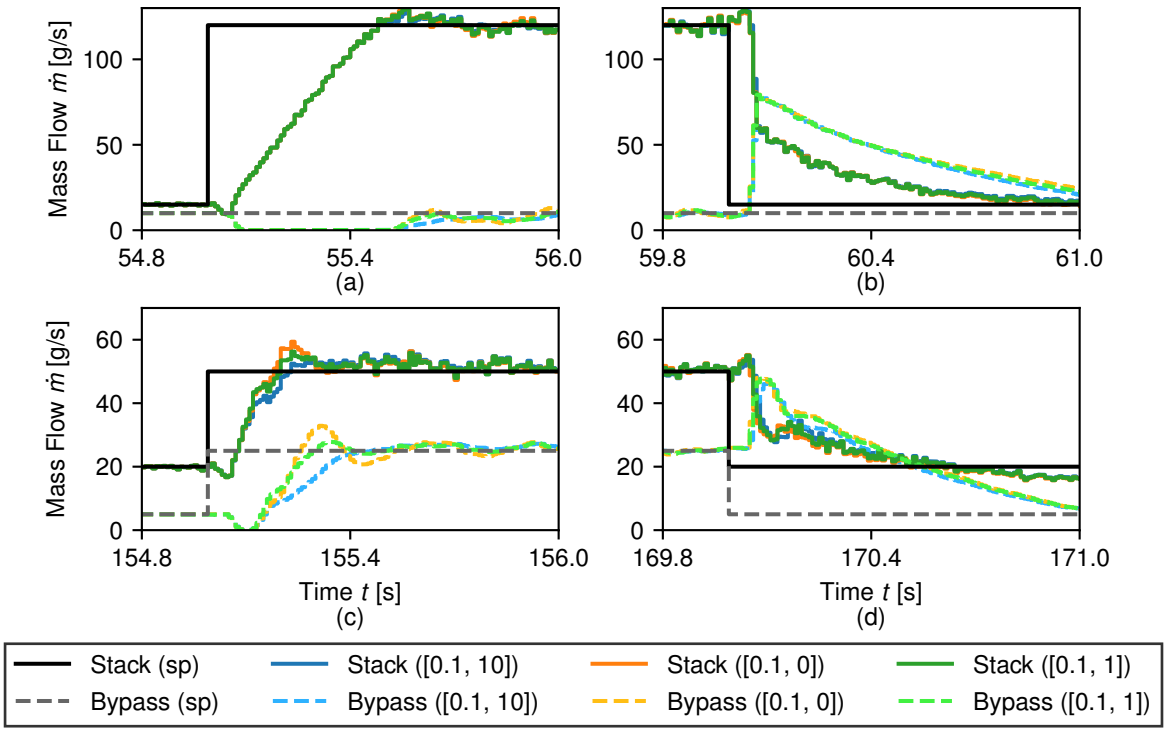

Figure 47: Air mass flows for closed-loop simulation results of the implicit linear MPC with $N_y = 7$, $N_u = 2$, $\boldsymbol{Q} = \left[\begin{smallmatrix} 10 & 0 \\ 0 & 1 \end{smallmatrix}\right]$, and $\boldsymbol{R} = \left[\begin{smallmatrix} 0.1 & 0 \\ 0 & 10 \end{smallmatrix}\right]$, $\boldsymbol{R} = \left[\begin{smallmatrix} 0.1 & 0 \\ 0 & 0 \end{smallmatrix}\right]$, or $\boldsymbol{R} = \left[\begin{smallmatrix} 0.1 & 0 \\ 0 & 1 \end{smallmatrix}\right]$.

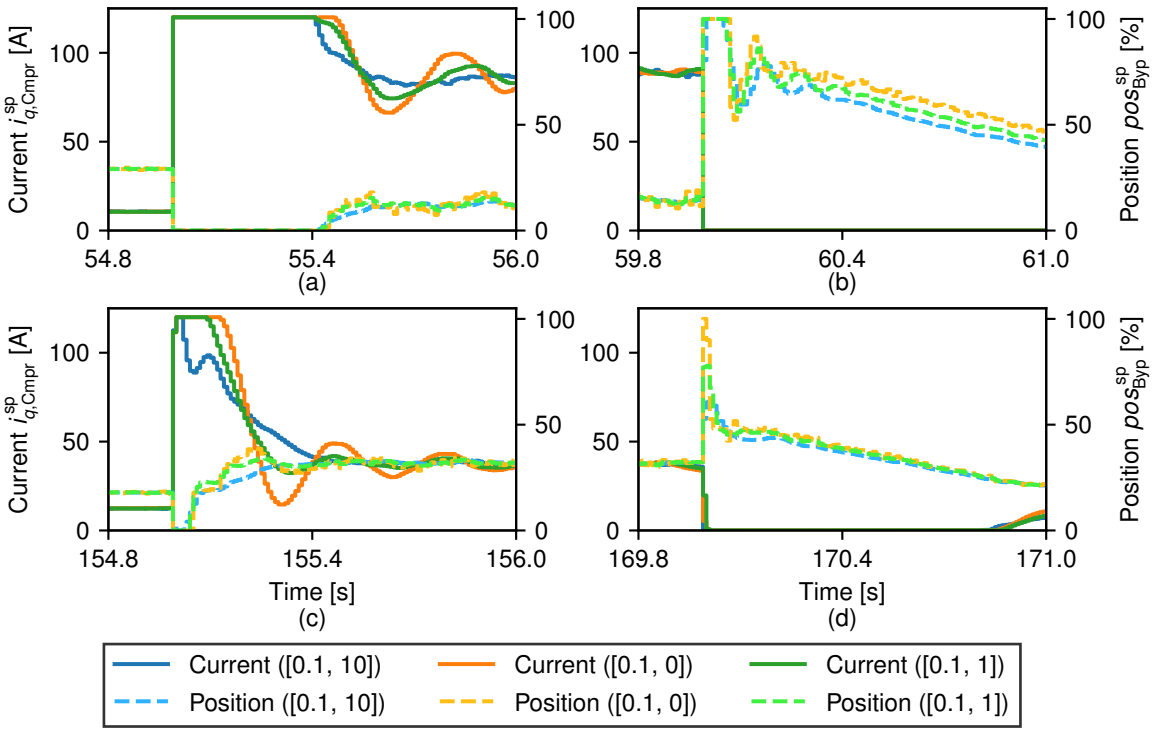

Figure 48: Control variables for closed-loop simulation results of the implicit linear MPC with $N_y = 7$, $N_u = 2$, $\boldsymbol{Q} = \left[\begin{smallmatrix} 10 & 0 \\ 0 & 1 \end{smallmatrix}\right]$, and $\boldsymbol{R} = \left[\begin{smallmatrix} 0.1 & 0 \\ 0 & 10 \end{smallmatrix}\right]$, $\boldsymbol{R} = \left[\begin{smallmatrix} 0.1 & 0 \\ 0 & 0 \end{smallmatrix}\right]$, or $\boldsymbol{R} = \left[\begin{smallmatrix} 0.1 & 0 \\ 0 & 1 \end{smallmatrix}\right]$.

Lastly, the explicit linear MPC was integrated into the control cascade of Figure 3. The corresponding closed-loop behavior is shown in Section 5.5.3. This final validation step on the FCS test stand was the prerequisite for the final application in the BMW iX5 Hydrogen presented in [27].

5.5.1 Comparison of Closed-Loop Behavior between Simulation and FCS Test Stand

The comparison of the closed-loop behavior for the simulation and the FCS test stand measurement was conducted with the setpoint trajectories of Figure 42. The resulting air mass flows for four representative step changes are shown in Figure 49. The closed-loop

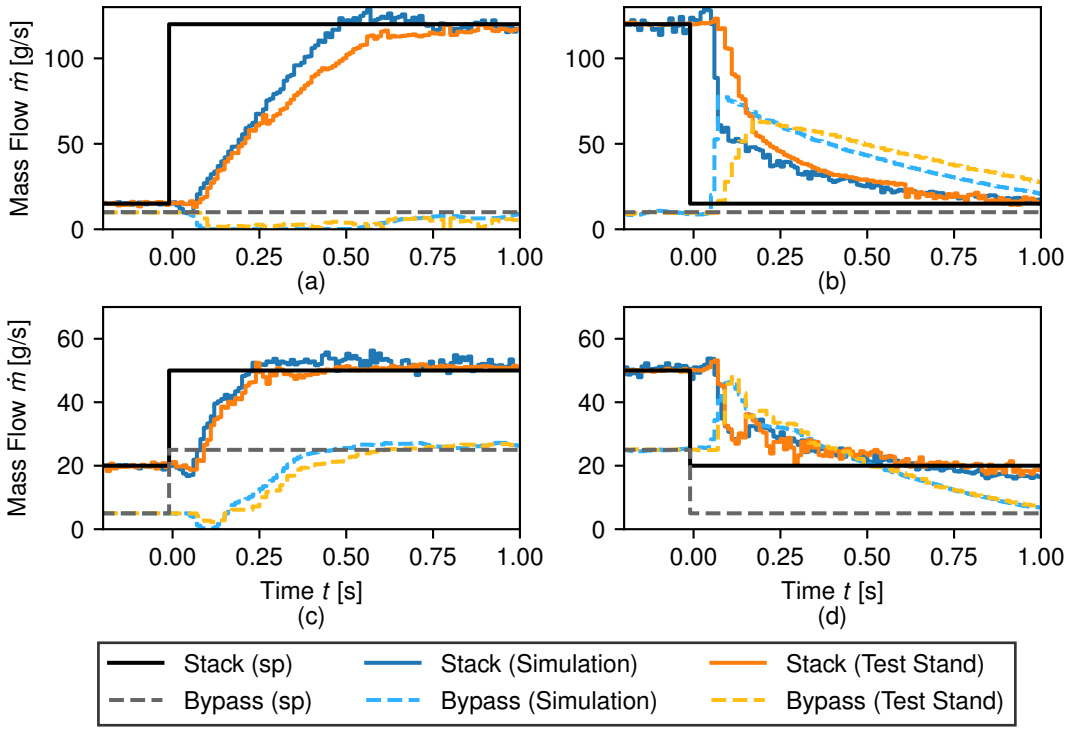

Figure 49: Air mass flows for closed-loop simulation results and test stand measurements of the linear MPC with $N_y = 7$, $N_u = 2$, $\boldsymbol{Q} = \left[\begin{smallmatrix} 10 & 0 \\ 0 & 1 \end{smallmatrix}\right]$, $\boldsymbol{R} = \left[\begin{smallmatrix} 0.1 & 0 \\ 0 & 10 \end{smallmatrix}\right]$, and $\boldsymbol{L}_\mathrm{d} = \left[\begin{smallmatrix} 0.05 & 0.05 & 0 & 0 & 0.1 & 0 \\ 0 & 0 & 0 & 0.05 & 0 & 0.15 \end{smallmatrix}\right]^\mathsf{T}$.

air mass flow dynamics on the FCS test stand were almost identical to the dynamics in the simulation. The two notable differences in Figure 49a) and b) indicated simulation model inaccuracies because the corresponding control variable trajectories in Figure 50 were almost alike for the simulation and the FCS test stand. Firstly, $\dot{m}_\mathrm{Ca}^\mathrm{in}$ rose faster in the simulation (Fig. 49a)), even though the compressor was accelerated with the maximum available torque with $I_{q,\mathrm{Cmpr}} = 120\,\mathrm{A}$ in the simulation and in the FCS test stand measurement. This deviation was partly caused by the bypass leakage in the FCS test stand measurement that led to a reduction of $\dot{m}_\mathrm{Ca}^\mathrm{in}$. Additionally, the small dip in the measured values of $\dot{m}_\mathrm{Ca}^\mathrm{in}$ at $t = 0.25\,\mathrm{s}$ was caused by the ECU switching from

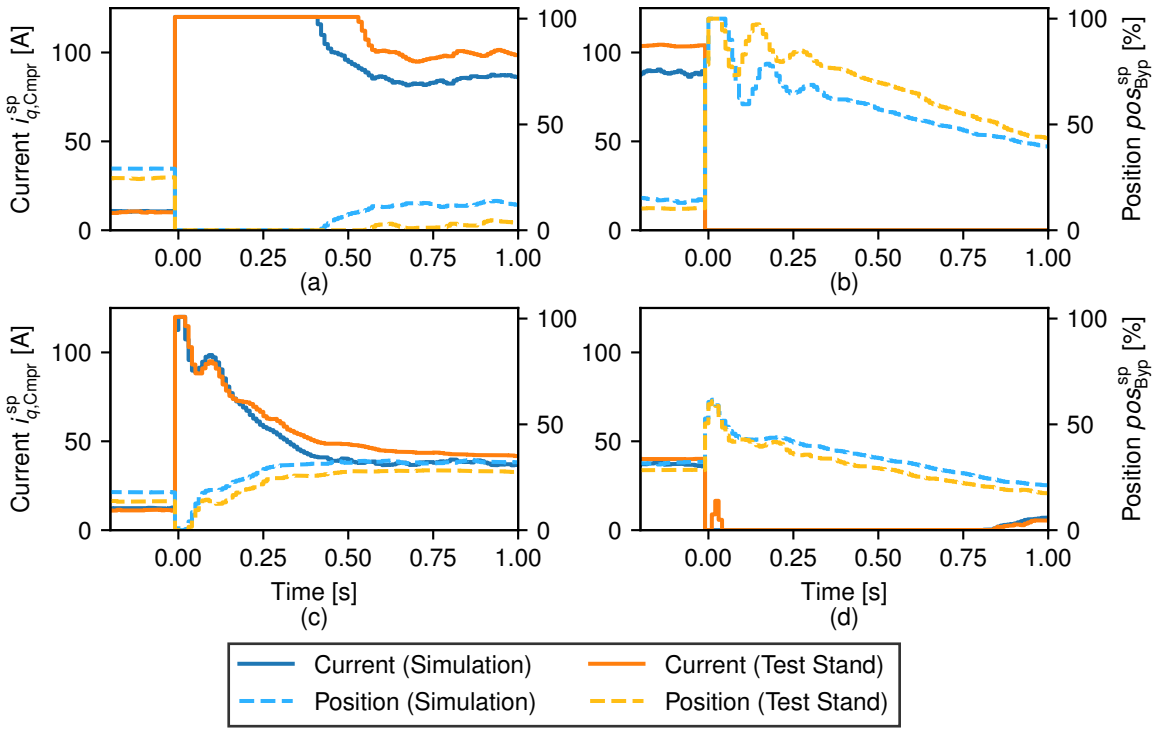

Figure 50: Control variables for closed-loop simulation results and test stand measurements of the linear MPC with $N_y = 7$, $N_u = 2$, $\boldsymbol{Q} = \left[\begin{smallmatrix} 10 & 0 \\ 0 & 1 \end{smallmatrix}\right]$, $\boldsymbol{R} = \left[\begin{smallmatrix} 0.1 & 0 \\ 0 & 10 \end{smallmatrix}\right]$, and $\boldsymbol{L}_{\mathrm{d}} = \left[\begin{smallmatrix} 0.05 & 0.05 & 0 & 0 & 0.1 & 0 \\ 0 & 0 & 0 & 0.05 & 0 & 0.15 \end{smallmatrix}\right]^{\mathsf{T}}$.

the sensor value to the model value for $\dot{m}_{\mathrm{AirFil}}^{\mathrm{meas}}$ as described in [26]. This model value for $\dot{m}_{\mathrm{AirFil}}^{\mathrm{meas}}$ was slightly smaller than the sensor value during the step change, which is why $\dot{m}_{\mathrm{Ca}}^{\mathrm{in}}$ was also smaller in the FCS test stand measurement.

Secondly, $\dot{m}_{\mathrm{Ca}}^{\mathrm{in}}$ fell faster in the simulation (Fig. 49b)) despite equal values for the control variables. This inconsistency must have resulted from a delayed sensor signal for $\dot{m}_{\mathrm{Byp}}$, since the values of pos_{Byp} were approximately the same in the simulation and the FCS test stand measurement.

Despite these slight differences, the overall accordance of the closed-loop behavior for the simulation and the test stand measurement was sufficient to continue the validation with $N_y = 7$, $N_u = 2$, $\boldsymbol{Q} = \left[\begin{smallmatrix} 10 & 0 \\ 0 & 1 \end{smallmatrix}\right]$, and $\boldsymbol{R} = \left[\begin{smallmatrix} 0.1 & 0 \\ 0 & 10 \end{smallmatrix}\right]$ without further cost function parameter adjustments on the FCS test stand.

5.5.2 Variation of Observer Gains

The cost function parameters $\boldsymbol{Q}$, $\boldsymbol{R}$, N_y, and N_u could only be changed before determining the explicit solution $\boldsymbol{u}(\boldsymbol{\theta})$. During the operation on the FCS test stand and in the FCEV, the remaining MPC tuning parameters were the observer gains in $\boldsymbol{L}_{\mathrm{d}}$. Thus, the influence of changing values in $\boldsymbol{L}_{\mathrm{d}}$ was investigated next. Three different parameterizations were evaluated on the FCS test stand. The most significant differences in the closed-loop behavior of the air mass flows are shown in Figures 51.

The first findings were that the neglection of the observer gain for x_2 with the third

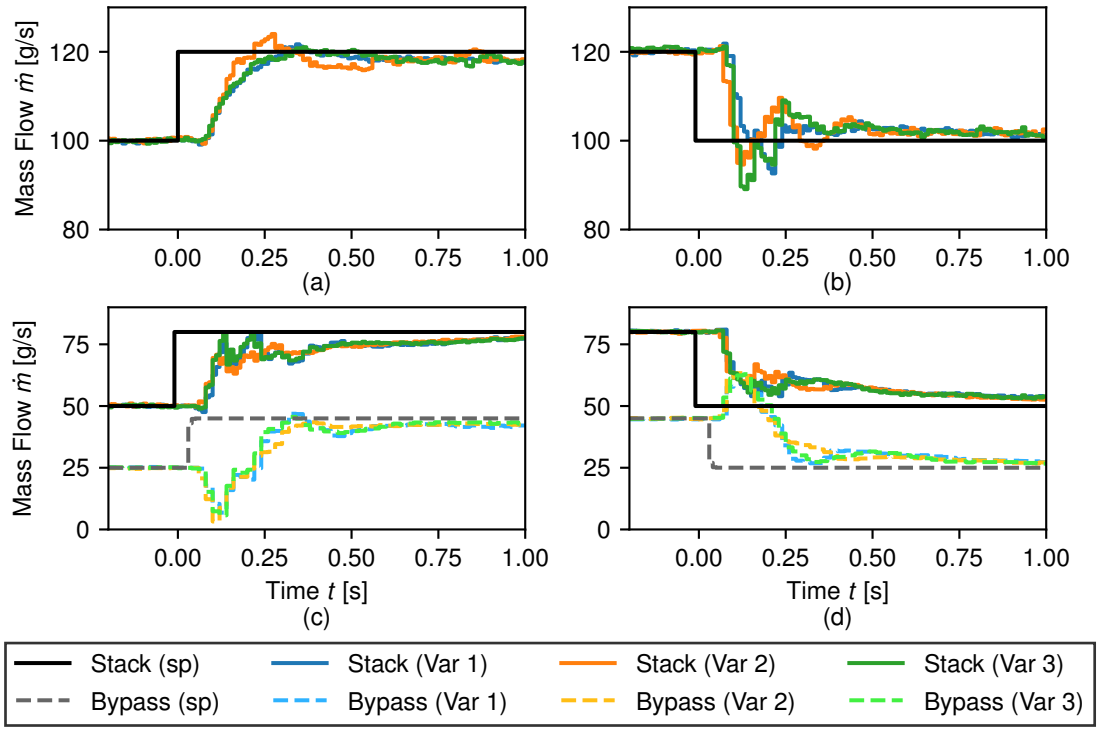

Figure 51: Air mass flows for closed-loop test stand measurements of the explicit linear MPC with $\boldsymbol{L}_\mathrm{d} = \left[\begin{smallmatrix} 0.05 & 0.05 & 0 & 0 & 0.1 & 0 \\ 0 & 0 & 0 & 0.05 & 0 & 0.15 \end{smallmatrix}\right]^T$ (Var 1), $\boldsymbol{L}_\mathrm{d} = \left[\begin{smallmatrix} 0.05 & 0.05 & 0 & 0 & 0.1 & 0 \\ 0 & 0 & 0 & 0.1 & 0 & 0.15 \end{smallmatrix}\right]^T$ (Var 2), and $\boldsymbol{L}_\mathrm{d} = \left[\begin{smallmatrix} 0.05 & 0 & 0 & 0 & 0.1 & 0 \\ 0 & 0 & 0 & 0.05 & 0 & 0.15 \end{smallmatrix}\right]^T$ (Var 3).

variant caused a significant undershoot in $\dot{m}_\mathrm{Ca}^\mathrm{in}$ in Figure 51. This undershoot had to be reduced to avoid oxygen starvation in the fuel cells. Similarly, a higher observer gain for x_4 with the second variant led to an undesirably aggressive MPC with considerable under- and overshoots of $\dot{m}_\mathrm{Ca}^\mathrm{in}$. This aggressive closed-loop behavior was also visible in the corresponding trajectories of the control variables displayed in Figure 52. The disadvantage of the oscillations of $i_{q,\mathrm{Cmpr}}^\mathrm{sp}$ in Figure 52a) and c) was their direct impact on the dynamic behavior of P_Cmpr. As mentioned before, P_Cmpr was the primary perturbation of the FCS net power controller. Fewer oscillations of P_Cmpr thus enabled a better perturbation compensation that further culminated in a better power response of the FCS. As a result, the original parameterization $\boldsymbol{L}_\mathrm{d} = \left[\begin{smallmatrix} 0.05 & 0.05 & 0 & 0 & 0.1 & 0 \\ 0 & 0 & 0 & 0.05 & 0 & 0.15 \end{smallmatrix}\right]^T$ was retained for the remainder of this work for the explicit linear MPC.

5.5.3 Validation in Combination with Fuel Cell System Net Power and Hydrogen Dilution Controller

The previous validation steps for the explicit linear MPC were conducted with a given profile of step changes for $\dot{m}_\mathrm{Ca}^\mathrm{in,sp}$ and $\dot{m}_\mathrm{Byp}^\mathrm{sp}$. In the target application in the FCEV, however, the values for $\dot{m}_\mathrm{Ca}^\mathrm{in,sp}$ and $\dot{m}_\mathrm{Byp}^\mathrm{sp}$ were given by the power and hydrogen dilution controller. Thus, the final validation step on the FCS test stand was the integration

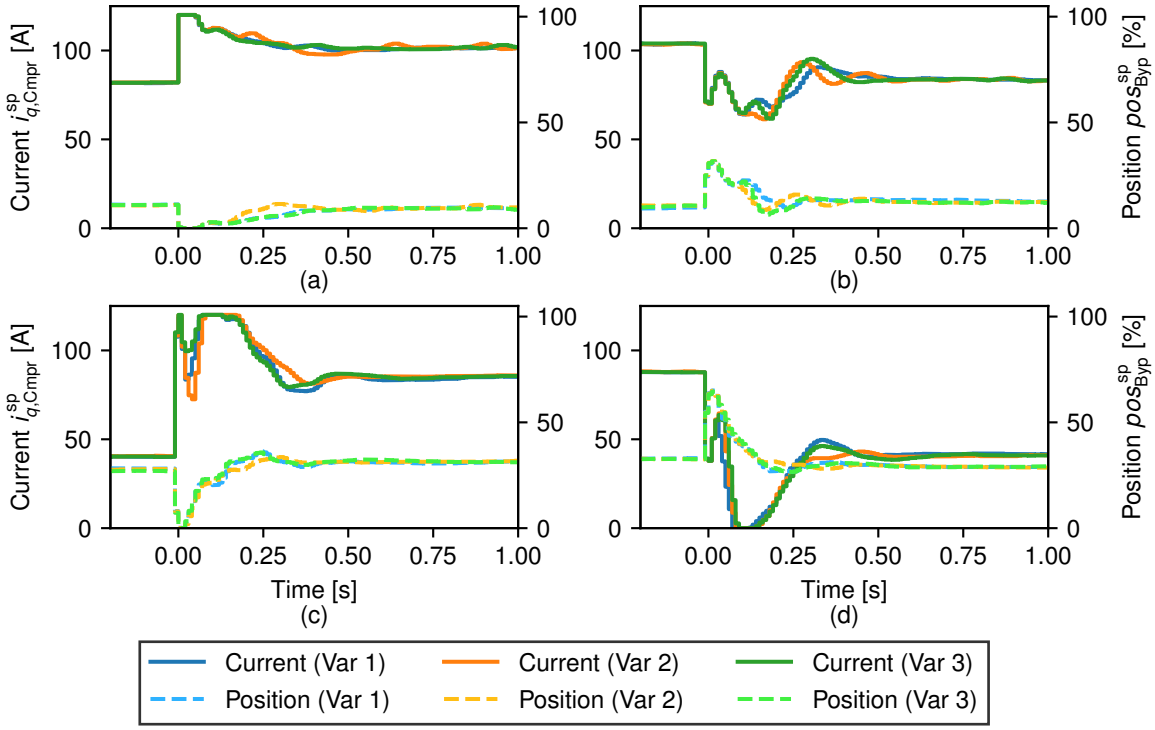

Figure 52: Control variables for closed-loop test stand measurements of the explicit linear MPC with $\boldsymbol{L}_\mathrm{d} = \begin{bmatrix} 0.05 & 0.05 & 0 & 0 & 0.1 & 0 \\ 0 & 0 & 0 & 0.05 & 0 & 0.15 \end{bmatrix}^T$ (Var 1), $\boldsymbol{L}_\mathrm{d} = \begin{bmatrix} 0.05 & 0.05 & 0 & 0 & 0.1 & 0 \\ 0 & 0 & 0 & 0.1 & 0 & 0.15 \end{bmatrix}^T$ (Var 2), and $\boldsymbol{L}_\mathrm{d} = \begin{bmatrix} 0.05 & 0 & 0 & 0 & 0.1 & 0 \\ 0 & 0 & 0 & 0.05 & 0 & 0.15 \end{bmatrix}^T$ (Var 3).

of the explicit linear MPC into the controller cascade of Figure 3. Then, the resulting closed-loop behavior was evaluated with the step changes of $P^\mathrm{sp}_\mathrm{FCS}$ depicted in Figure 53. The corresponding values of $\dot{m}^\mathrm{in,sp}_\mathrm{Ca}$ and $\dot{m}^\mathrm{sp}_\mathrm{Byp}$ are also displayed because they were not fixed for the given profile of $P^\mathrm{sp}_\mathrm{FCS}$. Instead, $\dot{m}^\mathrm{in,sp}_\mathrm{Ca}$ and $\dot{m}^\mathrm{sp}_\mathrm{Byp}$ depended on the closed-loop behavior of the FCS, which differed for each utilized air supply and bypass controller. This closed-loop behavior was decisively represented by the values of the air mass flows and the control variables. For the explicit linear MPC, these values are shown for two exemplary step changes in Figures 54 and 55. The main difference between the previously applied step changes and Figures 49 and 50 was the setpoint $\dot{m}^\mathrm{sp}_\mathrm{Byp} = 0\,\frac{\mathrm{g}}{\mathrm{s}}$. This setpoint was given by the hydrogen dilution controller for high values of $\dot{m}^\mathrm{in}_\mathrm{Ca}$ sufficient for the hydrogen dilution in the air exhaust. As a result, $pos^\mathrm{sp}_\mathrm{Byp} = 0\,\%$ was the second output of the explicit linear MPC. However, the valve controller could not keep the bypass valve fully shut, especially for high compressor outlet pressures and mass flows. This bypass leakage is highlighted in Figure 56 with a comparison of $pos^\mathrm{sp}_\mathrm{Byp}$ and the measured value of pos_Byp. The bypass leakage induced an additional disturbance for the explicit linear MPC leading to a decrease in $\dot{m}^\mathrm{in}_\mathrm{Ca}$. The explicit linear MPC could only compensate for this disturbance with $i^\mathrm{sp}_{q,\mathrm{Cmpr}}$, since $pos^\mathrm{sp}_\mathrm{Byp}$ was already at its lower bound. Although the compensation was necessary, it resulted in the undesirable oscillations of $i^\mathrm{sp}_{q,\mathrm{Cmpr}}$ displayed in Figure 54. These oscillations further caused oscillations in P_Cmpr, which were significant enough to affect P_FCS, as shown in Figure 57. The oscillations of $i^\mathrm{sp}_{q,\mathrm{Cmpr}}$ could be reduced by decreasing the values in $\boldsymbol{L}_\mathrm{d}$. However, the high stationary

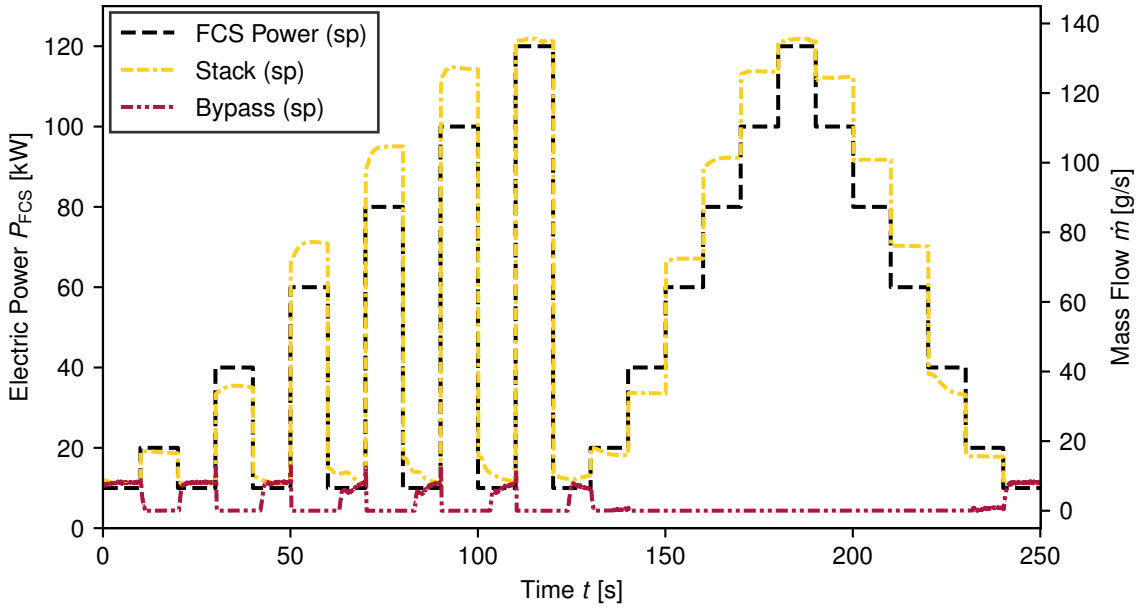

Figure 53: Step changes of P_{FCS}^{sp} for the validation of the explicit linear MPC in the FCS net power and hydrogen dilution control cascade with the corresponding values of $\dot{m}_{Ca}^{in,sp}$ and $\dot{m}_{Byp}^{sp}$.

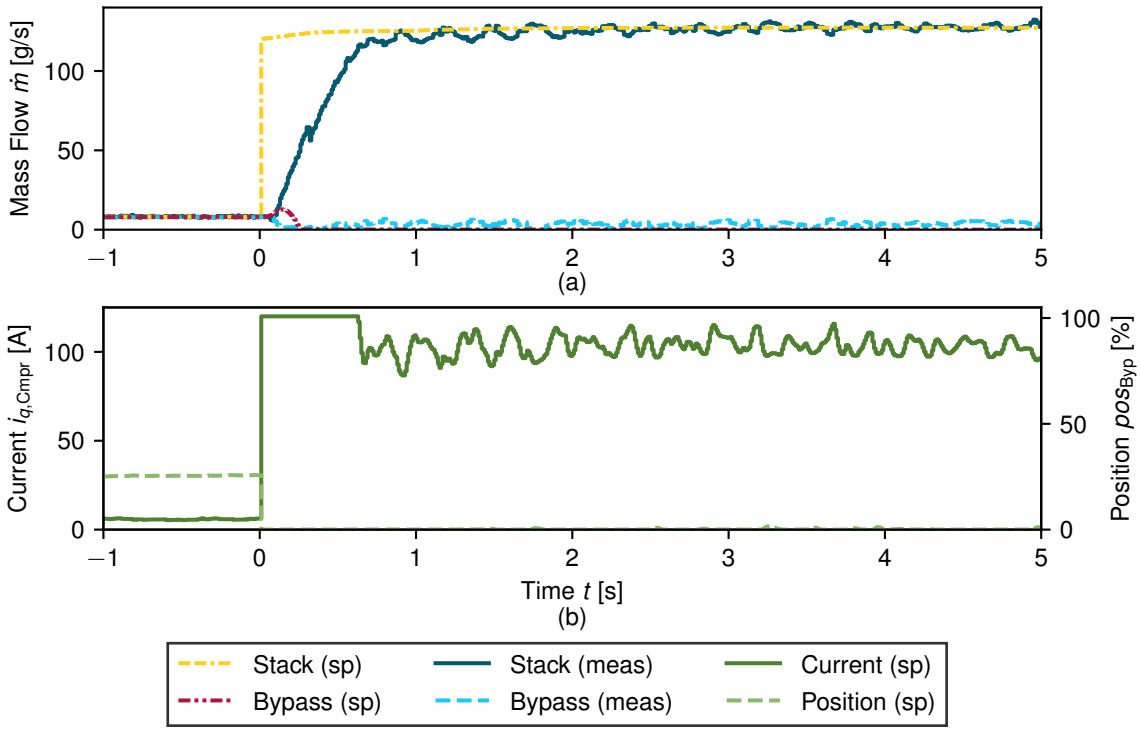

Figure 54: Measured air mass flows and control variables in the closed control loop with the explicit linear MPC and on the FCS test stand for the step change from $P_{FCS}^{sp} = 10\,\text{kW}$ to $P_{FCS}^{sp} = 100\,\text{kW}$.

deviations between the linear prediction model and the actual FCS (see Fig. 41) led to a high dependency on the perturbation compensation. Consequently, high observer

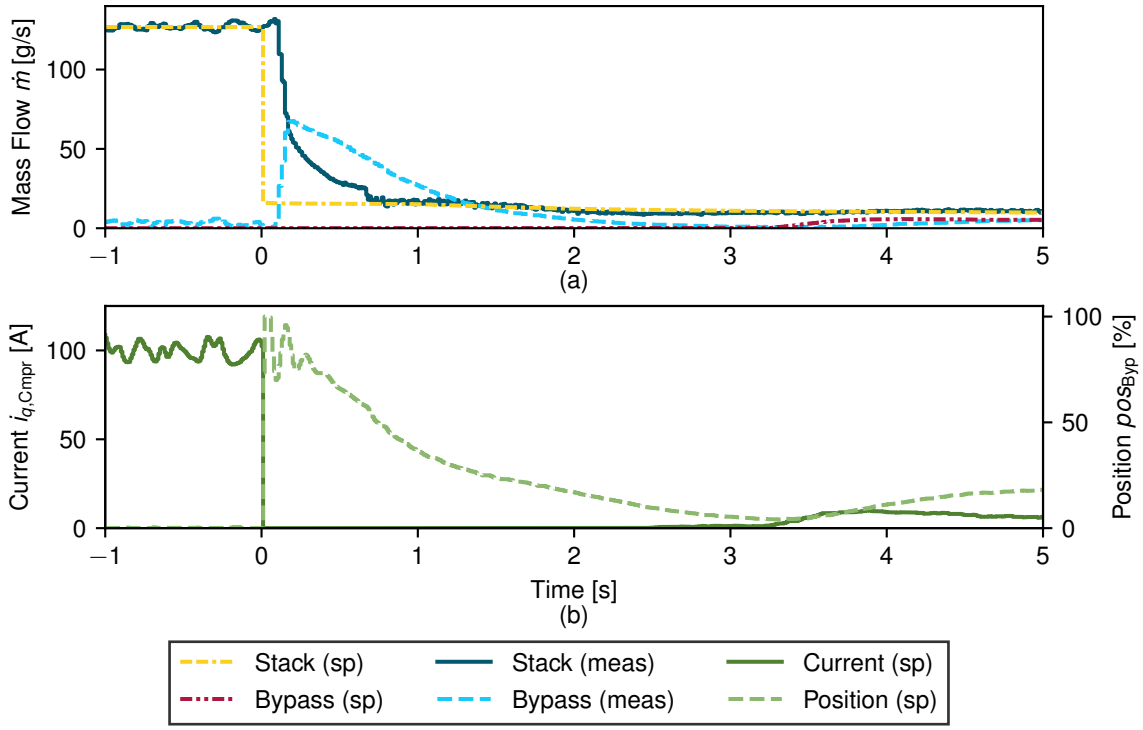

Figure 55: Measured air mass flows and control variables in the closed control loop with the explicit linear MPC and on the FCS test stand for the step change from $P_{FCS}^{sp} = 100\,\text{kW}$ to $P_{FCS}^{sp} = 10\,\text{kW}$.

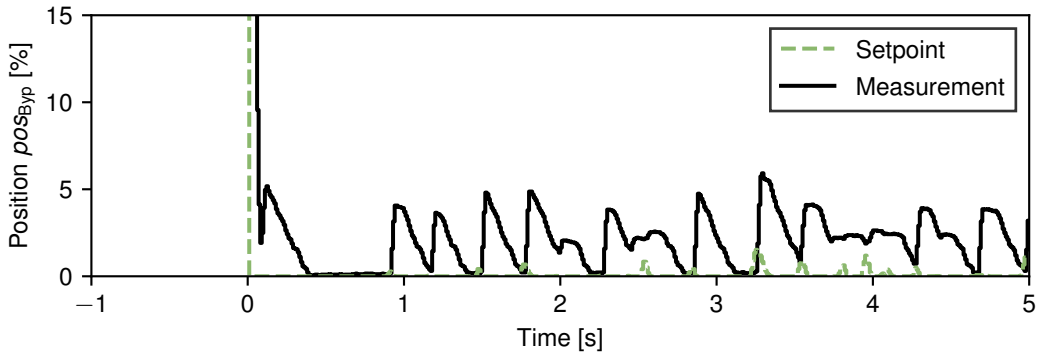

Figure 56: Leakage of the cathode bypass valve for high compressor outlet pressures and air mass flows.

gains were necessary to achieve a fast perturbation compensation, which contradicts the approach to filter the bypass leakage with small observer gains. This deficiency of the explicit linear MPC was the motivation for applying an explicit NMPC, introduced in Chapter 6. A more precise model decreased the dependency on the perturbations $\hat{\boldsymbol{d}}$. Thus, smaller observer gains allowed a similar closed-loop behavior with a better compensation of the bypass leakage.

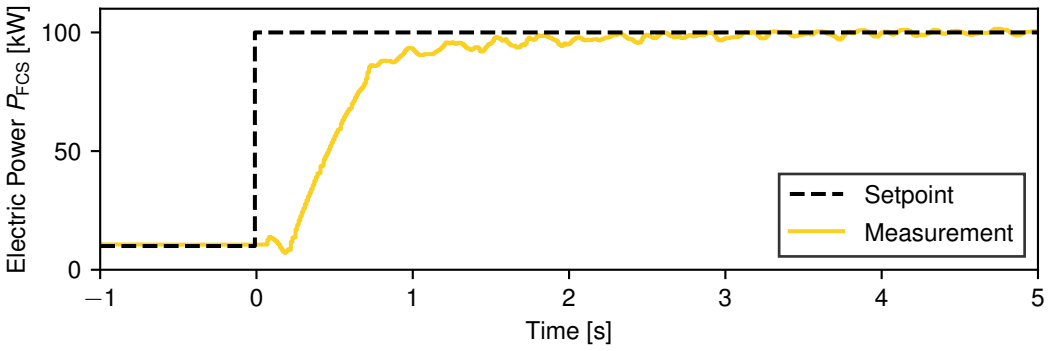

Figure 57: Oscillations in P_{FCS} due to the cathode bypass leakage.

6 Air Mass Flow Control with Explicit Nonlinear Model Predictive Control

The main advantage of NMPC is the possibility of utilizing a more precise nonlinear prediction model of the cathode subsystem. In this work, the prediction model was based on the simulation model of Chapter 4, with the additional simplifications described in Section 6.1. On the downside, the online application of an NLP solver was prevented by the limited computational capacity of the ECU and the relatively small sample time $\Delta t = 10\,\mathrm{ms}$. Moreover, geometric approaches for the explicit solution of the NMPC optimization problem (e.g., [54]) scale poorly with the problem size. Thus, $\boldsymbol{u}(\boldsymbol{\theta})$ was approximated by a NN.

Several control approaches have been reported in the literature that apply NNs to an FCS. Most of these approaches were summarized in the recently published review of Lin-Kwong-Chon *et al.* [67]. Extensive information on the control of an FCS with the help of NNs is found in this study, with a lack of experimental validation being one of the authors' conclusions. This research gap was addressed with parts of this work, as the NN approximation of the explicit NMPC was validated on an FCS test stand and in the BMW iX5 Hydrogen.

Even though an extensive list of studies on NN control in fuel cell systems is found in [67], some works are also summarized here to highlight the main approaches. Almeida *et al.* [2] utilized NNs to model and control the FCS. The NN model was further required for the online application of the proposed controller to provide feedback on the state of the FCS, similar to an observer in MPC. The NN controller was trained using a quadratic cost function for the control deviation and the control effort, comparable to MPC. The considered control task was the regulation of U_{Cell} with the partial pressures of oxygen and hydrogen. This approach was validated with a simulation in which the NN controller was successfully compared to a PID controller. Another NN controller was introduced by El-Sharkh *et al.* [104]. The proposed controller regulated the DC/AC inverter voltage and the reactive power output of an FCS. The authors used step responses of a system model alongside actual load profiles as training data. The approach was again only validated in a simulation. The same system setup and the same controlled variables were utilized in the work of Hatti *et al.* [42]. The authors applied NNs for modeling and controlling the system, with PI controllers employed to train the NN controller. Once again, the validation was conducted in a simulation. A combination of MPC and NNs for the control of an FCS was demonstrated by Bao *et al.* [8], [9]. In this study, the NN was the prediction model of the MPC. The control targets included λ_{O_2}, $p_{\mathrm{Ca}}^{\mathrm{in}}$, and the pressure difference between the anode and the cathode. Again, the approach was

validated in a simulation. Experimental validation was found in the work of Damour *et al.* [18]. The authors used a NN to obtain a real-time capable model of the FCS, which could be used in an online optimizer. The goal of the optimizer was to obtain the optimal parameters for the implemented PID controller for λ_{O_2}. The downside of this approach was the relatively large sample time $\Delta t = 3\,\mathrm{s}$ that rendered it infeasible for automotive applications. Instead of an online optimizer, Li *et al.* [65] used a NN to obtain the optimal PI controller parameters during operation. The control target was the feed air mass flow, and the approach was again only validated in a simulation. Therefore, the goal of this work was to experimentally demonstrate the applicability of approximating explicit NMPC using a NN for an FCS with an appropriate sample time $\Delta t = 10\,\mathrm{ms}$ for automotive applications.

In this work, a semi-empirical prediction model was applied for NMPC. This model is presented in Section 6.1 alongside the additional simplifications compared to the simulation model of Chapter 4. The model description is followed by an overview of the state and perturbation observer in Section 6.2 and the quadratic cost function in Section 6.3. The initial parameter values for the observer gains and the cost function weights were established with a simulation study. The main results of this study are summarized in Section 6.4. Subsequently, various training data sets were derived from the implicit NMPC and used to train many NNs with different setups. The two most accurate NNs from Section 6.5 were implemented on the ECU and tested on the FCS test stand. The main findings of this step are displayed in Section 6.6. Lastly, the proposed NN controller was validated in the BMW iX5 Hydrogen. This final validation step is shown in Section 6.7.

6.1 Nonlinear Prediction Model

A suitable nonlinear prediction model correctly predicts the dynamics and accurately approximates the stationary operating points of the controlled variables $\boldsymbol{y} = [\dot{m}^{\mathrm{in}}_{\mathrm{Ca}},\, \dot{m}_{\mathrm{Byp}}]^T$ subject to the control variables $\boldsymbol{u} = \left[i^{\mathrm{sp}}_{q,\mathrm{Cmpr}},\, pos^{\mathrm{sp}}_{\mathrm{Byp}}\right]^T$ of the considered plant. These two goals were achieved by the cathode subsystem simulation model presented in Chapter 4. However, the computational load and the numerical complexity were not a limiting factor for the simulation model. Firstly, the simulation model was not required to be real-time capable. Secondly, the simulation model was implemented in MATLAB Simulink. Therefore, the variable-step, variable-order solver ode15s was applied, which is better for numerically stiff problems. By contrast, the application of the observer on the ECU required a real-time capable prediction model. Furthermore, the implementation on the ECU only permitted a simple forward Euler with $\Delta t = 10\,\mathrm{ms}$ for the solution of the ODEs.

$$\boldsymbol{x}\,(k+1) = \boldsymbol{x}\,(k) + \Delta t \cdot \boldsymbol{f}\,(\boldsymbol{x}\,(k)\,, \boldsymbol{u}\,(k)) \tag{6.1}$$

A considerable disadvantage of the forward Euler is the numerical instability of stiff ODEs [56]. Hence, the simulation model was simplified before being employed as the nonlinear prediction model for the NMPC.

6.1.1 Model Equations

At the start, the numerical complexity was addressed. The first modification was reducing the number of model states in $\boldsymbol{x}$ by removing the cathode inlet and outlet manifolds as well as the turbine outlet manifold. On the one hand, this modification reduced the number of ODEs to five, one for each element of $\boldsymbol{x} = \left[i_{q,\mathrm{Cmpr}},\, \omega_{\mathrm{Cmpr}},\, pos_{\mathrm{Byp}},\, p^{\mathrm{out}}_{\mathrm{Cmpr}},\, p^{\mathrm{in}}_{\mathrm{Trb}}\right]^T$. On the other hand, the mass flow correlations with the smallest pressure losses were removed, namely $\dot{m}^{\mathrm{dry}}_{\mathrm{Hmdf}}$, $\dot{m}^{\mathrm{wet}}_{\mathrm{Hmdf}}$, $\dot{m}_{\mathrm{HByp}}$, and $\dot{m}_{\mathrm{Exh}}$. These correlations were the most probable cause for numerical instabilities because the forward Euler was likely to estimate too large a mass transfer between two manifolds for one sample time step. Thus, the pressure increase in the receiving manifold was too high, while the pressure decrease in the delivering manifold was too low. Accordingly, the pressure levels could be reversed, presumably resulting in permanent oscillations of both pressure values. The margin before this pressure reversal was higher for higher pressure losses. Therefore, mass flow correlations with higher pressure losses reduced the probability of numerical instabilities. The stationary model accuracy was nearly retained by including the pressure losses through the humidifier in a modified correlation $\tilde{\dot{m}}^{\mathrm{in}}_{\mathrm{Ca}}$ for the stack air mass flow.

$$\tilde{\dot{m}}^{\mathrm{in}}_{\mathrm{Ca}} = \tilde{C}^{\mathrm{in}}_{1,\mathrm{Ca}} \cdot \left[\rho^{\mathrm{out}}_{\mathrm{Cmpr}} \cdot \left(p^{\mathrm{out}}_{\mathrm{Cmpr}} - p^{\mathrm{in}}_{\mathrm{Trb}}\right)\right]^{\tilde{C}^{\mathrm{in}}_{2,\mathrm{Ca}}}, \qquad \rho^{\mathrm{out}}_{\mathrm{Cmpr}} = \frac{p^{\mathrm{out}}_{\mathrm{Cmpr}}}{R_{\mathrm{Air}} \cdot T^{\mathrm{out}}_{\mathrm{Cmpr}}} \tag{6.2}$$

By contrast, removing the turbine outlet manifold resulted in the neglection of the pressure loss through the cathode exhaust with $p^{\mathrm{out}}_{\mathrm{Trb}} = p_{\mathrm{Atm}}$. This neglection was inevitable because the corresponding pressure loss could not be integrated into another mass flow correlation. Consequently, the model accuracy was slightly decreased.

The second modification was the increase of the remaining two manifold volumes by a factor of four to partly compensate for the neglection of the other three manifolds.

$$\tilde{V}^{\mathrm{out}}_{\mathrm{Cmpr}} = \tilde{V}^{\mathrm{in}}_{\mathrm{Trb}} = 8 \cdot 10^{-3}\,\mathrm{m}^3 \tag{6.3}$$

Additionally, this modification slightly decreased the rate of change of $p^{\mathrm{out}}_{\mathrm{Cmpr}}$ and $p^{\mathrm{in}}_{\mathrm{Trb}}$ during load changes. As a result, the numerical complexity was further reduced.

The third modification was a limitation of Ψ_{Cmpr}, Φ_{Cmpr}, and $\dot{m}_{\mathrm{Cmpr}}$ in the compressor map model.

$$0.55 \leq \Psi_{\mathrm{Cmpr}} \leq 1.15 \tag{6.4}$$

$$0 \leq \Phi_{\mathrm{Cmpr}} \leq 0.11 \tag{6.5}$$

$$\dot{m}_{\mathrm{Cmpr}} \leq 200\,\frac{\mathrm{m}}{\mathrm{s}} \tag{6.6}$$

The boundary values in Equations (6.4)-(6.6) corresponded to the air compressor operating range displayed in Figure 7. Hence, the prediction model was forced to remain within the boundaries of the compressor map, even if the forward Euler determined an operating point outside of these boundaries through an inaccurate pressure prediction. Consequently, this limitation further reduced the probability of numerical instabilities.

The final simplification of the prediction model was utilizing constant values $pos_{\mathrm{VTG}} = 50\,\%$, $\eta_{Is,\mathrm{Cmpr}} = 70\,\%$, and $\eta_{Is,\mathrm{Trb}} = 80\,\%$. The first simplification reflected the omission of the VTG as an actuator of the NMPC and the mostly marginal deviations from $pos_{\mathrm{VTG}} = 50\,\%$ during the operation of the FCS. The other two simplifications were carried out solely to reduce the computational load of the nonlinear prediction model. The values of $\eta_{Is,\mathrm{Cmpr}}$ and $\eta_{Is,\mathrm{Trb}}$ were chosen to represent the average values of Figures 8 and 11. Unfortunately, the two values were mixed up by accident. The correct values were $\eta_{Is,\mathrm{Cmpr}} = 80\,\%$ and $\eta_{Is,\mathrm{Trb}} = 70\,\%$. However, this error was only noticed after all the measurements had been accomplished, which is why it was not fixed in this work.

6.1.2 Determination of Model Parameters

The parameter values of $\dot{\tilde{m}}^{\mathrm{in}}_{\mathrm{Ca}}$ were determined from the models for $\dot{m}^{\mathrm{dry}}_{\mathrm{Hmdf}}$, $\dot{m}^{\mathrm{in}}_{\mathrm{Ca}}$, and $\dot{m}^{\mathrm{wet}}_{\mathrm{Hmdf}}$, which were presented in Section 4.2. The fitting data was created by first specifying a grid of possible values $p^{\mathrm{out}}_{\mathrm{Cmpr}}$, $T^{\mathrm{out}}_{\mathrm{Cmpr}}$, and $p^{\mathrm{in}}_{\mathrm{Trb}}$. Then, the corresponding mass flows $\dot{\tilde{m}}^{\mathrm{in}}_{\mathrm{Ca}}$ were determined by equalizing $\dot{m}^{\mathrm{dry}}_{\mathrm{Hmdf}}$, $\dot{m}^{\mathrm{in}}_{\mathrm{Ca}}$, and $\dot{m}^{\mathrm{wet}}_{\mathrm{Hmdf}}$. Finally, the parameters $\tilde{C}^{\mathrm{in}}_{1,\mathrm{Ca}} = 9.75 \cdot 10^{-3}$ $\tilde{C}^{\mathrm{in}}_{2,\mathrm{Ca}} = 7.83 \cdot 10^{-1}$ were determined with a least squares approach achieving $R^2 = 0.9997$ with regard to $\dot{\tilde{m}}^{\mathrm{in}}_{\mathrm{Ca}}$. The data set from Figure 58 disregarded the impact of $\dot{m}_{\mathrm{HByp}}$. Nonetheless, this impact on the prediction model accuracy was marginal. The fully opened humidifier bypass valve led to a decreased pressure resistance in the cathode subsystem, which is why the neglection of the humidifier bypass valve increased the pressure resistance of the stack air path in the nonlinear prediction model. However, this increased pressure resistance might offset the neglection of other pressure resistances in the model, like the pressure losses of the CWS and the TWS. Thus, the accuracy of the nonlinear prediction model had to be reassessed, taking into account all simplifications. The findings of this reassessment are shown in the next section.

6.1.3 Validation of Nonlinear Prediction Model

The nonlinear prediction model was compared to the same FCS test stand measurement used in Section 4.4.1 to evaluate the impact of the model simplifications. Thus, the same model input trajectories for $i^{\mathrm{sp}}_{q,\mathrm{Cmpr}}$ and $pos^{\mathrm{sp}}_{\mathrm{Byp}}$ from Figure 21 were used. The corresponding values of n_{Cmpr} for the measurement and the nonlinear prediction model are displayed in Figure 59. The dynamics of n_{Cmpr} were still accurately predicted, whereas the stationary discrepancies between measurement and model values in Figure 59

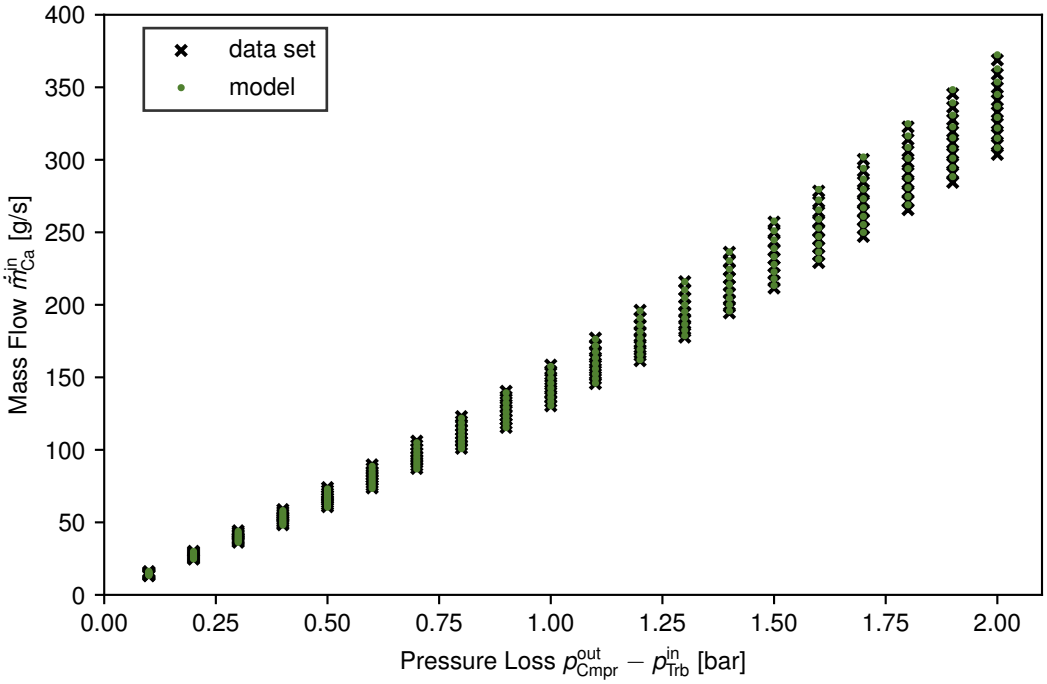

Figure 58: Comparison of $\dot{m}^{\text{in}}_{\text{Ca}}$ from the model (Eq. (6.2)) and the data set with $\dot{m}^{\text{dry}}_{\text{Hmdf}} = \dot{m}^{\text{in}}_{\text{Ca}}$ and $\dot{m}^{\text{in}}_{\text{Ca}} = \dot{m}^{\text{wet}}_{\text{Hmdf}}$.

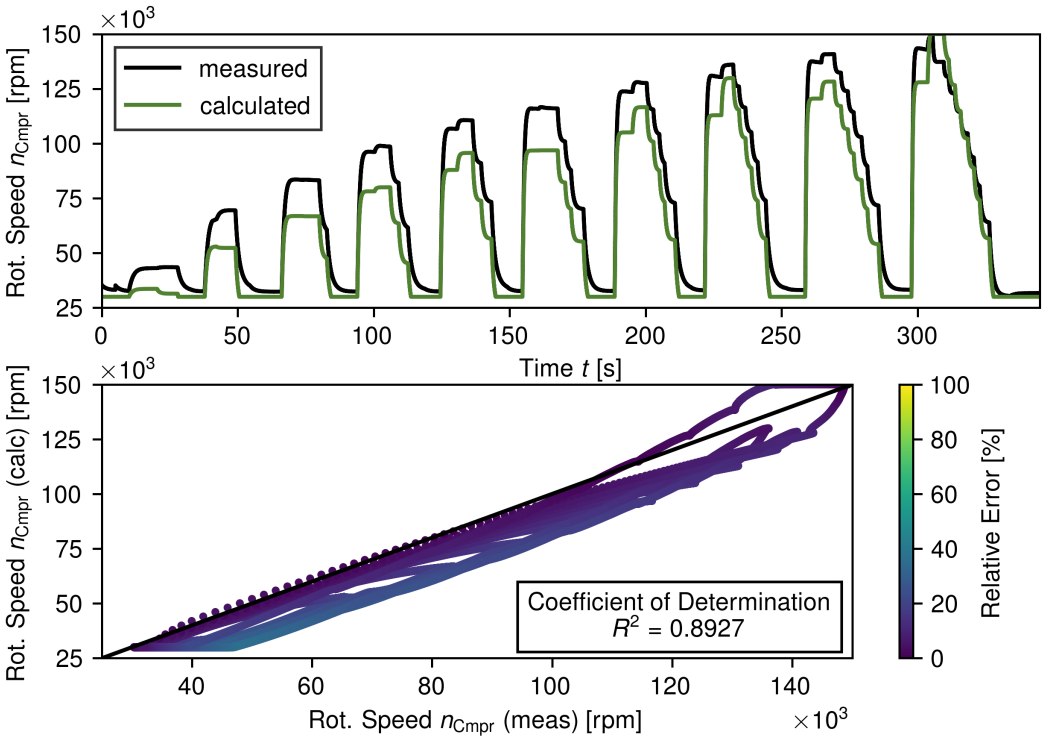

Figure 59: Comparison of n_{Cmpr} for the FCS test stand measurement and the corresponding nonlinear prediction model calculations.

were more significant than for the simulation model in Figure 22. This deteriorated

accuracy was most likely due to $\eta_{Is,\mathrm{Cmpr}} = 70\,\%$ and $\eta_{Is,\mathrm{Trb}} = 80\,\%$, because the stationary values of n_{Cmpr} were determined by a moment balance (Eq. (4.37)). The agreement between the measurement and prediction model was slightly improved by correcting the constant efficiencies to $\eta_{Is,\mathrm{Cmpr}} = 80\,\%$ and $\eta_{Is,\mathrm{Trb}} = 70\,\%$. Nevertheless, this modification only covered a small part of the deviation compared to the simulation model, especially at low rotational speeds. The remaining differences were caused by the neglected load-dependencies of $\eta_{Is,\mathrm{Cmpr}}$ and $\eta_{Is,\mathrm{Trb}}$, which were more distinct for small values of n_{Cmpr} (see Fig. 8).

An acceptable stationary accuracy was maintained for $\dot{m}_{\mathrm{AirFil}}$ despite the significant deviations of n_{Cmpr}. The associated comparison between the measurement and the nonlinear prediction model is shown in Figure 60. Figure 60 additionally unveils that

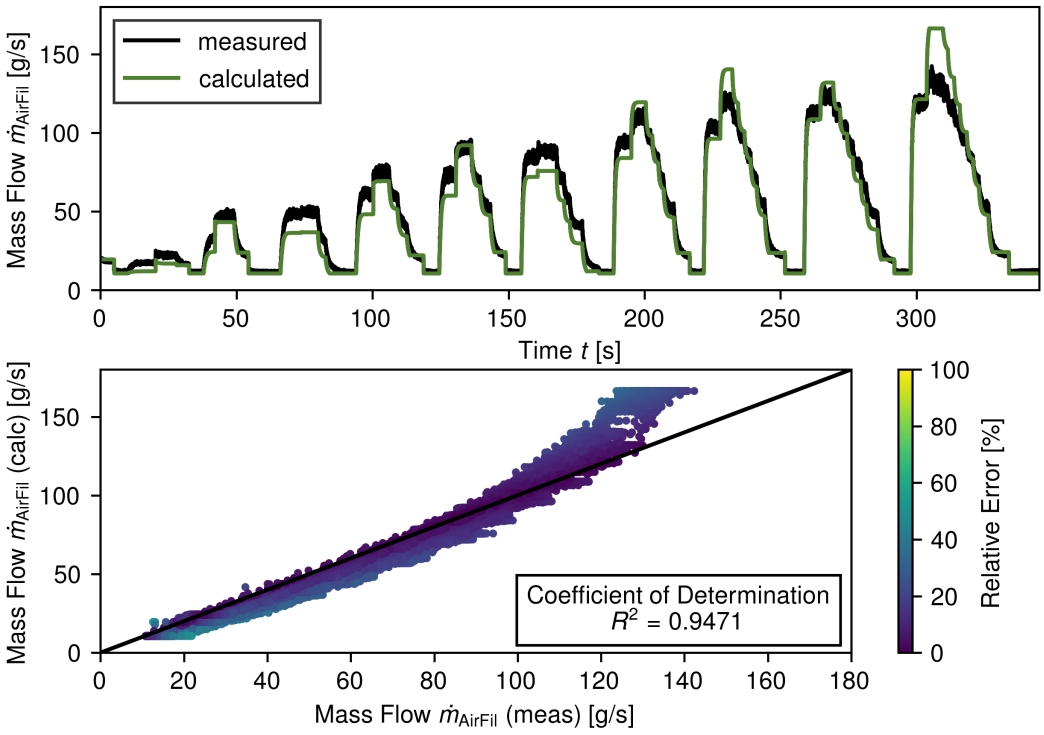

Figure 60: Comparison of $\dot{m}_{\mathrm{AirFil}}$ for the FCS test stand measurement and the corresponding nonlinear prediction model calculations.

the dynamics of $\dot{m}_{\mathrm{AirFil}}$ were adequately predicted. The most significant stationary discrepancy at $t = 310\,\mathrm{s}$ was affected by a falsely high n_{Cmpr}. At this point, the simulation model from Chapter 4 calculated $\eta_{Is,\mathrm{Cmpr}} = 64\,\%$ and $\eta_{Is,\mathrm{Trb}} = 35\,\%$. Thus, $\eta_{Is,\mathrm{Trb}} = 80\,\%$ was significantly higher in the simplified prediction model. This higher value resulted in a substantially higher $\tau_{\mathrm{Trb}} = 0.36\,\mathrm{N\,m}$ instead of $\tau_{\mathrm{Trb}} = 0.07\,\mathrm{N\,m}$. Accordingly, the equilibrium of the moment balance (Eq. (4.37)) was obtained for a higher n_{Cmpr} in the nonlinear prediction model.

This significant stationary discrepancy further induced a considerable deviation between the measured and the otherwise well-predicted value of $\dot{m}_{\mathrm{Byp}}$. The corresponding comparison is displayed in Figure 61. Furthermore, the dynamics of $\dot{m}_{\mathrm{Byp}}$ were accurately

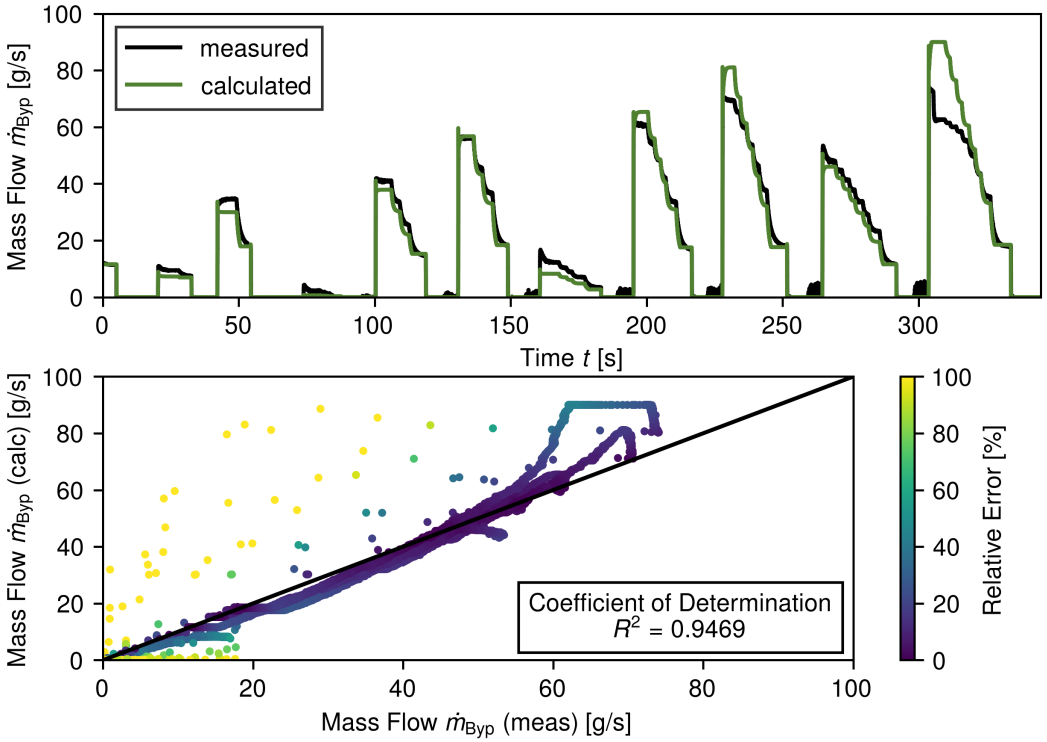

Figure 61: Comparison of $\dot{m}_{Byp}$ for the FCS test stand measurement and the corresponding nonlinear prediction model calculations.

calculated with the nonlinear prediction model.

The appreciable stationary accuracy of $\dot{m}_{Byp}$ contrasted with the significant deviations between the measurement and the nonlinear prediction model with regard to p^{out}_{Cmpr}. The associated comparison is shown in Figure 62. The considerably smaller values of p^{out}_{Cmpr} alongside similar values of $\dot{m}_{Byp}$ suggested smaller stationary values of p^{in}_{Trb} for the nonlinear prediction model. This suggestion was further supported by the higher values of p^{in}_{Trb} in the nonlinear simulation model. The neglected pressure loss through the air exhaust might have caused the smaller values of p^{out}_{Cmpr}. However, the final validation of this assumption would have required pressure sensors at the turbine inlet and outlet that were unavailable in this work. The increased manifold volumes were another simplification that affected p^{out}_{Cmpr}. Even though this simplification reduced the rate of change of p^{out}_{Cmpr} according to Equation (4.1), Figure 62 reveals accurate dynamics for the nonlinear prediction model.

Overall, the dynamics and the stationary values of the most critical variables, $\dot{m}_{AirFil}$ and $\dot{m}_{Byp}$, were appreciably well predicted, despite the simplifications. These crucial prerequisites for successfully applying of an NMPC outweighed the significant stationary discrepancies for n_{Cmpr} and p^{out}_{Cmpr}. Nonetheless, the persisting stationary model deviations had to be compensated to avoid stationary control deviations in the closed control loop with the NMPC. This compensation was handled by a perturbation observer introduced in the following section.

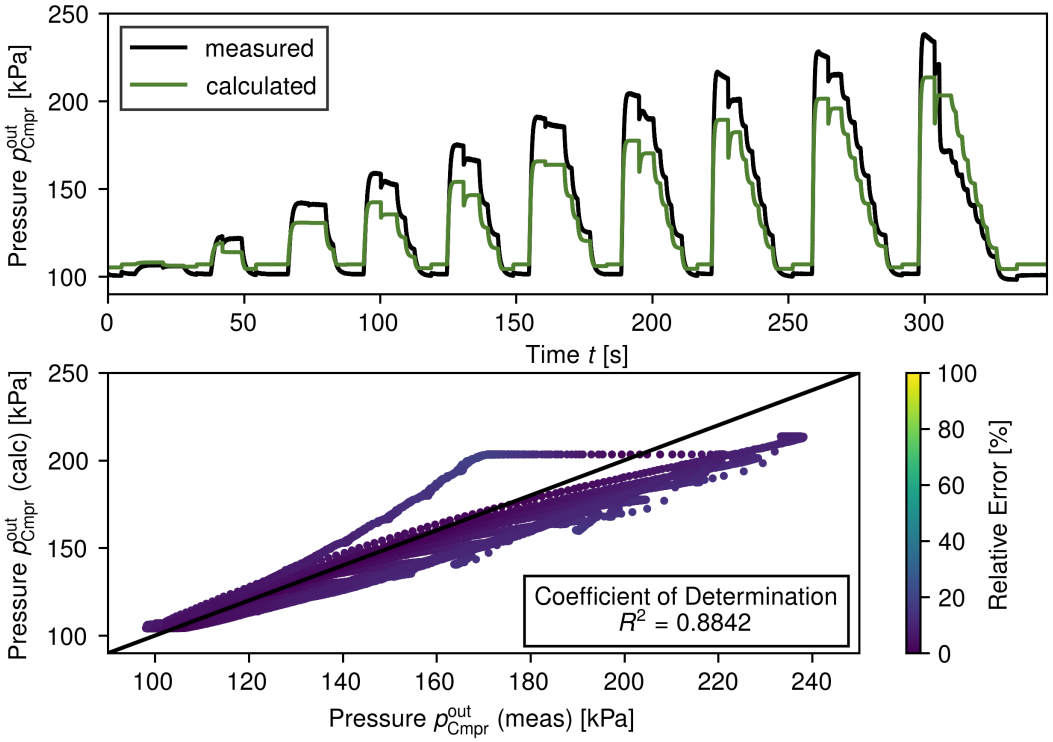

Figure 62: Comparison of p^{out}_{Cmpr} for the FCS test stand measurement and the corresponding nonlinear prediction model calculations.

6.2 State and Perturbation Observer

In this work, the nonlinear observer was set up as a Luenberger observer with additional estimated perturbation states $\hat{\boldsymbol{d}}$, similar to the linear observer in Section 5.2.

$$\begin{aligned}\begin{bmatrix}\hat{\boldsymbol{x}}(k+1)\\ \hat{\boldsymbol{d}}(k+1)\end{bmatrix} = \begin{bmatrix}\hat{\boldsymbol{x}}(k)\\ \hat{\boldsymbol{d}}(k)\end{bmatrix} + \Delta t \cdot \begin{bmatrix}\boldsymbol{f}(\hat{\boldsymbol{x}}(k), \boldsymbol{u}(k))\\ \boldsymbol{0}\end{bmatrix} \\ + \boldsymbol{L}_{\mathrm{d}} \cdot \left\{ \boldsymbol{y}^{\mathrm{meas}}_{\mathrm{FCS}}(k) - \begin{bmatrix}\hat{y}_{1,\mathrm{FCS}}(k)\\ \hat{y}_{2,\mathrm{FCS}}(k-4)\\ \hat{y}_{3,\mathrm{FCS}}(k)\\ \hat{y}_{4,\mathrm{FCS}}(k)\\ \hat{y}_{5,\mathrm{FCS}}(k)\end{bmatrix} \right\}\end{aligned} \tag{6.7}$$

The semi-empirical approach of the nonlinear prediction model allowed n_{Cmpr}, pos_{Byp}, and $p^{\mathrm{out}}_{\mathrm{Cmpr}}$ to be included as measurement feedback vector $\boldsymbol{y}_{\mathrm{FCS}}$ of the FCS.

$$\boldsymbol{y}_{\mathrm{FCS}} = \left[\dot{m}^{\mathrm{meas}}_{\mathrm{AirFil}},\ \dot{m}^{\mathrm{meas}}_{\mathrm{Byp}},\ n^{\mathrm{meas}}_{\mathrm{Cmpr}},\ pos^{\mathrm{meas}}_{\mathrm{Byp}},\ p^{\mathrm{out,meas}}_{\mathrm{Cmpr}}\right]^T \tag{6.8}$$

However, the initial parameter values in $\boldsymbol{L}_\mathrm{d}$ were chosen to compensate for perturbations only with the measured mass flows and with $\hat{\boldsymbol{d}}$.

$$\boldsymbol{L}_\mathrm{d} = \begin{bmatrix} 0 & 0 & 0 & 0 & 0 & 0.1 & 0 \\ 0 & 0 & 0 & 0 & 0 & 0 & 0.1 \\ 0 & 0 & 0 & 0 & 0 & 0 & 0 \\ 0 & 0 & 0 & 0 & 0 & 0 & 0 \\ 0 & 0 & 0 & 0 & 0 & 0 & 0 \end{bmatrix}^T \tag{6.9}$$

The measurements $n_\mathrm{Cmpr}^\mathrm{meas}$ and $p_\mathrm{Cmpr}^\mathrm{out,meas}$ were neglected with the observer gains of Equation (6.9) due to their high stationary deviations from the nonlinear prediction model. The compensation of these differences in $\hat{\boldsymbol{x}}$ and $\hat{\boldsymbol{d}}$ could unnecessarily increase the prediction errors for $\dot{m}_\mathrm{AirFil}$ and $\dot{m}_\mathrm{Byp}$. Consequently, this increased error could result in a less adequate compensation of the sensor noise and the bypass leakage with the NMPC.

Eventually, the values of $\hat{\boldsymbol{d}}$ were subtracted from the original setpoints $\boldsymbol{y}^\mathrm{sp}$, as shown in Equation (5.7). The resulting corrected setpoints $\tilde{\boldsymbol{y}}^\mathrm{sp}$ were then integrated into the cost function of the NMPC, which is presented in the following.

6.3 Cost Function for Nonlinear Model Predictive Controller

The cost function J of the NMPC was implemented in a quadratic form similar to Equation (5.8) for the linear MPC.

$$\begin{aligned} J\left(\boldsymbol{\theta}\left(k\right), \boldsymbol{U}\right) = {} & \left[\tilde{\boldsymbol{y}}^\mathrm{sp}\left(k\right) - \boldsymbol{y}\left(k+N_y\right)\right]^T \boldsymbol{P} \left[\tilde{\boldsymbol{y}}^\mathrm{sp}\left(k\right) - \boldsymbol{y}\left(k+N_y\right)\right] \\ & + \sum_{i=1}^{N_y-1} \left[\tilde{\boldsymbol{y}}^\mathrm{sp}\left(k\right) - \boldsymbol{y}\left(k+i\right)\right]^T \boldsymbol{Q} \left[\tilde{\boldsymbol{y}}^\mathrm{sp}\left(k\right) - \boldsymbol{y}\left(k+i\right)\right] \\ & + \sum_{j=0}^{N_u-1} \Delta\boldsymbol{u}\left(k+j\right)^T \boldsymbol{R} \Delta\boldsymbol{u}\left(k+j\right) \end{aligned} \tag{6.10}$$

The introduction of the terminal weight matrix $\boldsymbol{P}$ was motivated by the high accuracy of the nonlinear prediction model regarding $\boldsymbol{y}$. This accuracy led to a small impact of $\hat{\boldsymbol{d}}$ throughout the operating range of the FCS. Hence, the predicted model values $\boldsymbol{y}$ closely resembled the future outputs of the FCS along the entire prediction horizon N_y. This resemblance could be used to shape the dynamic transitions of the controlled system. The controlled system was likely to reach a setpoint y_i^sp after N_y time steps if the model predicted the achievement of this setpoint $\tilde{y}_i^\mathrm{sp}$ in J. Therefore, a higher weight on $\tilde{y}_i^\mathrm{sp} - y_i\left(k+N_y\right)$ forced the controlled plant towards y_i^sp, minimizing over- and undershoots of y_i in the closed control loop.

The optimal system trajectory of the NMPC generally minimizes J as a function of $\boldsymbol{U}$. In this work, the resulting optimization problem further considered the lower and

upper bounds of $\boldsymbol{u}$, $\boldsymbol{u}_{\mathrm{Min}} = [0\,\mathrm{A},\ 0\,\%]^T$ and $\boldsymbol{u}_{\mathrm{Max}} = [120\,\mathrm{A},\ 100\,\%]^T$.

$$\min_{\boldsymbol{U}} \quad J\left(\boldsymbol{\theta}\left(k\right), \boldsymbol{U}\right) \tag{6.11}$$

$$\text{s.t.} \quad \boldsymbol{u}_{\mathrm{Min}} \leq \boldsymbol{u}\left(k+j\right) \leq \boldsymbol{u}_{\mathrm{Max}}, \qquad j = 0, 1, ..., N_u - 1 \tag{6.12}$$

$$\boldsymbol{x}\left(k+i\right) = \boldsymbol{x}\left(k+i-1\right) + \Delta t \cdot \boldsymbol{f}^1, \qquad i = 1, 2, ..., N_y \tag{6.13}$$

$$\boldsymbol{y}\left(k+i\right) = \boldsymbol{h}\left(\boldsymbol{x}\left(k+i\right)\right), \qquad i = 1, 2, ..., N_y \tag{6.14}$$

The optimization problem of Equations (6.11)-(6.14) constituted an NLP problem.

6.4 Simulation Study with Implicit Nonlinear Model Predictive Controller

In this work, the explicit solution of the NMPC optimization problem was approximated with a NN to obtain a real-time capable controller with $\Delta t = 10\,\mathrm{ms}$. The offline training of this NN required tuning the cost function before applying the controller on the ECU. Therefore, the corresponding implicit NMPC was evaluated with closed-loop simulations that allowed fast modifications of $\boldsymbol{Q}$ and $\boldsymbol{R}$. Additionally, N_y and N_u were varied independently in this simulation study because their values did not affect the real-time capability of the proposed controller. Instead, the number of neurons and the number of layers in the NN determined the CPU core load, and these numbers were additional tuning parameters.

In the closed-loop simulations, the NLP problem of the implicit NMPC was solved with the sequential QP algorithm of the nonlinear optimizer FMINCON from the MATLAB OPTIMIZATION TOOLBOX. Additionally, central finite differences were utilized to estimate function gradients, and the objective function J and the constraints were normalized. The optimization was repeated six times at each time step, with each run starting from a different initial value $\boldsymbol{U}_0$. This repetition significantly improved the probability of detecting the global solution with a local optimizer like FMINCON.

The cost function parameters were initially set to $N_y = 7$, $N_u = 2$, $\boldsymbol{P} = \left[\begin{smallmatrix} 10 & 0 \\ 0 & 1 \end{smallmatrix}\right]$ and $\boldsymbol{Q} = \left[\begin{smallmatrix} 10 & 0 \\ 0 & 1 \end{smallmatrix}\right]$. These values were based on the best results obtained with the linear MPC. The only difference was $\boldsymbol{R} = \left[\begin{smallmatrix} 0 & 0 \\ 0 & 0 \end{smallmatrix}\right]$. The weighting of the control action stabilized the closed-loop behavior with the linear MPC. However, this stabilizing was unnecessary with the NMPC because of the significantly smaller dependency on the perturbation observer due to a more accurate prediction model. The first step in the closed-loop simulations was the evaluation of different N_y. Afterward, the best value of N_y was combined with different values of N_u, and the corresponding closed-loop simulation results were assessed. Finally, various weights in $\boldsymbol{P}$ and $\boldsymbol{Q}$ were compared to each other. All these comparisons were conducted with the trajectories of $\dot{m}_{\mathrm{Ca}}^{\mathrm{in,sp}}$ and $\dot{m}_{\mathrm{Byp}}^{\mathrm{sp}}$ from Figure 42.

[1] state and input dependencies were neglected to avoid a multi-line equation,
$\boldsymbol{f} = \boldsymbol{f}\left(\boldsymbol{x}\left(k+i-1\right), x_3\left(k+i-2\right), u_1\left(k+i-6\right), u_2\left(k+i-2\right), u_2\left(k+i-3\right)\right)$

6.4.1 Variation of Prediction and Control Horizon

The more precise nonlinear prediction model of the NMPC reduced the impact of $\hat{\boldsymbol{d}}$ on the closed-loop behavior. Thus, longer prediction horizons were more practicable compared to the linear MPC. The best closed-loop behavior of $\dot{m}_{\mathrm{Ca}}^{\mathrm{in}}$ and $\dot{m}_{\mathrm{Byp}}$ was achieved with $N_y = 15$. This closed-loop behavior is displayed in Figure 63 for four representative step changes alongside two other variants of the NMPC with $N_y = 7$ and $N_y = 10$. On the one hand, the decisive difference between $N_y = 15$ and $N_y = 10$

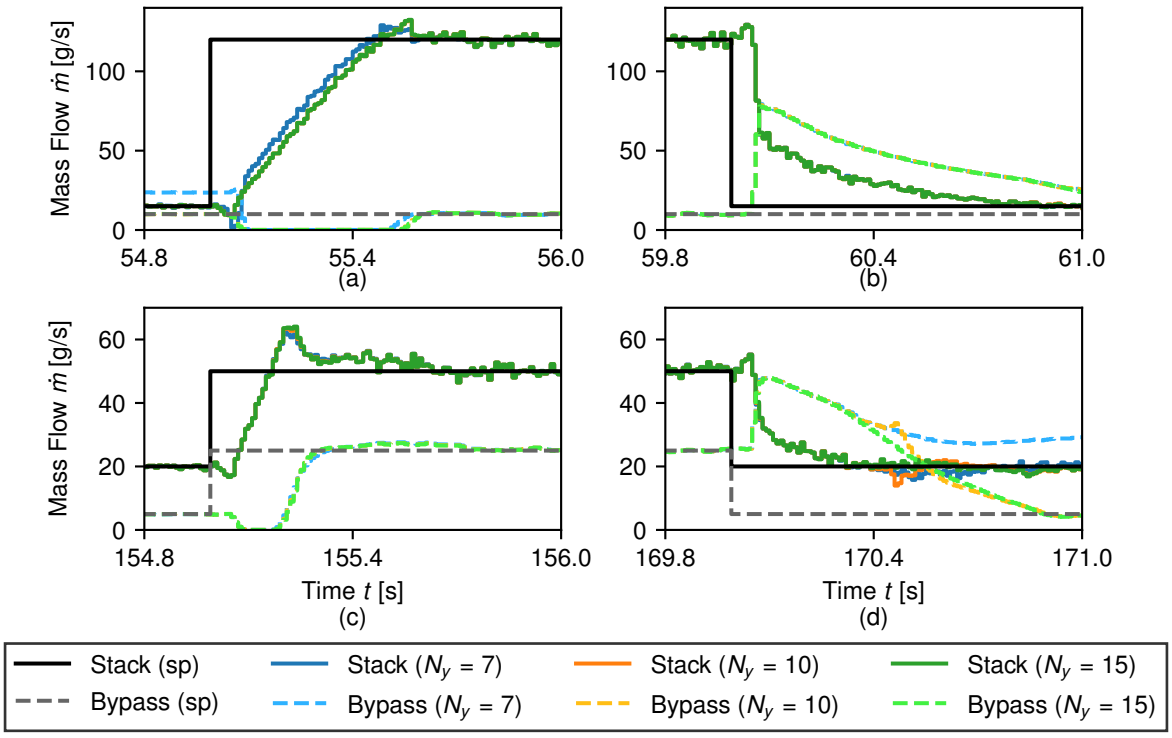

Figure 63: Air mass flows for closed-loop simulation results of the implicit nonlinear MPC with $N_u = 2$, $\boldsymbol{P} = \left[\begin{smallmatrix} 10 & 0 \\ 0 & 1 \end{smallmatrix}\right]$, $\boldsymbol{Q} = \left[\begin{smallmatrix} 10 & 0 \\ 0 & 1 \end{smallmatrix}\right]$, and $N_y = 7$, $N_y = 10$, or $N_y = 15$.

was the undershoot in $\dot{m}_{\mathrm{Ca}}^{\mathrm{in}}$ that is shown in Figure 63d). The absence of undershoots in $\dot{m}_{\mathrm{Ca}}^{\mathrm{in}}$ eliminated the risk of oxygen starvation in the fuel cells. On the other hand, the NMPC with $N_y = 7$ showed a permanent positive control deviation for $\dot{m}_{\mathrm{Byp}}$ in Figure 63a) and d). This control deviation reduced the efficiency of the cathode subsystem due to excessive power consumption of the air compressor.

The control deviation of $\dot{m}_{\mathrm{Byp}}$ resulted from a permanently saturated control variable $pos_{\mathrm{Byp}}^{\mathrm{sp}} = 100\,\%$, depicted in Figure 64. This comparison of the closed-loop behavior of $i_{q,\mathrm{Cmpr}}^{\mathrm{sp}}$ and $pos_{\mathrm{Byp}}^{\mathrm{sp}}$ further revealed a renewed increase from $pos_{\mathrm{Byp}}^{\mathrm{sp}} = 70\,\%$ to $pos_{\mathrm{Byp}}^{\mathrm{sp}} = 100\,\%$ for the NMPC with $N_y = 10$ in Figure 64b) and d). This suboptimal closed-loop behavior caused the undershoot of $\dot{m}_{\mathrm{Ca}}^{\mathrm{in}}$ in Figure 63d). It seems probable that the prediction horizons $N_y = 7$ and $N_y = 10$ were too short for the air mass flow dynamics to fully unfold in J. Thus, the correct stationary values of $pos_{\mathrm{Byp}}^{\mathrm{sp}}$ could not be determined by the solver, and the solver instead remained at a boundary of $pos_{\mathrm{Byp}}^{\mathrm{sp}}$.

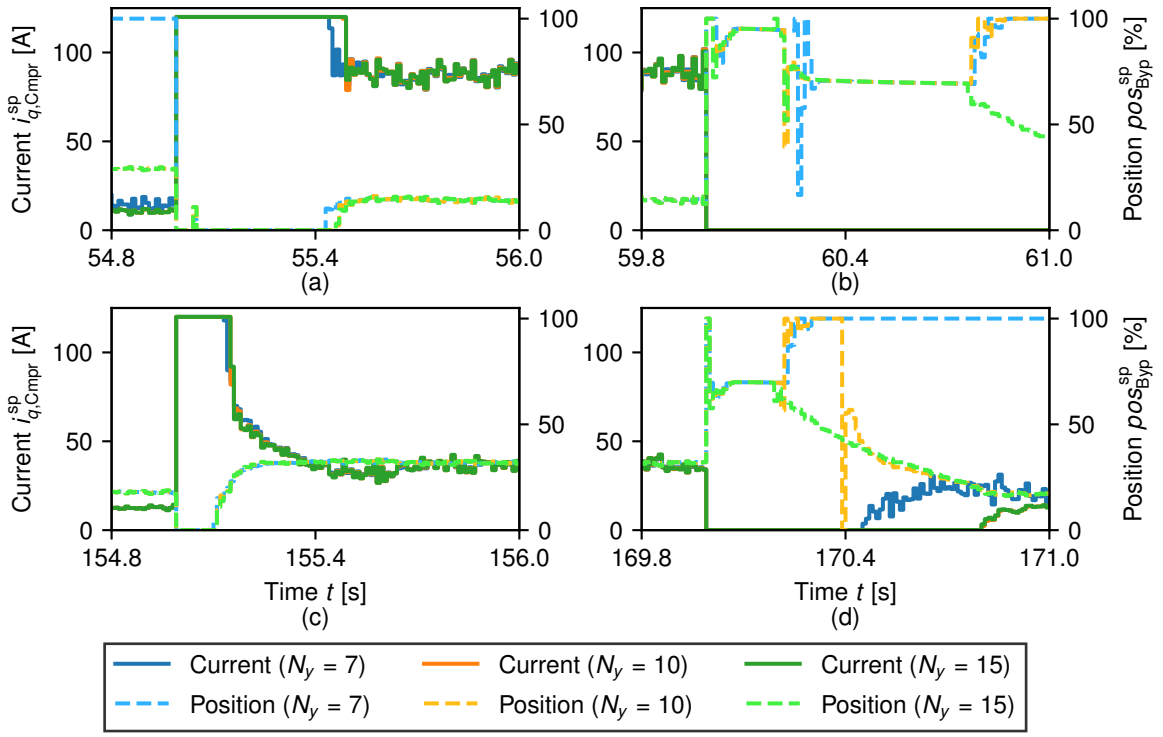

Figure 64: Control variables for closed-loop simulation results of the implicit nonlinear MPC with $N_u = 2$, $\boldsymbol{P} = \left[\begin{smallmatrix} 10 & 0 \\ 0 & 1 \end{smallmatrix}\right]$, $\boldsymbol{Q} = \left[\begin{smallmatrix} 10 & 0 \\ 0 & 1 \end{smallmatrix}\right]$, and $N_y = 7$, $N_y = 10$, or $N_y = 15$.

Therefore, the second part of the simulation study was conducted with $N_y = 15$ alongside $\boldsymbol{P} = \left[\begin{smallmatrix} 10 & 0 \\ 0 & 1 \end{smallmatrix}\right]$ and $\boldsymbol{Q} = \left[\begin{smallmatrix} 10 & 0 \\ 0 & 1 \end{smallmatrix}\right]$. The goal was to evaluate the impact of N_u on the closed-loop behavior. The resulting trajectories of $\dot{m}^{\text{in}}_{\text{Ca}}$ and $\dot{m}_{\text{Byp}}$ for $N_u = 1$, $N_u = 2$, and $N_u = 10$ are depicted in Figure 65. The differences between $N_u = 2$ and $N_u = 10$ were negligible, whereas $N_u = 1$ resulted in a significantly slower dynamic response of $\dot{m}_{\text{Byp}}$.

Nevertheless, the best closed-loop behavior was achieved for $N_u = 1$ because of the closed-loop trajectories of the control variables. These trajectories of $i^{\text{sp}}_{q,\text{Cmpr}}$ and $pos^{\text{sp}}_{\text{Byp}}$ are shown in Figure 66. The longer control horizons $N_u = 2$ and $N_u = 10$ generated significant oscillations in $i^{\text{sp}}_{q,\text{Cmpr}}$ and $pos^{\text{sp}}_{\text{Byp}}$. There is a definite possibility that these oscillations arose due to numerical uncertainties in the predicted trajectories in J. The most significant prediction error with the forward Euler generally occurs at the first time step after a change in the model inputs. Thus, repeated changes of $i^{\text{sp}}_{q,\text{Cmpr}}$ and $pos^{\text{sp}}_{\text{Byp}}$ along the prediction horizon led to oscillating mass flow trajectories in J. These oscillations then complicated a precise optimization of J, and the ensuing optimization uncertainties caused oscillating control variables. Oscillations in the trajectory of $pos^{\text{sp}}_{\text{Byp}}$ were generally acceptable, whereas oscillations in $i^{\text{sp}}_{q,\text{Cmpr}}$ led to undesirable oscillations in P_{Cmpr} that could potentially impact the power response of the FCS. Therefore, the absence of oscillations with $N_u = 1$ outweighed the drawback of slower dynamics most likely caused by the small number of optimization variables Δu with $N_u = 1$. Thus, NMPCs with $N_y = 15$ and $N_u = 1$ were implemented in the remainder of this work. $N_y = 15$ corresponded to a prediction time period of $\Delta t = 150\,\text{ms}$. This time period is

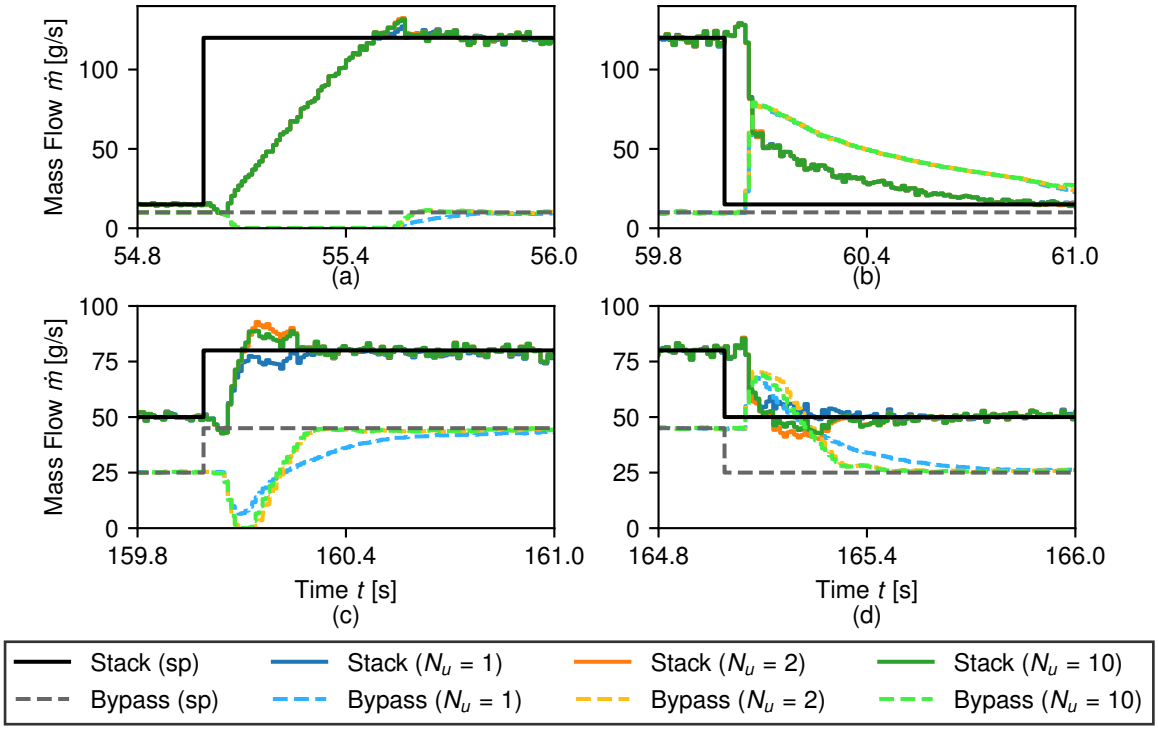

Figure 65: Air mass flows for closed-loop simulation results of the implicit nonlinear MPC with $N_y = 15$, $\boldsymbol{P} = \left[\begin{smallmatrix} 10 & 0 \\ 0 & 1 \end{smallmatrix}\right]$, $\boldsymbol{Q} = \left[\begin{smallmatrix} 10 & 0 \\ 0 & 1 \end{smallmatrix}\right]$, and $N_u = 1$, $N_u = 2$, or $N_u = 10$.

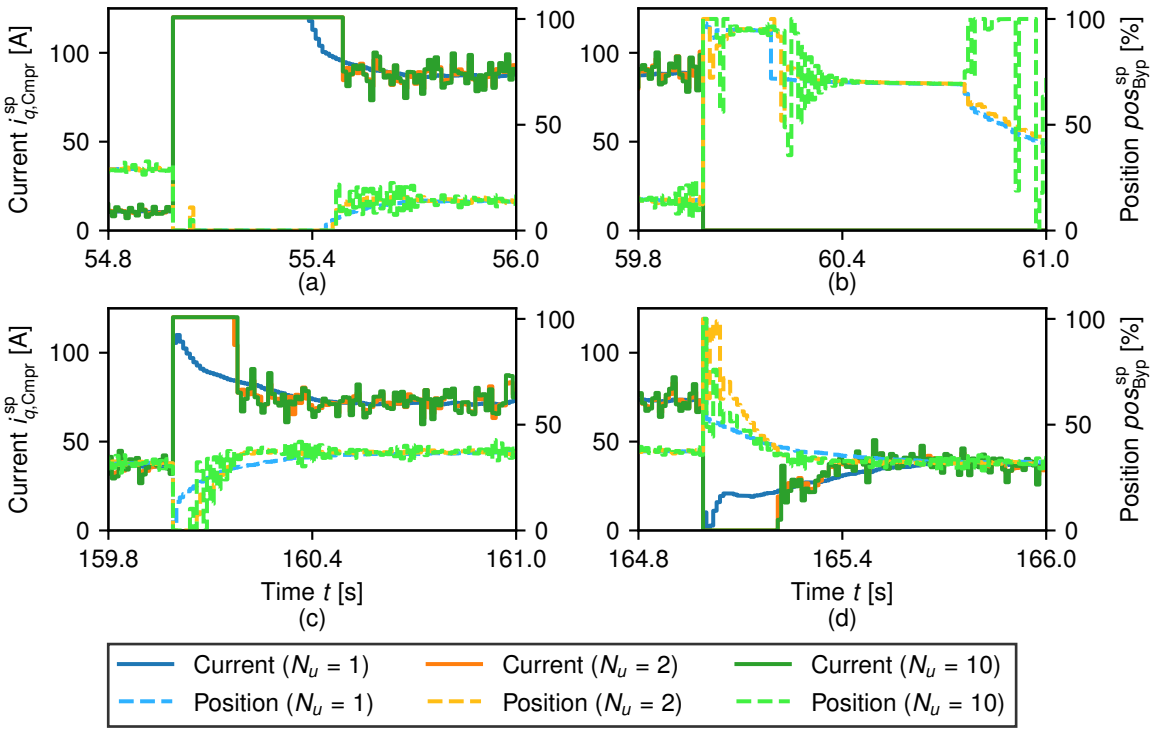

Figure 66: Control variables for closed-loop simulation results of the implicit nonlinear MPC with $N_y = 15$, $\boldsymbol{P} = \left[\begin{smallmatrix} 10 & 0 \\ 0 & 1 \end{smallmatrix}\right]$, $\boldsymbol{Q} = \left[\begin{smallmatrix} 10 & 0 \\ 0 & 1 \end{smallmatrix}\right]$, and $N_u = 1$, $N_u = 2$, or $N_u = 10$.

approximately twice as long as the suggested prediction horizons in previous studies on NMPC for the air supply control of an FCS. Gruber *et al.* applied prediction horizons with $\Delta t = 70\,\text{ms}$ ($N_y = 7$, [36]) and $\Delta t = 80\,\text{ms}$ ($N_y = 16$, [35]), respectively. The more extended prediction time period in this work was necessary to cover major step changes in the significantly more extensive operating range of the air compressor. However, Gruber *et al.* further reported successfully applying longer control horizons $N_u = 7$ [36] and $N_u = 5$ [35], which offer the controller greater freedom to optimize the dynamic trajectories of the air mass flows. Hence, future studies applying NMPC to the FCS of the BMW iX5 Hydrogen should focus on a numerically stable prediction to enable longer control horizons. These longer control horizons should further improve the closed-loop behavior of the cathode subsystem.

6.4.2 Variation of Weights

The subsequent step evaluated the closed-loop behavior with varying weights in P and Q. This evaluation was conducted with six parameter sets summarized in Table 6. Initially, different prioritizations of the two mass flow control tasks were compared

Table 6: Variants of the weight matrices ***P*** and ***Q*** for the parameterization of *J* with regard to the proposed NMPC for air mass flows.

Variant	***P***	***Q***	Variant	***P***	***Q***
1	$\left[\begin{smallmatrix}1 & 0\\ 0 & 1\end{smallmatrix}\right]$	$\left[\begin{smallmatrix}1 & 0\\ 0 & 1\end{smallmatrix}\right]$	4	$\left[\begin{smallmatrix}100 & 0\\ 0 & 1\end{smallmatrix}\right]$	$\left[\begin{smallmatrix}10 & 0\\ 0 & 1\end{smallmatrix}\right]$
2	$\left[\begin{smallmatrix}10 & 0\\ 0 & 1\end{smallmatrix}\right]$	$\left[\begin{smallmatrix}10 & 0\\ 0 & 1\end{smallmatrix}\right]$	5	$\left[\begin{smallmatrix}100 & 0\\ 0 & 1\end{smallmatrix}\right]$	$\left[\begin{smallmatrix}20 & 0\\ 0 & 1\end{smallmatrix}\right]$
3	$\left[\begin{smallmatrix}20 & 0\\ 0 & 1\end{smallmatrix}\right]$	$\left[\begin{smallmatrix}20 & 0\\ 0 & 1\end{smallmatrix}\right]$	6	$\left[\begin{smallmatrix}100 & 0\\ 0 & 10\end{smallmatrix}\right]$	$\left[\begin{smallmatrix}20 & 0\\ 0 & 1\end{smallmatrix}\right]$

to each other. This comparison included the first three variants from Table 6. The associated closed-loop trajectories of $\dot{m}_{\text{Ca}}^{\text{in}}$ and $\dot{m}_{\text{Byp}}$ are displayed in Figure 67 for four representative step changes. The most advantageous dynamics were accomplished with the initial weighting of variant 2. Firstly, an increased prioritization of the air supply control task with variant 3 resulted in an undershoot of $\dot{m}_{\text{Ca}}^{\text{in}}$ (Fig. 67d)). As a result, oxygen starvation might occur in the fuel cells. Secondly, the equal prioritization of both air mass flow control tasks with variant 1 significantly increased the response time of $\dot{m}_{\text{Ca}}^{\text{in}}$ during negative step changes in $\dot{m}_{\text{Ca}}^{\text{in,sp}}$. This increase resulted from a largely stationary operation of the bypass valve depicted in Figure 68. The application of variant 1 in the control cascade of Figure 3 would have substantially increased the response time of the superordinate FCS net power controller during negative step changes. Thus, the battery of the FCEV powertrain would have had to absorb more energy throughout this step change, which would have affected the necessary capacity of this battery. As a result, variant 1 of Table 6 was not an option for the explicit NMPC.

This conclusion additionally led to the other three weight matrix variants of Table 6 only including higher weights for the control deviation of $\dot{m}_{\text{Ca}}^{\text{in}}$. The closed-loop trajectories of

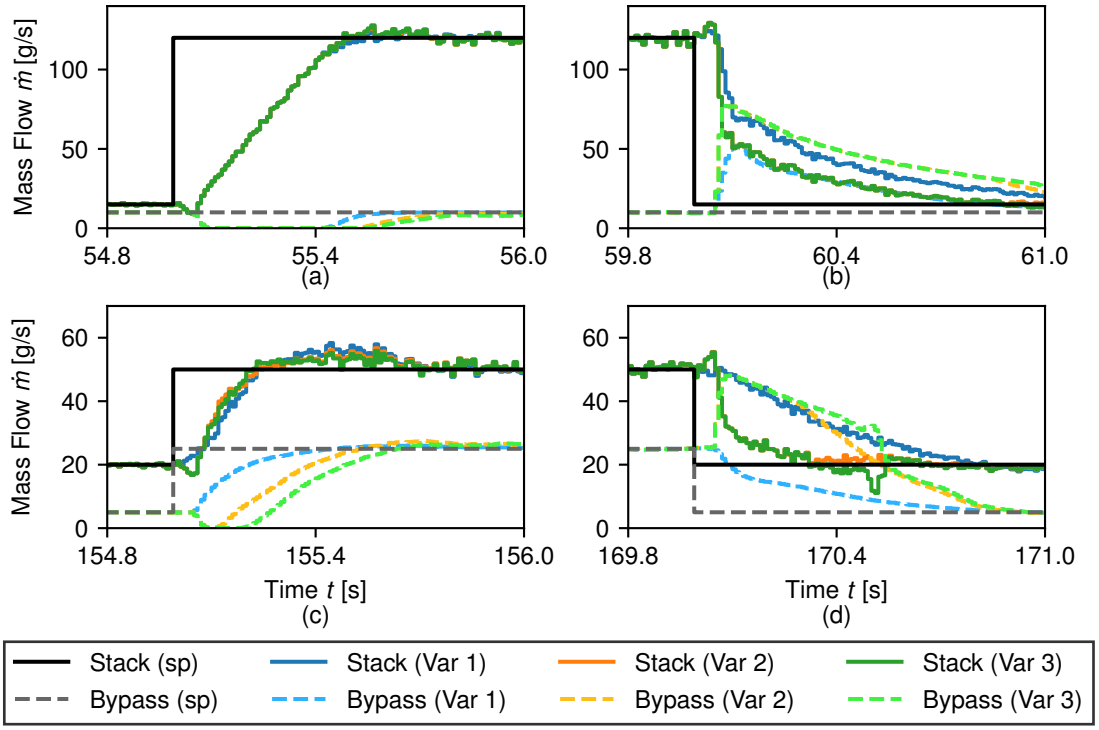

Figure 67: Air mass flows for closed-loop simulation results of the implicit nonlinear MPC with $N_y = 15$, $N_u = 1$, and variants 1, 2, and 3 from Table 6.

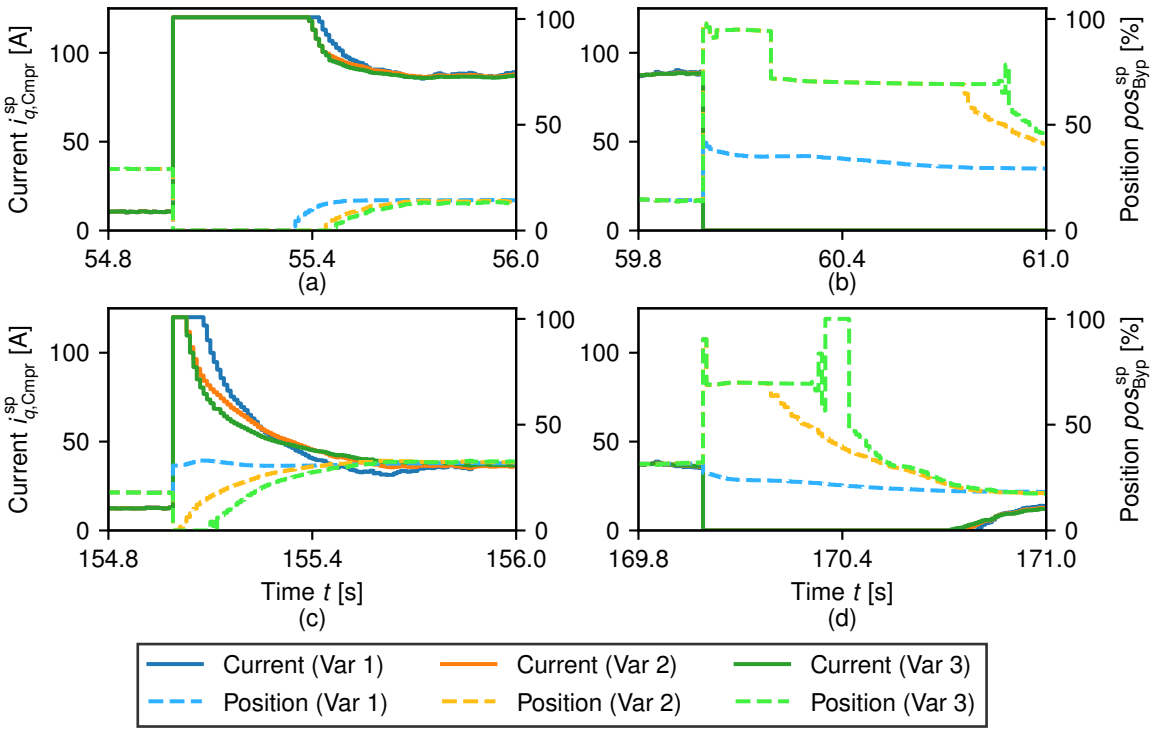

Figure 68: Control variables for closed-loop simulation results of the implicit nonlinear MPC with $N_y = 15$, $N_u = 1$, and variants 1, 2, and 3 from Table 6.

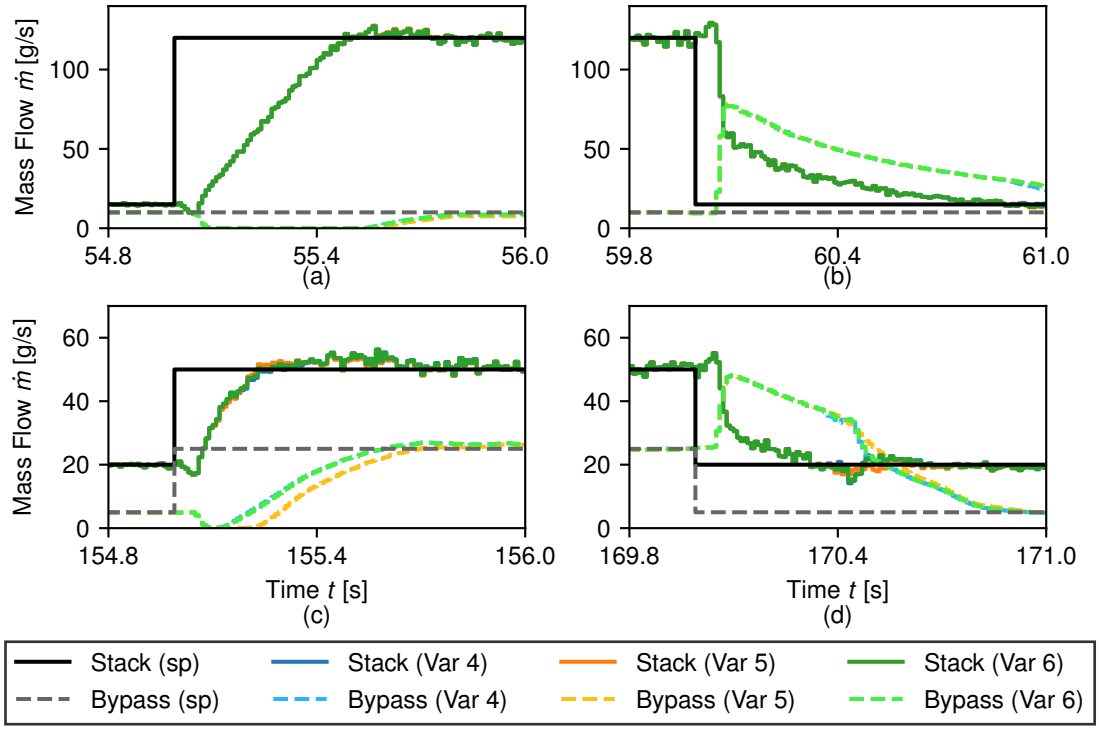

Figure 69: Air mass flows for closed-loop simulation results of the implicit nonlinear MPC with $N_y = 15$, $N_u = 1$, and variants 4, 5, and 6 from Table 6.

$\dot{m}_{\mathrm{Ca}}^{\mathrm{in}}$ and $\dot{m}_{\mathrm{Byp}}$ for variants 4, 5, and 6 of Table 6 are displayed in Figure 69. The dynamic behavior of the air mass flows was comparable for all three variants. By contrast, the closed-loop trajectories of the control variables in Figure 70 showed oscillations of $pos_{\mathrm{Byp}}^{\mathrm{sp}}$ for variants 4 and 6. These oscillations nevertheless did not impact the air mass flows and the dynamic response of P_{Cmpr}. Therefore, variants 4 and 6 were also considered viable training data candidates in the next section. This section covers the NN training to obtain approximated explicit NMPCs. Additionally, the impact of the cost function parameterization on the accuracy of the NNs was evaluated, which is why variants 2, 4, 5, and 6 were used to create training data sets.

6.5 Validation of Explicit Nonlinear Model Predictive Controller in Simulation

In this work, the explicit solution $\boldsymbol{u}(\boldsymbol{\theta})$ of the NMPC optimization problem was approximated with a NN. This approximation enabled the real-time capability of the proposed control approach. All NNs were set up and trained with Keras, an open-source deep learning application programming interface written in Python. However, the accumulation of training data and the validation of the trained NN controllers were conducted in MATLAB and Simulink with the implicit NMPC of Section 6.4 and the simulation model of Chapter 4.

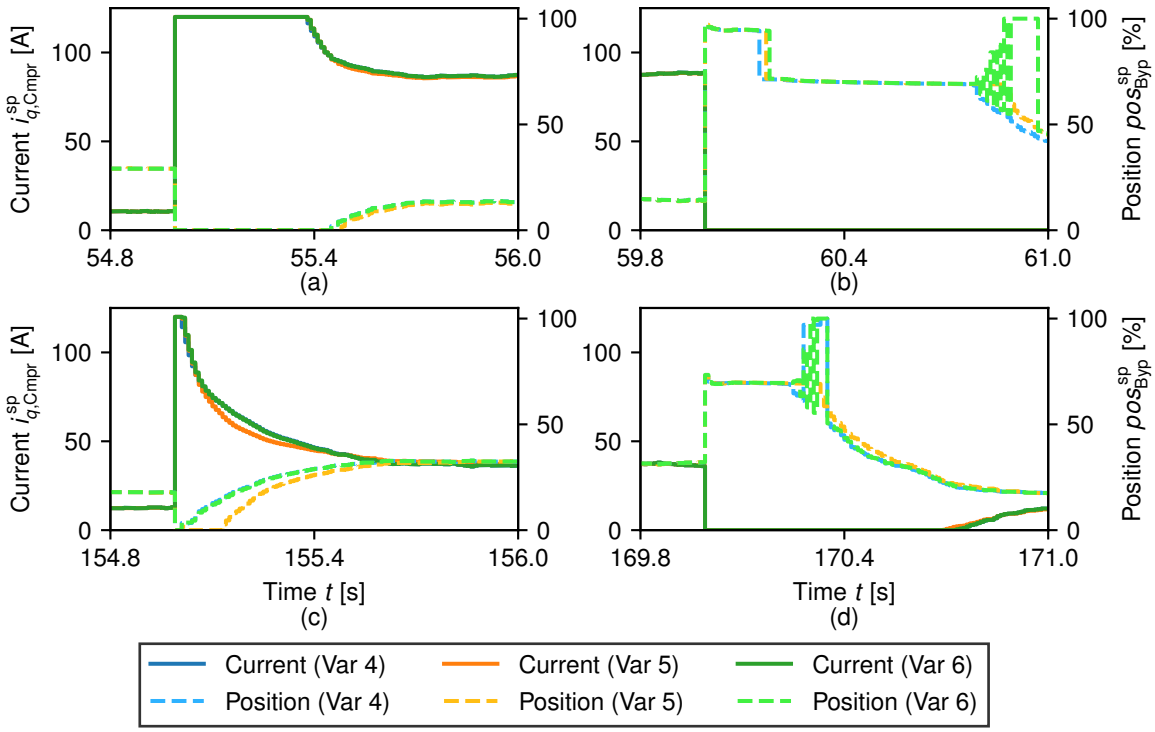

Figure 70: Control variables for closed-loop simulation results of the implicit nonlinear MPC with $N_y = 15$, $N_u = 1$, and variants 4, 5, and 6 from Table 6.

The training data of a NN has a significant impact on the accuracy of the trained NN. Thus, Latin hypercube sampling was applied to obtain a set of $\boldsymbol{\theta}$ with a uniform distribution over $\boldsymbol{\Theta}$. The states x_4 and x_5 were the only elements of $\boldsymbol{\theta}$ that were not considered independent variables of this sampling. Instead, the values of x_4 and x_5 were determined from the sampled values of x_2, which accounted for the correlation between the air pressures in the cathode subsystem and the rotational speed of the air compressor. Eventually, $\boldsymbol{U}^*$ was calculated for all $\boldsymbol{\theta}$ in a training data set.

In this work, a total of 45 unique training data sets were created. These data sets differed regarding their size and the parameterization of J. For each training data set, three different NN setups were tested. In preliminary studies, different combinations of the activation functions of Figure 1 were evaluated. Ultimately, NNs with three fully connected hidden layers with the ReLU activation function were used, which only differed in terms of the number of neurons per layer. Furthermore, the output layer consisted of two linear activation functions to avoid vanishing gradients during the training of the NN [48]. Every training was additionally repeated once to overcome the lack of determinism in the training process. Therefore, 270 NNs were trained and validated. The results of this validation are shown in Sections 6.5.1 and 6.5.2.

In preliminary studies, $pos_{\mathrm{Byp}}^{\mathrm{sp}} = 0\,\%$ emerged as the most challenging operating point to be learned by a NN. Thus, different target trajectories for $\dot{m}_{\mathrm{Ca}}^{\mathrm{in,sp}}$ and $\dot{m}_{\mathrm{Byp}}^{\mathrm{sp}}$ were employed to validate the NN controllers in closed-loop simulations. These trajectories are displayed in Figure 71. A second modification was the operating point with $\dot{m}_{\mathrm{Ca}}^{\mathrm{in,sp}} = 20\,\frac{\mathrm{g}}{\mathrm{s}}$ and

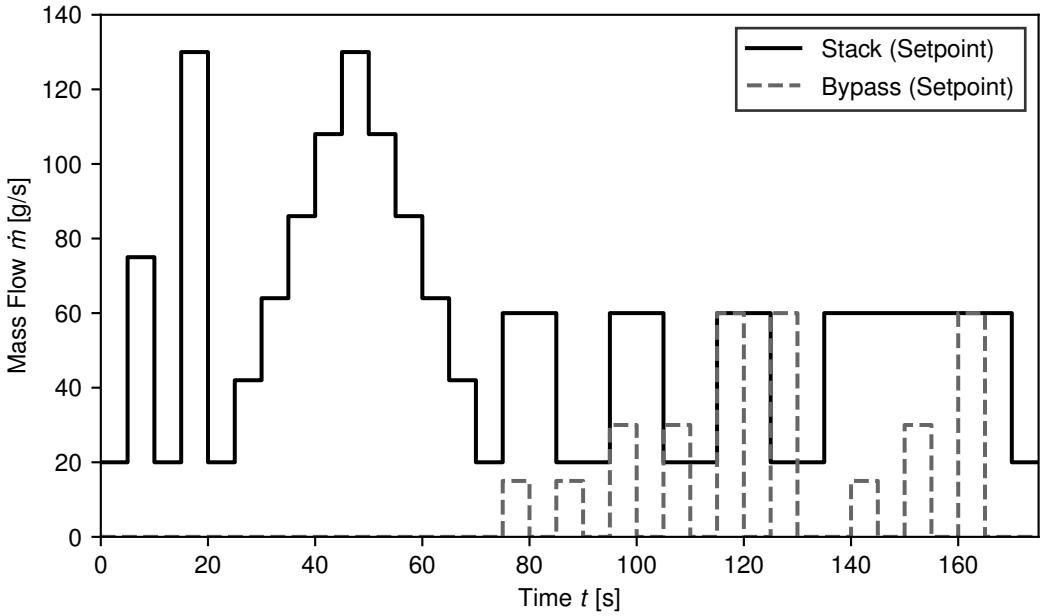

Figure 71: Target trajectories for $\dot{m}_{\mathrm{Ca}}^{\mathrm{in,sp}}$ and $\dot{m}_{\mathrm{Byp}}^{\mathrm{sp}}$ for validating the NN approximations of the explicit NMPC in closed-loop simulations.

$\dot{m}_{\mathrm{Byp}}^{\mathrm{sp}} = 60\,\frac{\mathrm{g}}{\mathrm{s}}$ in Figure 71. These two setpoints were impossible to reach simultaneously due to the physical limitations of the actuators. Nevertheless, this operating point was included to assess the behavior of the NN controllers when confronted with an infeasible setpoint combination.

The accuracy of each trained NN was determined by a root-mean-square error (RMSE). This error was calculated between the closed-loop trajectories of $\dot{m}_{\mathrm{Ca}}^{\mathrm{in,impl}}$ and $\dot{m}_{\mathrm{Byp}}^{\mathrm{impl}}$ of the implicit NMPC and $\dot{m}_{\mathrm{Ca}}^{\mathrm{in,expl}}$ and $\dot{m}_{\mathrm{Byp}}^{\mathrm{expl}}$ of the corresponding NN controller.

$$\mathrm{RMSE} = \sqrt{\frac{1}{n_{\mathrm{Data}} - 1} \cdot \sum_{i=0}^{n_{\mathrm{Data}}} \left(\dot{m}^{\mathrm{impl}}(i) - \dot{m}^{\mathrm{expl}}(i)\right)} \tag{6.15}$$

The mass flows were sampled with $\Delta t = 10\,\mathrm{ms}$. Therefore, each RMSE was comprised of $n_{\mathrm{Data}} = 17\,501$ data points.

6.5.1 Variation of Training Data for Neural Networks

At first, the impact of $\boldsymbol{P}$, $\boldsymbol{Q}$, and N_y on the accuracy of the trained NNs was examined. This examination included variants 2, 4, 5, and 6 from Table 6 and variant 5 with a shorter prediction horizon $N_y = 10$. The results are illustrated in Figure 72. Firstly, a longer prediction horizon seemingly improved the accuracy of the NNs for both air mass flows. Nevertheless, the wide error value spread prevented a distinct conclusion. Secondly, the prioritization of air supply control in J brought about a higher approximation accuracy of $\dot{m}_{\mathrm{Ca}}^{\mathrm{in}}$. Yet, the distinctly higher RMSE for $\dot{m}_{\mathrm{Byp}}$ might have also been caused by the considerable number of operating points with $\dot{m}_{\mathrm{Byp}}^{\mathrm{sp}} = 0\,\frac{\mathrm{g}}{\mathrm{s}}$

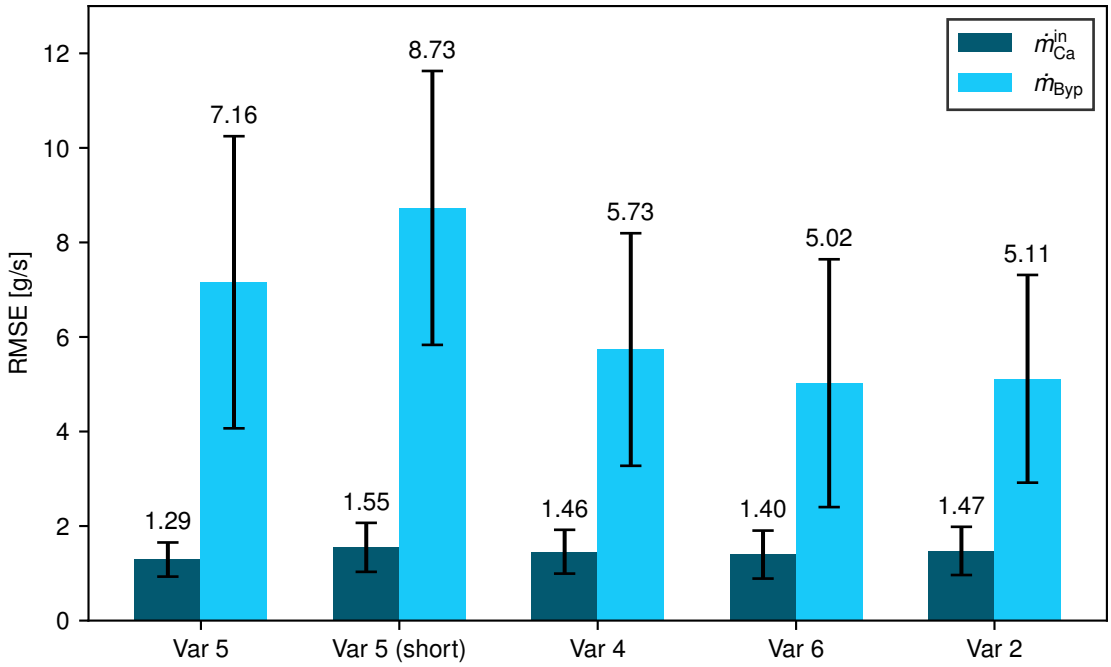

Figure 72: Average RMSE and corresponding standard deviation over 54 NNs for each of the five examined variants with different ***P***, ***Q***, and N_y.

in Figure 71. These operating points required the NN controller to operate at the lower control variable bound $pos^{\text{sp}}_{\text{Byp}} = 0\,\%$. The control variable saturation was, however, the most challenging part of the NMPC control law to be learned by the NNs. This difficulty was probably due to the lack of saturation in the linear output functions. Therefore, saturated output functions were tested in preliminary studies. This approach nonetheless failed to provide improvements, most likely as a result of the aforementioned problem of vanishing gradients.

In a second attempt to tackle this challenge, the application of a physically infeasible lower bound $pos^{\text{sp}}_{\text{Byp,Min}} < 0\,\%$ was investigated. The idea was to distribute all training data samples with $pos^{\text{sp}}_{\text{Byp,Min}} = 0\,\%$ across a small range better represented by the linear output functions. This work evaluated the two artificial lower bounds $pos^{\text{sp}}_{\text{Byp,Min}} = -5\,\%$ and $pos^{\text{sp}}_{\text{Byp,Min}} = -10\,\%$. The obtained average RMSEs are shown in Figure 73. Unfortunately, this second approach also failed to yield decisive improvements regarding the accuracy of the NNs.

A more significant correlation resulted from increasing the number of training data points from 120 000 to 480 000. The respective average RMSEs are depicted in Figure 74. Despite the high standard deviations of the error values, there is a strong possibility that the approximation accuracy is improved by increasing the number of training data points. These findings were especially promising for $\dot{m}_{\text{Byp}}$, because the lowest average RMSE for $\dot{m}_{\text{Byp}}$ in this section is found in Figure 74.

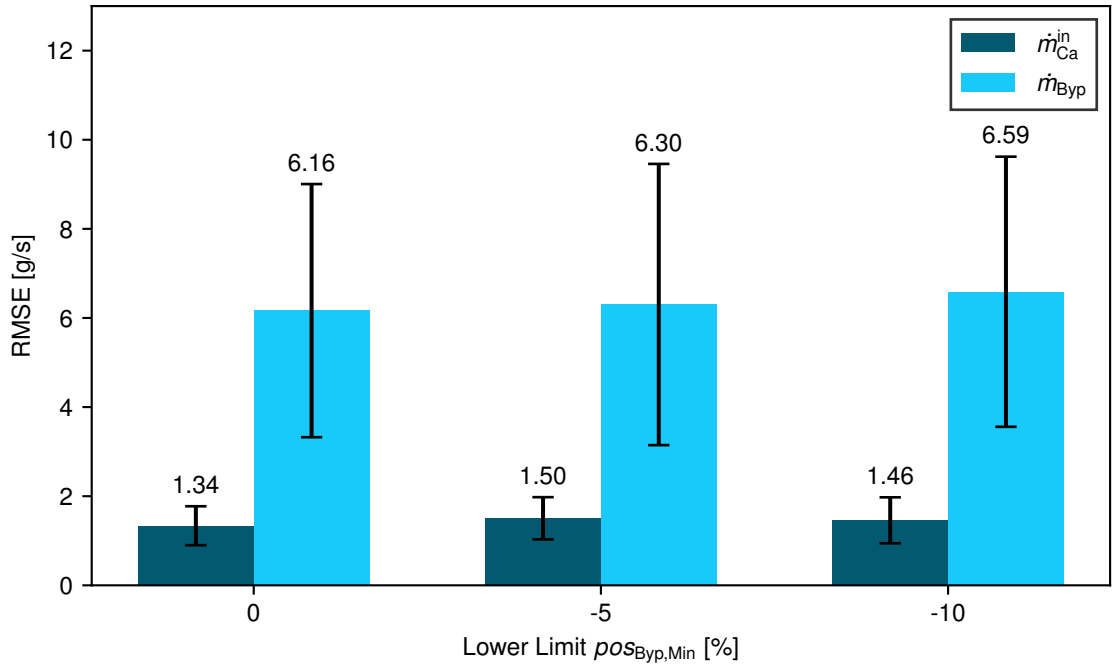

Figure 73: Average RMSE and corresponding standard deviation over 90 NNs for every examined lower bound $u_{2,Min}$.

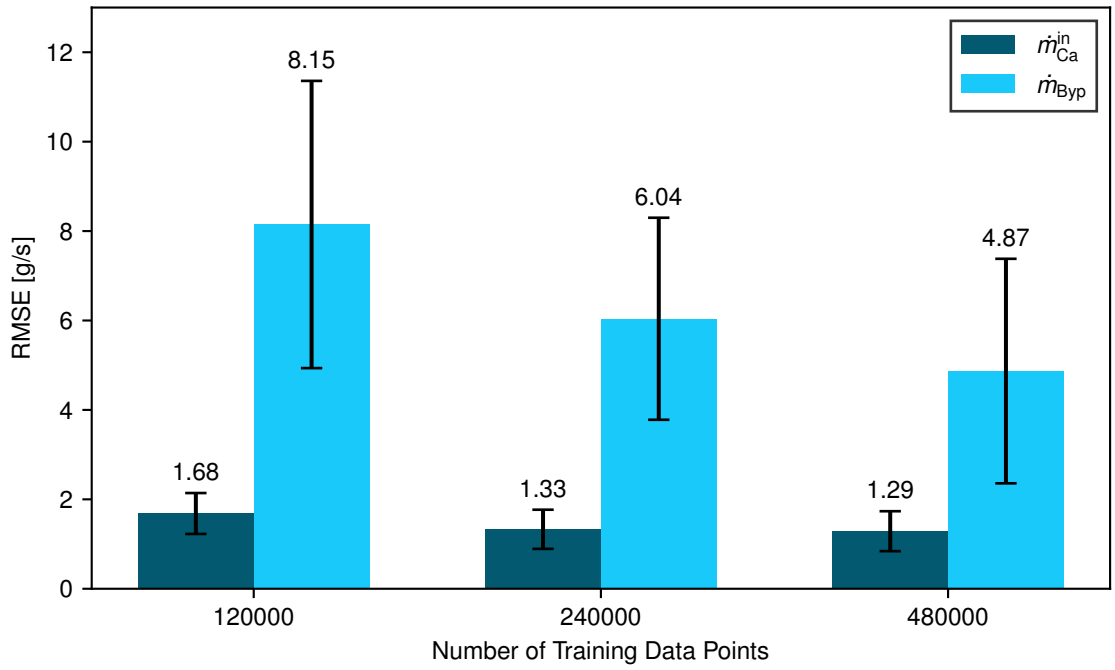

Figure 74: Average RMSE and corresponding standard deviation over 90 NNs for every examined size of the training data sets.

6.5.2 Variation of Neural Network Setup

By contrast, an increased number of neurons in every hidden layer did not impact the accuracy of the NNs at all. Figure 75 illustrates that the average RMSEs and

the associated standard deviations were almost identical for 64, 96 and 128 neurons, respectively. Additionally, a higher number of neurons equaled more function evaluations

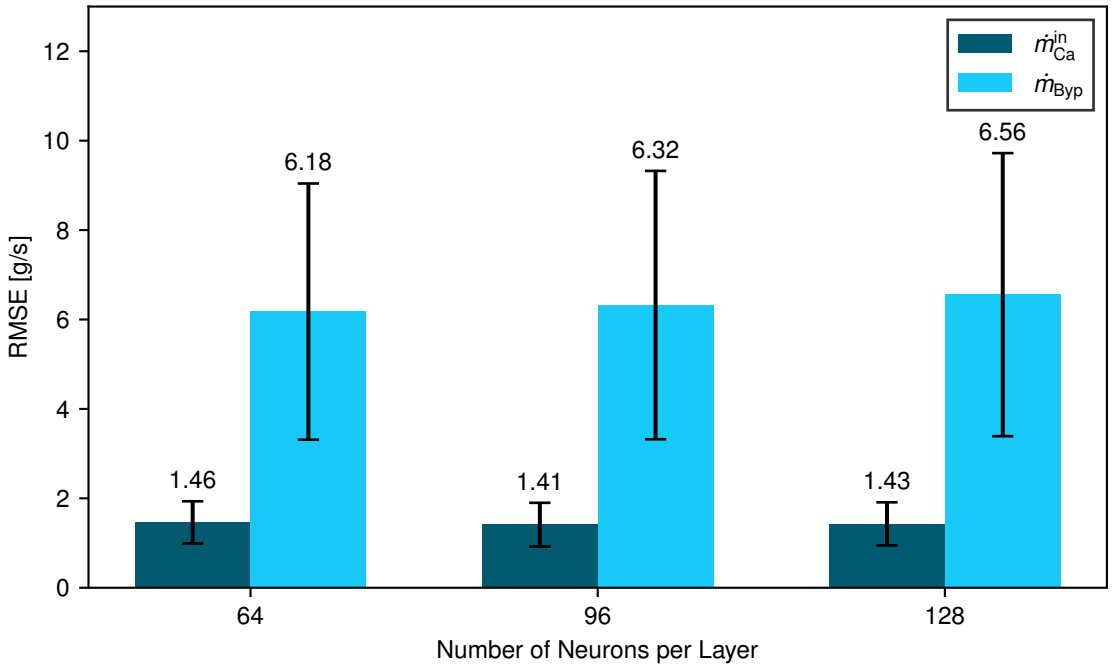

Figure 75: Average RMSE and corresponding standard deviation over 90 NNs for 64, 96, and 128 neurons in every hidden layer.

during one time step on the ECU, which increased the CPU core load of the proposed NN controller. In a preliminary test, this correlation culminated in a task overflow for a NN with 128 neurons in one hidden layer. Thus, on average, the best performance was achieved with NNs containing only 64 neurons in every hidden layer.

6.6 Validation of Explicit Nonlinear Model Predictive Controller on Fuel Cell System Test Stand

In the next step, the most accurate NN regarding $\dot{m}^{in}_{Ca}$ and the most accurate NN regarding $\dot{m}_{Byp}$ from Section 6.5 was implemented on the ECU. The detailed specifications of these two NNs are summarized in Table 7.

Table 7: Specifications of the two implemented NNs with the highest accuracy regarding $\dot{m}^{in}_{Ca}$ and $\dot{m}_{Byp}$.

Variant	RMSE ($\dot{m}^{in}_{Ca}$)	RMSE ($\dot{m}_{Byp}$)	NMPC	Neurons	Training data samples	$pos^{sp}_{Byp,Min}$
1	0.66 $\frac{g}{s}$	6.75 $\frac{g}{s}$	Var 5	96	240 000	0 %
2	1.88 $\frac{g}{s}$	1.13 $\frac{g}{s}$	Var 4	96	480 000	–5 %

6.6.1 Variation of Observer Gains

At first, on the FCS test stand, the observer gains for $\hat{\boldsymbol{d}}$ were altered to optimize the closed-loop behavior with the NN controllers. This optimization was conducted with the trajectories of $\dot{m}_{\mathrm{Ca}}^{\mathrm{in,sp}}$ and $\dot{m}_{\mathrm{Byp}}^{\mathrm{sp}}$ from Figure 42. The adjusted observer gains were the two non-zero elements of $\boldsymbol{L}_{\mathrm{d}}$ in Equation (6.9). Thus, only the combination of these two non-zero elements is given below to avoid a repeated presentation of the entire matrix. What is more, the nonlinear prediction model of the NMPC reduced the impact of $\hat{\boldsymbol{d}}$, which is why smaller observer gains were applied in comparison to the linear MPC.

On the FCS test stand, the three observer gain pairs [0.1, 0.1], [0.1, 0.01], and [0.05, 0.01] provided the best combination of robustness against sensor noise and a fast perturbation compensation. The associated comparison of the closed-loop trajectories of $\dot{m}_{\mathrm{Ca}}^{\mathrm{in}}$ and $\dot{m}_{\mathrm{Byp}}$ is displayed in Figure 76, containing four representative step changes for the first variant of Table 7. Firstly, Figure 76 highlights the inability of variant 1 to accurately

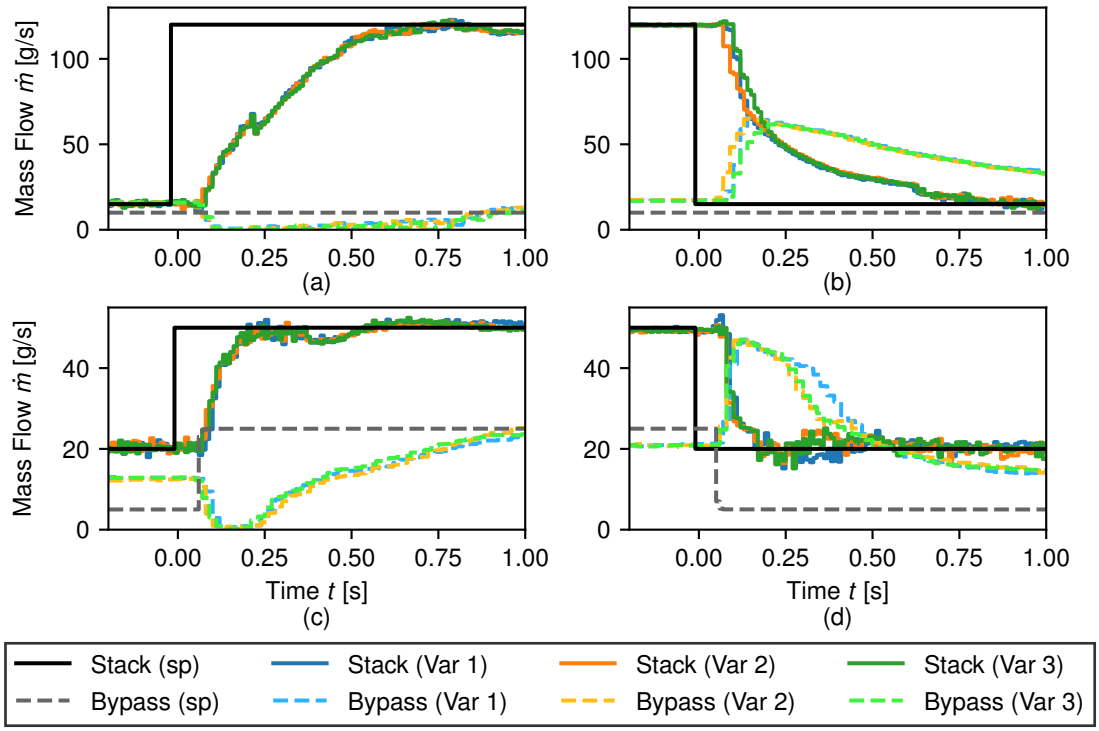

Figure 76: Air mass flows in the closed control loop with variant 1 of Table 7 as a result of the three different observer gains pairs [0.1, 0.1] (Var 1), [0.1, 0.01] (Var 2), and [0.05, 0.01] (Var 3).

control $\dot{m}_{\mathrm{Byp}}$. The implications of these stationary deviations are discussed in the next section in combination with the FCS net power controller. Secondly, the three different observer gain pairs did not significantly impact the dynamics in the closed control loop. Similar findings were obtained from the corresponding control variable trajectories shown in Figure 77. Hence, the observer gain pair [0.1, 0.01] was selected for the subsequent validation of the NN controllers in combination with the FCS net

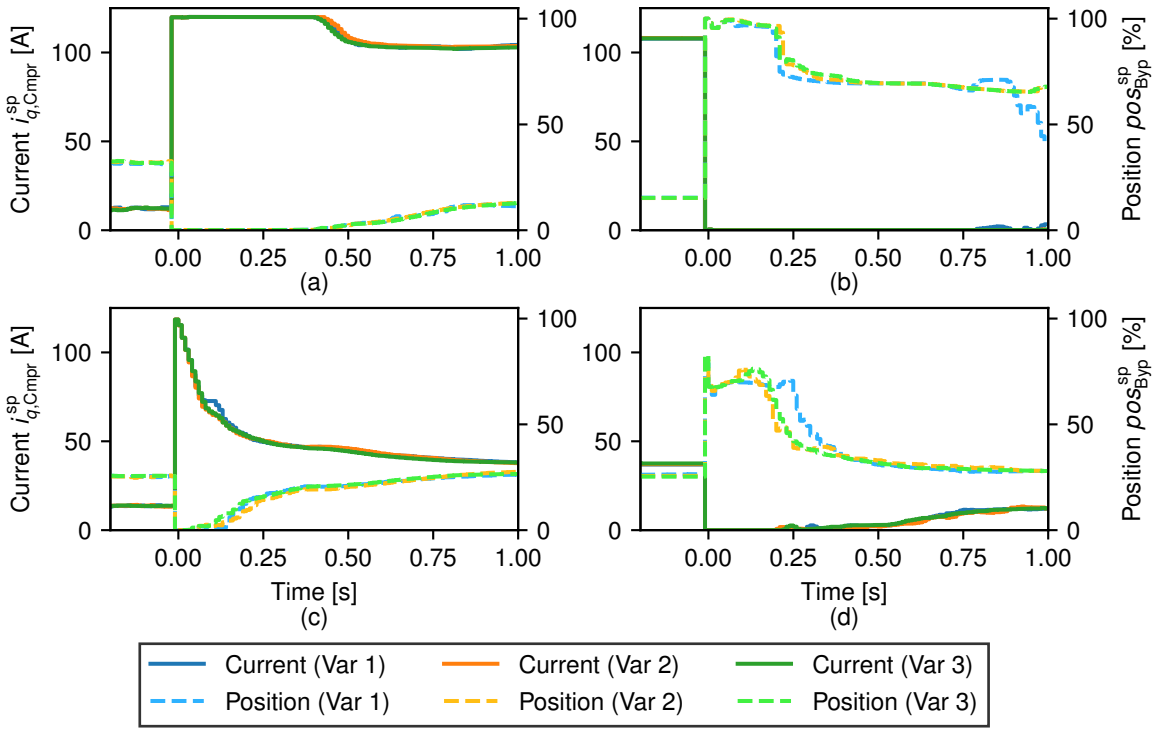

Figure 77: Control variables in the closed control loop with variant 1 of Table 7 as a result of the three different observer gains pairs [0.1, 0.1] (Var 1), [0.1, 0.01] (Var 2), and [0.05, 0.01] (Var 3).

power and hydrogen dilution controllers. On the one hand, the higher observer gain for $\hat{d}_1$ enabled a slightly faster perturbation compensation for $\dot{m}_{\mathrm{Ca}}^{\mathrm{in}}$ that was beneficial for the FCS net power controller. On the other hand, the smaller observer gain for $\hat{d}_2$ promised better compensation for the bypass leakage, which had been one of the primary motivations for implementing the explicit NMPC.

The findings were almost identical for the second variant of Table 7. Therefore, the corresponding results did not add substantial value to this work, which is why they are not displayed in this section.

6.6.2 Validation in Combination with Fuel Cell System Net Power and Hydrogen Dilution Controller

In the next step on the FCS test stand, the proposed NN-based controller was integrated into the FCS net power and hydrogen dilution controller cascade. The accompanying closed-loop behavior was validated with a step profile of $P_{\mathrm{FCS}}^{\mathrm{sp}}$, depicted in Figure 78. Additionally, the trajectories of $\dot{m}_{\mathrm{Ca}}^{\mathrm{in,sp}}$ and $\dot{m}_{\mathrm{Byp}}^{\mathrm{sp}}$ for variant 1 of Table 7 were displayed in Figure 78 since these trajectories changed for every implemented air mass flow controller. The constant setpoint $\dot{m}_{\mathrm{Byp}}^{\mathrm{sp}} = 0\,\frac{\mathrm{g}}{\mathrm{s}}$ was the result of a permanent control deviation of $\dot{m}_{\mathrm{Byp}}$. This deviation is depicted in Figures 79 and 80. The superordinate hydrogen dilution controller only requested $\dot{m}_{\mathrm{Byp}}^{\mathrm{sp}} > 0\,\frac{\mathrm{g}}{\mathrm{s}}$ to ensure a sufficient air mass flow in

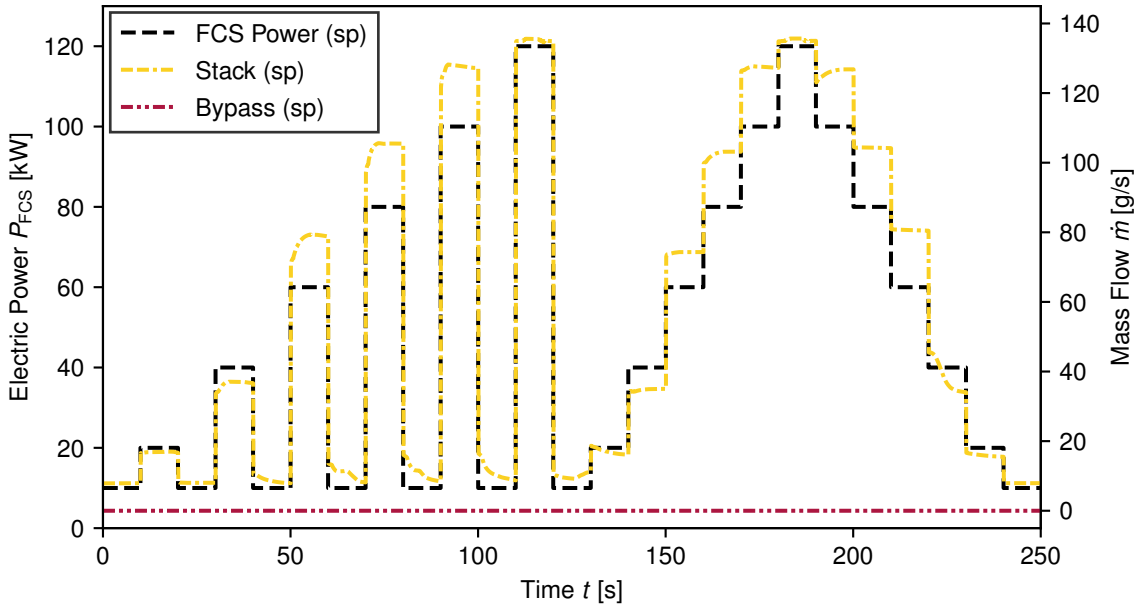

Figure 78: Step changes of P_{FCS}^{sp} for the validation of the first explicit NMPC of Table 7 in the FCS net power and hydrogen dilution control cascade with the corresponding values of $\dot{m}_{Ca}^{in,sp}$ and $\dot{m}_{Byp}^{sp}$.

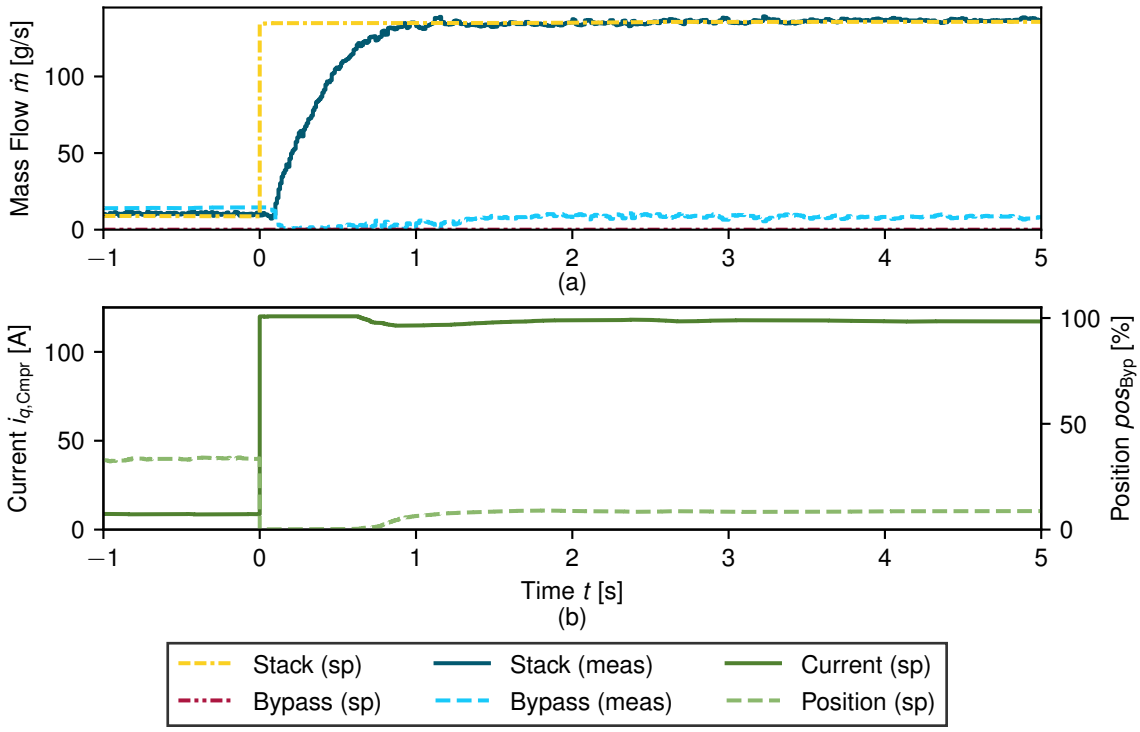

Figure 79: Measured air mass flows and control variables in the closed control loop with the first explicit NMPC of Table 7 and on the FCS test stand for the step change from $P_{FCS}^{sp} = 10\,\text{kW}$ to $P_{FCS}^{sp} = 120\,\text{kW}$.

the cathode exhaust for the dilution of hydrogen in the purge gas. This criterion was always fulfilled in Figures 79 and 80 due to a permanently open cathode bypass valve.

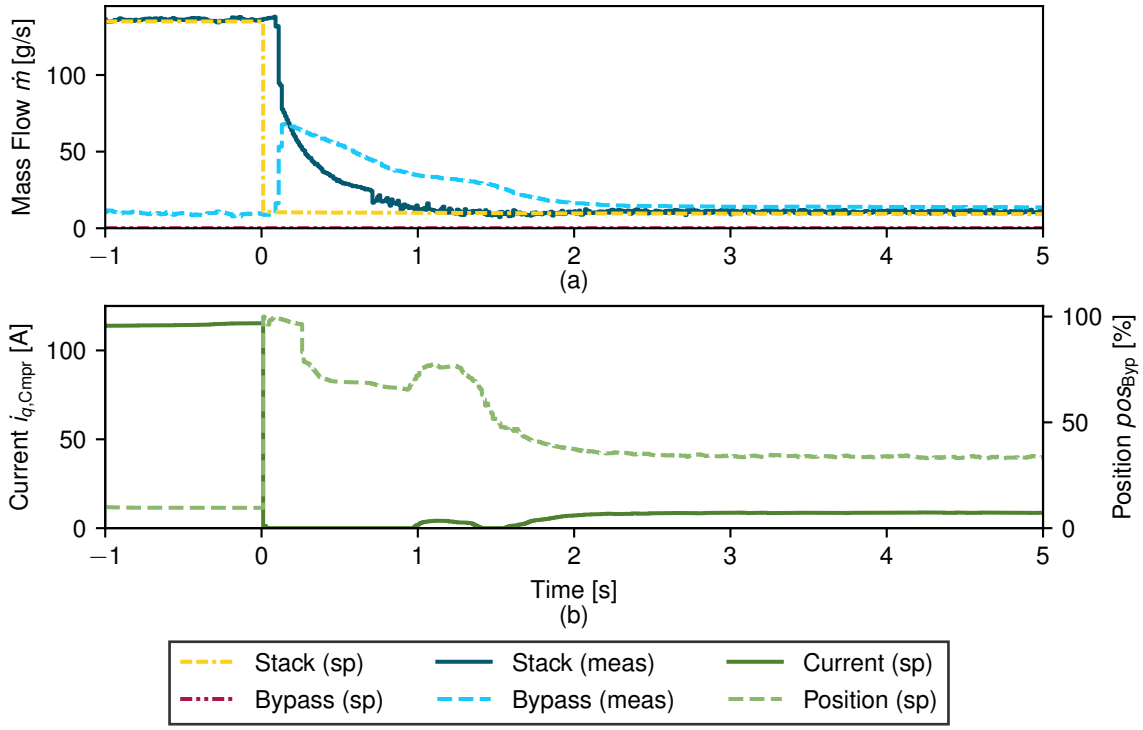

Figure 80: Measured air mass flows and control variables in the closed control loop with the first explicit NMPC of Table 7 and on the FCS test stand for the step change from $P_{\mathrm{FCS}}^{\mathrm{sp}} = 120\,\mathrm{kW}$ to $P_{\mathrm{FCS}}^{\mathrm{sp}} = 10\,\mathrm{kW}$.

The bypass valve was not closed even at a setpoint of $\dot{m}_{\mathrm{Byp}}^{\mathrm{sp}} = 0\,\frac{\mathrm{g}}{\mathrm{s}}$. This stationary control deviation was negligible for small $\dot{m}_{\mathrm{Ca}}^{\mathrm{in,sp}}$ that would have required additional air for hydrogen dilution. Conversely, $\dot{m}_{\mathrm{Byp}} = 10\,\frac{\mathrm{g}}{\mathrm{s}}$ was redundant for high values of $\dot{m}_{\mathrm{Ca}}^{\mathrm{in,sp}}$. The accompanying higher power consumption of the air compressor instead reduced the efficiency of the FCS. In the FCEV, a smaller FCS efficiency would lower the vehicle range, making this powertrain technology a less viable alternative to BEVs.

Therefore, the second explicit NMPC of Table 7 was better suited for the application in the FCEV. This NN controller variant was also validated with the step profile of $P_{\mathrm{FCS}}^{\mathrm{sp}}$ from Figure 78. The profile of $P_{\mathrm{FCS}}^{\mathrm{sp}}$ and the corresponding trajectories of $\dot{m}_{\mathrm{Ca}}^{\mathrm{in,sp}}$ and $\dot{m}_{\mathrm{Byp}}^{\mathrm{sp}}$ are shown in Figure 81. The values of $\dot{m}_{\mathrm{Byp}}^{\mathrm{sp}}$ changed over time on account of a proper bypass control, which is displayed in Figures 82 and 83. Additionally, $\dot{m}_{\mathrm{Ca}}^{\mathrm{in}}$ was precisely controlled within the noise bandwidth of the mass flow sensors. Apart from the stationary accuracy, the explicit NMPC also exploited the full dynamic potential of the cathode subsystem. The NN approximation pushed the control variables to their respective boundaries and, at the same time, avoided overshoots and undershoots for $\dot{m}_{\mathrm{Ca}}^{\mathrm{in}}$. Another advantage of the explicit NMPC was the absence of oscillations for $i_{q,\mathrm{Cmpr}}^{\mathrm{sp}}$ and $pos_{\mathrm{Byp}}^{\mathrm{sp}}$ despite the sensor noise and the bypass leakage. This absence demonstrated the ability of the NN-based NMPC to compensate the bypass leakage, which had been the primary motivation for developing an explicit NMPC. As a result, the second variant of Table 7 was selected to validate the proposed NN controller in the BMW iX5 Hydrogen. The corresponding results are summarized in the next section.

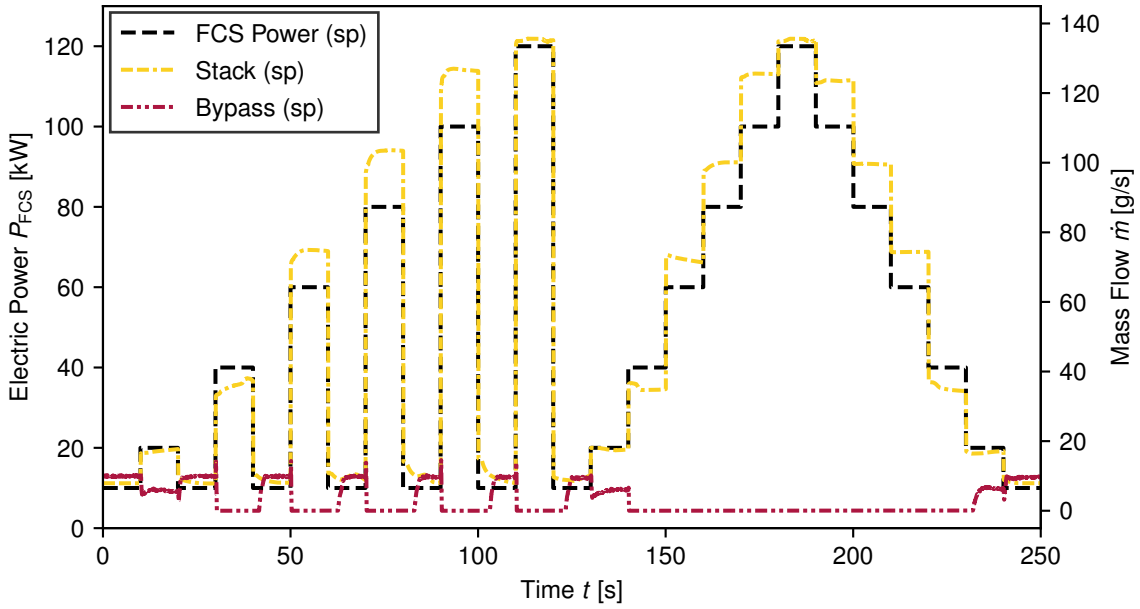

Figure 81: Step changes of P_{FCS}^{sp} for the validation of the second explicit NMPC of Table 7 in the FCS net power and hydrogen dilution control cascade with the corresponding values of $\dot{m}_{Ca}^{in,sp}$ and $\dot{m}_{Byp}^{sp}$.

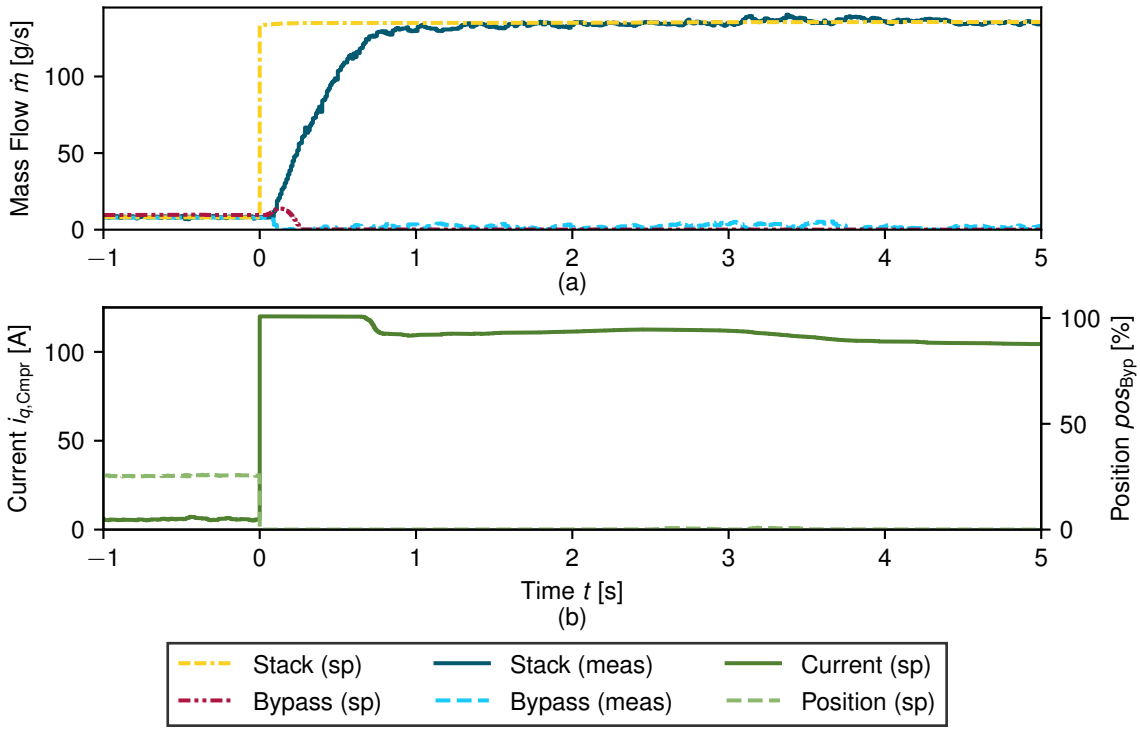

Figure 82: Measured air mass flows and control variables in the closed control loop with the second explicit NMPC of Table 7 and on the FCS test stand for the step change from $P_{FCS}^{sp} = 10\,\text{kW}$ to $P_{FCS}^{sp} = 120\,\text{kW}$.

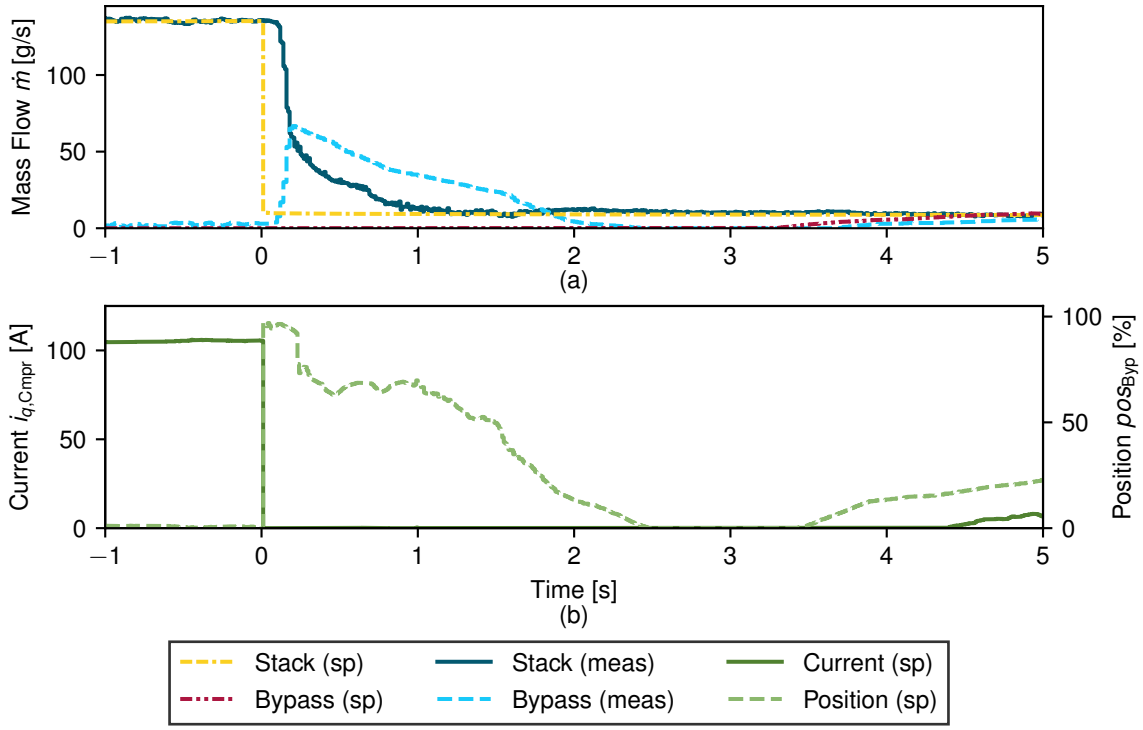

Figure 83: Measured air mass flows and control variables in the closed control loop with the second explicit NMPC of Table 7 and on the FCS test stand for the step change from $P_{\mathrm{FCS}}^{\mathrm{sp}} = 120\,\mathrm{kW}$ to $P_{\mathrm{FCS}}^{\mathrm{sp}} = 10\,\mathrm{kW}$.

6.7 Validation of Explicit Nonlinear Model Predictive Controller in Fuel Cell Electric Vehicle

In the closed control loop of the FCEV, the values of $\dot{m}_{\mathrm{Ca}}^{\mathrm{in,sp}}$ changed less rapidly compared to the final validation on the FCS test stand. Thus, a fast perturbation compensation was more relevant than exploiting the control variable boundaries. This controller requirement was fully met by the explicit NMPC, as shown in the measurement excerpt of Figure 84. Only one significant deviation occurred between $\dot{m}_{\mathrm{Ca}}^{\mathrm{in}}$ and $\dot{m}_{\mathrm{Ca}}^{\mathrm{in,sp}}$ with the explicit NMPC during the test drive in the BMW iX5 Hydrogen. This deviation is shown in the measurement excerpt of Figure 85. It is reasonable to assume that this control deviation originated from an approximation error of the NN. The nonlinear prediction model generally underestimated $\dot{m}_{\mathrm{AirFil}}$. Thus, the exact NMPC would most likely have caused an overshoot of $\dot{m}_{\mathrm{Ca}}^{\mathrm{in}}$ rather than the displayed initial undershoot. Apart from this controller error, the proposed NN-based NMPC performed as intended. The cathode bypass valve was purposefully used to reduce $\dot{m}_{\mathrm{Ca}}^{\mathrm{in}}$ more quickly, and $i_{q,\mathrm{Cmpr}}$ did not oscillate during stationary operation.

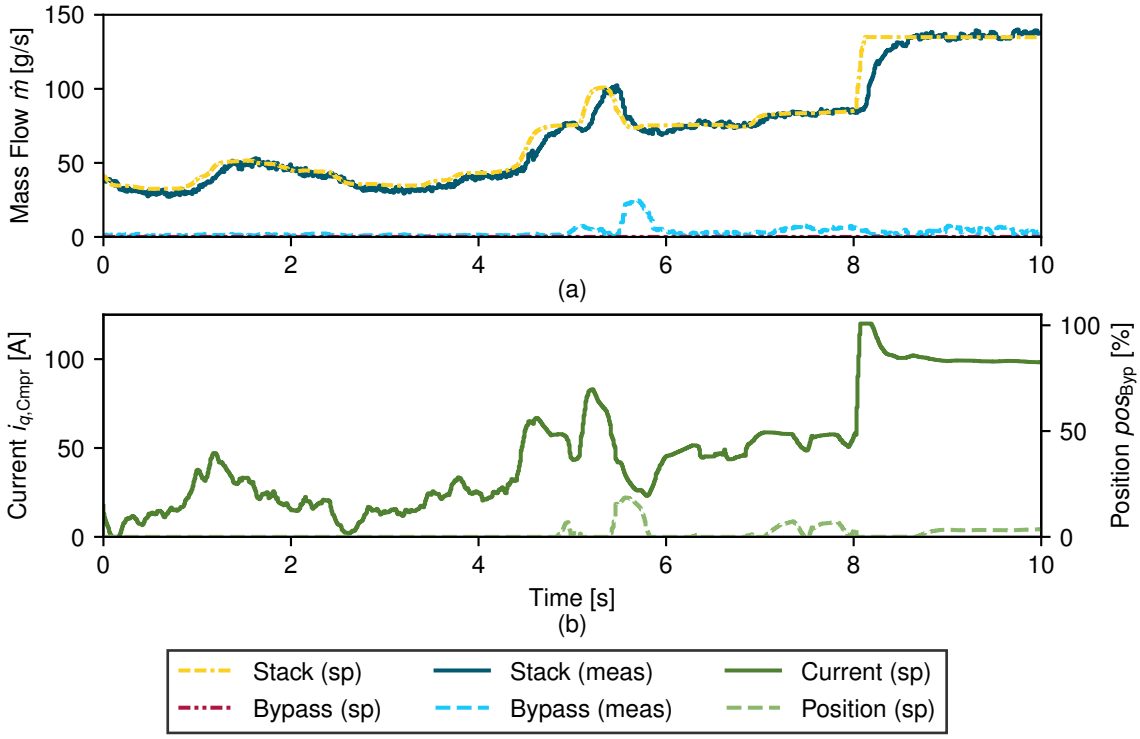

Figure 84: First excerpt of measured air mass flows and control variables in the closed control loop of the FCEV with the second explicit NMPC of Table 7.

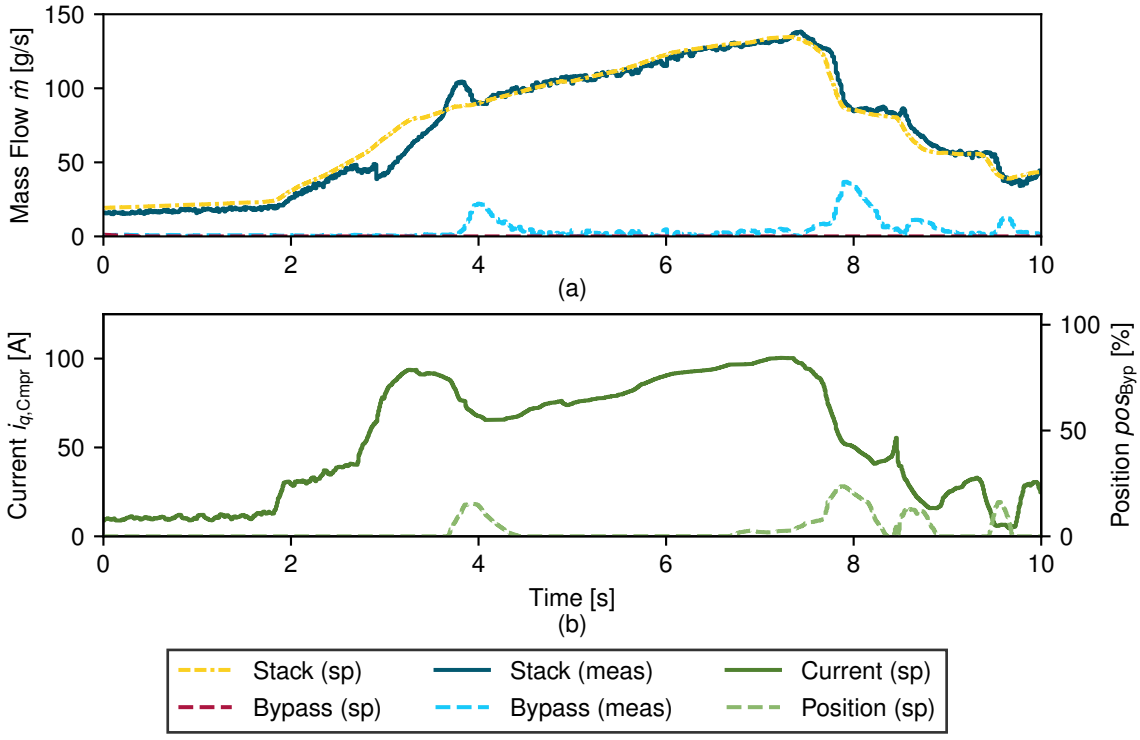

Figure 85: Second excerpt of measured air mass flows and control variables in the closed control loop of the FCEV with the second explicit NMPC of Table 7.

7 Comparison of Control Approaches for Air Mass Flow Control

The main goal of this work was to improve the air supply and bypass control of the BMW iX5 Hydrogen, which was initially carried out by two adaptive PI controllers. Thus, an explicit linear MPC and an explicit NMPC were implemented and validated on the FCS test stand and in the FCEV. Eventually, a comparison of the two MPCs and the PI controllers was conducted to determine the most suitable control approach concerning dynamics, robustness, and reusability. This comparison required reproducible setpoint profiles, so the measurements were only carried out on the FCS test stand. Firstly, the closed-loop behavior was compared for step changes of $\dot{m}_{\mathrm{Ca}}^{\mathrm{in,sp}}$ and $\dot{m}_{\mathrm{Byp}}^{\mathrm{sp}}$. The main results of this comparison are summarized in Section 7.1. Secondly, the impact on the FCS net power and the hydrogen dilution control cascade was evaluated. The differences in the closed-loop behavior are highlighted in Section 7.2. Lastly, conclusive remarks on the three examined control approaches are made in Section 7.3.

7.1 Comparison of Response to Steps in Air Mass Flow Setpoints

The initial comparison of the closed-loop behavior was conducted with the trajectories of $\dot{m}_{\mathrm{Ca}}^{\mathrm{in,sp}}$ and $\dot{m}_{\mathrm{Byp}}^{\mathrm{sp}}$ from Figure 42. The main differences between the PI controllers, the linear MPC, and the NMPC regarding the air mass flows are summarized in Figure 86 for four representative step changes.

Despite the permanent control deviation of $\dot{m}_{\mathrm{Byp}}$, which is most pronounced in Figure 86c), the explicit NMPC outperformed the PI controllers. Similarly, the explicit linear MPC was a considerably faster air supply controller than the corresponding PI controller. One advantage of MPC is its capability to handle MIMO systems, mainly demonstrated with the air mass flow trajectories in Figure 86c). The simultaneous rise of $\dot{m}_{\mathrm{Byp}}^{\mathrm{sp}}$ perturbed the air supply control. However, this perturbation was fully compensated by the linear MPC and compensated mainly by the NMPC using the cross-coupling properties of the prediction model. By contrast, the rise of $\dot{m}_{\mathrm{Byp}}$ significantly prolonged the adjustment of $\dot{m}_{\mathrm{Ca}}^{\mathrm{in}}$ with the PI controller. What is more, MPC enables the prioritization of air supply control over bypass control in the controller formulation. This prioritization led to the linear MPC and the NMPC temporarily disregarding $\dot{m}_{\mathrm{Byp}}^{\mathrm{sp}}$ during step changes to decrease the adjustment time of the air supply controller. The benefit was small for a rising $\dot{m}_{\mathrm{Ca}}^{\mathrm{in,sp}}$ displayed in Figure 86a), whereas

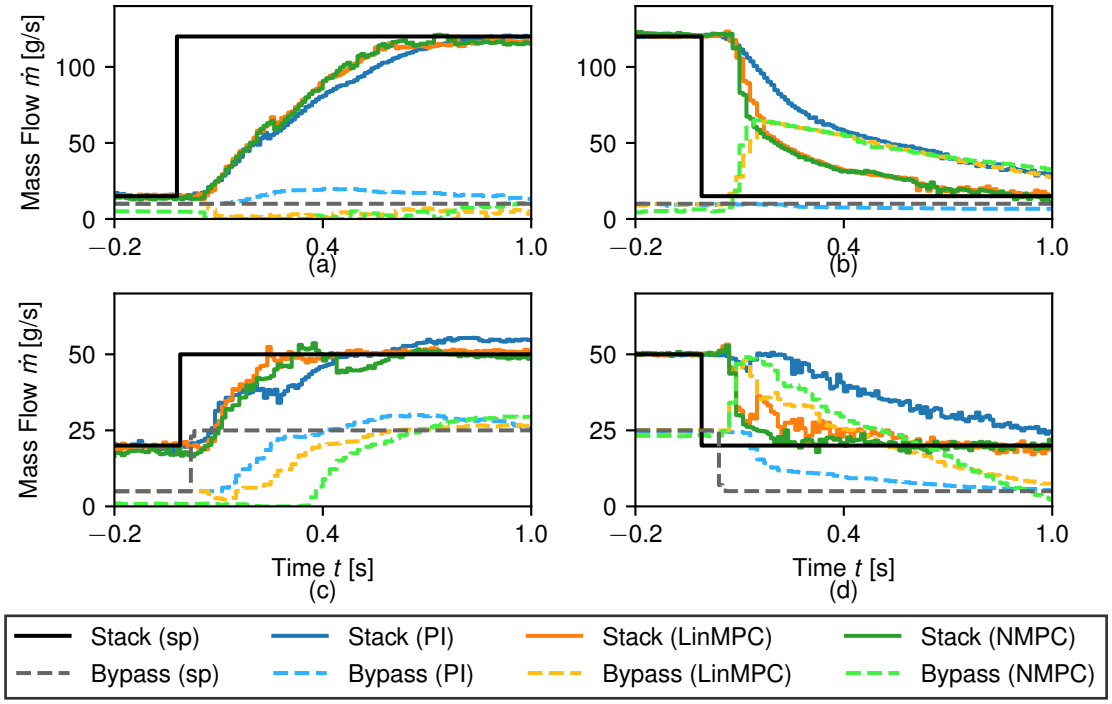

Figure 86: Four representative step changes of $\dot{m}_{\mathrm{Ca}}^{\mathrm{in,sp}}$ and $\dot{m}_{\mathrm{Byp}}^{\mathrm{sp}}$ to compare the closed-loop behavior of the air mass flows between the two PI controllers, the explicit linear MPC, and the explicit NMPC.

the reduction of $\dot{m}_{\mathrm{Ca}}^{\mathrm{in}}$ was considerably faster for the linear MPC and the NMPC, as shown in Figure 86b) and d).

This rapid reduction resulted from an instantly opened bypass valve, as highlighted by the associated control variable trajectories in Figure 87. Furthermore, the MPCs repeatedly resorted to the control variable boundaries $\boldsymbol{u}_{\mathrm{Min}} = [0\,\mathrm{A},\, 0\,\%]^T$ and $\boldsymbol{u}_{\mathrm{Max}} = [120\,\mathrm{A},\, 100\,\%]^T$ in Figure 87. Thus, the linear MPC and the NMPC exploited the full dynamic potential of the cathode subsystem, whereas the PI controllers often applied smaller changes to $i_{q,\mathrm{Cmpr}}^{\mathrm{sp}}$ and $pos_{\mathrm{Byp}}^{\mathrm{sp}}$.

In Figure 87b), the decrease of $i_{q,\mathrm{Cmpr}}^{\mathrm{sp}}$ was limited by the compressor surge line for the PI controllers. The corresponding air mass flow trajectories in the compressor map are shown in Figure 88 for the PI controllers, the linear MPC, and the NMPC. Despite the substantial distance to the surge line in Figure 88, a dynamic lower bound on the output $i_{q,\mathrm{Cmpr}}^{\mathrm{sp}}$ of PI controller was active during the step change. The considerable safety margin of this bound resulted from the high time delay $\Delta t = 50\,\mathrm{ms}$ for $i_{q,\mathrm{Cmpr}}^{\mathrm{sp}}$ that prevented a fast intervention at operating points close to the surge line. Thus, some of the dynamic potential of the cathode subsystem was lost with the PI controllers. The significant safety margin did not confine the linear MPC and the NMPC because the initial opening of the bypass valve reduced $p_{\mathrm{Cmpr}}^{\mathrm{out}}$ at once. As a result, the distance to the compressor surge line was further increased, which allowed the MPCs to instantly apply $i_{q,\mathrm{Cmpr}}^{\mathrm{sp}} = 0\,\mathrm{A}$.

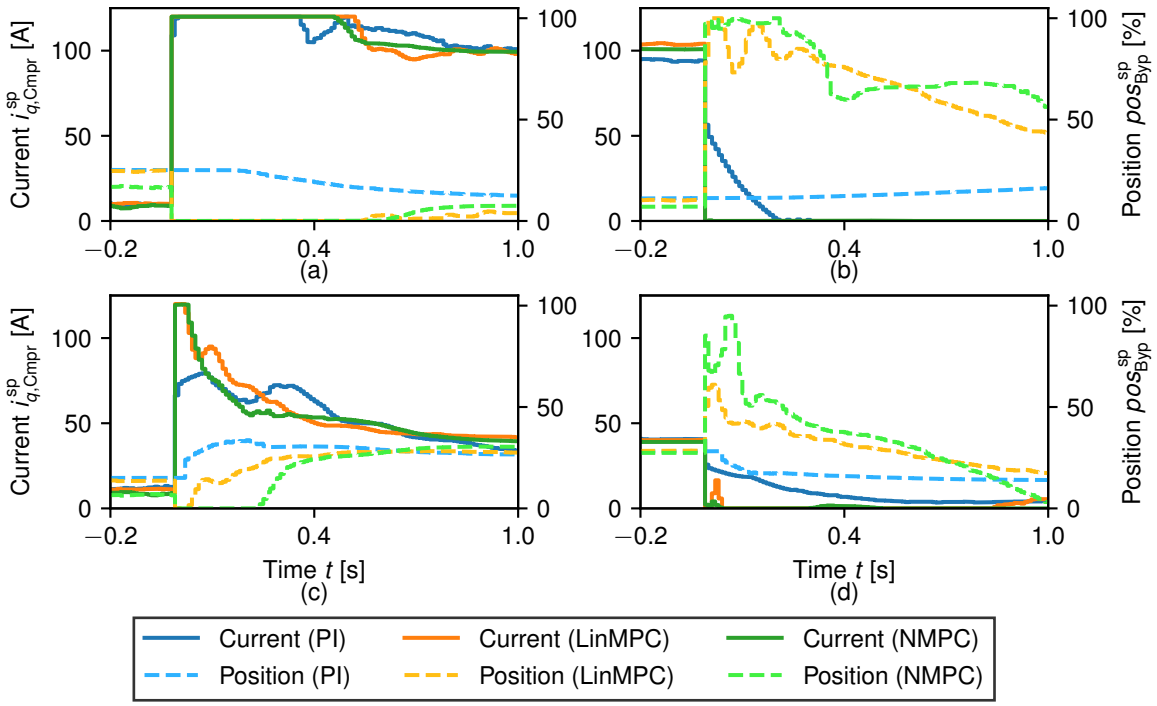

Figure 87: Four representative step changes of $\dot{m}_{\mathrm{Ca}}^{\mathrm{in,sp}}$ and $\dot{m}_{\mathrm{Byp}}^{\mathrm{sp}}$ to compare the closed-loop behavior of the control variables between the two PI controllers, the explicit linear MPC, and the explicit NMPC.

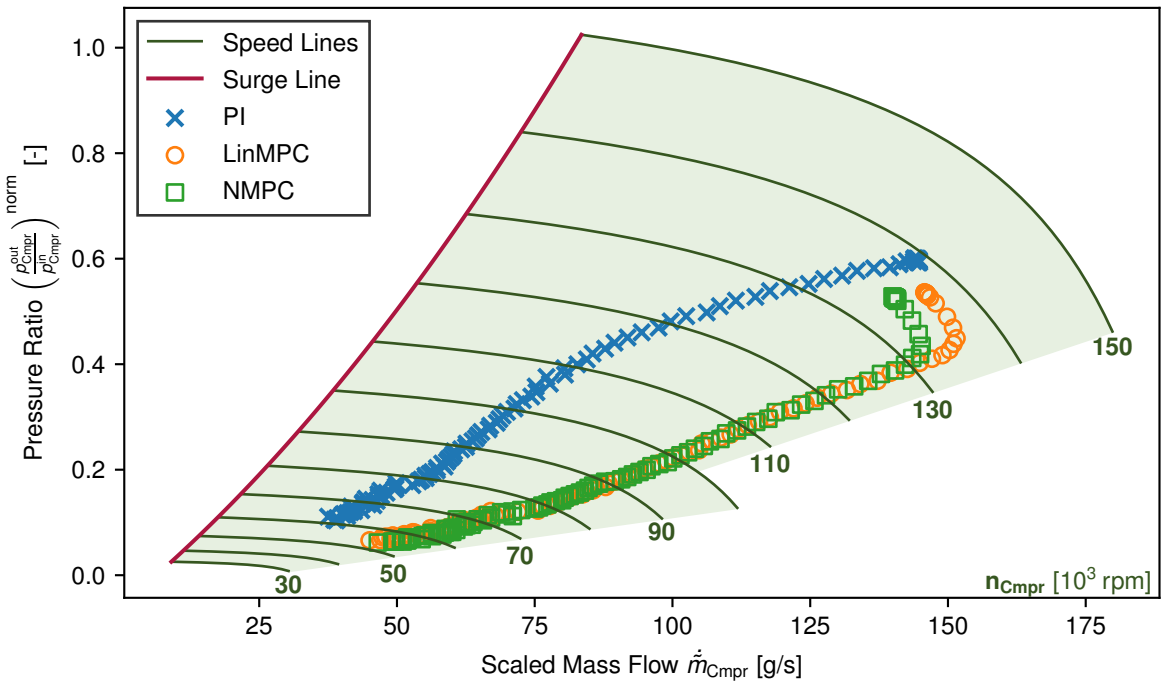

Figure 88: Comparison of the operating point trajectory in the compressor map for a step change from $\dot{m}_{\mathrm{Ca}}^{\mathrm{in,sp}} = 120\ \frac{\mathrm{g}}{\mathrm{s}}$ to $\dot{m}_{\mathrm{Ca}}^{\mathrm{in,sp}} = 15\ \frac{\mathrm{g}}{\mathrm{s}}$ with $\dot{m}_{\mathrm{Byp}}^{\mathrm{sp}} = 10\ \frac{\mathrm{g}}{\mathrm{s}}$ between the two PI controllers, the explicit linear MPC, and the explicit NMPC.

7.2 Comparison of Response to Steps in Fuel Cell System Net Power Setpoint

Air supply control was the limiting factor for a rapid dynamic response of P_{FCS} in the FCS of the BMW iX5 Hydrogen, which is why exploiting the full dynamic potential of the cathode subsystem was an essential requirement for successfully implementing an air mass flow controller. Section 7.1 demonstrated that the two adaptive PI controllers failed to meet this criterion. Hence, a step change detection algorithm on $P_{\mathrm{FCS}}^{\mathrm{sp}}$ had been included in the implementation of the two PI controllers before this work. This algorithm improved the corresponding closed-loop behavior of the cathode subsystem in the FCS net power and hydrogen dilution control cascade. First, a significant decrease in $P_{\mathrm{FCS}}^{\mathrm{sp}}$ was detected with a difference quotient. Then, the outputs of both controllers were replaced with predetermined values, taking advantage of the MIMO character of the cathode subsystem. Additionally, the bypass leakage was handled by replacing the actual sensor value with $\dot{m}_{\mathrm{Byp}}^{\mathrm{meas}} = 0\,\frac{\mathrm{g}}{\mathrm{s}}$ in the calculation of $\dot{m}_{\mathrm{Ca}}^{\mathrm{in}}$ for $pos_{\mathrm{Byp}}^{\mathrm{sp}} = 0\,\%$ and small values of pos_{Byp}, and disabling the bypass controller with a constant $pos_{\mathrm{Byp}}^{\mathrm{sp}} = 0\,\%$ for small values of $\dot{m}_{\mathrm{Byp}}^{\mathrm{sp}}$.

The resulting closed-loop behavior of the air mass flows was comparable to the dynamic responses of the cathode subsystem with the linear MPC and the NMPC. The remaining differences between the three control approaches were evaluated with the step profile of $P_{\mathrm{FCS}}^{\mathrm{sp}}$ from Figure 53. The main findings from this evaluation are represented by Figure 89, which displays the closed-loop trajectories of $\dot{m}_{\mathrm{Ca}}^{\mathrm{in}}$ and $\dot{m}_{\mathrm{Byp}}$ for the step changes from $P_{\mathrm{FCS}}^{\mathrm{sp}} = 10\,\mathrm{kW}$ to $P_{\mathrm{FCS}}^{\mathrm{sp}} = 120\,\mathrm{kW}$ and vice versa. Despite the additional step change detection, the NMPC still slightly outperformed the two PI controllers for the negative step change of $\dot{m}_{\mathrm{Ca}}^{\mathrm{in,sp}}$ in Figure 89b). Firstly, calculating the slope of $P_{\mathrm{FCS}}^{\mathrm{sp}}$ took a few time steps to calculate. Thus, the dynamic response of the PI controllers was delayed. This delay is also shown in Figure 90, which illustrates the associated trajectories of the control variables. Secondly, the sudden closing of the bypass valve at the end of the step change detection led to an overshoot in $\dot{m}_{\mathrm{Ca}}^{\mathrm{in}}$ for the PI controllers, highlighted in the zoomed area of Figure 89b). This overshoot demonstrated the inability of PI controllers to efficiently compensate for the disturbances imposed by the cross-coupling effects in the cathode subsystem. The behavior of a MIMO controller was only approximated with the step change detection. Moreover, the step change detection requires substantial calibrations for the considered FCS and has to be repeated after each hardware modification in the cathode subsystem. These adjustments need expert knowledge on the controlled plant and the overall operating strategy. By contrast, for the explicit NMPC, only the respective parameters of the nonlinear prediction model must be adjusted to the modified hardware, and the NN must be retrained to duplicate the closed-loop behavior of Figures 89 and 90. These two steps can be executed with automated scripts that do not require expert knowledge of the controlled plant. Furthermore, the development of the NN-based explicit NMPC is entirely independent of the overall operating strategy.

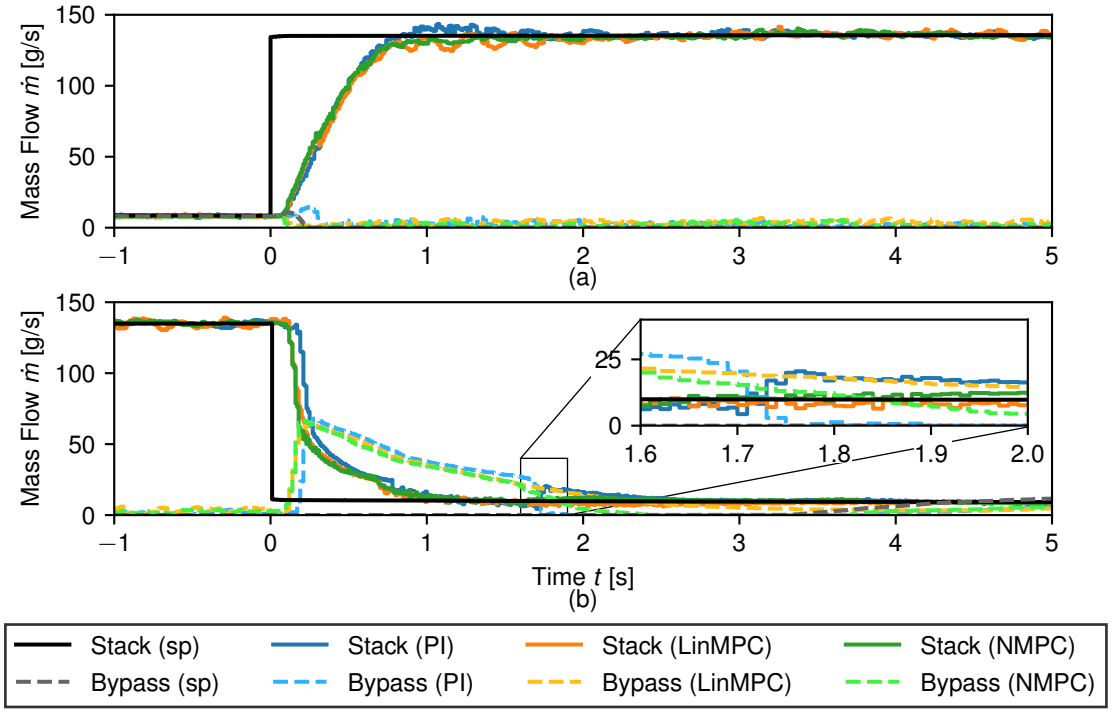

Figure 89: Two representative step changes of $P_{\mathrm{FCS}}^{\mathrm{sp}}$ for the comparison of the closed-loop behavior of the air mass flows between the two PI controllers, the explicit linear MPC, and the explicit NMPC.

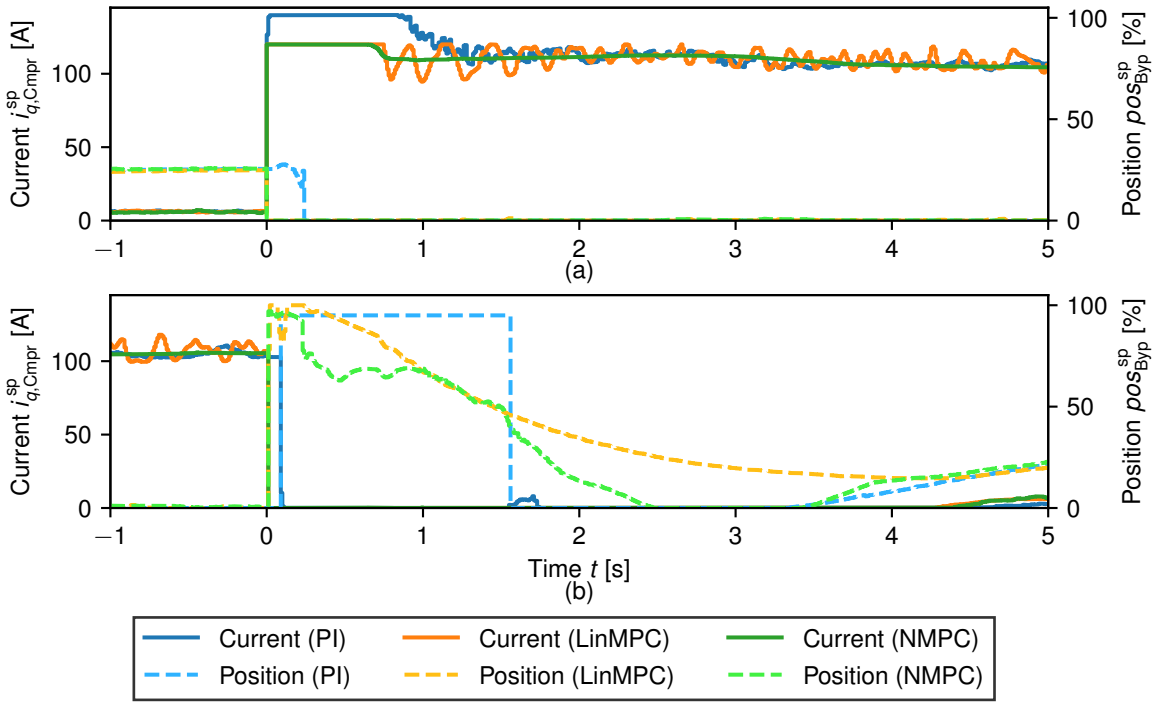

Figure 90: Two representative step changes of $P_{\mathrm{FCS}}^{\mathrm{sp}}$ to compare the closed-loop behavior of the control variables between the two PI controllers, the explicit linear MPC, and the explicit NMPC.

The dynamic behavior was comparable for the closed control loops with the linear MPC and the NMPC. However, the explicit NMPC better compensated the stationary bypass leakage, which caused significant oscillations in $\dot{m}_{\mathrm{Ca}}^{\mathrm{in}}$ for the linear MPC, as shown in Figure 89. These oscillations resulted from considerable oscillations in the trajectory of $i_{q,\mathrm{Cmpr}}^{\mathrm{sp}}$ in Figure 90. Consequently, P_{Cmpr} was oscillating, which further gave rise to oscillations in P_{FCS}, highlighted in the zoomed area of Figure 91. The oscillations

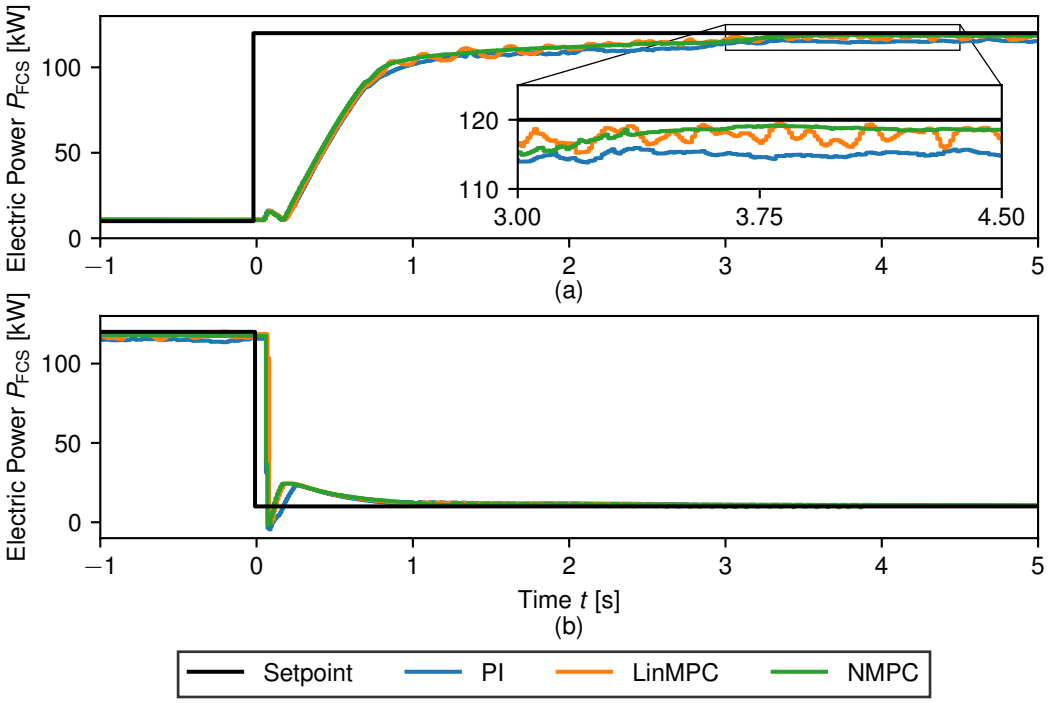

Figure 91: Two representative step changes of $P_{\mathrm{FCS}}^{\mathrm{sp}}$ to compare the closed-loop behavior of the FCS net power between the two PI controllers, the explicit linear MPC, and the explicit NMPC.

in P_{FCS} outweighed the availability of the exact explicit solution for the linear MPC, which prevented stationary control deviations.

Oscillations in $i_{q,\mathrm{Cmpr}}$ were also visible in Figure 90a) for the PI controllers. However, these oscillations were small enough to avoid a substantial impact on P_{FCS}, which is demonstrated in the zoomed area of Figure 91a). Thus, the PI controllers slightly outperformed the explicit linear MPC during stationary operation, especially at high system loads, whereas the linear MPC displayed a better dynamic response of $\dot{m}_{\mathrm{Ca}}^{\mathrm{in}}$ in Figure 89.

7.3 Conclusion

Overall, this work demonstrated that the NN approximation of an explicit NMPC outperforms an explicit linear MPC and adaptive PI controllers for the air mass flow control in the FCS of the BMW iX5 Hydrogen. Despite the small approximation errors

of the NN causing permanent control deviations of $\dot{m}_{\mathrm{Byp}}$, the NMPC provides the best combination of optimal dynamic responses during setpoint step changes and efficient perturbation compensation during stationary operation. Additionally, the high initial effort for setting up the explicit NMPC is outweighed by the transferability of this approach to modified systems. The transferability is also a significant advantage over the adaptive PI control approach with step change detection, which requires extensive fine-tuning for each system modification. This additional effort outweighs the easy implementation on an ECU and the possibility of tuning PI controllers in real-time. By contrast, the explicit NMPC and the explicit linear MPC both require closed-loop simulations to efficiently adjust the parameters of the cost function.

Another advantage of the NMPC is the straightforward extension to more control variables, which only necessitates the extension of the semi-empirical nonlinear prediction model. The next chapter demonstrates this advantage by extending the NMPC to include the FCS net power and the hydrogen dilution controllers.

8 Fuel Cell System Net Power and Hydrogen Dilution Control with Nonlinear Model Predictive Control

In this work, the response time of the air supply controller was minimized with NMPC. Nevertheless, the cascaded control structure of Figure 3 still limited the dynamics of the superordinate FCS net power controller. The FCS net power controller had to be seven to ten times slower than the air supply controller to attain an advantageous closed control loop [68]. Thus, merging the cascaded FCS net power, hydrogen dilution, and air mass flow controllers into one MIMO controller was likely to shorten the response time of P_{FCS}. The nonlinearity of the air mass flow and electric power correlations from Chapter 4 and the promising results from Chapter 7 further suggested the application of NMPC to the arising control task.

The fundamentals of this NMPC are presented in the following. At first, the nonlinear prediction model is introduced and validated in Section 8.1. This nonlinear prediction model was a prerequisite for the state and perturbation observer, presented in Section 8.2. Moreover, the nonlinear prediction model was essential to the cost function of the NMPC. In this work, four different variants of this cost function were developed, all of which are introduced in Section 8.3. Eventually, the implicit NMPC for FCS net power and hydrogen dilution control was evaluated in closed-loop simulations. The corresponding results are presented and discussed in Section 8.4. The subsequent steps would have been the fitting of a NN and the validation on the FCS test stand. However, these steps were out of the scope of this work.

8.1 Nonlinear Prediction Model

The FCS net power and hydrogen dilution controller was implemented as an extension of the air mass flow controller from Chapter 6. Thus, the discrete nonlinear prediction model of Section 6.1 was expanded to represent the dynamics of the new controlled variables $\boldsymbol{y} = [P_{\mathrm{FCS}},\, \lambda_{\mathrm{O_2}},\, \dot{m}_{\mathrm{Dil}}]^T$ subject to changes in the available control variables $\boldsymbol{u} = \left[i_{q,\mathrm{Cmpr}}^{\mathrm{sp}},\, pos_{\mathrm{Byp}}^{\mathrm{so}},\, I_{\mathrm{Stck}}^{\mathrm{sp}}\right]^T$. The additional stationary correlations for the electric powers were taken from Section 4.3.

8.1.1 Model Equations

Expanding the nonlinear prediction model from Section 6.1 included the simplifications from Section 6.1.1. Thus, $p_{\mathrm{O_2}}$ was calculated from $p^{\mathrm{out}}_{\mathrm{Cmpr}}$ and $p^{\mathrm{in}}_{\mathrm{Trb}}$ instead of $p^{\mathrm{in}}_{\mathrm{Ca}}$ and $p^{\mathrm{out}}_{\mathrm{Ca}}$, and $\lambda_{\mathrm{O_2}}$ was determined with $\dot{\tilde{m}}^{\mathrm{in}}_{\mathrm{Ca}}$ from Equation (6.2). Another simplification in this work was the approximation of $\dot{m}_{\mathrm{Dil}}$ with $\dot{m}_{\mathrm{AirFil}}$, despite the air mass flow reduction in the fuel cell stack. However, the active control of $\dot{m}_{\mathrm{Dil}}$ was only necessary for very small fuel cell stack loads, corresponding to small oxygen consumption. Hence, the approximation error was marginal in the relevant operating range. Furthermore, the electric power correlations from Section 4.3 did not introduce additional dynamic states, which is why $\boldsymbol{x} = \left[i_{q,\mathrm{Cmpr}},\, \omega_{\mathrm{Cmpr}},\, pos_{\mathrm{Byp}},\, p^{\mathrm{out}}_{\mathrm{Cmpr}},\, p^{\mathrm{in}}_{\mathrm{Trb}}\right]$ was retained.

8.1.2 Validation of Prediction Model

The accuracy of the nonlinear prediction model was evaluated with the FCEV measurement from Section 4.4.2. Thus, the model inputs $\boldsymbol{u}$ are displayed in Figure 29. This measurement allowed a thorough comparison of the dynamics and stationary values of the electric powers and the associated states between the simplified prediction model and the experimental FCS.

At first, the comparison of model and measurement values for n_{Cmpr} is shown in Figure 92. The dynamics of n_{Cmpr} were accurately predicted, whereas the considerable

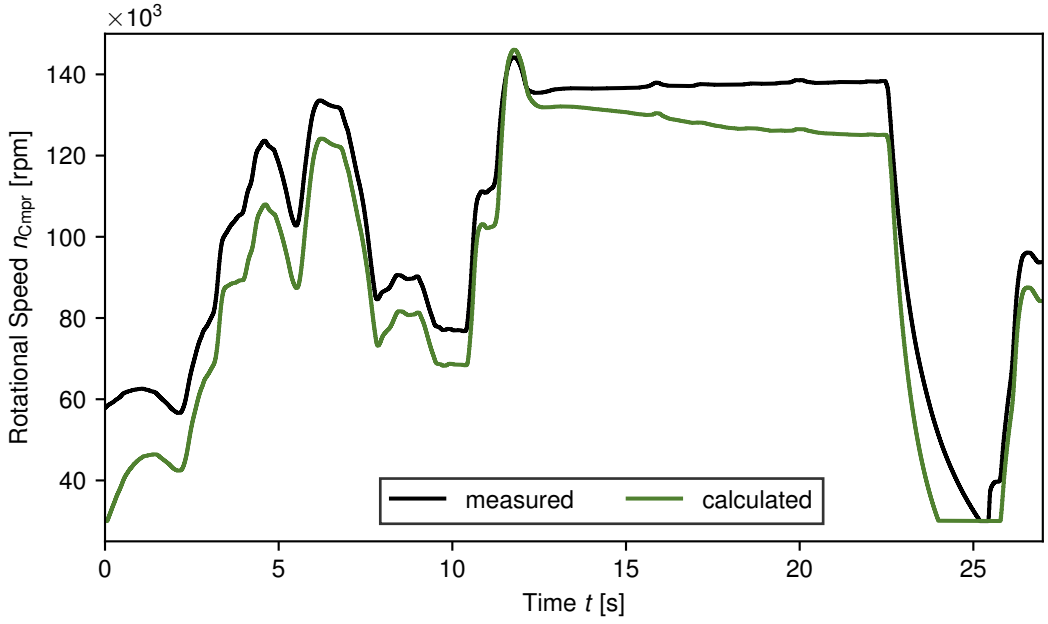

Figure 92: Comparison of n_{Cmpr} for the FCEV measurement and the corresponding nonlinear prediction model calculations.

stationary deviations primarily resulted from the assumed constant $\eta_{Is,\mathrm{Cmpr}} = 70\,\%$ and $\eta_{Is,\mathrm{Trb}} = 80\,\%$. Additionally, the difference between measurement and model prediction increased from $t = 12\,\mathrm{s}$ to $t = 22\,\mathrm{s}$ in Figure 92. This growing deviation was caused by

the assumption of a constant $pos_{\mathrm{VTG}} = 50\,\%$ in the nonlinear prediction model, whereas pos_{VTG} was actually decreased in the measurement. Nevertheless, changes in pos_{VTG} were generally slow, which is why these perturbations were effortlessly compensated by the observer.

This perturbation compensation was even more straightforward for P_{Cmpr}. The impact of a changing pos_{VTG} was insignificant, as shown by the comparison of measurement values and model predictions for P_{Cmpr} in Figure 93. Moreover, the substantial impact

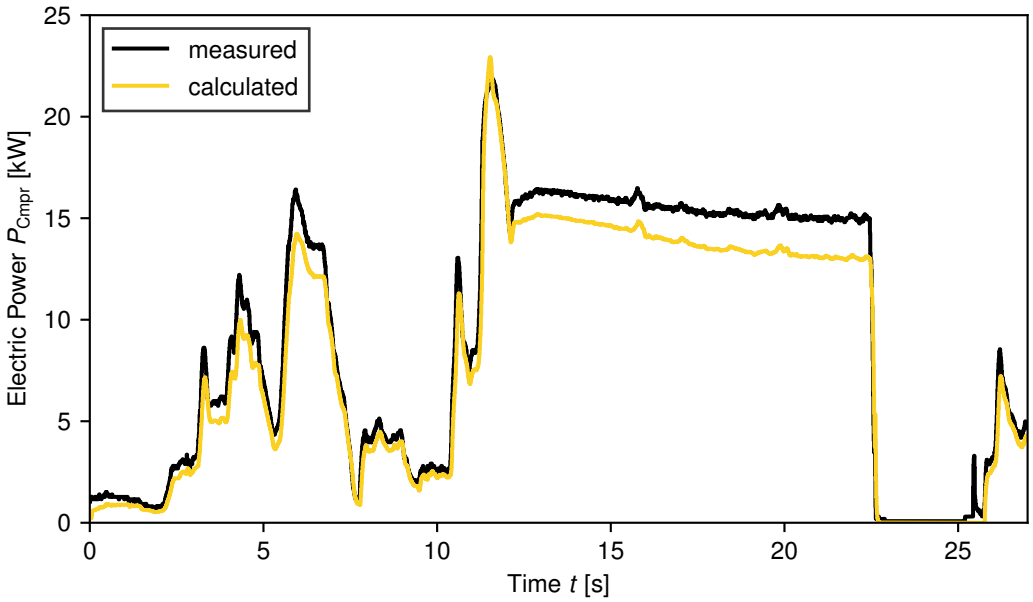

Figure 93: Comparison of P_{Cmpr} for the FCEV measurement and the corresponding nonlinear prediction model calculations.

of $i_{q,\mathrm{Cmpr}}$ on P_{Cmpr} reduced the overall stationary deviations compared to n_{Cmpr}, since the stationary value of $i_{q,\mathrm{Cmpr}}$ was equal to the model input $i^{\mathrm{sp}}_{q,\mathrm{Cmpr}}$. This correlation also led to the dynamics of P_{Cmpr} being correctly predicted in Figure 93.

Similarly, I_{Stck} was equal to the model input $I^{\mathrm{sp}}_{\mathrm{Stck}}$ with a time delay of 50 ms, which is why all the differences between model prediction and measurement of $\lambda_{\mathrm{O_2}}$ in Figure 94 resulted from deviations in $\dot{m}^{\mathrm{in}}_{\mathrm{Ca}}$. However, these deviations in $\dot{m}^{\mathrm{in}}_{\mathrm{Ca}}$ were sufficiently compensated with the perturbation observer, as demonstrated in Chapter 6 for the nonlinear air mass flow controller. Additionally, the dynamics were fairly well predicted, which is why this nonlinear prediction model was sufficient for controlling $\lambda_{\mathrm{O_2}}$.

The second controlled variable was P_{FCS}, which mainly depended on P_{Stck}. As a result, the accuracy of the predicted U_{Stck} significantly impacted the closed-loop behavior of the proposed NMPC. The associated comparison between the FCEV measurement and the nonlinear prediction model is displayed in Figure 95. The dynamics of U_{Stck} were reasonably well predicted in Figure 95. Mostly, the variations in U_{Stck} resulted from changes in I_{Stck}, which were directly adopted from the altered model input $I^{\mathrm{sp}}_{\mathrm{Stck}}$. Additionally, the time period from $t = 23\,\mathrm{s}$ to $t = 26\,\mathrm{s}$ was negligible due to the deactivation of the FCS net power controller.

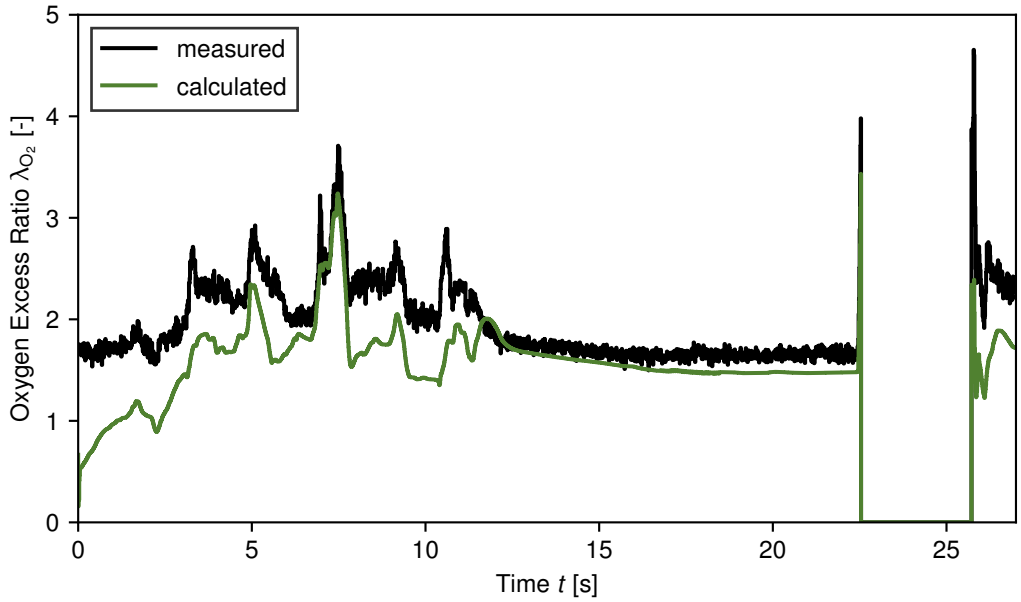

Figure 94: Comparison of λ_{O_2} for the FCEV measurement and the corresponding nonlinear prediction model calculations.

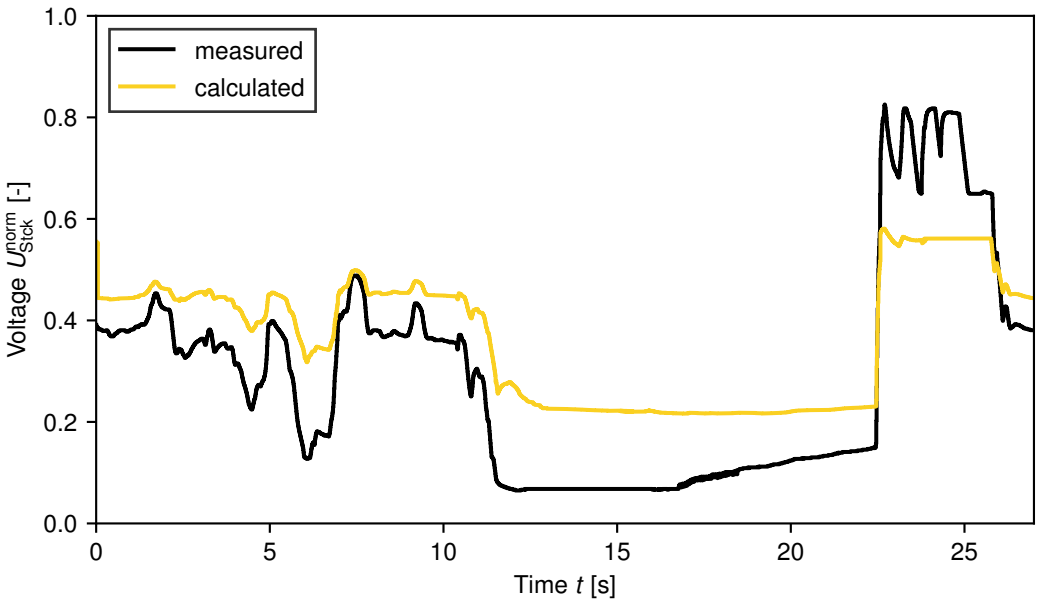

Figure 95: Comparison of U_{Stck}^{norm} for the FCEV measurement and the corresponding nonlinear prediction model calculations.

By contrast, the stationary deviations between the FCEV measurement and the nonlinear prediction model were considerable. These deviations were partly caused by the culminated simplifications of a constant p_{H_2} as well as a constant fuel cell temperature and humidity. Furthermore, the approximation of p_{O_2} was inaccurate in the simplified cathode subsystem model. Firstly, the neglection of p_{Ca}^{in} and p_{Ca}^{out} generated a higher p_{O_2}. In the cathode subsystem, the humidifier bypass valve led to a smaller pressure loss between p_{Ca}^{out} and p_{Trb}^{in} compared to the difference between p_{Cmpr}^{out} and p_{Ca}^{in}. Thus, the

average pressure between $p_{\mathrm{Ca}}^{\mathrm{in}}$ and $p_{\mathrm{Ca}}^{\mathrm{out}}$, the main contributor to $p_{\mathrm{O_2}}$, was smaller than the average pressure between $p_{\mathrm{Cmpr}}^{\mathrm{out}}$ and $p_{\mathrm{Trb}}^{\mathrm{in}}$. As a result, U_{Stck} was higher in the nonlinear prediction model than the FCEV measurement. Secondly, some pressure changes were not represented by the nonlinear prediction model as a consequence of the assumed constant $pos_{\mathrm{VTG}} = 50\,\%$. Hence, the decrease of pos_{VTG} between $t = 17\,\mathrm{s}$ and $t = 23\,\mathrm{s}$ only increased $U_{\mathrm{Stck}}^{\mathrm{meas}}$ in Figure 95 owing to the rise of $p_{\mathrm{O_2}}$ in the FCEV measurement. By contrast, the pressure level in the nonlinear prediction model decreased, as shown by the pressure comparison between the FCEV measurement and the nonlinear prediction model in Figure 96. The benefit of taking pos_{VTG} into account is shown in the higher

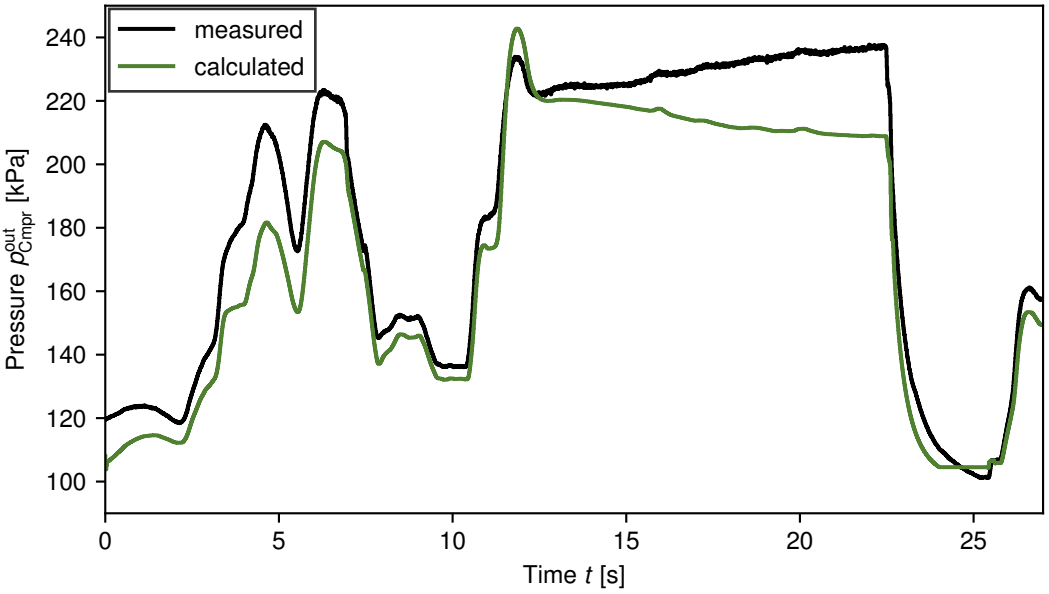

Figure 96: Comparison of $p_{\mathrm{Cmpr}}^{\mathrm{out}}$ for the FCEV measurement and the corresponding nonlinear prediction model calculations.

accuracy of U_{Stck} for the simulation model in Figure 37. Moreover, the higher accuracy mostly involved the low levels of U_{Stck} at high I_{Stck}. Therefore, the high stationary deviations in P_{Stck} between the FCEV measurement and the nonlinear prediction model in Figure 97 were, to some extent, the result of the assumed constant $pos_{\mathrm{VTG}} = 50\,\%$. The stationary accuracy of P_{Stck} was also only dependent on U_{Stck}, because the second factor, I_{Stck}, was identical to the model input $I_{\mathrm{Stck}}^{\mathrm{sp}}$ for stationary operating points. The dynamics of P_{Stck} were nevertheless precisely modeled, which is an essential prerequisite for successfully implementing a model-based controller.

The NMPC heavily relied on the prediction of P_{Stck}, which was the leading contributor to the primary controlled variable, P_{FCS}. Thus, the dynamics of P_{FCS} were well predicted, whereas significant stationary deviations occurred at higher FCS loads. These deviations are shown in Figure 98 for the associated comparison of P_{FCS} between the FCEV measurement and the nonlinear prediction model. Similar to the air mass flow controller in Chapter 6, zero control deviation with regard to P_{FCS} was achieved by compensating the stationary deviations with a perturbation observer. This perturbation observer for the FCS net power and hydrogen dilution controller is presented in the

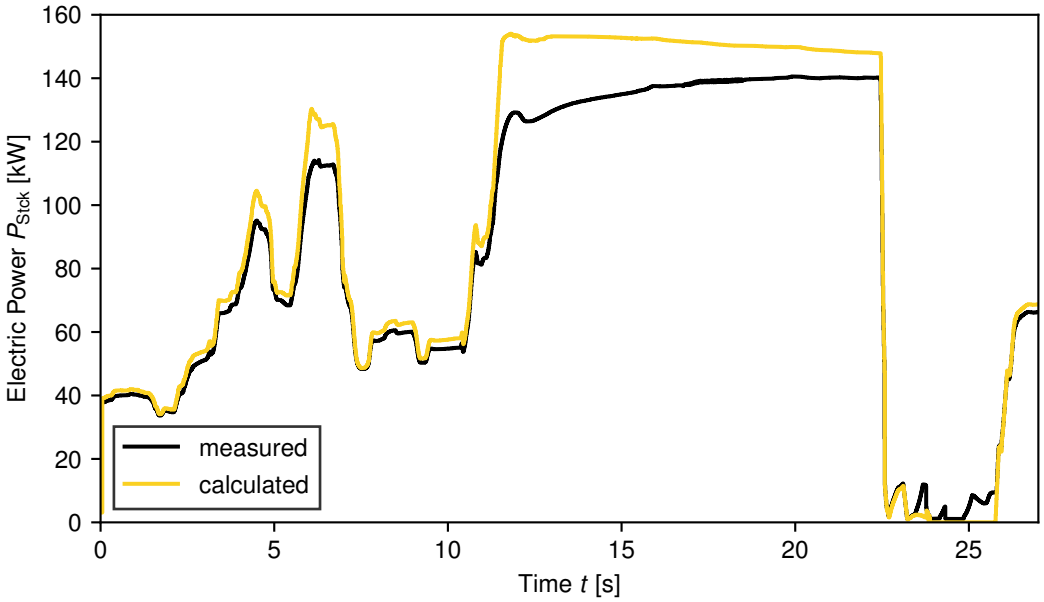

Figure 97: Comparison of P_{Stck} for the FCEV measurement and the corresponding nonlinear prediction model calculations.

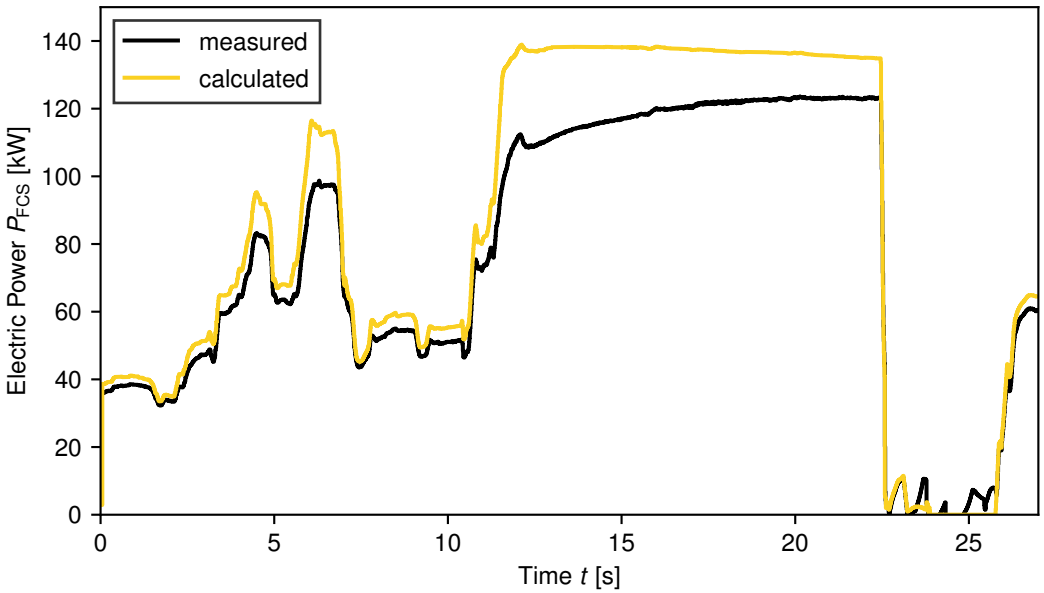

Figure 98: Comparison of P_{FCS} for the FCEV measurement and the corresponding nonlinear prediction model calculations.

next section.

8.2 State and Perturbation Observer

The state and perturbation observer was again a Luenberger observer, which was extended with estimated perturbation states $\hat{\boldsymbol{d}}$ to compensate for the stationary deviations

between the nonlinear prediction model and the controlled plant.

$$\begin{bmatrix} \hat{\boldsymbol{x}}\,(k+1) \\ \hat{\boldsymbol{d}}\,(k+1) \end{bmatrix} = \begin{bmatrix} \hat{\boldsymbol{x}}\,(k) \\ \hat{\boldsymbol{d}}\,(k) \end{bmatrix} + \Delta t \cdot \begin{bmatrix} \boldsymbol{f}\,(\hat{\boldsymbol{x}}\,(k)\,, \boldsymbol{u}\,(k)) \\ \boldsymbol{0} \end{bmatrix} + \boldsymbol{L}_{\mathrm{d}} \cdot \left\{ \boldsymbol{y}_{\mathrm{FCS}}^{\mathrm{meas}}\,(k) - \begin{bmatrix} \hat{y}_{1,\mathrm{FCS}}\,(k) \\ \hat{y}_{2,\mathrm{FCS}}\,(k-4) \\ \hat{y}_{3,\mathrm{FCS}}\,(k) \end{bmatrix} \right\} \tag{8.1}$$

The three sensor values $n_{\mathrm{Cmpr}}^{\mathrm{meas}}$, $pos_{\mathrm{Byp}}^{\mathrm{meas}}$, and $p_{\mathrm{Cmpr}}^{\mathrm{out,meas}}$ were neglected in this observer. These sensor values were unnecessary for the NMPC to properly control the air mass flows, as shown in Chapter 6. Instead, all perturbations concerning P_{FCS} were initially compensated with one perturbation state $\hat{d}_3$. The value of $\hat{d}_3$ was estimated from the difference between the estimated $\hat{P}_{\mathrm{FCS}}$ and the measured $P_{\mathrm{FCS}}^{\mathrm{meas}}$, which was part of the measurement feedback vector $\boldsymbol{y}_{\mathrm{FCS}}^{\mathrm{meas}}$.

$$\boldsymbol{y}_{\mathrm{FCS}}^{\mathrm{meas}} = \left[\dot{m}_{\mathrm{AirFil}}^{\mathrm{meas}},\, \dot{m}_{\mathrm{Byp}}^{\mathrm{meas}},\, P_{\mathrm{FCS}}^{\mathrm{meas}}\right]^{T} \tag{8.2}$$

Similar to the nonlinear air mass flow controller, all differences between the nonlinear prediction model and the controlled plant were compensated for with $\hat{\boldsymbol{d}}$. Thus, only the three appropriate observer gains in $\boldsymbol{L}_{\mathrm{d}}$ were unequal to zero.

$$\boldsymbol{L}_{\mathrm{d}} = \begin{bmatrix} 0 & 0 & 0 & 0 & 0 & 0.1 & 0 & 0 \\ 0 & 0 & 0 & 0 & 0 & 0 & 0.01 & 0 \\ 0 & 0 & 0 & 0 & 0 & 0 & 0 & 0.1 \end{bmatrix}^{T} \tag{8.3}$$

In Equation (8.3), the observer gains for $y_{1,FCS}^{\mathrm{meas}}$ and $y_{2,FCS}^{\mathrm{meas}}$ were taken over from the final parameterization of L_{d} in Chapter 6.

Eventually, the predicted control variables $\boldsymbol{y}$ in the cost function were modified with $\hat{\boldsymbol{d}}$ to obtain corrected values $\tilde{\boldsymbol{y}}$ instead of directly subtracting the estimated perturbations from $\boldsymbol{y}^{\mathrm{sp}}$. This approach for the perturbation compensation was necessary because $\lambda_{\mathrm{O_2}}$ was not directly measured. Instead, the prediction of $\dot{m}_{\mathrm{Ca}}^{\mathrm{in}}$ in the cost function was corrected with $\hat{d}_1$ for $\dot{m}_{\mathrm{AirFil}}$ as well as d_2 for $\dot{m}_{\mathrm{Byp}}$. Afterward, the corrected value of $\lambda_{\mathrm{O_2}}$ was calculated from the corrected $\dot{m}_{\mathrm{Ca}}^{\mathrm{in}}$ and I_{Stck}. Thus, $\hat{\boldsymbol{d}}$ was part of the parameter vector $\boldsymbol{\theta}$, an input variable of the NMPC cost function J. This cost function is presented in the next section.

8.3 Cost Function for Nonlinear Model Predictive Controller

In this work, a quadratic form was chosen for J of FCS net power and hydrogen dilution NMPC.

$$\begin{aligned} J\left(\boldsymbol{\theta}\left(k\right),\boldsymbol{U}\right) = & \begin{bmatrix} y_1^{\mathrm{sp}}\left(k\right) - \tilde{y}_1\left(k+N_y\right) \\ y_2^{\mathrm{sp}}\left(k\right) - \tilde{y}_2\left(k+N_y\right) \end{bmatrix}^T \boldsymbol{P} \begin{bmatrix} y_1^{\mathrm{sp}}\left(k\right) - \tilde{y}_1\left(k+N_y\right) \\ y_2^{\mathrm{sp}}\left(k\right) - \tilde{y}_2\left(k+N_y\right) \end{bmatrix} \\ & + \sum_{i=1}^{N_y-1} \begin{bmatrix} y_1^{\mathrm{sp}}\left(k\right) - \tilde{y}_1\left(k+i\right) \\ y_2^{\mathrm{sp}}\left(k\right) - \tilde{y}_2\left(k+i\right) \end{bmatrix}^T \boldsymbol{Q} \begin{bmatrix} y_1^{\mathrm{sp}}\left(k\right) - \tilde{y}_1\left(k+i\right) \\ y_2^{\mathrm{sp}}\left(k\right) - \tilde{y}_2\left(k+i\right) \end{bmatrix} \\ & + \sum_{j=0}^{N_u-1} \Delta\boldsymbol{u}\left(k+j\right)^T \boldsymbol{R} \Delta\boldsymbol{u}\left(k+j\right) \end{aligned} \tag{8.4}$$

The controlled variable y_3 was not considered in J. Instead, hydrogen dilution control was achieved by maintaining a lower limit $y_3 \geq y_3^{\mathrm{sp}}$. Thus, y_3 was part of the constraints of the NMPC optimization problem alongside the lower and upper boundaries $\boldsymbol{u}_{\min} = [0\,\mathrm{A},\ 0\,\%,\ 0\,\mathrm{A}]^T$ and $\boldsymbol{u}_{\max} = [120\,\mathrm{A},\ 100\,\%,\ I_{\mathrm{Cell,Max}}]^T$. Additionally, local oxygen starvation was prevented by imposing a global lower bound $y_{2,\mathrm{Min}} = 1.6$, whereas membrane drying was inhibited by limiting y_2 from above with $y_{2,\mathrm{Max}} = 4.0$.

$$\min_{\boldsymbol{U}} \quad J\left(\boldsymbol{\theta}\left(k\right),\boldsymbol{U}\right) \tag{8.5}$$

$$\text{s.t.} \quad \boldsymbol{u}_{\mathrm{Min}} \leq \boldsymbol{u}\left(k+j\right) \leq \boldsymbol{u}_{\mathrm{Max}}, \qquad j = 0,1,...,N_u-1 \tag{8.6}$$

$$y_{2,\mathrm{Min}} \leq y_2\left(k+i\right) \leq y_{2,\mathrm{Max}}, \qquad i = 1,2,...,N_y \tag{8.7}$$

$$y_{3,\mathrm{Min}} \leq y_3\left(k+i\right), \qquad i = 1,2,...,N_y \tag{8.8}$$

$$\boldsymbol{x}\left(k+i\right) = \boldsymbol{x}\left(k+i-1\right) + \Delta t \cdot \boldsymbol{f}^1, \qquad i = 1,2,...,N_y \tag{8.9}$$

$$\boldsymbol{y}\left(k+i\right) = \boldsymbol{h}\left(\boldsymbol{x}\left(k+i\right)\right), \qquad i = 1,2,...,N_y \tag{8.10}$$

The control targets and constraints mentioned above ensured the proper operation of the FCS. Furthermore, maintaining a high FCS efficiency was essential to minimize hydrogen consumption and, thus, increase the range of the FCEV. This additional control target is commonly met with a mapping $\lambda_{\mathrm{O_2}} = f\left(I_{\mathrm{Stck}}\right)$ that maximizes P_{FCS} for a given I_{Stck} (see e.g., [6], [15]). In this work, however, the control of $\lambda_{\mathrm{O_2}}$ alone was insufficient to maximize the FCS efficiency. Moreover, stationary air mass flow losses through the cathode bypass had to be limited to operating points that require additional air for hydrogen dilution, preventing excessive power consumption of the air compressor. In this work, attempts to achieve this goal were made with three different optimization criteria. Firstly, $\dot{m}_{\mathrm{Byp}}$ was minimized by applying the ratio $y_{4,1} = \frac{\dot{m}_{\mathrm{Byp}}}{\dot{m}_{\mathrm{Ca}}^{\mathrm{in}}}$ and $y_4^{\mathrm{sp}} = 0$ to J. Secondly, the total air mass flow was minimized with $y_{4,2} = \dot{m}_{\mathrm{AirFil}}$ and $y_4^{\mathrm{sp}} = 0$. Thirdly, the FCS efficiency with regard to P_{Stck} and P_{Cmpr} was maximized by integrating $y_{4,3} = \frac{1}{\eta_{\mathrm{FCS}}} = \frac{P_{\mathrm{Stck}}}{P_{\mathrm{Stck}} - P_{\mathrm{Cmpr}}}$ and $y_4^{\mathrm{sp}} = 0$ into J. Eventually, the impact of

[1] state and input dependencies were neglected to avoid a multi-line equation,
$\boldsymbol{f} = \boldsymbol{f}\left(\boldsymbol{x}\left(k+i-1\right), x_3\left(k+i-2\right), u_1\left(k+i-6\right), u_2\left(k+i-2\right), u_2\left(k+i-3\right), u_3\left(k+i-6\right)\right)$

each criterion on the closed-loop behavior of the proposed NMPC was evaluated. The results are summarized in Section 8.4.3.

8.4 Simulation Study with Implicit Nonlinear Model Predictive Controller

Within the scope of this work, the NMPC for FCS net power and hydrogen dilution control was only validated in closed-loop simulations. The NMPC optimization problem in these simulations was solved with the MATLAB implementation (Release R2018b) of the GLOBAL SEARCH algorithm [116]. This algorithm solves a local optimization problem from a set of initial points, which was carried out with the sequential QP algorithm of FMINCON. Additionally, central finite differences were applied for gradient approximations, and the optimal solution from the previous time step was the initial guess for each GLOBAL SEARCH run.

Initially, the closed-loop simulations were focused on the control of P_{FCS}, $\lambda_{\mathrm{O_2}}$, and $\dot{m}_{\mathrm{Dil}}$, while neglecting the FCS efficiency. The initial cost function parameter values $N_y = 15$ and $N_u = 1$ were adopted from the best-performing NMPC of Chapter 6. However, the weight matrices were adjusted to $\boldsymbol{P} = \left[\begin{smallmatrix} 10 & 0 \\ 0 & 10 \end{smallmatrix}\right]$ and $\boldsymbol{Q} = \left[\begin{smallmatrix} 1 & 0 \\ 0 & 1 \end{smallmatrix}\right]$, which reflected the equal significance of the two main control tasks for P_{FCS} and $\lambda_{\mathrm{O_2}}$. The control effort was not penalized with $\boldsymbol{R} = [\mathbf{0}]$ to achieve maximum dynamics within the boundaries of the control variables.

The first part of this simulation study was focused on optimizing the closed-loop behavior of P_{FCS} and $\lambda_{\mathrm{O_2}}$ with N_y and N_u. Then, the weight matrices $\boldsymbol{P}$ and $\boldsymbol{Q}$ were adjusted to further improve the dynamic response of the FCS net power and hydrogen dilution controller. Eventually, the most suitable third optimization target was identified by evaluating the impact of all three efficiency criteria on the closed-loop behavior.

Each part of the simulation study was conducted with a short validation scenario. This validation scenario involved a constant setpoint $\lambda_{\mathrm{O_2}}^{\mathrm{sp}} = 1.7$ and a constant hydrogen dilution mass flow request $\dot{m}_{\mathrm{Dil}}^{\mathrm{sp}} = 20\,\frac{\mathrm{g}}{\mathrm{s}}$ as well as three step changes from $P_{\mathrm{FCS}}^{\mathrm{sp}} = 20\,\mathrm{kW}$ to $P_{\mathrm{FCS}}^{\mathrm{sp}} = 100\,\mathrm{kW}$, from $P_{\mathrm{FCS}}^{\mathrm{sp}} = 100\,\mathrm{kW}$ to $P_{\mathrm{FCS}}^{\mathrm{sp}} = 50\,\mathrm{kW}$, and then again down to $P_{\mathrm{FCS}}^{\mathrm{sp}} = 20\,\mathrm{kW}$. Even though the validation scenario only covered a small area of the entire operating range, the three step changes were sufficient for statements about the impact of each cost function parameter and the best efficiency criterion.

8.4.1 Variation of Prediction and Control Horizon

In the cost function, the constraints on $\lambda_{\mathrm{O_2}}$ imposed dynamic boundaries on $I_{\mathrm{Stck}}^{\mathrm{sp}}$, since the available $\dot{m}_{\mathrm{Ca}}^{\mathrm{in}}$ limited the maximum and the minimum values of I_{Stck}. As a result, long prediction and control horizons were necessary to reflect these complex dynamic correlations and enable the NMPC to act on them accordingly. The evaluated combinations of N_y and N_u are summarized in Table 8.

Table 8: Variants of N_y and N_u for the parameterization of J with regard to the proposed NMPC for FCS net power and hydrogen dilution control.

Variant	N_y	N_u	Variant	N_y	N_u	Variant	N_y	N_u
1	15	1	2	15	10	3	30	25
4	60	25	5	60	35			

The comparison of P_{FCS}, $\lambda_{\mathrm{O_2}}$, and $\dot{m}_{\mathrm{Dil}}$ for the first three variants of Table 8 is shown in Figure 99. The trajectories in Figure 99 suggest that $N_u > 1$ was a prerequisite for

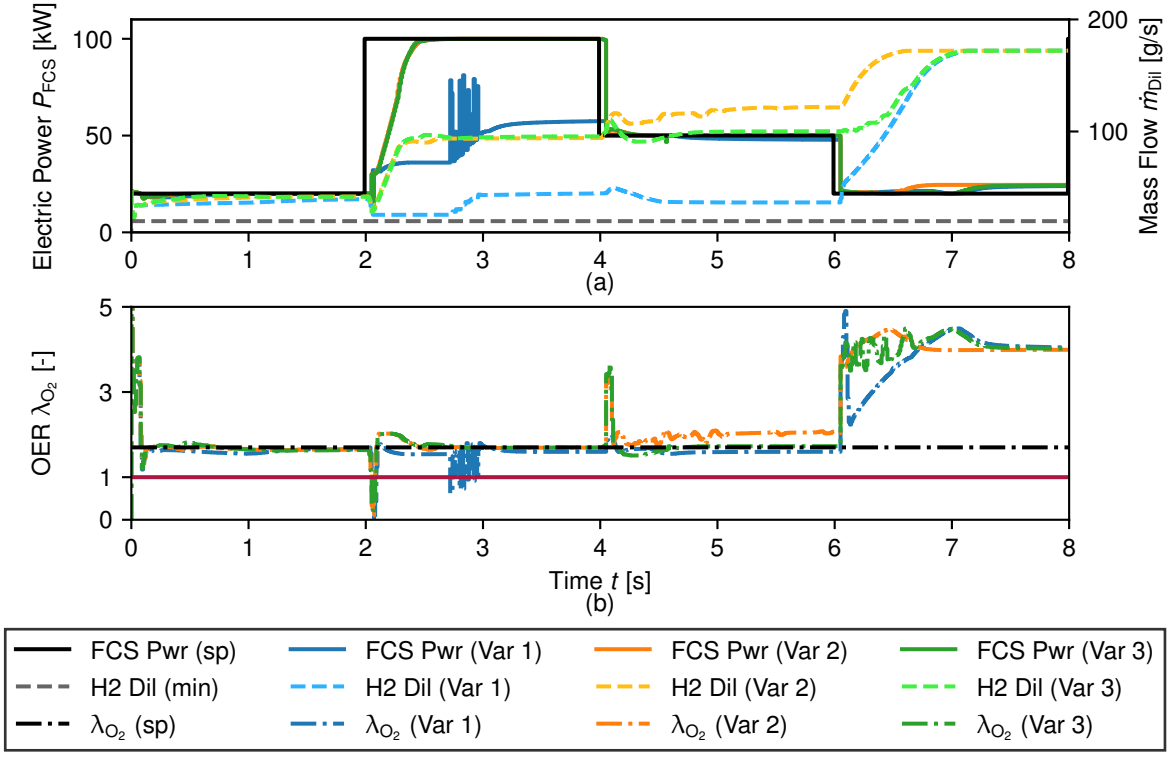

Figure 99: Comparison of controlled variables for variants 1, 2, and 3 from Table 8.

properly controlling P_{FCS}. A significant increase in P_{FCS} required a considerable rise in $\dot{m}_{\mathrm{Ca}}^{\mathrm{in}}$ to provide enough oxygen for a higher I_{Stck}. However, the dynamics of the cathode subsystem were slow, which is why higher values of $I_{\mathrm{Stck}}^{\mathrm{sp}}$ were only applicable later in the prediction. This delayed increase of $I_{\mathrm{Stck}}^{\mathrm{sp}}$ was infeasible for $N_u = 1$, which only allowed one change in $I_{\mathrm{Stck}}^{\mathrm{sp}}$ at the beginning of the prediction horizon. Furthermore, the rise in $\dot{m}_{\mathrm{Ca}}^{\mathrm{in}}$ was linked to a substantially higher $i_{q,\mathrm{Cmpr}}^{\mathrm{sp}}$, which resulted in an increased P_{Cmpr}. Thus, P_{FCS} was initially reduced in the prediction. Higher values of $I_{\mathrm{Stck}}^{\mathrm{sp}}$ compensated for this initial reduction, but these higher values were infeasible for $N_u = 1$. Hence, $i_{q,\mathrm{Cmpr}}^{\mathrm{sp}}$ remained low for $N_u = 1$, avoiding large control deviations for P_{FCS}. This behavior of the control variables is displayed in Figure 100, which further depicts the considerable changes in $i_{q,\mathrm{Cmpr}}^{\mathrm{sp}}$ and $I_{\mathrm{Stck}}^{\mathrm{sp}}$ for $N_u > 1$, allowing proper control of P_{FCS}. Nonetheless, the main disadvantage of $N_u > 1$ remained the numerical uncertainties with the forward Euler that reduced the prediction accuracy. These numerical uncertainties most likely

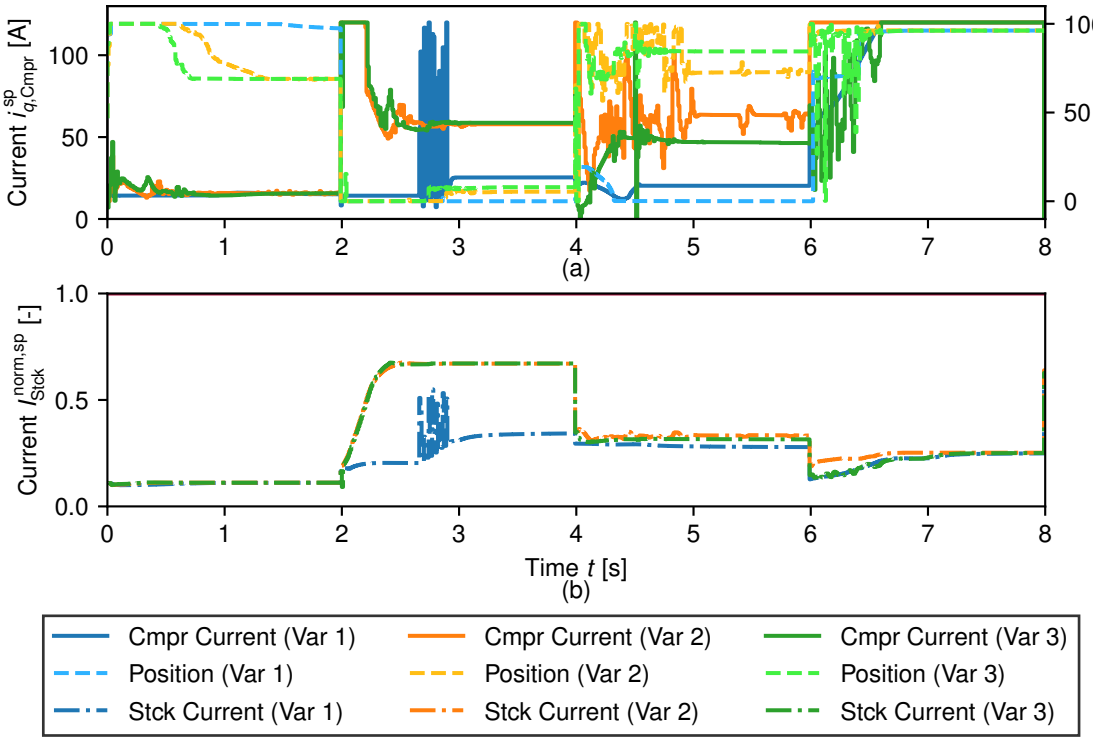

Figure 100: Comparison of control variables for variants 1, 2, and 3 from Table 8.

caused the oscillations in $i^{sp}_{q,Cmpr}$ and pos^{sp}_{Byp} for variants 2 and 3 in Figure 100.

Despite the appreciable improvements in the closed-loop behavior of P_{FCS}, $N_y = 30$ and $N_u = 25$ of variant 3 were insufficient to properly control λ_{O_2}. Instead, the best closed-loop behavior of P_{FCS} and λ_{O_2} was achieved with $N_y = 60$ and $N_u = 35$. The corresponding comparison of the controlled variables between variants 3, 4, and 5 of Table 8 is displayed in Figure 101. The longer prediction horizon $N_y = 60$ allowed the NMPC to properly control λ_{O_2} for every stationary operating point. At medium to low loads of the compressor, the maximum deceleration with $i_{q,Cmpr} = 0\,A$ was slow because the applied torque difference was small. Thus, the time constant of this dynamic transition was relatively high. Eventually, the prediction with $N_y = 30$ did not fully cover the last step change in Figure 101, whereas $N_y = 60$ was long enough the reflect the corresponding slow dynamics.

Moreover, the NMPC with $N_u = 35$ outperformed the NMPC with $N_u = 25$ since the latter induced significant disruptions in P_{FCS} and λ_{O_2} at $t = 4.6\,s$ in Figure 101. These disruptions resulted from a sudden increase and decrease of all three control variables, as highlighted in Figure 102. In this figure, the control variable trajectories of variants 3, 4, and 5 of Table 8 are compared. The disruptions were preceded by two consecutive optimization runs failing to determine a feasible point. Accordingly, it is reasonable to assume that the disruptions were caused by the high difference between $N_y = 60$ and $N_u = 25$. Minus the delays, the control variables remained constant for the last 30 time steps in the prediction. Therefore, the last set of control variables had to ensure that all constraints were met for 30 time steps with variant 4. By contrast, variant 5

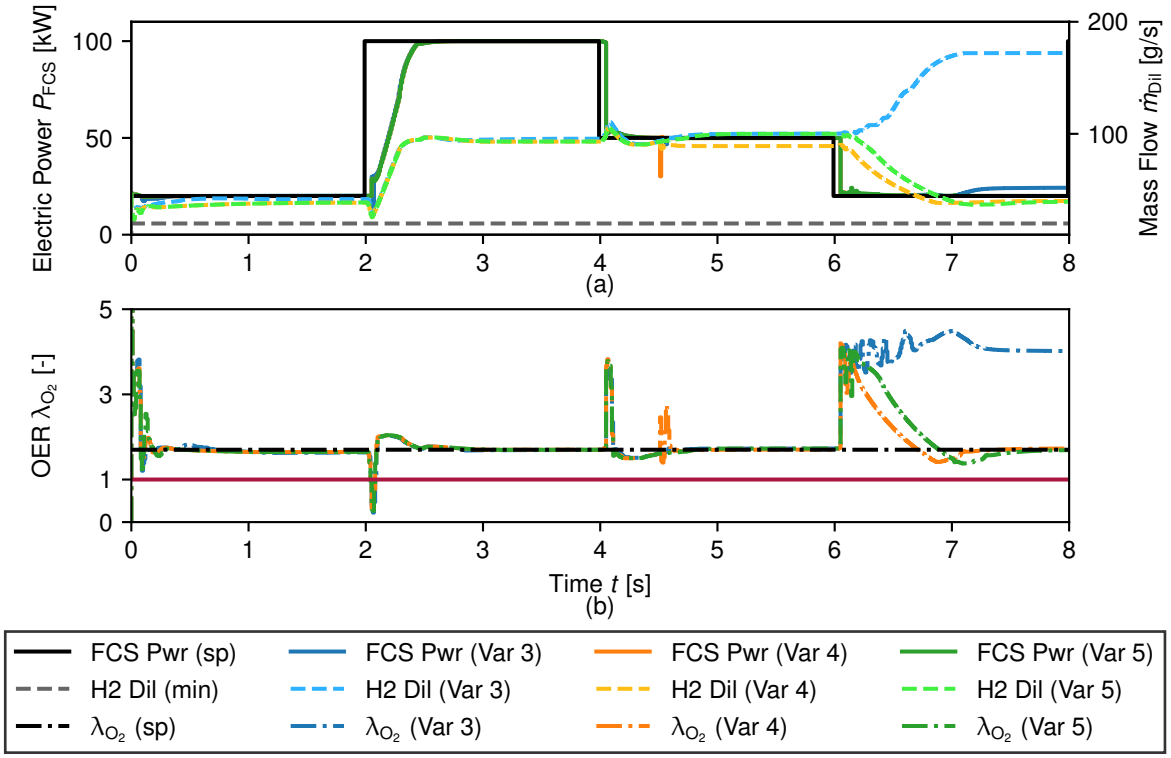

Figure 101: Comparison of controlled variables for variants 3, 4, and 5 from Table 8.

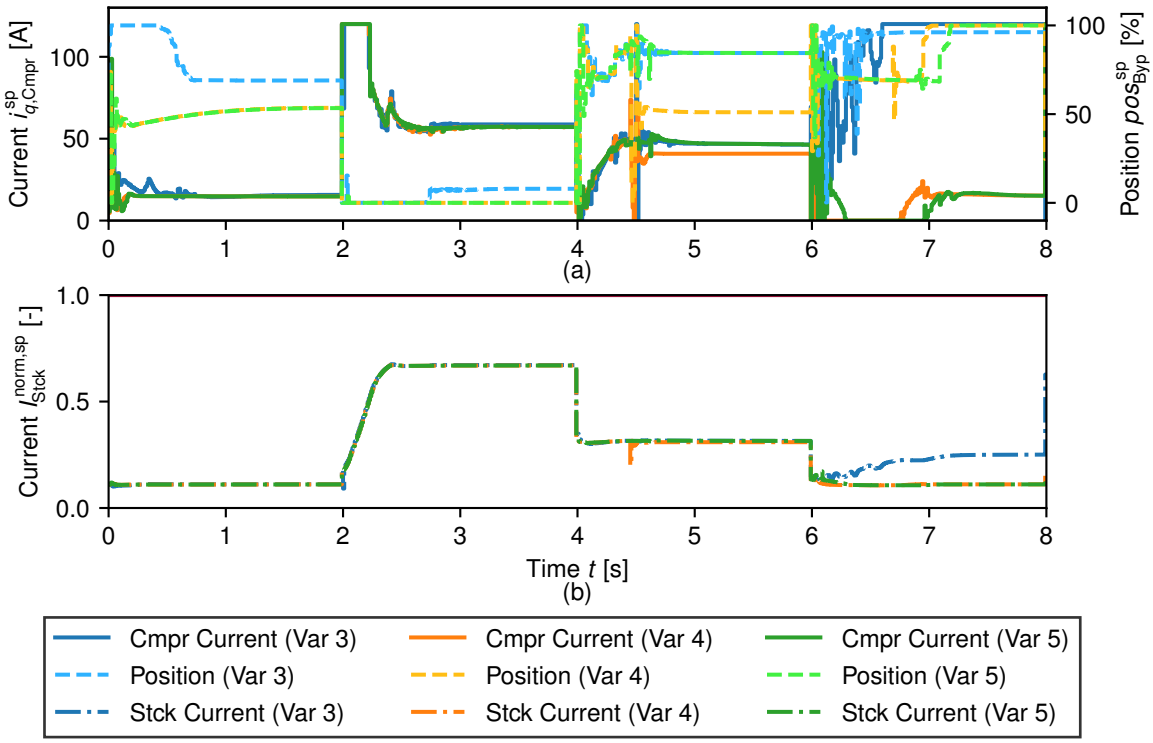

Figure 102: Comparison of control variables for variants 3, 4, and 5 from Table 8.

only required the solver to determine a last set of control variables that covered the constraints for 20 times steps, which was considerably more manageable. Eventually,

$N_y = 60$ and $N_u = 35$ were used throughout the remainder of this simulation study on NMPC for FCS net power and hydrogen dilution control.

Another unresolved issue of this control setup was the occurrence of oxygen starvation with $\lambda_{\mathrm{O}_2} < 1$ at $t = 2\,\mathrm{s}$ in Figure 101b). The instantaneous closing of the bypass valve before the acceleration of the air compressor temporarily increased $p_{\mathrm{Cmpr}}^{\mathrm{out}}$. This pressure increase caused a drop in $\dot{m}_{\mathrm{Cmpr}}$, which decreased $\dot{m}_{\mathrm{Ca}}^{\mathrm{Ca}}$. However, this oxygen starvation was not predicted by the NMPC. The optimizer did not return the flag related to an infeasible solution, even though the constraint $1.6 < \lambda_{\mathrm{O}_2}$ was clearly violated. Ultimately, this issue was resolved with the consideration of an efficiency criterion, as shown in Section 8.4.3.

8.4.2 Variation of Cost Function Weights

Before the consideration of an efficiency criterion, however, the impact of the weights in $\boldsymbol{P}$ and $\boldsymbol{Q}$ on the closed-loop behavior was evaluated. Thus, the three different variants from Table 9 were compared. The resulting trajectories of P_{FCS}, $\dot{m}_{\mathrm{Dil}}$ and λ_{O_2} are

Table 9: Variants of $\boldsymbol{P}$ and $\boldsymbol{Q}$ for the parameterization of J with regard to the proposed NMPC for FCS net power and hydrogen dilution control.

Variant	$\boldsymbol{P}$	$\boldsymbol{Q}$	Variant	$\boldsymbol{P}$	$\boldsymbol{Q}$	Variant	$\boldsymbol{P}$	$\boldsymbol{Q}$
5	$\left[\begin{smallmatrix}10 & 0\\ 0 & 10\end{smallmatrix}\right]$	$\left[\begin{smallmatrix}1 & 0\\ 0 & 1\end{smallmatrix}\right]$	6	$\left[\begin{smallmatrix}10 & 0\\ 0 & 10\end{smallmatrix}\right]$	$\left[\begin{smallmatrix}5 & 0\\ 0 & 1\end{smallmatrix}\right]$	7	$\left[\begin{smallmatrix}100 & 0\\ 0 & 100\end{smallmatrix}\right]$	$\left[\begin{smallmatrix}1 & 0\\ 0 & 1\end{smallmatrix}\right]$

illustrated in Figure 103. Generally, the differences between the three variants were not as significant as for the variation of N_y and N_u. The only considerable deviation in the controlled variables was the drop in P_{FCS} for variant 6 at $t = 2.1\,\mathrm{s}$ (Fig. 103a)). Eventually, $\boldsymbol{P} = \left[\begin{smallmatrix}100 & 0\\ 0 & 100\end{smallmatrix}\right]$ and $\boldsymbol{Q} = \left[\begin{smallmatrix}1 & 0\\ 0 & 1\end{smallmatrix}\right]$ from variant 7 were selected for the subsequent evaluation of the efficiency criteria. The corresponding trajectory of $i_{q,\mathrm{Cmpr}}^{\mathrm{sp}}$ in Figure 104 showed fewer oscillations than the trajectory of variant 5. Although these oscillations barely impacted P_{FCS} (Fig. 103a)), the repeated acceleration and deceleration of the compressor motor should be avoided. Otherwise, the stress on the motor and the attached compressor bearing might reduce the lifetime of the component.

The remaining oscillations for variant 7 were most likely caused by the prediction errors of the forward Euler for $N_u > 1$. Additionally, the optimization solver more often than not failed to converge to an optimal solution, which was probably partly caused by the predictions errors. However, an improvement of the nonlinear model predictions and implementing a better-performing optimization solver were out of the scope of this work. Instead, the available tools were used to evaluate the impact of different efficiency criteria on the closed-loop behavior of the FCS with regard to net power and hydrogen dilution control. The associated results are summarized in the subsequent section.

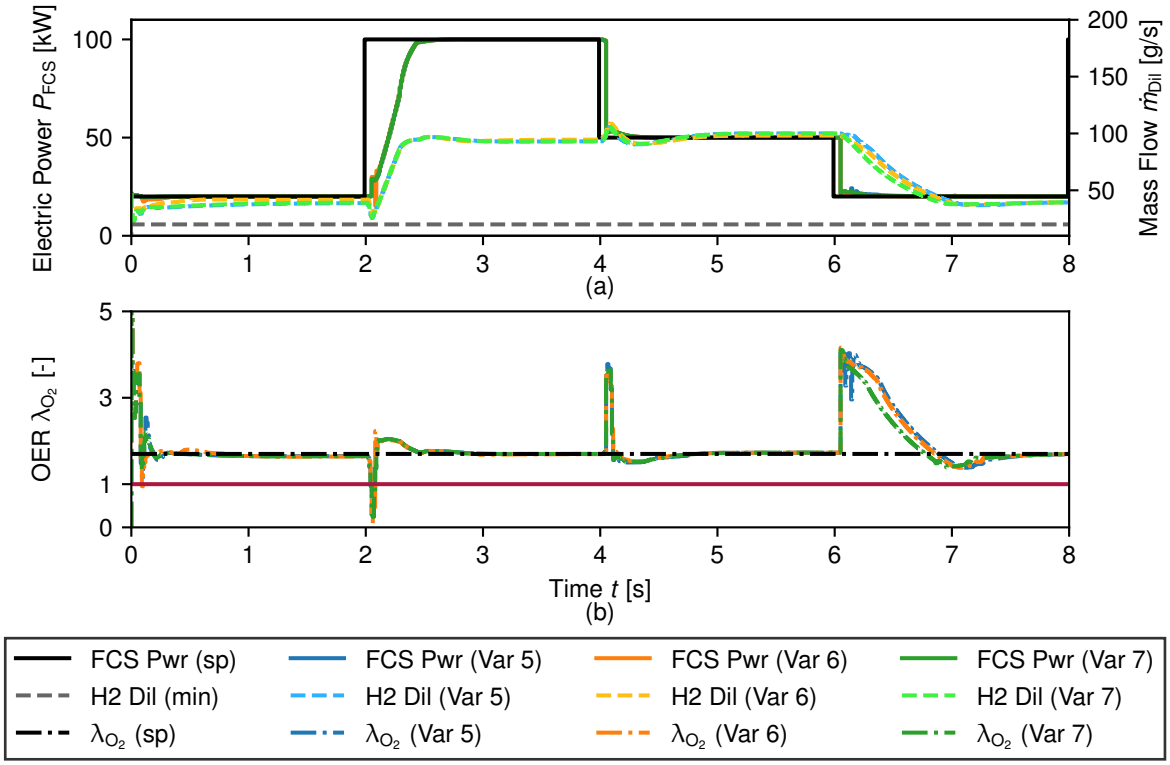

Figure 103: Comparison of controlled variables for variants 5, 6, and 7 from Table 9.

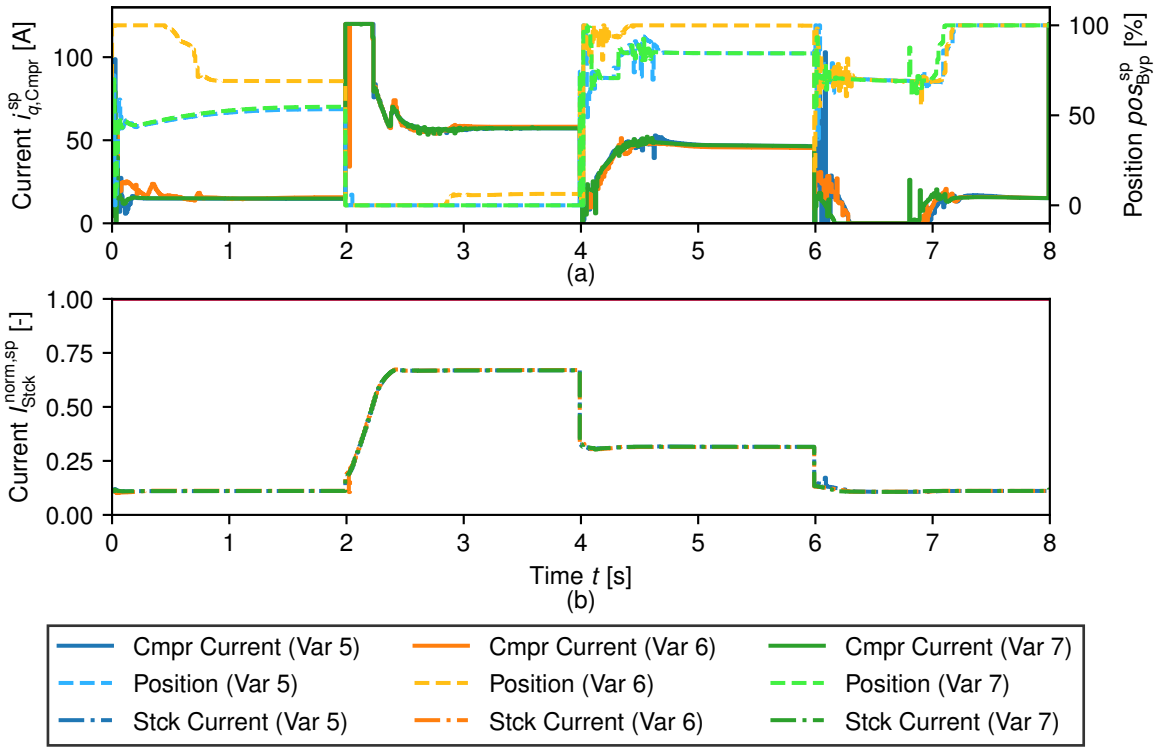

Figure 104: Comparison of control variables for variants 5, 6, and 7 from Table 9.

8.4.3 Variation of Efficiency Criterion

In the applied validation scenario, additional air for hydrogen dilution was only required for the operating point with $P_{\mathrm{FCS}}^{\mathrm{sp}} = 20\,\mathrm{kW}$. Nonetheless, the bypass valve was seldom fully closed for the other two operating points in Sections 8.4.1 and 8.4.2. Thus, the air compressor supplied unnecessary excess air to the FCS. This excess air supply resulted in excessive power consumption of the compressor motor, which reduced the efficiency of the FCS. Therefore, the three different efficiency criteria from Section 8.3 were additionally integrated into the cost function of the NMPC. This integration included an extension of the weight matrices to $\boldsymbol{P} = \left[\begin{smallmatrix} 100 & 0 & 0 \\ 0 & 100 & 0 \\ 0 & 0 & 1 \end{smallmatrix}\right]$ and $\boldsymbol{Q} = \left[\begin{smallmatrix} 1 & 0 & 0 \\ 0 & 1 & 0 \\ 0 & 0 & 0.01 \end{smallmatrix}\right]$, with the smaller values for the efficiency reflecting the lesser significance of this control task during transients. The proper operation of the FCS was more crucial than maintaining high efficiency. In Figure 105, the resulting closed-loop behavior of P_{FCS}, $\dot{m}_{\mathrm{Dil}}$, and $\lambda_{\mathrm{O_2}}$ is compared. Variant 2 with the efficiency criterion $y_{4,2} = \dot{m}_{\mathrm{AirFil}}$ was the only variant

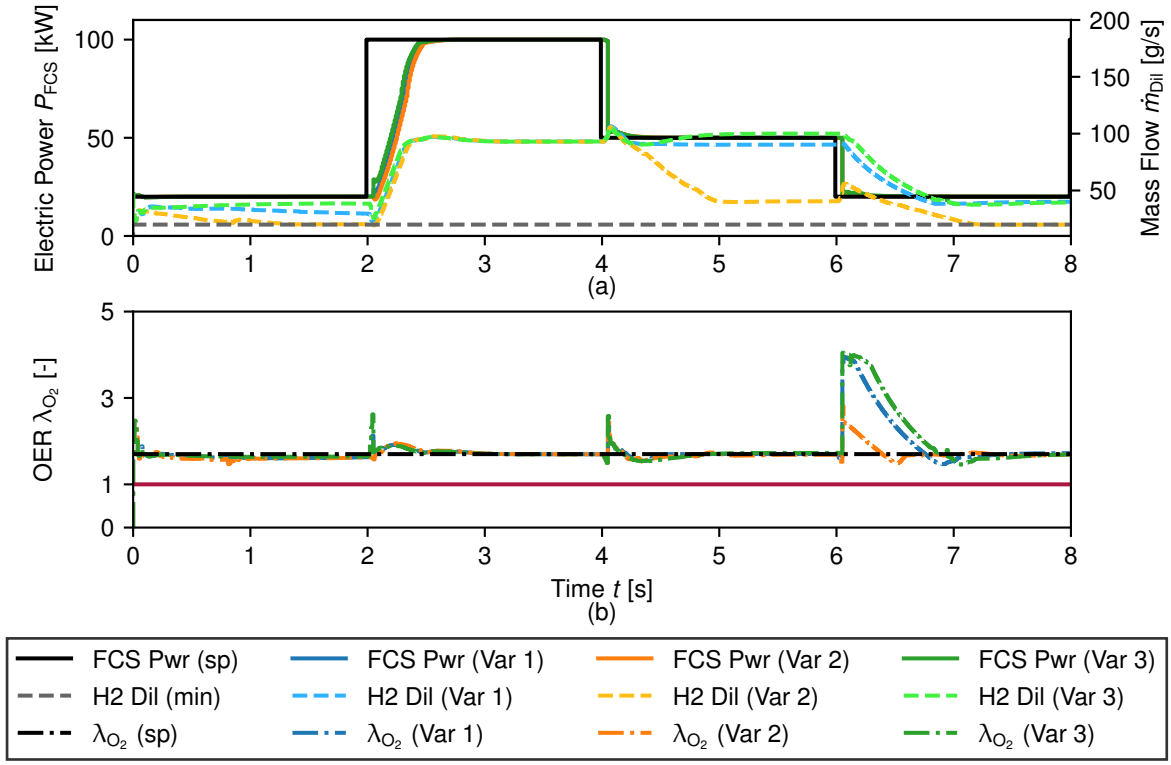

Figure 105: Comparison of controlled variables for the extended cost functions including $y_{4,1} = \frac{\dot{m}_{\mathrm{Byp}}}{\dot{m}_{\mathrm{Ca}}^{\mathrm{in}}}$ (Var 1), $y_{4,2} = \dot{m}_{\mathrm{AirFil}}$ (Var 2), and $y_{4,3} = \frac{1}{\eta_{\mathrm{FCS}}} = \frac{P_{\mathrm{Stck}}}{P_{\mathrm{Stck}} - P_{\mathrm{Cmpr}}}$ (Var 3).

with an active constraint $\dot{m}_{\mathrm{Dil}} = \dot{m}_{\mathrm{Dil,Min}}$ for $P_{\mathrm{FCS}}^{\mathrm{sp}} = 20\,\mathrm{kW}$. Thus, the air compressor supplied the minimum amount of air that still sufficed for hydrogen dilution. What is more, the NMPC with variant 2 was the only controller that fully closed the bypass valve for $P_{\mathrm{FCS}}^{\mathrm{sp}} = 50\,\mathrm{kW}$, as shown in Figure 106. As a result, $y_{4,2} = \dot{m}_{\mathrm{AirFil}}$ was best suited for additionally maximizing the FCS efficiency. Variant 2 had the advantage that the FCS efficiency and the hydrogen dilution air mass flow were each represented by $\dot{m}_{\mathrm{AirFil}}$. Therefore, the optimization solver probably struggled less to reconcile both

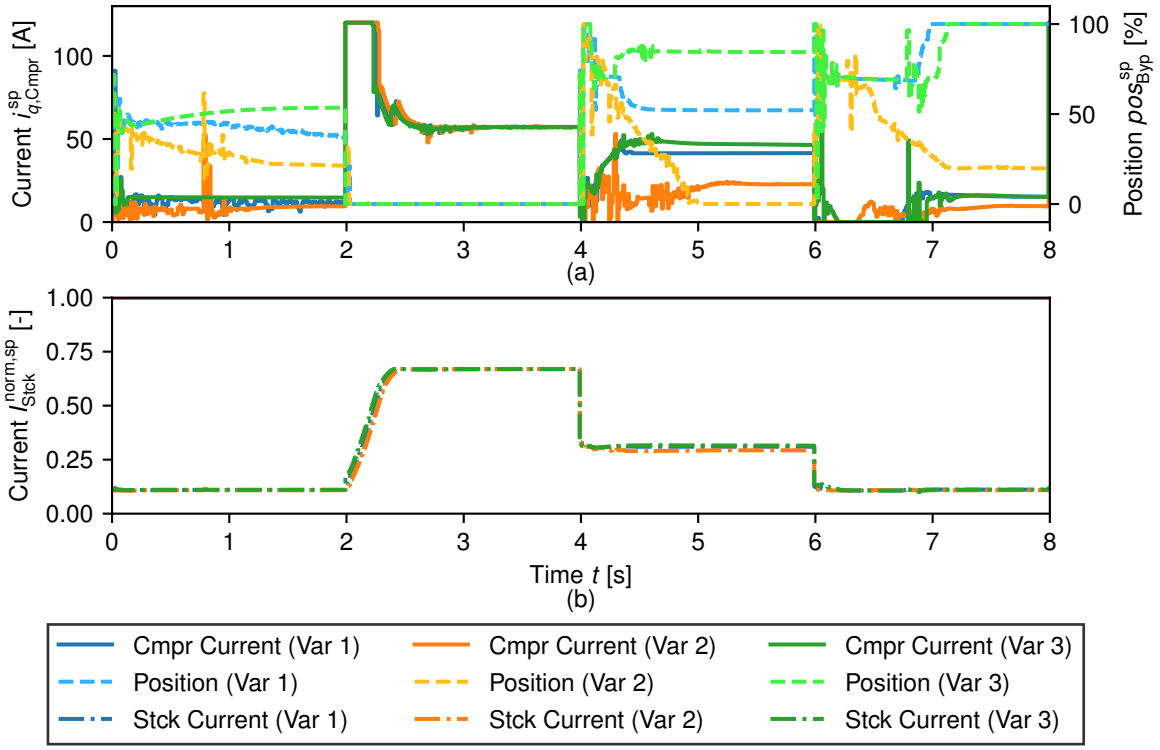

Figure 106: Comparison of control variables for the extended cost functions including $y_{4,1} = \frac{\dot{m}_{Byp}}{\dot{m}^{in}_{Ca}}$ (Var 1), $y_{4,2} = \dot{m}_{AirFil}$ (Var 2), and $y_{4,3} = \frac{1}{\eta_{FCS}} = \frac{P_{Stck}}{P_{Stck} - P_{Cmpr}}$ (Var 3).

control tasks, as no other dependencies had to be considered.

A drawback of the efficiency criterion $\dot{m}_{AirFil}$ was the increased occurrence of oscillations in $i^{sp}_{q,Cmpr}$. This increase might be related to the higher FCS efficiency with lower $i_{q,Cmpr}$, which resulted in lower rotational speeds of the air compressor. Consequently, $\dot{m}_{Cmpr}$ was more pressure-sensitive, and the numerical shortcomings of the forward Euler were more likely to impair the predictions of the NMPC.

Nevertheless, the potential of NMPC for FCS net power and hydrogen dilution control was demonstrated in this chapter. Removing the control cascade enabled an optimized closed-loop behavior with maximum dynamics of P_{FCS}. Additionally, all operating constraints were considered. As a result of the maximum dynamics of P_{FCS}, the application of this NMPC to the FCEV can reduce the necessary peak power of the secondary energy source. Hence, the total cost of the FCEV is decreased, while additionally, the available storage space for hydrogen is enlarged. Eventually, the vehicle range is extended, which increases the viability of the FCEV as an alternative to BEVs.

9 Summary and Outlook

In the present work, the primary objective was to improve the closed-loop behavior of the FCS of the BMW iX5 Hydrogen. Consequently, linear and nonlinear MPC was applied to the air mass flow control in the cathode subsystem, which was the limiting factor in the dynamic response of the FCS net power. Moreover, the experimental validation of the proposed controllers required a real-time capable approach, so explicit MPC was employed. The exact explicit solution to the QP problem was available for the linear MPC, whereas the explicit solution to the NLP problem of the NMPC was approximated with a NN. Before determining the explicit solutions, the parameters of the respective cost functions were adjusted in closed-loop simulations. The corresponding lumped-parameter simulation model was also introduced in this work. Eventually, the explicit NMPC outperformed the explicit linear MPC and the reference control setup with two adaptive PI controllers. On the one side, the bypass leakage was insufficiently compensated by the linear MPC. On the other side, the two PI controllers were unable to fully offset the cross-coupling between the stack and bypass mass flow, despite the additional load step detection algorithm allowing the two PI controllers to mimic MIMO behavior.

The remaining challenges for the air mass flow NMPC are twofold. On the one hand, the approximation accuracy of the NN must be further improved to remove the stationary control deviations of the bypass mass flow. Hence, future works should improve the training data set by increasing the number of samples and refining the sampling algorithm. On the other hand, the discretization of the nonlinear prediction model with the forward Euler entailed numerical inaccuracies, preventing the application of longer control horizons. However, longer prediction horizons allow exploiting the full dynamic potential of the cathode subsystem, which is why future works must also consider more refined integration approaches like higher-order Runge-Kutta methods.

The last part of this study revolved around extending the NMPC to control the FCS net power. Closed-loop simulations demonstrated that the FCS net power and the air mass flow for hydrogen dilution are directly controllable with the stack current, the quadrature current of the air compressor motor, and the position of the bypass valve. Furthermore, the NMPC enabled the consideration of all FCS operating range boundaries in the controller formulation.

However, several challenges must be addressed before validating the NMPC on the FCS test stand. Firstly, a refined NLP solver must be identified to increase the convergence rate during closed-loop simulations and for the training data preparation. Secondly, the closed-loop simulations must consider a more comprehensive range of operating points and step changes. The extension of the validation scenario was prevented by the

high computational time of the Global Search optimization solver, which is why this second challenge is connected to the first challenge. Thirdly, a more sophisticated integration method is even more crucial for FCS net power control than for air mass flow control. In the present study, long prediction and control horizons were the major prerequisites for successfully fulfilling every control target.

What is more, future works must aim to improve the nonlinear prediction model for FCS net power control. Firstly, the direct integration of the VTG in the model equations reduces the prediction error of the oxygen partial pressure. As a result, the fuel cell voltage is determined more accurately. Secondly, the consideration of variable isentropic efficiencies for the air compressor and turbine enhances the stationary accuracy of the predicted air mass flows. Thirdly, the ambient temperature and pressure substantially impacted the predicted stationary operating point. Therefore, considering the ambient conditions as model inputs also improves the prediction accuracy of the nonlinear model.

List of Tables

List of Figures

Bibliography

[1] M. S. AbouOmar, Y. Su, H. Zhang, B. Shi, and L. Wan, "Observer-based interval type-2 fuzzy pid controller for pemfc air feeding system using novel hybrid neural network algorithm-differential evolution optimizer," *Alexandria Engineering Journal*, vol. 61, no. 9, pp. 7353–7375, 2022, ISSN: 11100168. DOI: 10.1016/j.aej.2021.12.072.

[2] P. Almeida and M. G. Simoes, "Neural optimal control of pem-fuel cells with parametric cmac networks," in *38th IAS Annual Meeting on Conference Record of the Industry Applications Conference, 2003*, IEEE, 2003, pp. 723–730, ISBN: 0-7803-7883-0. DOI: 10.1109/IAS.2003.1257600.

[3] J. C. Amphlett, R. M. Baumert, R. F. Mann, B. A. Peppley, P. R. Roberge, and T. J. Harris, "Performance modeling of the ballard mark iv solid polymer electrolyte fuel cell: I . mechanistic model development," *Journal of The Electrochemical Society*, vol. 142, no. 1, pp. 1–8, 1995, ISSN: 0022-3239. DOI: 10.1149/1.2043866.

[4] J. C. Amphlett, R. M. Baumert, R. F. Mann, B. A. Peppley, P. R. Roberge, and A. Rodrigues, "Parametric modelling of the performance of a 5-kw proton-exchange membrane fuel cell stack," *Journal of Power Sources*, vol. 49, no. 1-3, pp. 349–356, 1994, ISSN: 03787753. DOI: 10.1016/0378-7753(93)01835-6.

[5] J. C. Amphlett, R. F. Mann, B. A. Peppley, P. R. Roberge, and A. Rodrigues, "A model predicting transient responses of proton exchange membrane fuel cells," *Journal of Power Sources*, vol. 61, no. 1-2, pp. 183–188, 1996, ISSN: 03787753. DOI: 10.1016/S0378-7753(96)02360-9.

[6] A. Arce, D. R. Ramirez, A. J. del Real, and C. Bordons, "Constrained explicit predictive control strategies for pem fuel cell systems," in *2007 46th IEEE Conference on Decision and Control*, IEEE, 2007, pp. 6088–6093, ISBN: 978-1-4244-1497-0. DOI: 10.1109/CDC.2007.4434556.

[7] A. Arce, C. Panos, C. Bordons, and E. N. Pistikopoulos, "Design and experimental validation of an explicit mpc controller for regulating temperature in pem fuel cell systems*," *IFAC Proceedings Volumes*, vol. 44, no. 1, pp. 2476–2481, 2011, ISSN: 14746670. DOI: 10.3182/20110828-6-IT-1002.02819.

[8] C. Bao, M. Ouyang, and B. Yi, "Modeling and control of air stream and hydrogen flow with recirculation in a pem fuel cell system—i. control-oriented modeling," *International Journal of Hydrogen Energy*, vol. 31, no. 13, pp. 1879–1896, 2006, ISSN: 03603199. DOI: 10.1016/j.ijhydene.2006.02.031.

[9] C. Bao, M. Ouyang, and B. Yi, "Modeling and control of air stream and hydrogen flow with recirculation in a pem fuel cell system—ii. linear and adaptive nonlinear control," *International Journal of Hydrogen Energy*, vol. 31, no. 13, pp. 1897–1913, 2006, ISSN: 03603199. DOI: 10.1016/j.ijhydene.2006.02.030.

[10] Z. Baroud, M. Benmiloud, A. Benalia, and C. Ocampo-Martinez, "Novel hybrid fuzzy-pid control scheme for air supply in pem fuel-cell-based systems," *International Journal of Hydrogen Energy*, vol. 42, no. 15, pp. 10 435–10 447, 2017, ISSN: 03603199. DOI: 10.1016/j.ijhydene.2017.01.014.

[11] A. Bemporad, M. Morari, V. Dua, and E. N. Pistikopoulos, "The explicit linear quadratic regulator for constrained systems," *Automatica*, vol. 38, no. 1, pp. 3–20, 2002, ISSN: 00051098. DOI: 10.1016/S0005-1098(01)00174-1.

[12] A. Bemporad, A. Oliveri, T. Poggi, and M. Storace, "Synthesis of stabilizing model predictive controllers via canonical piecewise affine approximations," in *49th IEEE Conference on Decision and Control (CDC)*, IEEE, 2010, pp. 5296–5301, ISBN: 978-1-4244-7745-6. DOI: 10.1109/CDC.2010.5717868.

[13] C. Bordons, A. Arce, and A. J. del Real, "Constrained predictive control strategies for pem fuel cells," in *2006 American Control Conference*, IEEE, 2006, 6 pp, ISBN: 1-4244-0209-3. DOI: 10.1109/ACC.2006.1656595.

[14] M. Canale, L. Fagiano, and M. Milanese, "Set membership approximation theory for fast implementation of model predictive control laws," *Automatica*, vol. 45, no. 1, pp. 45–54, 2009, ISSN: 00051098. DOI: 10.1016/j.automatica.2008.06.015.

[15] Y. A. Chang and S. J. Moura, "Air flow control in fuel cell systems: An extremum seeking approach," in *2009 American Control Conference*, IEEE, 2009, pp. 1052–1059, ISBN: 978-1-4244-4523-3. DOI: 10.1109/ACC.2009.5160016.

[16] S. Chen *et al.*, "Approximating explicit model predictive control using constrained neural networks," in *2018 Annual American Control Conference (ACC)*, IEEE, 2018, pp. 1520–1527, ISBN: 978-1-5386-5428-6. DOI: 10.23919/ACC.2018.8431275.

[17] L. H. Cseko, M. Kvasnica, and B. Lantos, "Explicit mpc-based rbf neural network controller design with discrete-time actual kalman filter for semiactive suspension," *IEEE Transactions on Control Systems Technology*, vol. 23, no. 5, pp. 1736–1753, 2015, ISSN: 1063-6536. DOI: 10.1109/TCST.2014.2382571.

[18] C. Damour, M. Benne, C. Lebreton, J. Deseure, and B. Grondin-Perez, "Real-time implementation of a neural model-based self-tuning pid strategy for oxygen stoichiometry control in pem fuel cell," *International Journal of Hydrogen Energy*, vol. 39, no. 24, pp. 12 819–12 825, 2014, ISSN: 03603199. DOI: 10.1016/j.ijhydene.2014.06.039.

[19] W. Daud, R. E. Rosli, E. H. Majlan, S. Hamid, R. Mohamed, and T. Husaini, "Pem fuel cell system control: A review," *Renewable Energy*, vol. 113, pp. 620–638, 2017, ISSN: 09601481. DOI: 10.1016/j.renene.2017.06.027.

[20] A. J. del Real, A. Arce, and C. Bordons, "Development and experimental validation of a pem fuel cell dynamic model," *Journal of Power Sources*, vol. 173, no. 1, pp. 310–324, 2007, ISSN: 03787753. DOI: 10.1016/j.jpowsour.2007.04.066.

[21] H. Deng, Q. Li, W. Chen, and G. Zhang, "High-order sliding mode observer based oer control for pem fuel cell air-feed system," *IEEE Transactions on Energy Conversion*, vol. 33, no. 1, pp. 232–244, 2018, ISSN: 0885-8969. DOI: 10.1109/TEC.2017.2742144.

[22] H. Deng, Q. Li, Y. Cui, Y. Zhu, and W. Chen, "Nonlinear controller design based on cascade adaptive sliding mode control for pem fuel cell air supply systems," *International Journal of Hydrogen Energy*, vol. 44, no. 35, pp. 19 357–19 369, 2019, ISSN: 03603199. DOI: 10.1016/j.ijhydene.2018.10.180.

[23] A. Domahidi, M. N. Zeilinger, M. Morari, and C. N. Jones, "Learning a feasible and stabilizing explicit model predictive control law by robust optimization," in *IEEE Conference on Decision and Control and European Control Conference*, IEEE, 2011, pp. 513–519, ISBN: 978-1-61284-801-3. DOI: 10.1109/CDC.2011.6161258.

[24] L. F. Domínguez and E. N. Pistikopoulos, "A novel mp-nlp algorithm for explicit/multi-parametric nmpc *," *IFAC Proceedings Volumes*, vol. 43, no. 14, pp. 539–544, 2010, ISSN: 14746670. DOI: 10.3182/20100901-3-IT-2016.00073.

[25] S. Dutta, S. Shimpalee, and J. W. van Zee, "Numerical prediction of mass-exchange between cathode and anode channels in a pem fuel cell," *International Journal of Heat and Mass Transfer*, vol. 44, no. 11, pp. 2029–2042, 2001, ISSN: 00179310. DOI: 10.1016/S0017-9310(00)00257-X.

[26] M. K. Eisner, Z. Zhou, V. Formanski, and R. M. Kennel, "Improving the air supply control of a fuel cell electric vehicle," in *11th International Conference on Power Electronics, Machines and Drives (PEMD 2022)*, Institution of Engineering and Technology, 2022, pp. 146–151, ISBN: 978-1-83953-718-9. DOI: 10.1049/icp.2022.1036.

[27] M. K. Eisner, Z. Zhou, V. Formanski, and R. M. Kennel, "Improving the air supply and hydrogen dilution control of a fuel cell electric vehicle with explicit model predictive control," *International Journal of Hydrogen Energy*, vol. 52, pp. 1236–1247, 2024. DOI: 10.1016/j.ijhydene.2023.07.113.

[28] C. Feller and T. A. Johansen, "Explicit mpc of higher-order linear processes via combinatorial multi-parametric quadratic programming," in *2013 European Control Conference (ECC)*, IEEE, 2013, pp. 536–541, ISBN: 978-3-033-03962-9. DOI: 10.23919/ECC.2013.6669708.

[29] J. Gao, M. Li, Y. Hu, H. Chen, and Y. Ma, "Challenges and developments of automotive fuel cell hybrid power system and control," *Science China Information Sciences*, vol. 62, no. 5, p. 620, 2019, ISSN: 1674-733X. DOI: 10.1007/s11432-018-9690-y.

[30] W. Garcia-Gabin, F. Dorado, and C. Bordons, "Real-time implementation of a sliding mode controller for air supply on a pem fuel cell," *Journal of Process Control*, vol. 20, no. 3, pp. 325–336, 2010, ISSN: 09591524. DOI: 10.1016/j.jprocont.2009.11.006.

[31] J. C. Gómez, M. Serra, and A. Husar, "Controller design for polymer electrolyte membrane fuel cell systems for automotive applications," *International Journal of Hydrogen Energy*, vol. 113, no. 19, p. 620, 2021, ISSN: 03603199. DOI: 10.1016/j.ijhydene.2021.04.136.

[32] A. Goshtasbi and T. Ersal, "Degradation-conscious control for enhanced lifetime of automotive polymer electrolyte membrane fuel cells," *Journal of Power Sources*, vol. 457, no. 1, p. 227 996, 2020, ISSN: 03787753. DOI: 10.1016/j.jpowsour.2020.227996.

[33] A. Grancharova and T. A. Johansen, "Approaches to explicit nonlinear model predictive control with reduced partition complexity," in *2009 European Control Conference (ECC)*, IEEE, 2009, pp. 2414–2419, ISBN: 978-3-9524173-9-3. DOI: 10.23919/ECC.2009.7074767.

[34] A. Grancharova and S. Olaru, "Explicit interpolation-based nonlinear model predictive control with a convex approximation of the feasible set," in *2014 IEEE Conference on Control Applications (CCA)*, IEEE, 2014, pp. 1824–1830, ISBN: 978-1-4799-7409-2. DOI: 10.1109/CCA.2014.6981578.

[35] J. K. Gruber, C. Bordons, and A. Oliva, "Nonlinear mpc for the airflow in a pem fuel cell using a volterra series model," *Control Engineering Practice*, vol. 20, no. 2, pp. 205–217, 2012, ISSN: 09670661. DOI: 10.1016/j.conengprac.2011.10.014.

[36] J. K. Gruber, M. Doll, and C. Bordons, "Design and experimental validation of a constrained mpc for the air feed of a fuel cell," *Control Engineering Practice*, vol. 17, no. 8, pp. 874–885, 2009, ISSN: 09670661. DOI: 10.1016/j.conengprac.2009.02.006.

[37] J. K. Gruber, C. Bordons, and F. Dorado, "Nonlinear control of the air feed of a fuel cell," in *2008 American Control Conference*, IEEE, 2008, pp. 1121–1126, ISBN: 978-1-4244-2078-0. DOI: 10.1109/ACC.2008.4586643.

[38] M. Grujicic, K. M. Chittajallu, E. H. Law, and J. T. Pukrushpan, "Model-based control strategies in the dynamic interaction of air supply and fuel cell," *Proceedings of the Institution of Mechanical Engineers, Part A: Journal of Power and Energy*, vol. 218, no. 7, pp. 487–499, 2004, ISSN: 0957-6509. DOI: 10.1243/0957650042456999.

[39] S. Hahn, J. Braun, H. Kemmer, and H.-C. Reuss, "Adaptive operation strategy of a polymer electrolyte membrane fuel cell air system based on model predictive control," *International Journal of Hydrogen Energy*, vol. 46, no. 33, pp. 17 306–17 321, 2021, ISSN: 03603199. DOI: 10.1016/j.ijhydene.2021.02.135.

[40] C. Hähnel, V. Aul, and J. Horn, "Power control for efficient operation of a pem fuel cell system by nonlinear model predictive control," *IFAC-PapersOnLine*, vol. 48, no. 11, pp. 174–179, 2015, ISSN: 24058963. DOI: 10.1016/j.ifacol.2015.09.179.

[41] J. Han, S. Yu, and S. Yi, "Adaptive control for robust air flow management in an automotive fuel cell system," *Applied Energy*, vol. 190, no. 1, pp. 73–83, 2017, ISSN: 03062619. DOI: 10.1016/j.apenergy.2016.12.115.

[42] M. Hatti and M. Tioursi, "Dynamic neural network controller model of pem fuel cell system," *International Journal of Hydrogen Energy*, vol. 34, no. 11, pp. 5015–5021, 2009, ISSN: 03603199. DOI: 10.1016/j.ijhydene.2008.12.094.

[43] D. Hernandez-Torres, O. Sename, and D. Riu, "An lpv control approach for a fuel cell power generator air supply system," in *2012 American Control Conference (ACC)*, IEEE, 2012, pp. 4299–4304, ISBN: 978-1-4577-1096-4. DOI: 10.1109/ACC.2012.6314814.

[44] D. Hernández-Torres, D. Riu, and O. Sename, "Reduced-order robust control of a fuel cell air supply system," *IFAC-PapersOnLine*, vol. 50, no. 1, pp. 96–101, 2017, ISSN: 24058963. DOI: 10.1016/j.ifacol.2017.08.017.

[45] M. Hertneck, J. Kohler, S. Trimpe, and F. Allgower, "Learning an approximate model predictive controller with guarantees," *IEEE Control Systems Letters*, vol. 2, no. 3, pp. 543–548, 2018. DOI: 10.1109/LCSYS.2018.2843682.

[46] J. B. Heywood, *Internal combustion engine fundamentals* (McGraw-Hill series in mechanical engineering), International ed. New York: McGraw-Hill, 1988, ISBN: 0-07-028637-X.

[47] C. Hildreth, "A quadratic programming procedure," *Naval Research Logistics Quarterly*, vol. 4, no. 1, pp. 79–85, 1957, ISSN: 00281441. DOI: 10.1002/nav.3800040113.

[48] S. Hochreiter, "The vanishing gradient problem during learning recurrent neural nets and problem solutions," *International Journal of Uncertainty, Fuzziness and Knowledge-Based Systems*, vol. 06, no. 02, pp. 107–116, 1998, ISSN: 0218-4885. DOI: 10.1142/S0218488598000094.

[49] J. Hou, M. Yang, C. Ke, and J. Zhang, "Control logics and strategies for air supply in pem fuel cell engines," *Applied Energy*, vol. 269, p. 115 059, 2020, ISSN: 03062619. DOI: 10.1016/j.apenergy.2020.115059.

[50] IEA, *Transport*, Paris, 2022. [Online]. Available: https://www.iea.org/reports/transport.

[51] IEA, *Co2 emissions in 2022*, Paris, 2023. [Online]. Available: https://www.iea.org/reports/co2-emissions-in-2022.

[52] IEA, *Global ev outlook 2023*, Paris, 2023. [Online]. Available: https://www.iea.org/reports/global-ev-outlook-2023.

[53] J.-P. Jensen, A. F. Kristensen, S. C. Sorenson, N. Houbak, and E. Hendricks, "Mean value modeling of a small turbocharged diesel engine," in *SAE Technical Paper Series*, ser. SAE Technical Paper Series, SAE International400 Commonwealth Drive, Warrendale, PA, United States, 1991. DOI: 10.4271/910070.

[54] T. A. Johansen, "On multi-parametric nonlinear programming and explicit nonlinear model predictive control," in *Proceedings of the 41st IEEE Conference on Decision and Control, 2002*, IEEE, 2002, pp. 2768–2773, ISBN: 0-7803-7516-5. DOI: 10.1109/CDC.2002.1184260.

[55] T. A. Johansen, "Approximate explicit receding horizon control of constrained nonlinear systems," *Automatica*, vol. 40, no. 2, pp. 293–300, 2004, ISSN: 00051098. DOI: 10.1016/j.automatica.2003.09.021.

[56] P. Karamanakos, E. Liegmann, T. Geyer, and R. Kennel, "Model predictive control of power electronic systems: Methods, results, and challenges," *IEEE Open Journal of Industry Applications*, vol. 1, pp. 95–114, 2020. DOI: 10.1109/OJIA.2020.3020184.

[57] B. Karg and S. Lucia, "Deep learning-based embedded mixed-integer model predictive control," in *2018 European Control Conference (ECC)*, IEEE, 2018, pp. 2075–2080, ISBN: 978-3-9524-2698-2. DOI: 10.23919/ECC.2018.8550234.

[58] B. Karg and S. Lucia, "Efficient representation and approximation of model predictive control laws via deep learning," *IEEE transactions on cybernetics*, vol. 50, no. 9, pp. 3866–3878, 2020. DOI: 10.1109/TCYB.2020.2999556.

[59] T.-H. Kim, S.-H. Kim, W. Kim, J.-H. Lee, and W. Choi, "Development of the novel control algorithm for the small proton exchange membrane fuel cell stack without external humidification," in *2010 Twenty-Fifth Annual IEEE Applied Power Electronics Conference and Exposition (APEC)*, IEEE, 2010, pp. 2166–2173, ISBN: 978-1-4244-4782-4. DOI: 10.1109/APEC.2010.5433537.

[60] C. Kunusch, P. F. Puleston, M. A. Mayosky, and J. Riera, "Sliding mode strategy for pem fuel cells stacks breathing control using a super-twisting algorithm," *IEEE Transactions on Control Systems Technology*, vol. 17, no. 1, pp. 167–174, 2009, ISSN: 1063-6536. DOI: 10.1109/TCST.2008.922504.

[61] C. Kunusch, P. F. Puleston, M. A. Mayosky, and A. P. Husar, "Control-oriented modeling and experimental validation of a pemfc generation system," *IEEE Transactions on Energy Conversion*, vol. 26, no. 3, pp. 851–861, 2011, ISSN: 0885-8969. DOI: 10.1109/TEC.2011.2124462.

[62] H. P. Künzi, W. Krelle, and R. Randow, *Nichtlineare Programmierung*. Berlin, Heidelberg: Springer Berlin Heidelberg, 1979, ISBN: 978-3-540-09343-5. DOI: 10.1007/978-3-642-81331-3.

[63] M. Kvasnica, J. Lofberg, M. Herceg, L. Cirka, and M. Fikar, "Low-complexity polynomial approximation of explicit mpc via linear programming," in *Proceedings of the 2010 American Control Conference*, IEEE, 2010, pp. 4713–4718, ISBN: 978-1-4244-7427-1. DOI: 10.1109/ACC.2010.5531092.

[64] M. Kvasnica, J. Hledík, I. Rauová, and M. Fikar, "Complexity reduction of explicit model predictive control via separation," *Automatica*, vol. 49, no. 6, pp. 1776–1781, 2013, ISSN: 00051098. DOI: 10.1016/j.automatica.2013.02.018.

[65] J. Li and T. Yu, "A new adaptive controller based on distributed deep reinforcement learning for pemfc air supply system," *Energy Reports*, vol. 7, pp. 1267–1279, 2021, ISSN: 23524847. DOI: 10.1016/j.egyr.2021.02.043.

[66] M. Li, H. Yin, T. Ding, J. Zhao, J. Gao, and H. Chen, "Air flow rate and pressure control approach for the air supply subsystems in pemfcs," *ISA transactions*, vol. 128, no. Pt A, pp. 624–634, 2022. DOI: 10.1016/j.isatra.2021.08.046.

[67] C. Lin-Kwong-Chon, B. Grondin-Pérez, J.-J. A. Kadjo, C. Damour, and M. Benne, "A review of adaptive neural control applied to proton exchange membrane fuel cell systems," *Annual Reviews in Control*, vol. 47, pp. 133–154, 2019, ISSN: 13675788. DOI: 10.1016/j.arcontrol.2019.03.009.

[68] A. Linder, R. Kanchan, P. Stolze, and R. Kennel, *Model-based predictive control of electric drives*. Cuvillier Verlag, 2010.

[69] J. Liu, Y. Gao, X. Su, M. Wack, and L. Wu, "Disturbance-observer-based control for air management of pem fuel cell systems via sliding mode technique," *IEEE Transactions on Control Systems Technology*, vol. 27, no. 3, pp. 1129–1138, 2019, ISSN: 1063-6536. DOI: 10.1109/TCST.2018.2802467.

[70] S. Liu, Y. Bin, Y. Li, and B. Scheppat, "Hierarchical mpc control scheme for fuel cell hybrid electric vehicles," *IFAC-PapersOnLine*, vol. 51, no. 31, pp. 646–652, 2018, ISSN: 24058963. DOI: 10.1016/j.ifacol.2018.10.151.

[71] Z. Liu, H. Chen, L. Peng, X. Ye, S. Xu, and T. Zhang, "Feedforward-decoupled closed-loop fuzzy proportion-integral-derivative control of air supply system of proton exchange membrane fuel cell," *Energy*, vol. 204, p. 122 490, 2021, ISSN: 03605442. DOI: 10.1016/j.energy.2021.122490.

[72] S. Lucia and B. Karg, "A deep learning-based approach to robust nonlinear model predictive control," *IFAC-PapersOnLine*, vol. 51, no. 20, pp. 511–516, 2018, ISSN: 24058963. DOI: 10.1016/j.ifacol.2018.11.038.

[73] J. Luna, S. Jemei, N. Yousfi-Steiner, A. Husar, M. Serra, and D. Hissel, "Nonlinear predictive control for durability enhancement and efficiency improvement in a fuel cell power system," *Journal of Power Sources*, vol. 328, no. 3, pp. 250–261, 2016, ISSN: 03787753. DOI: 10.1016/j.jpowsour.2016.08.019.

[74] J. Luna, E. Usai, A. Husar, and M. Serra, "Enhancing the efficiency and lifetime of a proton exchange membrane fuel cell using nonlinear model-predictive control with nonlinear observation," *IEEE Transactions on Industrial Electronics*, vol. 64, no. 8, pp. 6649–6659, 2017, ISSN: 0278-0046. DOI: 10.1109/TIE.2017.2682787.

[75] M. Lynas, B. Z. Houlton, and S. Perry, "Greater than 99% consensus on human caused climate change in the peer-reviewed scientific literature," *Environmental Research Letters*, vol. 16, no. 11, p. 114 005, 2021. DOI: 10.1088/1748-9326/ac2966.

[76] M. Herceg, M. Kvasnica, C.N. Jones, and M. Morari, "Multi-parametric toolbox 3.0," in *Proc. of the European Control Conference*, Zürich, Switzerland, 2013, pp. 502–510.

[77] Y. Ma, F. Zhang, J. Gao, H. Chen, and T. Shen, "Oxygen excess ratio control of pem fuel cells using observer-based nonlinear triple-step controller," *International Journal of Hydrogen Energy*, vol. 45, no. 54, pp. 29 705–29 717, 2020, ISSN: 03603199. DOI: 10.1016/j.ijhydene.2019.10.089.

[78] E. T. Maddalena, C. G. Da S. Moraes, G. Waltrich, and C. N. Jones, "A neural network architecture to learn explicit mpc controllers from data," *IFAC-PapersOnLine*, vol. 53, no. 2, pp. 11 362–11 367, 2020, ISSN: 24058963. DOI: 10.1016/j.ifacol.2020.12.546.

[79] R. F. Mann, J. C. Amphlett, M. A. Hooper, H. M. Jensen, B. A. Peppley, and P. R. Roberge, "Development and application of a generalised steady-state electrochemical model for a pem fuel cell," *Journal of Power Sources*, vol. 86, no. 1-2, pp. 173–180, 2000, ISSN: 03787753. DOI: 10.1016/S0378-7753(99)00484-X.

[80] S. Martinez-Boggio, D. Di Blasio, T. Fletcher, R. Burke, A. García, and J. Monsalve-Serrano, "Optimization of the air loop system in a hydrogen fuel cell for vehicle application," *Energy Conversion and Management*, vol. 283, p. 116 911, 2023, ISSN: 01968904. DOI: 10.1016/j.enconman.2023.116911.

[81] I. Matraji, S. Laghrouche, S. Jemei, and M. Wack, "Robust control of the pem fuel cell air-feed system via sub-optimal second order sliding mode," *Applied Energy*, vol. 104, no. 1, pp. 945–957, 2013, ISSN: 03062619. DOI: 10.1016/j.apenergy.2012.12.012.

[82] I. Matraji, S. Laghrouche, and M. Wack, "Cascade control of the moto-compressor of a pem fuel cell via second order sliding mode," in *IEEE Conference on Decision and Control and European Control Conference*, IEEE, 2011, pp. 633–638, ISBN: 978-1-61284-801-3. DOI: 10.1109/CDC.2011.6161412.

[83] R. N. Methekar, V. Prasad, and R. D. Gudi, "Dynamic analysis and linear control strategies for proton exchange membrane fuel cell using a distributed parameter model," *Journal of Power Sources*, vol. 165, no. 1, pp. 152–170, 2007, ISSN: 03787753. DOI: 10.1016/j.jpowsour.2006.11.047.

[84] P. Moraal and I. Kolmanovsky, "Turbocharger modeling for automotive control applications," in *SAE Technical Paper Series*, ser. SAE Technical Paper Series, SAE International400 Commonwealth Drive, Warrendale, PA, United States, 1999. DOI: 10.4271/1999-01-0908.

[85] V. Neisen, J. Mannhardt, and D. Abel, "Dynamic tracking of power demand for integrated fuel cell systems using nonlinear model predictive control," *IFAC-PapersOnLine*, vol. 53, no. 2, pp. 13 216–13 223, 2020, ISSN: 24058963. DOI: 10.1016/j.ifacol.2020.12.148.

[86] A. Niknezhadi, M. Allué-Fantova, C. Kunusch, and C. Ocampo-Martínez, "Design and implementation of lqr/lqg strategies for oxygen stoichiometry control in pem fuel cells based systems," *Journal of Power Sources*, vol. 196, no. 9, pp. 4277–4282, 2011, ISSN: 03787753. DOI: 10.1016/j.jpowsour.2010.11.059.

[87] J. O'Rourke, M. Arcak, and M. Ramani, "Real-time optimization of net power in a fuel cell system," *Journal of Power Sources*, vol. 187, no. 2, pp. 422–430, 2009, ISSN: 03787753. DOI: 10.1016/j.jpowsour.2008.11.060.

[88] G. Pannocchia, J. B. Rawlings, and S. J. Wright, "Fast, large-scale model predictive control by partial enumeration," *Automatica*, vol. 43, no. 5, pp. 852–860, 2007, ISSN: 00051098. DOI: 10.1016/j.automatica.2006.10.019.

[89] T. Parisini, M. Sanguineti, and R. Zoppoli, "Nonlinear stabilization by receding-horizon neural regulators," *International Journal of Control*, vol. 70, no. 3, pp. 341–362, 1998, ISSN: 0020-7179. DOI: 10.1080/002071798222271.

[90] T. Parisini and R. Zoppoli, "A receding-horizon regulator for nonlinear systems and a neural approximation," *Automatica*, vol. 31, no. 10, pp. 1443–1451, 1995, ISSN: 00051098. DOI: 10.1016/0005-1098(95)00044-W.

[91] A. Pilloni, A. Pisano, and E. Usai, "Observer-based air excess ratio control of a pem fuel cell system via high-order sliding mode," *IEEE Transactions on Industrial Electronics*, vol. 62, no. 8, pp. 5236–5246, 2015, ISSN: 0278-0046. DOI: 10.1109/TIE.2015.2412520.

[92] V. Puig, A. Rosich, C. Ocampo-Martinez, and R. Sarrate, "Fault-tolerant explicit mpc of pem fuel cells," in *2007 46th IEEE Conference on Decision and Control*, IEEE, 2007, pp. 2657–2662, ISBN: 978-1-4244-1497-0. DOI: 10.1109/CDC.2007.4434655.

[93] V. Puig, D. Feroldi, M. Serra, J. Quevedo, and J. Riera, "Fault-tolerant mpc control of pem fuel cells," *IFAC Proceedings Volumes*, vol. 41, no. 2, pp. 11 112–11 117, 2008, ISSN: 14746670. DOI: 10.3182/20080706-5-KR-1001.01883.

[94] J. T. Pukrushpan, A. G. Stefanopoulou, and H. Peng, "Modeling and control for pem fuel cell stack system," in *Proceedings of the 2002 American Control Conference (IEEE Cat. No.CH37301)*, IEEE, 2002, 3117–3122 vol.4, ISBN: 0-7803-7298-0. DOI: 10.1109/ACC.2002.1025268.

[95] J. T. Pukrushpan, A. G. Stefanopoulou, and H. Peng, "Control of fuel cell breathing," *IEEE Control Systems*, vol. 24, no. 2, pp. 30–46, 2004, ISSN: 1066-033X. DOI: 10.1109/MCS.2004.1275430.

[96] J. T. Pukrushpan, *Modeling and Control of Fuel Cell Systems and Fuel Processors*. 2003.

[97] J. T. Pukrushpan, A. G. Stefanopoulou, and H. Peng, *Control of Fuel Cell Power Systems*. London: Springer London, 2004, ISBN: 978-1-84996-928-4. DOI: 10.1007/978-1-4471-3792-4.

[98] S. M. Rakhtala, A. R. Noei, R. Ghaderi, and E. Usai, "Design of finite-time high-order sliding mode state observer: A practical insight to pem fuel cell system," *Journal of Process Control*, vol. 24, no. 1, pp. 203–224, 2014, ISSN: 09591524. DOI: 10.1016/j.jprocont.2013.08.006.

[99] C. A. Ramos-Paja, C. Bordons, A. Romero, R. Giral, and L. Martinez-Salamero, "Minimum fuel consumption strategy for pem fuel cells," *IEEE Transactions on Industrial Electronics*, vol. 56, no. 3, pp. 685–696, 2009, ISSN: 0278-0046. DOI: 10.1109/TIE.2008.2007993.

[100] *Roadmap towards zero emissions*, 2021. [Online]. Available: https://hydrogencouncil.com/wp-content/uploads/2021/10/Transport-Study-Full-Report-Hydrogen-Council-1.pdf.

[101] S. Rodatz, G. Paganelli, and L. Guzzella, "Optimizing air supply control of a pem fuel cell system," in *Proceedings of the 2003 American Control Conference, 2003*, IEEE, 2003, pp. 2043–2048, ISBN: 0-7803-7896-2. DOI: 10.1109/ACC.2003.1243375.

[102] K. Sankar and A. K. Jana, "Nonlinear multivariable sliding mode control of a reversible pem fuel cell integrated system," *Energy Conversion and Management*, vol. 171, pp. 541–565, 2018, ISSN: 01968904. DOI: 10.1016/j.enconman.2018.05.079.

[103] S. Sayadi, G. Tsatsaronis, and C. Duelk, "Exergoeconomic analysis of vehicular pem (proton exchange membrane) fuel cell systems with and without expander," *Energy*, vol. 77, pp. 608–622, 2014, ISSN: 03605442. DOI: 10.1016/j.energy.2014.09.054.

[104] M. Y. El-Sharkh, A. Rahman, and M. S. Alam, "Neural networks-based control of active and reactive power of a stand-alone pem fuel cell power plant," *Journal of Power Sources*, vol. 135, no. 1-2, pp. 88–94, 2004, ISSN: 03787753. DOI: 10.1016/j.jpowsour.2004.03.071.

[105] M. Y. El-Sharkh, A. Rahman, M. S. Alam, A. A. Sakla, P. C. Byrne, and T. Thomas, "Analysis of active and reactive power control of a stand-alone pem fuel cell power plant," *IEEE Transactions on Power Systems*, vol. 19, no. 4, pp. 2022–2028, 2004, ISSN: 0885-8950. DOI: 10.1109/TPWRS.2004.836191.

[106] T. E. Springer, T. A. Zawodzinski, and S. Gottesfeld, "Polymer electrolyte fuel cell model," *Journal of The Electrochemical Society*, vol. 138, no. 8, pp. 2334–2342, 1991, ISSN: 0022-3239. DOI: 10.1149/1.2085971.

[107] K. W. Suh, *Modeling, Analysis and Control of Fuel Cell Hybrid Power Systems*. 2006.

[108] S. Summers, C. N. Jones, J. Lygeros, and M. Morari, "A multiscale approximation scheme for explicit model predictive control with stability, feasibility, and performance guarantees," in *Proceedings of the 48h IEEE Conference on Decision and Control (CDC) held jointly with 2009 28th Chinese Control Conference*, IEEE, 2009, pp. 6327–6332, ISBN: 978-1-4244-3871-6. DOI: 10.1109/CDC.2009.5400583.

[109] J. Sun and I. V. Kolmanovsky, "Load governor for fuel cell oxygen starvation protection: A robust nonlinear reference governor approach," *IEEE Transactions on Control Systems Technology*, vol. 13, no. 6, pp. 911–920, 2005, ISSN: 1063-6536. DOI: 10.1109/TCST.2005.854323.

[110] T. Sun, X. Zhang, B. Chen, and X. Liu, "Coordination control strategy for the air management of heavy vehicle fuel cell engine," *International Journal of Hydrogen Energy*, vol. 45, no. 39, pp. 20 360–20 368, 2020, ISSN: 03603199. DOI: 10.1016/j.ijhydene.2019.10.134.

[111] R. Talj, M. Hilairet, and R. Ortega, "Second order sliding mode control of the moto-compressor of a pem fuel cell air feeding system, with experimental validation," in *2009 35th Annual Conference of IEEE Industrial Electronics*, IEEE, 2009, pp. 2790–2795, ISBN: 978-1-4244-4648-3. DOI: 10.1109/IECON.2009.5415414.

[112] R. J. Talj, R. Ortega, and M. Hilairet, "A controller tuning methodology for the air supply system of a pem fuel-cell system with guaranteed stability properties," *International Journal of Control*, vol. 82, no. 9, pp. 1706–1719, 2009, ISSN: 0020-7179. DOI: 10.1080/00207170802713992.

[113] R. J. Talj, D. Hissel, R. Ortega, M. Becherif, and M. Hilairet, "Experimental validation of a pem fuel-cell reduced-order model and a moto-compressor higher order sliding-mode control," *IEEE Transactions on Industrial Electronics*, vol. 57, no. 6, pp. 1906–1913, 2010, ISSN: 0278-0046. DOI: 10.1109/TIE.2009.2029588.

[114] M. Tekin, D. Hissel, M.-C. Pera, and J. M. Kauffmann, "Energy-management strategy for embedded fuel-cell systems using fuzzy logic," *IEEE Transactions on Industrial Electronics*, vol. 54, no. 1, pp. 595–603, 2007, ISSN: 0278-0046. DOI: 10.1109/TIE.2006.885471.

[115] N. Tomi, S. Hasegawa, J. Farnsworth, H. Imanishi, Y. Ikogi, and K. Sato, "Development of air supply controller for fcv based on model-based development approach," in *SAE Technical Paper Series*, ser. SAE Technical Paper Series, SAE International400 Commonwealth Drive, Warrendale, PA, United States, 2021. DOI: 10.4271/2021-01-0742.

[116] Z. Ugray, L. Lasdon, J. Plummer, F. Glover, J. Kelly, and R. Martí, "Scatter search and local nlp solvers: A multistart framework for global optimization," *INFORMS Journal on Computing*, vol. 19, no. 3, pp. 328–340, 2007, ISSN: 1091-9856. DOI: 10.1287/ijoc.1060.0175.

[117] A. Ulbig, S. Olaru, D. Dumur, and P. Boucher, "Explicit solutions for nonlinear model predictive control: A linear mapping approach," in *2007 European Control Conference (ECC)*, IEEE, 2007, pp. 3295–3302, ISBN: 978-3-9524173-8-6. DOI: 10.23919/ECC.2007.7068278.

[118] A. Vahidi, A. Stefanopoulou, and H. Peng, "Current management in a hybrid fuel cell power system: A model-predictive control approach," *IEEE Transactions on Control Systems Technology*, vol. 14, no. 6, pp. 1047–1057, 2006, ISSN: 1063-6536. DOI: 10.1109/TCST.2006.880199.

[119] A. Vahidi, A. Stefanopoulou, and H. Peng, "Model predictive control for starvation prevention in a hybrid fuel cell system," in *Proceedings of the 2004 American Control Conference*, IEEE, 2004, 834–839 vol.1, ISBN: 0-7803-8335-4. DOI: 10.23919/ACC.2004.1383709.

[120] M. Vrlić, D. Ritzberger, and S. Jakubek, "Model-predictive-control-based reference governor for fuel cells in automotive application compared with performance from a real vehicle," *Energies*, vol. 14, no. 8, p. 2206, 2021. DOI: 10.3390/en14082206.

[121] Y.-X. Wang, D.-J. Xuan, and Y.-B. Kim, "Design and experimental implementation of time delay control for air supply in a polymer electrolyte membrane fuel cell system," *International Journal of Hydrogen Energy*, vol. 38, no. 30, pp. 13 381–13 392, 2013, ISSN: 03603199. DOI: 10.1016/j.ijhydene.2013.06.040.

[122] L. Xu *et al.*, "Robust control of internal states in a polymer electrolyte membrane fuel cell air-feed system by considering actuator properties," *International Journal of Hydrogen Energy*, vol. 42, no. 18, pp. 13 171–13 191, 2017, ISSN: 03603199. DOI: 10.1016/j.ijhydene.2017.03.191.

[123] D. Yang, R. Pan, Y. Wang, and Z. Chen, "Modeling and control of pemfc air supply system based on t-s fuzzy theory and predictive control," *Energy*, vol. 188, p. 116 078, 2019, ISSN: 03605442. DOI: 10.1016/j.energy.2019.116078.

[124] R. Yang, Z. Liu, and H. Su, "Control lyapunov function based control strategy for air supply system of pem fuel cells," in *2017 29th Chinese Control And Decision Conference (CCDC)*, IEEE, 2017, pp. 1964–1969, ISBN: 978-1-5090-4657-7. DOI: 10.1109/CCDC.2017.7978838.

[125] H. Yuan, H. Dai, P. Ming, J. Zhan, X. Wang, and X. Wei, "A fuzzy extend state observer-based cascade decoupling controller of air supply for vehicular fuel cell system," *Energy Conversion and Management*, vol. 236, p. 114 080, 2021, ISSN: 01968904. DOI: 10.1016/j.enconman.2021.114080.

[126] M. N. Zeilinger, "Real-time model predictive control," Ph.D. dissertation, ETH Zurich, 2011. DOI: 10.3929/ethz-a-6619878.

[127] H. K. Zhang, Y. F. Wang, D. H. Wang, and Y. L. Wang, "Adaptive robust control of oxygen excess ratio for pemfc system based on type-2 fuzzy logic system," *Information Sciences*, vol. 511, pp. 1–17, 2020, ISSN: 00200255. DOI: 10.1016/j.ins.2019.08.005.

[128] X. Zhang, M. Bujarbaruah, and F. Borrelli, "Near-optimal rapid mpc using neural networks: A primal-dual policy learning framework," *IEEE Transactions on Control Systems Technology*, vol. 29, no. 5, pp. 2102–2114, 2021, ISSN: 1063-6536. DOI: 10.1109/TCST.2020.3024571.

[129] Y. Zhang, S. Xu, and C. Lin, "Performance improvement of fuel cell systems based on turbine design and supercharging system matching," *Applied Thermal Engineering*, vol. 180, p. 115 806, 2020, ISSN: 13594311. DOI: 10.1016/j.applthermaleng.2020.115806.

[130] D. Zhao, Q. Zheng, F. Gao, D. Bouquain, M. Dou, and A. Miraoui, "Disturbance decoupling control of an ultra-high speed centrifugal compressor for the air management of fuel cell systems," *International Journal of Hydrogen Energy*, vol. 39, no. 4, pp. 1788–1798, 2014, ISSN: 03603199. DOI: 10.1016/j.ijhydene.2013.11.057.

[131] Q. Zhou, N. Li, X. Chen, T. Xu, S. Hui, and Di Zhang, "Analysis of water drop erosion on turbine blades based on a nonlinear liquid–solid impact model," *International Journal of Impact Engineering*, vol. 36, no. 9, pp. 1156–1171, 2009, ISSN: 0734743X. DOI: 10.1016/j.ijimpeng.2009.02.007.

[132] C. Ziogou, S. Papadopoulou, M. C. Georgiadis, and S. Voutetakis, "On-line nonlinear model predictive control of a pem fuel cell system," *Journal of Process Control*, vol. 23, no. 4, pp. 483–492, 2013, ISSN: 09591524. DOI: 10.1016/j.jprocont.2013.01.011.

[133] C. Ziogou, S. Voutetakis, M. C. Georgiadis, and S. Papadopoulou, "Model predictive control (mpc) strategies for pem fuel cell systems – a comparative experimental demonstration," *Chemical Engineering Research and Design*, vol. 131, pp. 656–670, 2018, ISSN: 02638762. DOI: 10.1016/j.cherd.2018.01.024.

[134] C. Ziogou, S. Voutetakis, S. Papadopoulou, and M. C. Georgiadis, "Modeling, simulation and experimental validation of a pem fuel cell system," *Computers & Chemical Engineering*, vol. 35, no. 9, pp. 1886–1900, 2011, ISSN: 00981354. DOI: 10.1016/j.compchemeng.2011.03.013.